Understanding the Responses of Deep Convective Clouds to a Changing Thermodynamic Environment

Marieanne Christie Leong

Submitted in accordance with the requirements for the degree of
Doctor of Philosophy

The University of Leeds
School of Earth and Environment

September 2018

Declaration of Authorship

The candidate confirms that the work submitted is her own and that appropriate credit has been given where reference has been made to the work of others.

This copy has been supplied on the understanding that it is copyright material and that no quotation from the thesis may be published without proper acknowledgement.

The right of Marieanne Christie Leong to be identified as Author of this work has been asserted by her in accordance with the Copyright, Designs and Patents Act 1988.

Copyright 2018 The University of Leeds and Marieanne Christie Leong.

"I wanna show the nation my appreciation."
- Shaggy

This thesis is dedicated to the people of my country, Malaysia,
and to my family.

Duc in altum.

“ I willingly boast of my weaknesses,
so that the power of Christ may rest upon me.
Therefore I am content with weakness,
with mistreatment, with distress,
with persecutions and difficulties for the sake of Christ;
for when I am powerless, it is then that I am strong.
Do you know how clouds float in the sky,
the work of God’s amazing skill?
Can you shout orders to the clouds
and make them drench you with rain?
At God’s command, amazing things happen,
wonderful things that we can’t understand. ”

— 2 Corinthians 12:9-10, Job 37:5,16; 38:34

Acknowledgements

This thesis represents not only my work at the computer and perpetual contemplation throughout the time of my PhD candidacy. It is also an outpouring of my sincerest gratitude from the core of my being, for having the chance to commence on such an honourable degree and experience of a lifetime. My gratitude goes out to my lecturers-turned-colleagues (especially Dr Marinah Muhammad, Prof. Razak Wahab, Ir Arham Bahar) for nurturing the little seed of potential in me from my undergraduate years, paving the way for me to be where I am now. Of course, my being here would hardly be made possible without the administrative and financial support from Universiti Malaysia Kelantan and the government of Malaysia.

My highest thanksgiving goes out to my family members who encouraged me to pursue my dreams. I would like to thank my mother, Catherine Ganang, the most for her unwavering motherly patience in dealing with my tantrums that never seem to go away with age and distance, and for her constant shower of prayers, motivation and inspiration. I would also like to thank my brother, Malcom Leong, for his brotherly duty of fulfilling his sister's finicky requests.

With immense gratitude, I would like to extend my acknowledgement to a number of people who have helped me at every step of my journey:

First and foremost, I would like to acknowledge and thank Steven Dobbie, who is not only a supervisor. He is also a mentor and, to some extent, like a father to me. His exceptional guidance advanced me academically and indirectly contributed to my personal development. He taught me to let science speak for itself, and that irregularities in research are not wrong; rather, they are evolving understanding. His advice on "be more analog in your analysis" is forever engraved in my being, and his kind and gentle nature will always be treasured.

I would also like to extend my acknowledgement to Cecille Villanueva-Birriel and Sonia Lasher-Trapp for providing the data and information necessary for my research, and to Hugh Morrison, Bethan White and Zhiqiang Cui for their guidance and opinion regarding the cloud microphysics scheme, as well as to Richard Rigby, whom I hailed as the IT wizard for resolving my technical issues, and to Huiyi Yang for helping out with some IDL codes. Grateful thanks also to my examiners, Satyajit Ghosh and Alan Gadian for taking the time to read and examine my work.

I would like to thank all the angels who came my way, who are very much integral to my work-life see-saw: they give me a life of balance by lifting me up when I'm down and anchor me down when I'm up in the air for too long. Deniche Leoncio, for smoothly steering me in my cultural transition and entertaining my love for snow and western civilisation. Karim Ouda, for saving me from drowning in the sea of Fortran codes. Du Yinghan and Ahlam Abumughli, for wonderful memories in the first year and now generously sacrificing their sleep to offer their time for our occasional video-calls across three different time zones.

To Laurynas Pukenas, whose gentleness and patience helped me to be comfortable in discussing my research, whose rigid emphasis on efficiency and quality made me succumb to using LaTeX and Spyder, as well as introducing me to the *.svg* format and Inkscape, and whose cheekiness recruited me to join in his endless pranks. To Weronika Paukszta, for being the loveliest listener and whose passion for Taizé seeped into my veins and henceforth became a powerhouse of grace and motivation throughout my entire research. To Anna Sinyangwe, who is always ready to be the recipient of my curious queries and provide enlightenment to my oddities and wonderings, in addition to providing me with a list of period dramas for my keen indulgence on life in the early civilisation. To Robin Sebolino, for his wise counsel, and for his enduring patience in entertaining my philosophical ramblings and in putting up with my occasional feistiness. To Giorgio Taverna, for his unconditional support as I go through life's trials and challenges, and for engaging in honest and open conversations on challenging topics. To Henri Hägglund, for bearing my tantrums ever so patiently, for challenging my opinions and perspectives, and for fulfilling my dreams of camping in the silence and tranquility of the alpine tundra with reindeers and glaciers in the Swedish wilderness, and for canoeing in the beautiful, sparkly Swedish waters. To Luke Boxall, whose brief encounter not only brought cheer to my life but awakened me inside out, and thereafter set me on a path of spiritual transformation that brought new breath to my life. I owe him much for that, and I look forward to the day when I can return the favour.

It is commonly believed that spirituality ought to be confined within the private sphere, but the guidance of these spiritual people have taught me otherwise. Their counsel on my religiousity were just as helpful, as my lessons that are academic. I would like to thank our University Catholic Chaplain, Fr Peter Kravos, whose eloquent homilies kept me thirsting for more. The Franciscan friars, Fr Gabriel and Br Joshua, whose joy and lightheartedness effortlessly lifted my spirit. A Benedictine monk, Fr Kevin Hayden, for his transcendent empathy that soothes my soul. Mgr. Philip Moger, for his warmth and kind counsel at Leeds Cathedral. Fr John Bartunek, Bishop Barron, Fr Mike Schmitz and Fr Henri Nouwen, whose writings and digital resources enriched my ever-enquiring minds on spiritual physics.

Last but not least, I would like to thank my kindred in Leeds and Sheffield who are central to my journey here. They teach me, coach me, and feed me like a princess. To Stephania Albert, for her sisterly care and counsel, and the gift of tears. To Farm Yan Yan and Aroland Kiring, for their open arms and listening ears when I am at my lows. I am especially grateful for being a godmother to their daughter, Hannah Grace, who has been a great inspiration and has brought out a part (and skills) of me that I never knew I had. And to Josiah Wang, I thank you so much for your patience in teaching me Python, especially during the times when I robbed you of your sleep and peace.

Finally, I would like to thank many others who have, in one way or another, guided me through the ebbs and flows of life, and left an indelible imprint on my life.

Abstract

Deep convective clouds play a key role in regulating the Earth's water and energy cycles and are therefore an important component of the Earth's climate system. Much work has been done on investigating factors such as how aerosols affect these clouds but much less emphasis has been on how the future changes in thermodynamic structure of the atmosphere will affect these clouds. It is vitally important to know how clouds will respond to these changed thermodynamic conditions.

This study explores how modelled deep convective clouds respond to the projected future warmer climate and compares it with past (current) climate. Atmospheric thermodynamic profiles are taken from NCAR CCSM3 global climate model and the modelling study was based on simulations of idealised deep convective clouds using the Weather Research Forecast (WRF) model with a double-moment cloud microphysics scheme.

The modelling study showed that the future thermodynamic environment produced deep convective clouds that are on average 32% lower in cloud base height, 8.5% higher in freezing level and 9% lower in cloud-top height compared to the past climate results. This results in the future clouds having an average of 15% deeper warm-phase cloud layer and 18% shallower cold-phase cloud layer than in the past climate, signifying a strong warm rain process and reduced cold rain process, where the cold rain process is traditionally known to be the dominant precipitation-forming process in the current climate. The strong warm rain process leads to intense heavy rainfall, which reduces the availability of water in the updraught reaching the ice phase, thus reducing the clouds' vertical and horizontal extent.

An in-depth investigation was performed to assess the factors associated with the changes of the future thermodynamic environment influencing the cloud development. Such factors include assessment of the significance of temperature structure, relative humidity structure, both structural changes, and increased moisture due to the warmer mean temperature. It was found that the structural effects of temperature and relative humidity have greater impact on the cloud development compared to the increase in the mean temperature. The temperature structure factor significantly reduces the average total water content and cloud vertical extent by 75% and 8 km, respectively. On the other hand, the relative humidity

structure significantly increases the average total water content and cloud vertical extent by 80% and 1.8 km, respectively. Separately assessing these two factors gives significant opposing effects on the cloud's total water content and vertical height. When combined, these two effects cancels out to some extent, but they still produce weaker and smaller deep convective clouds than the effects that arise from the mean temperature increase.

Following from the differences in the cloud development between the past and future environments, the strong warm rain process and weak cold rain process results in the cloud fraction in the future reduced by half of that in the past environment. This reduced cloud horizontal extent results in cloud radiative forcing at the top of the atmosphere that is positive, indicating an increased warming in the future environment. The average local cloud radiative forcing was evaluated to be 43.7 and 54.7 W m^{-2} for the whole cloud and anvil cloud, respectively. If this is extended to midlatitude deep convective region over land with a coverage of 3% or global coverage of deep convective clouds of less than 1%, a simplistic approximation of the cloud radiative forcing is evaluated to be +1.31 and +0.44 W m^{-2}, respectively. This is opposite to the radiative forcing exerted by aerosol-cloud interaction reported in the Intergovernmental Panel on Climate Change Fifth Assessment Report (IPCC AR5), which was estimated at -0.55 W m^{-2}.

The results from this study highlight that the changes in the vertical thermodynamic structure affect the cloud development significantly. This study was based on the output of one global climate model, however, it does suggest that it is important that climate modelling groups pay particular attention to the way their models forecast the thermodynamic structure in both temperature and moisture of the future climate.

Contents

List of Figures

List of Tables

List of Abbreviations

CAPE	Convective available potential energy
CIN	Convective inhibition
CCSM3	Community Climate System Model Version 3
CONUS	Contiguous United States
DALR	Dry adiabatic lapse rate
DCC	Deep convective cloud
ELR	Environmental lapse rate
IPCC AR5	Intergovernmental Panel on Climate Change Fifth Assessment Report
LW	Longwave
NCAR	National Center for Atmospheric Research
RF	Radiative forcing
SALR	Saturated adiabatic lapse rate
SW	Shortwave
SST	Sea surface temperature
TOA	Top-of-the-atmosphere
TRMM	Tropical Rainfall Measuring Mission
WRF	Weather Research Forecast

Units

J kg^{-1}	Joules per kilogram
ppmv	parts per million by volume
μm	micrometre
W m^{-2}	Watts per square metre

Study locations

AND	Anderson, South Carolina
BIR	Birmingham, Alabama
CHA	Charlotte, North Carolina
DAY	Dayton, Ohio
JAS	Jasper, Indiana
MAD	Madison, Wisconsin
MIN	Minneapolis, Minnesota

Chapter 1

Introduction

1.1 Background and motivation

Most of us have had a fascination with the elusive nature of clouds at some point of time in our lives. Leonardo da Vincci described clouds as 'bodies without surface' – they are ghostlike, ephemeral, nebulous; you can see their shapes, yet it's hard to say where their forms begin and end (Pretor-Pinney, 2007). In general, clouds form from the condensation of water vapour in the atmosphere. The atmosphere contains about 0.001% of the total water content on earth (Schneider *et al.*, 2017). If all the condensed water in clouds were spread as a liquid layer on the earth's surface, it would correspond to the thickness of a human hair of 0.1 mm thin (Schneider *et al.*, 2017).

The formation of clouds is associated with the development of atmospheric circulations. The thermodynamic and dynamic components of the atmospheric circulations redistribute heat and moisture throughout the Earth-atmosphere system, leading to the formation of clouds within space and time scales of a few tens of metres to a few hundreds of kilometres and from a few minutes to several hours, respectively (Emanuel, 1994). The formation of clouds involves complex thermodynamic and microphysical processes that are crucial in regulating the earth's water and energy cycle (Allen and Ingram, 2002). For example, the low decks of stratocumulus clouds do not produce precipitation, however their extensive coverage effectively reflects a large proportion of the incoming shortwave radiation from

the sun, thereby cools the earth (Chen *et al.*, 2000). In contrast, deep convective clouds transport moisture from the surface to the far reaches of the troposphere and manifest as thunderstorms that produce rain that are essential for life on earth. In addition, the generation of extensive anvil outflows at the top of the deep convective cloud traps outgoing longwave radiation, thus warms the earth (Ramanathan and Collins, 1991).

The IPCC AR5 (Boucher *et al.*, 2013) reported an unprecedented warming of the earth since the pre-industrial times and projected an increased warming in the future climate. The global temperatures have increased 1 °C from pre-industrial times and the concentration of carbon dioxide is 120 ppmv higher since then (Morice *et al.*, 2012). In the 2015 Paris Agreement (UNFCCC, 2015), 193 countries have agreed to keep global temperature increases below 2 °C in order to reduce the risks of climate change that can come about from anthropogenic advances. Just recently, the 2018 Nobel Prize in Economics was awarded to Nordhaus and Romer, who integrated technological innovations and climate change with economic growth in their Dynamic Integrated Climate-Economy (DICE) model. This allows us to examine the consequences of climate policy interventions, which was not included in the 'SRES A1B' future climate scenario (which assumes a globalised future with rapid economic and technological growth with moderate consumption of fossil fuel) used in this study.

Given the profound influence of clouds and precipitation on Earth's water and energy budgets, it raises concern and interests to the scientific community and policy makers as to how clouds would respond to warming. An increase in carbon dioxide concentration results in atmospheric warming which usually accompanies an increase in atmospheric moisture, which not only increase the total amount of precipitation (Trenberth *et al.*, 2003; Del Genio and Kovari, 2002; Pall *et al.*, 2007; Kendon *et al.*, 2012; Kendon *et al.*, 2014; Prein *et al.*, 2016) but can change the flow field of other meteorological phenomena, e.g. intensification of tropical cyclones (Takayabu *et al.*, 2015), and also influence the distribution of radiative heating within the atmosphere (Stevens *et al.*, 2017). Despite the numerous studies undertaken to study the future changes in clouds and precipitation in response to warming, the variability in cloud responses remains a prominent source of uncer-

tainty in climate projections (e.g. Stephens, 2005; Held and Soden, 2006; Webb *et al.*, 2006; Dufresne and Bony, 2008; Gettelman *et al.*, 2012; Schneider *et al.*, 2017) as is further discussed in **Section 1.2**.

1.2 Challenges

Most studies have used coarse resolution models that do not adequately represent the fine-scale cloud and precipitation processes critical for understanding the physical mechanisms that may result in changes in convective activities in response to warming (Volosciuk *et al.*, 2015; Rasmussen *et al.*, 2017). Unlike cloud-resolving models, the fine-scale grid size in cloud-resolving models allows numerous couplings to occur between convective motions and physical processes to be resolved (Prein *et al.*, 2015; Guichard and Couvreux, 2017). However, the accuracy of the models are often questioned due to the different physical processes employed in various models which are often poorly defined by theory or experiment (Lee *et al.*, 2016). The models are usually evaluated against measurements so that the model state matches the observed state as closely as possible, however, Lee *et al.* (2016) demonstrated that observational constraints do not necessarily reduce the uncertainty in predicted simulations.

For example, many statistical studies (e.g. Kharin *et al.*, 2013; Ban *et al.*, 2015; Mizuta *et al.*, 2017) found that the increase in the amount of extreme precipitation reported in the IPCC AR5 (Boucher *et al.*, 2013) is consistent with the deduction that more moisture is converted into precipitation in a warmer atmosphere according to the Clausius-Clapeyron relationship, that is, an increase of approximately 7% per degree warming. With this increased temperature and moisture, it is generally expected that there will be an increase in cyclogenesis that accompanies it (Launder, 2017). However, there are studies that found non-conformity of precipitation amount to the Clausius-Clapeyron relationship (e.g. Berg *et al.*, 2013; Prein *et al.*, 2017) because it may be affected by other factors such as local thermodynamic and weather systems and moisture availability, as well as regional circulation patterns (Hibino *et al.*, 2018). The IPCC AR5 (Boucher *et al.*, 2013) does not include the relative contributions of different weather systems to future changes in clouds and precipitation (Utsumi *et al.*, 2016), which led to studies being undertaken based

on individual meteorological phenomena (e.g. Xu, 2013; Sohn *et al.*, 2013; Shiogama *et al.*, 2014; Hamada *et al.*, 2015; Takayabu *et al.*, 2015; Pall *et al.*, 2017; Song *et al.*, 2017). Different weather systems exhibit different vertical thermodynamic structures, hence understanding how the vertical thermodynamic structure influence cloud development is central to improving the representation of deep convective clouds in climate models. This would be one aspect of many possible improvements needed for models to accurately model future climate change and variability. It is crucial to understand how thermodynamic structure affects cloud development because climate change not only bring about an increased warming, but also changes to the vertical thermodynamic structure as well as in the distribution of water vapour in the atmosphere (e.g. Emori and Brown, 2005; Sherwood *et al.*, 2010). Furthermore, much work has been done on investigating factors such as how aerosols affect these clouds but much less emphasis has been on how the future changes in thermodynamic structure of the atmosphere will affect these clouds. It is vitally important to know how clouds will respond to changes in thermodynamic conditions that arise from climate change, and this thesis sets out to address this concern.

1.3 Aims of the thesis

For the challenges stated in **Section 1.2**, this thesis aims to assess the responses of deep convective clouds to changing thermodynamic environment predicted by climate change. In particular, the thesis aims to answer the question, *"How do deep convective clouds behave in a warmer climate?"* Following that, a further investigation is aimed at understanding how clouds respond to changes in the vertical structure of temperature and moisture. Finally, the thesis aims to assess the consequential impact on the radiative properties following the changes in the cloud responses to warming. The aims are summarised and detailed as follows:

Aims:

1. To understand the way in which future climate will change the thermodynamic structure of the atmosphere.

2. To understand the way in which future climate will affect the macroscopic features of deep convective clouds relative to our current climate. The macroscopic features include cloud base height, cloud top height, cloud cover, and anvil extent.

3. To understand the microphysical changes in the clouds that give rise to the macroscopic changes. These will include especially heat and moisture changes that give rise to changes in buoyancy, updraft speeds, rates of nucleation, etc.

4. To understand the way in which the macroscopic changes in the cloud affect the cloud radiative properties. Will the clouds have a change in their net radiative forcing in the future?

1.4 Thesis outline

The thesis is organised as follows.

Chapter 2 provides a review of the literature prior to this study.

Chapter 3 describes the methodology applied in this study, including the atmospheric profiles utilised in this study.

Chapter 4 presents the findings of simulated, idealised deep convective clouds' responses to a changing thermodynamic environment. The emphasis is on comparing the responses of clouds between the past and future, warmer climates.

Chapter 5 explores the role of temperature and moisture in contributing to the changes in the responses of deep convective clouds. This approach advances the understanding on how the thermodynamic environments' influences on convection may vary with changes in temperature and moisture.

Chapter 6 assesses the radiative properties of deep convective clouds in response to changing thermodynamic environments.

Chapter 7 summarises the overall discussion and conclusion of the thesis. The study limitations of this thesis are also addressed and recommendations for future work are suggested.

Chapter 2

Literature review

2.1 Introduction

Clouds are ubiquitous over the entire earth, covering two thirds of the earth's surface. They determine a large proportion of the water and energy budgets on Earth and are thus a critical component of the climate system (Allen and Ingram, 2002). For example, clouds transport heat and moisture from the surface to the atmosphere and produce precipitation essential for life on earth. In addition, the globally-averaged cloud radiative effect is - 20 W m^{-2} (Allan, 2011), which gives a cooling effect to the earth. However, in recent years, the globally-averaged temperatures have increased unprecedentedly (Boucher *et al.*, 2013) and it is expected to continue to increase in the future climate (Morice *et al.*, 2012). Changes in temperature can bring about many changes to the climate system, including clouds, at global, regional and local scales (Bony *et al.*, 2016). To first order, cloud characteristics are determined by the state of the thermodynamic environment. As the climate changes, the environment that clouds form in will also change. This, in turn, can affect the environment. Therefore, a natural, and perhaps one of the most frequently asked questions regarding climate change arise, *"how will clouds evolve with climate change?"* In other words, *"how would a thermodynamically-changed environment affect the way clouds would form and evolve?"*

The remainder of this chapter is sequenced as follows. To provide a background knowledge to the innate characteristics of deep convective clouds, **Section 2.2**

presents a brief description on the nature of convection that generate deep convective clouds, and the microphysical processes that occur throughout the lifetime of the deep convective clouds. **Section 2.3** presents the cloud radiative properties and **Section 2.4** discusses the observational and numerical modelling studies that have been carried out to examine cloud response to warming, including the various hypotheses put forth by different researchers. Finally, **Section 2.5** concludes the chapter by identifying the limitation of existing hypotheses and studies.

2.2 Convection and deep convective clouds

Convective clouds are an integral part of the earth's climate system. They redistribute water, heat and momentum from the surface to the atmosphere. They begin as shallow cumulus clouds and develop into deep convective clouds if there is sufficient updraught and water vapour for vertical development. Deep convective clouds are traditionally divided into two portions (Houze, 1993; Emanuel, 1994; Feng *et al.*, 2011; Feng *et al.*, 2012), that is the deep convective precipitating tower and the non-precipitating anvil canopy. Therefore, they are important to the atmospheric hydrological cycle due to the heavy rainfall they produce, as well as to the earth's energy budget due to their phase changes and radiative properties.

The formation of deep convective clouds typically begin within the boundary layer (e.g. Bennett *et al.*, 2006). For example, unequal surface heating in the boundary layer can cause localised air parcels to be warmer than the surrounding. As such, they rise from the surface up into the overlying boundary layer. These rising air parcels are known as thermals or plumes and they usually lose their buoyancy in the upper part of the boundary layer (Lenschow and Stephens, 1980). However, stronger thermals that have sufficient momentum may penetrate into the capping inversion above the boundary layer, thereby initiating convection (e.g. Browning *et al.*, 2007). On the other hand, convection can also occur above the boundary layer, known as elevated convection (e.g. Corfidi *et al.*, 2008; White, 2012). The mechanisms that trigger elevated convection are (i) orographic lifting, when air is forced to rise over a mountainous barrier; (ii) frontal wedging, where warmer, less dense air is forced over colder, denser air along a front.

In addition, the triggering of deep convection varies with latitudes due to the action of the Coriolis force on the large-scale meridional temperature and pressure gradient between air masses. The weaker (stronger) Coriolis force in the tropics (mid-latitudes) flattens out (enhances) the temperature and pressure gradient between air masses. As a result, convection in the tropics is usually triggered by local differential heating from the sun, while in the mid-latitudes, convection is often triggered by large-scale forcing (e.g. large-scale lifting of air along cold fronts). In the summertime mid-latitudes, however, the large-scale forcing is weak and the characteristics of temperature and pressure gradients are similar to that of the tropics and so convection is often triggered from a response towards localised differential heating.

In this thesis, the work undertaken focuses on deep convection arising from the boundary layer. From the viewpoint of atmospheric thermodynamics, convection results as a consequence of unstable atmosphere and can be further sustained by the release of latent heat through phase changes as the convective clouds develop. Convection from unstable air is referred to as originating from convective instability (further discussed in **Section 2.2.1**), whereas the enhancing of convection of diabatic latent processes is related to cloud microphysical processes (further discussed in **Section 2.2.2**).

2.2.1 Atmospheric instability

Atmospheric instability is a measure of the atmosphere's tendency to allow or deter vertical motion. This can be largely influenced by large-scale circulation, but can also be influenced by local processes such as turbulence and differential heating in the planetary boundary layer. A thermodynamic parameter known as the convective available potential energy (CAPE, Emanuel, 1994) is often used as an indicator of atmospheric instability. Meteorologists use CAPE as an indicator for the potential of thunderstorms. CAPE gives an idea of 'how much' a convective cell is able to grow and develop on its own, but only in the case that the capping inversion of the boundary layer is overcome. The energy required to overcome the negatively-buoyant energy exerted by the capping inversion on the parcel is known as the convective inhibition (CIN). The two convective energy, CIN and CAPE are

differentiated by the negative and positive signs in their values. Values below 0 J kg^{-1} indicate CIN, while values above 0 J kg^{-1} indicate CAPE. The more negative the values of CIN are, the more stable the atmosphere is and thus more energy is needed to initiate convection. On the other hand, the more positive the values of CAPE are, the more unstable the atmosphere is, thus increases the possibility for convection.

One of the causes of atmospheric instability is the differential heating on the surface. Instability can increase through daytime heating of the surface. This surface heating results in some parcels of air being warmer relative to the surrounding air, consequentially inducing instability. As the parcel of air gets warmer, it expands, gains in density and thus rises. In expanding, the air parcel pushes surrounding air and expends energy in doing so. As a result, the temperature of the parcel drops. This process of expansion and cooling without exchange of heat with the surrounding is known as the adiabatic cooling. The rate of adiabatic cooling is known as the adiabatic lapse rate. There are two adiabatic lapse rates: dry adiabatic lapse rate (DALR) and saturated adiabatic lapse rates (SALR) that cools at a rate of approximately 10 °C km^{-1} and 5.5 °C km^{-1}, respectively. On the other hand, the decreasing pressure with height results in the decrease in environmental temperature due to slower molecular motions with decreasing pressure. This gives rise to the environmental lapse rate, that is the rate of cooling of environmental temperature with height. The environmental lapse rate (ELR) varies between regions, but is typically an average of 6.5 °C km^{-1}.

These three lapse rates determine the stability of air. The stability of air is associated with the difference in density between the rising air parcel and the environment. Air is stable when the ELR is less than both the DALR and SALR. This is because the environment will cool at a slower rate, whereas the rising air parcel cools at a faster rate, causing it to lose buoyancy thus restricting further vertical displacement. On the other hand, air can be unstable in two conditions. The first condition is known as absolute instability, and happens when the ELR is greater than both the DALR and SALR. Due to the slower cooling of the rising air parcel and faster cooling of the environmental air, the rising air parcel stays warmer than environment and therefore can continue to rise. The second condition is known as

conditional stability, and happens when the ELR is less than the DALR but greater than the SALR. In this case, the air is stable for unsaturated air parcel unless the air is forced to rise (e.g. orographic lifting) to an altitude where it is cool enough for condensation to occur. At this altitude, the rising air parcel is now saturated and cools at a rate less than that at which the environmental temperature cools with height. The rising air parcel is therefore warmer than the environment and continues to rise.

Deep convection generally results from an absolutely unstable atmosphere. When an unsaturated air parcel rises and reaches its dew-point temperature, condensation ensues. The dew-point temperature is the temperature at which the water vapour within the rising air parcel begin to condense into liquid droplets, which results in cloud formation. The height at which the parcel reaches its dew-point temperature is called the lifted condensation level (LCL) and this identifies the cloud base. The microphysical processes associated with the evolution of cloud development will be described in **Section 2.2.2**.

2.2.2 Cloud microphysical processes

The microphysical processes inside deep convective clouds are closely linked to cloud dynamics (Cotton *et al.*, 1986; Johnson *et al.*, 2015) and largely determine the macrophysical structure of the clouds. For example, the release of latent heat during condensation, freezing and sublimation enhances buoyancy that drives the updraughts, while hydrometeor mass loading reduces the cloud buoyancy. In turn, the convective strength determines the vertical and horizontal extent over which cloud hydrometeors are distributed (e.g. Machado and Rossow, 1993; Igel *et al.*, 2014; Masunaga and Luo, 2016; Protopapadaki *et al.*, 2017), and this can have an impact on the earth's radiation budget (e.g. Phillips and Donner, 2006; Cotton *et al.*, 2010; Fan *et al.*, 2013; Bouniol *et al.*, 2016; Chen *et al.*, 2017). Thus, the interplay between the cloud macro- and microphysical processes as well as cloud dynamics play an important role in the climate system.

In deep convective clouds, the microphysical processes can be categorised according to the precipitation-forming mechanisms – warm rain process and cold rain

process. The warm rain process refers to the warm phase microphysical processes that involve only liquid hydrometeors, and can take place up to -12 °C as long as liquid particles are in supercooled liquid form. On the other hand, cold rain process takes place at temperature below 0 °C and includes mixed- and ice phase, thus involving both liquid and ice hydrometeors. The rate of ascent influences the balance between warm and cold rain processes by determining the rates of nucleation of cloud water (Phillips and Donner, 2006), and whether there is enough time for collision-coalescence between cloud water and rain to occur (e.g. Tao and Li, 2016), as well as whether supercooled cloud liquid can survive in the presence of ice (e.g. Heymsfield *et al.*, 2005; Phillips and Donner, 2006) and thereafter sustain ice processes (Rangno and Hobbs, 2005; Lawson *et al.*, 2015; Field *et al.*, 2017). In deep convective clouds, the cold rain process is widely known to be the dominant precipitation-forming mechanism.

Warm rain process

The cloud microphysical processes begin with the nucleation of cloud droplets through the transition of water molecules from the gas phase into the liquid phase. This phase transition can proceed either homogeneously or heterogeneously. Homogeneous nucleation is the formation of cloud droplets and ice from water vapour in the absence of external foreign substance. Homogeneous nucleation of cloud droplets is very unlikely to happen in nature as it requires levels of supersaturation up to 120%, which rarely occurs in the troposphere (e.g. Miller *et al.*, 1983; Viisanen *et al.*, 1993; Andreae and Rosenfeld, 2008; Murray *et al.*, 2012). Therefore, the most plausible way cloud droplets form in the troposphere is via heterogeneous nucleation. In contrast, ice nucleation can be achieved through both homogeneous and heterogeneous nucleation. Heterogeneous nucleation is the formation of cloud droplets and cloud ice with the aid of hygroscopic aerosol particles acting as the cloud condensation nuclei (CCN) or ice nuclei (IN), respectively (Pruppacher and Klett, 1997). These aerosol particles are ubiquitous in the atmosphere and their concentrations vary depending on location and season. In general, the aerosol concentration is lower in marine or pristine environment than in continental or polluted environment. They range from $< 10^2$ cm^{-3} in pristine environment to

10^3 – 10^4 cm^{-3} in polluted environment, and 10^2 – 10^3 cm^{-3} in the free troposphere (Spracklen *et al.*, 2010; Murray *et al.*, 2012).

Aerosol particles that can act as CCN and IN are determined by their size and chemical composition (McFiggans *et al.*, 2006; Farmer *et al.*, 2015; Seinfeld *et al.*, 2016). CCN are generally soluble, while IN are usually insoluble (Pruppacher and Klett, 1997). They can be in the form of dust, sea salt, haze particles and even biological matters (Murray *et al.*, 2012). The activation of CCN into cloud drops can be explained from the Köhler curve (Köhler, 1936), which describes the relationship between equilibrium saturation ratio (S_{eq}) and the size of a solution droplet. The Köhler curve is a combination of two effects: the solute (Raoult's law) effect and the curvature (Kelvin) effect. For instance, for each droplet in a sea salt solution, the presence of solute (i.e. Na and Cl; solute effect) acts as a barrier and decreases the evaporation rate of water molecules out of the solution. This reduces the saturation vapour pressure, which reduces the ambient supersaturation needed for aerosol activation. On the other hand, the curvature effect describes the enhancement of the saturation vapour pressure over a curved surface of droplet compared to a flat liquid surface, and is most pronounced for nanometre-sized droplets. In a smaller droplet, the water molecules are more exposed to the surface of the droplet than larger droplet or flat liquid surface. Hence, the water molecules are more likely to evaporate. As a result, more water molecules enter into the solution via condensation in order to maintain the equilibrium in the solution. Subsequently, saturation vapour pressure is greater over a curved surface than that over a flat liquid surface, and thus requiring greater ambient supersaturation for aerosol activation.

The solute and curvature effects determine the activation of aerosol particles. For an aerosol particle to activate, it has to grow to a critical radius and/or the ambient saturation ratio has to exceed the saturation ratio of the aerosol particle. Therefore, aerosol particles with larger sizes and/or with greater solute content have the advantage for easier activation into cloud droplet. Once activated, the smaller droplets evaporate and the larger droplets will continue to grow as long as the ambient supersaturation can sustain the droplet growth. Cloud droplets initially grow via condensation until they achieve diameter of about 20 μm (e.g.

Straka, 2009; Witte *et al.*, 2017) whereafter they grow via other mechanisms, i.e. collision-coalescence. Usually, it takes several hours for a cloud droplet of radius 10 μm to grow into drizzle particles of about 200 μm in diameter by condensation (Pruppacher and Klett, 1997). When the cloud droplet spectrum broadens to include small and large sizes drops, collision-coalescence processes between cloud droplets (represented by self-collection and autoconversion processes in cloud microphysics scheme as detailed in the following paragraph) can occur, which aids in a relatively faster growth of cloud droplets into raindrops of 2 mm in diameter. Besides that, earlier studies (e.g. Ghosh and Jonas, 2001) also suggested the effect of turbulence (i.e. turbulent vortices around a falling droplets) promotes droplet growth.

In cloud microphysical schemes, the liquid drops in clouds are commonly divided into two categories: cloud droplets and raindrops (e.g. Berry, 1968; Kessler, 1969; Beheng, 1994). According to the classification, collision between drops in clouds is divided into (i) collision between cloud droplets, (ii) collision between cloud droplets and raindrops, and (iii) collision between raindrops. The last two classification is known as the accretion processes, while the first classification is further divided into self-collection and autoconversion. Self-collection is the collisional growth of cloud droplets into larger sizes, whereas autoconversion is the collisional growth of cloud droplets into embryonic raindrops (e.g. Berry, 1968; Kessler, 1969; Baker, 1993; Cheng *et al.*, 2007; Tao *et al.*, 2012). Autoconversion does not happen in nature but are instead parameterised in cloud microphysics schemes. The parameterisation of autoconversion represents the transfer of mass and number concentration from the cloud droplet category to raindrop category. Several parameterisations for autoconversion exist as summarised by (Lee and Baik, 2017). They are classified into four categories: (i) parameterisations using the Heaviside function (e.g. Kessler, 1969; Liu and Daum, 2004), (ii) parameterisations using the time scale that is obtained by employing bin microphysics schemes (e.g. Berry and Reinhardt, 1974), (iii) parameterisations using the power-law fitting function (Khairoutdinov and Kogan, 2000; Kogan, 2013), and (iv) parameterisations obtained by solving the stochastic collection equation (e.g. Beheng, 1994; Seifert and Beheng, 2001). In this thesis, the autoconversion scheme used in the chosen cloud microphysics scheme is that of Kogan (2013) and is further described in **Chapter 3**.

Once cloud droplets and raindrops form and co-exist, accretion process becomes important. Accretion refers to the collision-coalescence process between cloud droplets and raindrops, and between raindrops. It is when larger raindrops collide and collect smaller cloud droplets and raindrops. As the cloud updraught pushes air aloft, if the cloud droplets and raindrops in the updraught rises above the freezing level, they enter into the mixed and/or ice phase.

Cold rain process

In the mixed- and ice phase, ice nucleation occur via both homogeneous and heterogeneous nucleation. In homogeneous nucleation, ice crystals can form directly from liquid drops at temperatures below -35 °C (e.g. Sassen and Dodd, 1988; Heymsfield and Sabin, 1989; Pruppacher and Klett, 1997; Koop *et al.*, 2000; Rosenfeld and Woodley, 2000; Peter *et al.*, 2006; Kraemer *et al.*, 2016). In heterogeneous nucleation, ice nucleation involves IN, which are typically aerosol particles in the form of mineral dusts, volcanic ash and biological species such as pollen and bacteria. According to Murray *et al.* (2012), ice nucleation below -15 °C is dominated by soot and mineral dusts, and by biological aerosol species at temperatures above -15 °C. Heterogeneous ice nucleation can occur in several forms: deposition, contact freezing (Young, 1974), immersion freezing (Bigg, 1953), and condensation followed by freezing (Rogers and Yau, 1989). Primary ice nucleation form via heterogeneous nucleation of aerosol and condensation of supercooled liquid droplets. The ice crystal theory was pioneered by the works of Wegener (1911), Bergeron (1935) and Findeisen (1938) and is known as the Wegener-Bergeron-Findeisen (WBF) process, or simply the Bergeron process. In this process, ice crystals grow at the expense of liquid drops. This is because the equilibrium vapour pressure of water vapour with respect to ice is less than that with respect to liquid water at the same given temperature. Therefore, liquid water loses mass via evaporation and the mass is gained by ice crystals via vapour deposition.

Cloud microphysics schemes typically assume three classes of solid hydrometeors: cloud ice, snow and graupel and/or hail. The graupel and/or hail category is distinguished by their density and intercept parameter (i.e. number concentration). Graupel has a lower density and a higher intercept parameter, whereas hail has a

higher density and small intercept parameter. In general, graupel is representative of tropical storms and hail of midlatitude storms (Tao and Moncrieff, 2014). Once ice crystals are formed, they continue to grow via diffusion to many tens of micrometers in a span of a few minutes (e.g. Lohmann *et al.*, 2016). Ice crystals that collide or clump together with other ice crystals form aggregated snowflakes (e.g. Lin *et al.*, 1983; Cotton *et al.*, 1986; Murakami, 1990; Reisner *et al.*, 1998). This process is known as aggregation, which is analogous to the collision-coalescence processes in liquid hydrometeors. As ice crystals and snowflakes begin to fall into warmer temperatures than the temperatures where they are initially formed, they undergo interactions with supercooled liquid drops via accretion processes, thus forming graupel or hail particles.

Secondary ice formation (also known as ice multiplication) soon follows as these solid hydrometeors rise or fall within the clouds, melt and evaporate. Secondary ice formation is a mechanism or process in which new ice crystals are produced in the presence of pre-existing ice without requiring an IN. It can occur via fracturing of ice particles due to ice-ice or graupel-graupel collisions, especially when graupel encounters dendritic crystals in which the dendritic crystals can break and leave a multitude of small ice particles behind (e.g. Takahashi *et al.*, 1995; Lohmann *et al.*, 2016). In addition, it can also occur via rime-splintering process, commonly known as the Hallett-Mossop process (Hallett and Mossop, 1974). This process involves the capturing of supercooled liquid drops with diameters smaller than 13 μm and larger than 25 μm by large ice particles (rimed aggregates, graupel or large frozen drops) in temperatures no colder than -10 °C; it is most favourable between -3 and -5 °C, with maximum production at -8 °C (Hallett and Mossop, 1974; Field *et al.*, 2017; Huang *et al.*, 2017).

2.3 Cloud radiative properties

Clouds influence the radiative transfer of energy in the earth's atmosphere by reflecting incoming solar radiation, and by absorbing or emitting longwave radiation (e.g. Kiehl and Ramanathan, 1990; Zhou *et al.*, 2017). These are known as the cloud albedo effect and cloud greenhouse effect, respectively (Coley and Jonas, 1999). They are also known as the shortwave and longwave cloud radiative effects

(CRE), respectively. The magnitude of these two effects vary depending on the optical depth and cloud cover (e.g. Zelinka *et al.*, 2013; Khain *et al.*, 2015, as well as on size and number concentration of cloud particles, cloud phase and height (e.g. King *et al.*, 2013; Read *et al.*, 2016; Krisna *et al.*, 2018). For example, optically thin cirrus clouds pose weaker albedo effect but stronger greenhouse effect, thus exerting a warming effect in contrast to optically thick cirrus clouds which exert a cooling effect (Liou, 1986; Voigt *et al.*, 2017). In addition, the areal coverage of the clouds can amplify either of the two cloud radiative effects.

For deep convective clouds, the deep convective tower generally exerts a cooling effect at the surface given its high optical depth that reflects more of the incoming shortwave radiation at the top of the cloud. On the other hand, the anvil canopy generally exerts a warming effect that heats the atmosphere due to the absorption of longwave terrestrial radiation and re-emission at a lower temperature (Hartmann *et al.*, 1992; Chen *et al.*, 2000; Tian and Ramanathan, 2002). Although these two radiative effects are both large in deep convective clouds (Ramanathan *et al.*, 1989; Harrison *et al.*, 1990), they tend to cancel out thus giving a net radiation that is similar to nearby non-convective regions (Hartmann and Berry, 2017). Furthermore, the changes in the local and regional cloud radiative effects still present some uncertainties (Norris and Slingo, 2009) despite significant research focus from projects such as the Earth Radiation Budget Experiment and the Clouds and the Earth's Radiant Energy System (CERES) (e.g. Stephens and Webster, 1981; Arking, 1991; Wielicki *et al.*, 1996; Boucher *et al.*, 2013) and utilization of satellite data such as the A-Train Constellation (e.g. Kato *et al.*, 2011). In addition, climate models predict different low- and high-level cloud responses to a warming climate, which results in a large dispersion in model-based estimated climate sensitivity (e.g. Bony and Dufresne, 2005; Webb *et al.*, 2006; Satoh *et al.*, 2012). It is therefore highly uncertain how clouds will develop in a warmer climate; weaker (stronger) development may result in greater cooling (warming) (Randall *et al.*, 2007; Norris and Slingo, 2009; Boucher *et al.*, 2013; Zelinka *et al.*, 2013).

Using satellite measurements and numerical forecast model reanalysis data, Allan (2011) computed the global cloud radiative effect on the earth's energy budget and reported that the cloud albedo effect dominates over the cloud greenhouse

effect, resulting in a net cooling of -21 W m^{-2} in the climate system. Therefore, a reduction in optically thick clouds and/or cloud cover may result in a net warming effect. Cess and Udelhofen (2003) noted a significant increase in the absorbed solar radiation at the surface and outgoing longwave radiation at the top of the atmosphere; they attributed this increase to reduction in the observed cloud cover. Ohmura (2009) reported that a 4% reduction in global total cloud cover led to an increase of 2.5 W m^{-2} in surface solar radiation (SSR) for the period between 1990 and 2005. Similarly, Longman *et al.* (2014) found that per decade reduction of 5 – 11% cloud cover led to a 9 – 18 W m^{-2} increase in SSR in Hawaii between the period 1983 and 2010.

Kirchhoff's law states that the amount of radiation that objects emit is a function of their temperature, with radiative emission being proportional to $\boldsymbol{T}^4$ where $\boldsymbol{T}$ is the absolute temperature, according to Stefan-Boltzmann law. The increase in absorbed solar radiation at the surface due to the reduction in cloud cover, therefore means that the longwave radiation emitted will be of warmer temperature. The amplified warming will inevitably alter the atmospheric thermodynamic environment in which clouds form, thereby influencing changes in cloud properties (e.g. Bony *et al.*, 2004). Therefore, it is important to know how clouds would respond under perturbed thermodynamic environments (Bourgeois *et al.*, 2016).

2.4 Cloud responses to a warming climate

Throughout this thesis, the past climate is labelled as 'cold' to indicate that it is colder than the projected globally-averaged warmer temperature in the future climate which is labelled as 'warm'. Several studies (e.g. Sohn *et al.*, 2013; Villanueva-Birriel, 2014; Rasmussen *et al.*, 2017; Hibino *et al.*, 2018) compared the simulated cloud processes associated with past (cold) and future (warm) climate changes and reported that clouds behave differently in cold and warm climates, therein also acknowledged that the cloud response is more complex than previously expected. This section provides existing literature on cloud responses to warming, which includes changes in macro- and microstructure of clouds that influence the overall structure and extent of the cloud as well as their surface precipitation and radiative properties.

2.4.1 Precipitation changes according to Clausius-Clapeyron relationship

Precipitation is expected to be more intense and longer-lasting in a warmer environment due to higher temperatures that lead to increased atmospheric water vapour, i.e. increased specific humidity (Trenberth *et al.*, 2003). As a basis for predicting the effect of climate change on extreme rainfall, the relationship between environmental temperature and precipitation intensity has been extensively investigated over the years (e.g. Lepore *et al.*, 2015). Observational studies reported increased heavy and extreme precipitation events associated with a warming climate (e.g. Allan and Soden, 2008; Lau and Wu, 2007; Lau and Wu, 2011) and Berg *et al.* (2013) concluded that convective precipitation is more sensitive to increasing temperatures than stratiform precipitation. Allan and Soden (2008) used the natural climate variability of the atmosphere to find a relationship between heavy precipitation events and a warmer climate. They found an increase in heavy precipitation events during El Niño periods and a decrease during La Niña periods, which correspond to warm and cold periods, respectively. On the other hand, Lau and Wu (2007) and Lau and Wu (2011) used space-based and ground-based global rainfall data to examine the climatology of oceanic rainfall features for the periods of 1979-2003 and 1998-2009, respectively. They found that extreme precipitation events associated with deep convection increased substantially over a warmer ocean.

Findings from these studies are usually compared to the Clausius-Clapeyron (CC) relation. The CC relation shows the increase in the water-holding capacity of the atmosphere by 7% per degree Celsius increase in temperature. However, other regional studies have observed super-CC rates over certain ranges of temperature (e.g. Prein *et al.*, 2017). The observed super-CC rates are attributed to the increased intensity of convection (Lenderink and Van Meijgaard, 2008; Lenderink *et al.*, 2011; Berg *et al.*, 2013), as well as increased contribution in precipitation from convective storms than from frontal storms (Haerter and Berg, 2009; Berg *et al.*, 2013). These studies, however, do not address the details of the exact processes responsible for the changes in precipitation.

As mentioned in **Section 2.2.2**, there are two precipitation-forming mechanisms in deep convective clouds: warm rain process (liquid phase) and cold rain process (mixed- and ice phases). In the lifecycle of deep convective clouds, warm rain process precedes cold rain process, and the cold rain process is known to contribute to most of the precipitation in deep convective clouds. However, several recent studies (e.g. Sohn *et al.*, 2013; Xu, 2013; Song *et al.*, 2017) have shown otherwise and suggested that either process can be dominant in deep convective clouds depending on the environmental thermodynamics in different regions. Further, Caracena *et al.* (1979) detected strong radar reflectivity just below the freezing level in the storm that caused the Big Thompson flood in Colorado, thereby suggesting enhanced growth of precipitating particles through the warm rain process.

2.4.2 Changes in precipitation-forming mechanism

Xu and Zipser (2012) used satellite measurement and found that heavy convective rainfall from monsoon and oceanic rain systems are less dominated by mixed-phase processes unlike continental-type convection. Further, by analysing TRMM measurements from five distinct regions in East Asia, Xu (2013) reported that deep convection over high elevation above sea level is weaker than that over low elevation due to the different local environment (e.g. less CAPE and drier environment). Deep convective clouds over high elevation are also smaller in horizontal extent and have higher cloud bases and shallower mixed-phase depths than lowland regions. Hamada *et al.* (2015) showed that most extreme rainfall events in the tropics are characterised by less intense convection that does not extend to extremely high altitudes. An in-depth study utilising the Tropical Rainfall Measuring Mission (TRMM) and CloudSat measurements by Sohn *et al.* (2013) found that heavy rain systems over the Korean peninsula are more associated with clouds having relatively low echo-top height (which they referred to as "warm-type" heavy rainfall), contrasting with the traditional cold rain process deep convective clouds. They suggested that convective clouds with lower ice water content can also produce heavy rainfall if water vapour is continuously supplied along the western periphery of the North Pacific high.

Sohn *et al.* (2013) proposed a hypothesis for the microphysical formation of warm-type heavy rainfall. They proposed that ice particles first grow via aggregation and accretion above the freezing level, followed by rigorous growth of rain drops via collision and coalescence processes below the freezing level due to the great reservoir of water vapour below the freezing level. Their study is further extended by Song *et al.* (2017) who examined the impact of thermodynamic conditions on the microphysical evolution of the "warm-type" heavy rainfall and the traditional, continental deep convective clouds. Their finding showed the different mechanisms involved in the production of graupel that subsequently melts into rain. For the warm-type experiment, graupel is formed via riming process between the super-cooled raindrops and ice particles. On the other hand, the graupel production in cold-type experiment is formed from snow particles via the aggregation and accretion processes. In addition, they also found a lower storm height and earlier onset of precipitation in warm-type experiments than were found for cold-type experiments.

2.4.3 Hypotheses on cloud behaviour with warming

Various notable studies have tried to hypothesise the behaviour of deep convective clouds in a warmer climate and its feedbacks upon the climate system. The adaptive iris hypothesis by Lindzen *et al.* (2001) argues that higher sea surface temperature (SST) in the future will enhance deep convection that precipitate very efficiently, causing less condensate to reach the upper level thus results in reduced high cloud cover. The reduction in high cloud cover means that the upper atmosphere is not moistened, resulting in enlargement of drier areas, allowing earth to emit more longwave radiation, thus cooling the earth. On the other hand, Ramanathan and Collins (1991) proposed that increased SST enhance deep convection which transports condensate further up in the atmosphere, leading to more detrainment and hence thicker and more extensive anvil clouds. These thicker and more extensive anvils reflect more shortwave radiation back to space and thus cool the earth.

In contrast, other observational studies provide conflicting hypotheses that suggest strong warming of the earth. For example, Lin *et al.* (2002) used TRMM data and found a reduction in cloud cover with increasing SST, but weaker than that

was found by Lindzen *et al.* (2001). They argued that high reflectivity of thick anvil clouds, when reduced, should result in a warming effect because more solar radiation gets transmitted to the earth's surface, as opposed to explanation given by Lindzen *et al.* (2001). On the other hand, Hartmann and Larson (2002) proposed the Fixed Anvil Temperature (FAT) hypothesis, which was later modified to proportionately higher anvil temperature (PHAT) hypothesis by Zelinka and Hartmann (2010), which states that the anvil cloud height may shift upward in a warmer climate, but the temperature remains nearly unchanged or exhibit only a slight warming, thus still produce a warming effect on earth due to the absorption of longwave radiation by anvil clouds.

The recent study by Bony *et al.* (2016) reported that anvil cloud coverage shrinks as the climate warms, which is consistent with the reduction in anvil cloud amount from Lin *et al.* (2002) and Lindzen *et al.* (2001). Unlike the microphysical mechanism provided by Lindzen *et al.* (2001), Bony *et al.* (2016) proposed the convective 'self-aggregation' mechanism to explain the reduction in anvil cloud amount. The mechanism describes that in a warmer environment, convective clouds self-aggregate into clusters, reducing the areas covered by clouds (resulting in increasing dry, non-cloudy areas), thus allowing more infrared radiation to escape to space. This 'self-aggregation' depends on surface temperature and are most pronounced at higher temperature. In addition, they found that the height of upper level clouds (anvils) rises, resulting in reduced anvil cloud amount because the clouds find themselves in a more stable environment due to the dry upper level that results from convective self-aggregation. They termed this as the 'stability iris effect', which is a combination of Lindzen *et al.* (2001) and Zelinka and Hartmann (2010) hypotheses.

To sum up, the application of these hypotheses might not be sufficient or appropriate for other regions with different thermodynamic environments. This is because these hypotheses are mainly based on studies in the tropics that utilise SST variations caused by seasonal shifts and El Niño-Southern Oscillation (ENSO), whereas other regions could have distinctly different thermodynamic and dynamic environments (Li and Zhou, 2012; Hibino *et al.*, 2018).

2.5 Summary

This chapter described the characteristics of deep convective clouds and the important roles that they play in the earth's climate system. Their role in regulating the earth's water and energy budget is highlighted and drawn from their microphysical and radiative properties. Further, this chapter also discussed the hypotheses and results from existing observational and modelling studies associated with cloud responses to warming. These existing studies, however, disregard the details of how specifically clouds may or may not change due to a warmer environment and/or changed thermodynamic structure. They also overly simplify important details in the cloud evolution processes. This thesis, therefore, fills the gap by assessing how changes in the thermodynamic environment affect the cloud macro- and microphysical properties and its subsequent impact on the cloud radiative properties. The data and methodology employed in this study are described in **Chapter 3**.

Chapter 3

Research data and tools

3.1 Introduction

This chapter presents the methodology adopted for the study in this thesis. This includes the data utilised for the idealised simulations of deep convective clouds described in **Section 3.2**, and the cloud-resolving model used for the simulations described in **Section 3.3**, as well as the radiative transfer model used in assessing the cloud radiative properties described in **Section 3.4**.

3.2 Study location

3.2.1 Background of study location

In this thesis, eight locations in the contiguous United States (CONUS) was chosen as the study location. Deep convection is ubiquitous across the CONUS albeit governed by different perturbations. Located in the mid-latitudes and in small part of the subtropics, the winds over the CONUS are predominantly westerlies, originating from the high pressure areas in the horse latitudes and tend towards the poles. The westerlies carry warm waters and winds northward from the equator to the mid-latitudes. Due to the Coriolis force, the winds are deflected to the east, resulting in the winds moving from west to east across the continent.

The weather patterns in the CONUS are largely governed by baroclinic instabil-

ity, that is, the temperature difference between the poles and the tropics. This large-scale baroclinic-driven perturbations transport mass and energy horizontally and vertically and is most pronounced in the winter, when the temperature and pressure gradient is the greatest and the westerly winds are strongest, resulting in deep convection in the winter. In the summer, the baroclinicity weakens and deep convection is mainly governed by thermodynamic instability in response to the strong diurnal cycle of solar heating (Wallace, 1975; Yang and Slingo, 2001; Tian *et al.*, 2004).

Several studies have reported a 10% increase in precipitation occurring in the summer months in the CONUS throughout the twentieth century (e.g. Allan and Soden, 2008; Lau and Wu, 2007; Lau and Wu, 2011). Following the findings of Villanueva-Birriel *et al.* (2014) (hereinafter denoted as VB14), two regions in the CONUS – the Midwest and the Southeast - comprising a total of eight states were investigated. These locations, shown in Figure 3.1 were chosen as they show substantial changes in the thermodynamic environment leading to an enhanced warm rain process in the simulated future warmer climate, which is in keeping with the aims of this thesis of assessing the impact of a changing thermodynamic environment from the past to future climate on the responses of deep convective clouds.

The Midwest refers to the north-central states of the United States that spans from the foothills of the Appalachian Mountains in the east, including the Great Lakes in the northeast and some parts of the Great Plains in the west. The states in the Midwest chosen for this study include Minneapolis (MIN), Madison (MAD), Jasper (JAS) and Dayton (DAY), all of which are in close proximity to the Great Lakes. The Southeast spans from the Appalachian Mountains to expansive coastal plains. Most states in the Southeast are along the Gulf of Mexico and the Atlantic Ocean. The Southeastern locations chosen for this study comprise Anderson (AND), Charlotte (CHA), Birmingham (BIR) and Owensboro (OWE). Anderson and Charlotte lie along the coast of the Atlantic Ocean, while Birmingham is close to the Gulf of Mexico. Owensboro, however, is further inland. In both of the study regions collectively, the climate is generally hot and humid in the summer, owing to the westerly winds picking up warm, humid air masses from tropical origins.

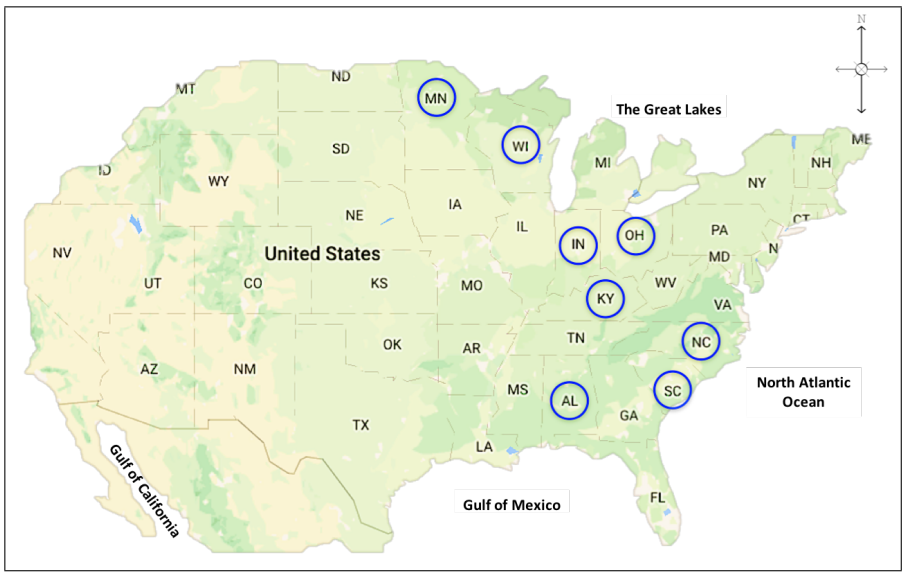

Figure 3.1: Map of the contiguous United States showing eight study locations in blue circles. **The Midwest:** Minneapolis, MN (MIN), Madison, WI (MAD), Jasper, IN (JAS), Dayton, OH (DAY). **The Southeast:** Owensboro, KY (OWE), Birmingham, AL (BIR), Anderson, SC (AND), Charlotte, NC (CHA). Source: Google Maps

3.2.2 Data: Atmospheric thermodynamic profiles

The past and future atmospheric environments of the eight locations chosen for this study were obtained from one of the National Center for Atmospheric Research Community Climate System Model version 3 (NCAR CCSM 3) (Collins *et al.*, 2006) simulations described in Trapp *et al.* (2009) for the period from 1970 to 2099, in the SRES A1B scenario. In the CCSM3 model, the process of deep convection is treated with a parameterisation scheme from Zhang and McFarlane (1995).

The atmospheric parameters of temperature, pressure, water vapour and winds were computed as averages over the summer months (June, July, August) at 00 UTC for all simulated soundings with convective available potential energy (CAPE) values exceeding 1000 J kg^{-1} over the 30-year period for past (1970-1999) and future (2070-2099) periods. These environmental conditions were chosen because they are representative of the summer environment with strong late afternoon and evening maxima of precipitation observed in most of the U.S. (Trenberth *et al.*, 2003). In addition, by computing CAPE at the other CCSM3 output times,

Trapp *et al.* (2007) confirmed that 00 UTC represents the typical time of maximum CAPE.

VB14 and Hack *et al.* (2006) reported that the averaged profiles contained a significant dry bias in the lower atmosphere when compared with those created with the same criteria from the 30-year averages of North American Regional Reanalysis (NARR; Mesinger *et al.*, 2006) data and 20-year averages of NCEP-NCAR Reanalysis Project (NNRP; Kalnay *et al.*, 1996) data. This dry bias prevented convective development in the cloud-resolving model and was thus adjusted by VB14 using the NARR and NCEP reanalysis data in order to allow for convective initiation. VB14 altered the original CCSM3-derived 1970-1999 profiles by dividing the sounding into three layers (1000-700 mb, 700-300 mb, 300-100 mb). For each layer, a regression analysis was run for temperature, water vapour mixing ratio, and the east-west u and north-south v wind components, and a correction factor was computed for each variable. These same correction factors were then used to adjust the original CCSM3-dervied 2070-2099 profiles. These adjusted profiles are utilised as the initial conditions for the idealised deep convective cloud simulations in this study using the WRF model described in the **Section 3.3**.

3.3 Cloud-resolving model

The high-resolution numerical model employed in this study is the Advanced Research Weather Research and Forecasting model (ARW) version 3.7.1 (Skamarock *et al.*, 2008). The model was developed by the NCAR in the United States. It is designed as a tool for use in both research and operational forecasting situations as well as for application in wider field such as in land-use, hydrology and oceanography. In this study, it is used as a cloud-resolving model to perform idealised simulations of deep convective clouds.

3.3.1 Model description

The ARW is a subset of the WRF modelling system encompassing physics schemes, numeric/dynamic options and initialisation routines that uses the ARW dynamics solver to produce a simulation (Skamarock *et al.*, 2008). The ARW solver comprises

a set of fully compressible, Euler non-hydrostatic equations which are conservative for scalar variables. The prognostic variables include horizontal velocity components u and v in Cartesian coordinates, vertical velocity w, perturbation potential temperature, perturbation geopotential, perturbation surface pressure of dry air, and various cloud microphysical variables, i.e. cloud water, rain, ice, snow and graupel mixing ratios. The governing equations are solved using a time-split integration with a third-order Runge-Kutta scheme and a smaller time step for acoustic and gravity wave modes. The horizontal and vertical advection are calculated using the fifth and third-order discretisation schemes, respectively. The horizontal and vertical turbulent diffusion are calculated using a 1.5-order turbulent kinetic energy (TKE) scheme. The upper and lower boundaries are free-slip with zero vertical velocity, and the open lateral boundary conditions (also called gravity-wave radiating boundary conditions) specified to the west, east, north, south boundary or any combination thereof, are employed. Skamarock *et al.* (2008) recommend the setting the time step to 6*dx, where dx is the horizontal resolution in km. Since the horizontal resolution in this study is set to 500 m, a time step of three seconds was therefore used for the model integration period for two hours. Parameterisations for radiation, boundary layer, surface layer, land surface and cumulus were not included in the simulations performed in this study.

3.3.2 Model setup

For all the deep convective cloud simulations performed in this study, the cases were set up similar to the standard 3D idealised supercell cases available in the WRF modelling package. The model was configured with a domain size of 100 km (west-east) x 60 km (south-north) with a constant 500 m grid spacing in each direction, and 24 km in the vertical with 70 irregularly-spaced levels (an average of approximately 340 m between each vertical level but more closely-spaced near the surface to allow the boundary layer to be better resolved).

In the WRF model, the basic trigger for convection is a single thermal perturbation bubble (Skamarock *et al.*, 2008). Following previous study by Villanueva-Birriel (2014) who simulated deep convective clouds in the same study locations as this thesis, the horizontal and vertical radii of the thermal perturbation bubble is set at

10 km and 1.5 km, respectively. The maximum thermal perturbation for initiating deep convection is typically 3 or 4 K and is located at 1.5 km above ground level, with a Gaussian temperature decrease toward the bubble's outer edges (e.g. French and Parker, 2008; Schumacher and Johnson, 2008; Song *et al.*, 2017). In this study, the magnitude of the thermal perturbation bubble was modified to create typical summertime midlatitude deep convective clouds. The magnitude of the thermal perturbation bubble vary depending on the atmospheric stability in each location and they are set the same for both past and future environments in each location as shown in Table 3.1. By keeping the thermal perturbation magnitude the same for the past and future environments, it allows for us to assess the changes on the cloud development between the two environments.

The parameters employed in the model setup (i.e. in the *namelist.input*) is as listed in Table A.1 in **Appendix A**.

Table 3.1: Thermal bubble perturbation magnitude in Kelvin

Location	**Bubble perturbation temperature (K)**
MIN	2.5
DAY	2.5
AND	2.0
JAS	3.5
OWE	3.0
CHA	2.0
BIR	4.0
MAD	2.5

3.3.3 Morrison two-moment bulk microphysics scheme

The cloud microphysics schemes deal with explicitly-resolved water vapour, cloud and precipitation processes. Skamarock *et al.* (2008) recommend that mixed-phase schemes should be used in convective or icing situations. Mixed-phase schemes include processes where water and ice particles interact, such as riming that produces graupel or hail. The Morrison two-moment bulk microphysics scheme (Morrison *et al.*, 2005; Morrison *et al.*, 2009) which include warm, mixed- and ice phases has been chosen for use in the idealised cloud-resolving simulations presented in this thesis. The Morrison scheme was chosen due to its flexibility in representing hydrometeor size distributions and its demonstrated capability in representing sub-grid processes that control cloud and precipitation formation (e.g. Mayor and Mesquita, 2015; Shrestha *et al.*, 2017).

Six species of water are included in the scheme, in the form of vapour, cloud water, cloud ice, rain, snow, and graupel or hail (the category can be specified by the user). For this study, the hail category was selected since it was shown in Bryan and Morrison (2012) to produce a more realistic reflectivity and thermodynamic structure for a simulated squall line in the mid-latitudes. Additionally, the storms simulated in this study contain large liquid water contents, a necessary component for the formation of highly-dense rimed particles. The Morrison scheme contains a total of nine prognostic variables: the mixing ratios of all hydrometeor species and the number concentration of all hydrometeor species except cloud water droplets. Because the number concentration of cloud water is not predicted, an external, modified version of the Morrison scheme was obtained from Bethan White of Oxford University, which is not available in the WRF modelling system package. The inclusion of an additional prognostic variable, which is the number concentration of cloud droplet allows for additional degrees of freedom used to characterise particle size distributions (Milbrandt and Yau, 2005; Morrison *et al.*, 2009; Lim and Hong, 2010). Including the prognostic number concentration for liquid water was an important addition to this work since it allows an evaluation of not only the concentration changes but also effects of the water phase directly on the radiation (Meyers *et al.*, 1997; Morrison *et al.*, 2005).

Other modifications made to the standard Morrison scheme is the replacement of the autoconversion and accretion rates for liquid hydrometeors. The standard Morrison scheme uses the autoconversion and accretion rates of Khairoutdinov and Kogan (2000), which is based upon the simulated marine stratocumulus drop spectra by four large-eddy simulation (LES) models. Villanueva-Birriel (2014) found that the new formulation by Kogan (2013) based on drop spectra predicted from simulated shallow warm cumuli better represented deep convective cloud and is therefore used to replace the standard autoconversion and droplet accretion parameters. For other microphysical options employed in this thesis, the list of microphysical switches can be referred to in Table B.1 in **Appendix B**.

3.3.3.1 Particle size distribution

Each hydrometeor species is represented by a gamma size distribution of the form

$$N_j(D) = N_0 D^{\mu_j} e^{-\lambda D} \tag{3.1}$$

where D is the diameter and μ_j, N_0 and λ are the spectral index, intercept and slope, respectively. Values for the spectral index for droplets (μ_c) follows the theoretical formulations of Khvorostyanov and Curry (1999) and varies from 2 to 10. All other hydrometeor species have μ_j equal to zero. The intercept and slope parameters are derived from the predicted number concentration and mixing ratios as in Equations 3.2 and 3.3.

$$\lambda_j = [\frac{c_j N_j \Gamma(\mu_j + d_j + 1)}{q_j \Gamma(\mu_j + 1)}]^{\frac{1}{d_j}} \tag{3.2}$$

$$N_0 = \frac{N_j \lambda_j^{\mu_j + 1}}{\Gamma(\mu_j + 1)} \tag{3.3}$$

In these two equations, Γ is the Euler gamma function with c and d given by the power-law mass-diameter relationship of each hydrometeor species, $m_j = c_j D^{d_j}$. In the mass-diameter relationship, the parameter d_j is equal to 3 for all hydrometeor species, while $c_j = \rho_j \pi/6$, where and $\rho_j \pi$ represents the bulk density for each hydrometeor species given in Table 3.2.

Table 3.2: Constants for the physical properties of hydrometeor species

Symbol	**Variable**	**Value**	**Units**
a_c	V-D constant for cloud water	3 x 10^7	m^{1-bc} s^{-1}
a_r	V-D constant for rain	842.0	m^{1-br} s^{-1}
a_i	V-D constant for ice	700.0	m^{1-bi} s^{-1}
a_s	V-D constant for snow	11.72	m^{1-bs} s^{-1}
a_g	V-D constant for graupel/hail	19.3/114.5	m^{1-bg} s^{-1}
b_c	V-D constant for cloud water	2.0	
b_r	V-D constant for rain	0.8	
b_i	V-D constant for ice	1.0	
b_s	V-D constant for snow	0.41	
b_g	V-D constant for graupel/hail	0.37/0.5	
ρ_c, $\rho_r = \rho_w$	Density of water (applicable for cloud water and rain)	997	kg m^{-3}
ρ_i	Bulk density of ice	500	kg m^{-3}
ρ_s	Bulk density of snow	100	kg m^{-3}
ρ_g	Bulk density of graupel/hail	400/900	kg m^{-3}

3.3.3.2 Microphysical processes

The calculations of the microphysical process rates and evolution of cloud and precipitation depend strongly on the particle size distributions. The predicted mixing ratio (q_j) and number concentration (N_j) of a given hydrometeor species depend on space (x, y, z) and time (t) following Equations 3.4 and 3.5.

$$\frac{\partial q_j}{\partial t} = -\nabla \cdot (\mathbf{v} q_j) + \frac{\partial}{\partial z}(V_{q_j}) + \nabla_D q_j + S_{q_j} \tag{3.4}$$

$$\frac{\partial N_j}{\partial t} = -\nabla \cdot (\mathbf{v} N_j) + \frac{\partial}{\partial z}(V_{N_j}) + \nabla_N q_j + S_{N_j} \tag{3.5}$$

The first three terms on the right-hand side of these equations represents advection, sedimentation and turbulent diffusion of q or N. The $\mathbf{v}$ in the advection term is the $3D$ wind vector. The parameters V_{q_j} and V_{N_j} in the sedimentation term are the mass- and number-weighted terminal fall speed for each hydrometeor as expressed below.

$$V_{q_j} = \frac{\eta a_j \Gamma(\mu_j + b_j + 4)}{\lambda_j^{b_j} \Gamma(\mu_j + 4)} \tag{3.6}$$

$$V_{N_j} = \frac{\eta a_j \Gamma(\mu_j + b_j + 1)}{\lambda_j^{b_j} \Gamma(\mu_j + 1)} \tag{3.7}$$

Here, η is the air density correction factor and is equal to $(\rho_0/\rho)^{0.54}$, where ρ_0 and ρ are equal to the air density near the surface and aloft, respectively. Equations 3.6 and 3.7 could be updated to include a diffusional correction factor which would improve the microphysical representation (particularly the warm rain microphysics) more realistically, as demonstrated by Ghosh *et al.* (2017). The a_j and b_j parameters are summarised in Table 3.2.

The fourth term of Equations 3.4 and 3.5 are the parameterised microphysical sources and sinks for each hydrometeor (S). The microphysical processes represented by the Morrison scheme incorporate: primary production terms (droplet activation or ice nucleation), water vapour and hydrometeor phase changes (condensation/evaporation, deposition/sublimation), autoconversion processes (diffusional and collisional growth of rain from cloud water and snow from cloud ice, respectively), collection/accretion growth, phase changes between solid and liquid hydrometeors (melting/freezing), and ice multiplication from aggregation of ice particles and riming processes between precipitating solid hydrometeors and liquid particles. Equations 3.8-3.12 describe the transfer of mass and number concentration between hydrometeor species owing to these microphysical processes for each hydrometeor.

The source and sink terms for the mass mixing ratio and number concentration for each species are as follows. The description of the source and sink terms are listed in Table 3.3 and Figure 3.2 illustrates the microphysical processes between hydrometeors.

For cloud water:

$$S_{qc} = -S_{PRA} + S_{PCC} - S_{MNUCCC} - S_{PSACWS} - S_{PSACWI} - S_{QMULTS} - S_{QMULTG} - S_{PSACWG} - S_{PGSACW} \tag{3.8}$$

For rain water:

$$S_{qr} = S_{PRE} + S_{PRA} + S_{PRC} - S_{PSMLT} - S_{PGMLT} - S_{PRACS} - S_{MNUCCR} - S_{QMULTR} - S_{QMULTRG} - S_{PIACR} - S_{PRACG} - S_{PGRACS} \tag{3.9}$$

For cloud ice:

$$S_{qi} = S_{PRD} + S_{EPRD} + S_{PSACWI} + S_{MNUCCC} - S_{PRCI} - S_{PRAI} + S_{QMULTS} + S_{QMULTG} + S_{QMULTR} + S_{QMULTRG} + S_{MNUCCD} - S_{PRACI} - S_{PRACIS} \tag{3.10}$$

For snow:

$$S_{qs} = S_{PSMLT} + S_{EVPMS} + S_{PRAI} + S_{PSACWS} + S_{PRDS} + S_{PRACS} + S_{PRCI} + S_{EPRDS} - S_{PSACR} + S_{PIACRS} + S_{PRACIS} \tag{3.11}$$

For graupel/hail:

$$S_{qg} = S_{PGMLT} + S_{EVPMG} + S_{PRACG} + S_{PSACWG} + S_{PGSACW} + S_{PGRACS} + S_{PRDG} + S_{EPRDG} + S_{MNUCCR} + S_{PIACR} + S_{PRACI} + S_{PSACR} \tag{3.12}$$

Table 3.3: Microphysical sources/sinks for prognostic mixing ratios in kg kg^{-1} s^{-1}

Notation	**Description**
EPRD	Sublimation of cloud ice
EPRDG	Sublimation of graupel/hail
EPRDS	Sublimation of snow
EVPMG	Melting of graupel/hail and evaporation
EVPMS	Melting of snow and evaporation
MNUCCC	Immersion and contact
MNUCCD	Ice nucleation from freezing of aerosol
MNUCCR	Immersion freezing of rain
PCC	Condensation/ evaporation of droplets
PGMLT	Melting of graupel/hail
PGRACS	Conversion to graupel/hail due to collection of rain onto snow
PGSACW	Conversion to graupel/hail due to collection of droplets onto snow
PIACR	Change in rain mixing ratio, ice-rain collection, added to graupel/hail
PIACRS	Change in rain mixing ratio, ice-rain collection, added to snow
PRA	Droplet accretion by rain
PRACG	Collection of rain by graupel/hail
PRACI	Change in cloud ice mixing ratio, ice-rain collision, added to graupel/hail
PRACIS	Change in cloud ice mixing ratio, ice-rain collision, added to snow
PRACS	Collection of rain by snow
PRAI	Accretion of cloud ice by snow
PRC	Autoconversion of droplets
PRCI	Autoconversion of cloud ice
PRD	Deposition of cloud ice
PRDG	Deposition of graupel/hail
PRDS	Deposition of snow
PRE	Evaporation of rain
PSACR	Conversion to graupel/hail due to collection of snow by rain
PSACWG	Collection of droplets by graupel/hail
PSACWI	Droplet accretion by cloud ice
PSACWS	Droplet accretion by snow
PSMLT	Melting of snow
QMULTG	Ice multiplication due to riming of droplets by graupel/hail
QMULTR	Ice multiplication due to riming of rain by snow
QMULTRG	Ice multiplication due to riming of rain by graupel/hail
QMULTS	Ice multiplication due to riming of droplets by snow

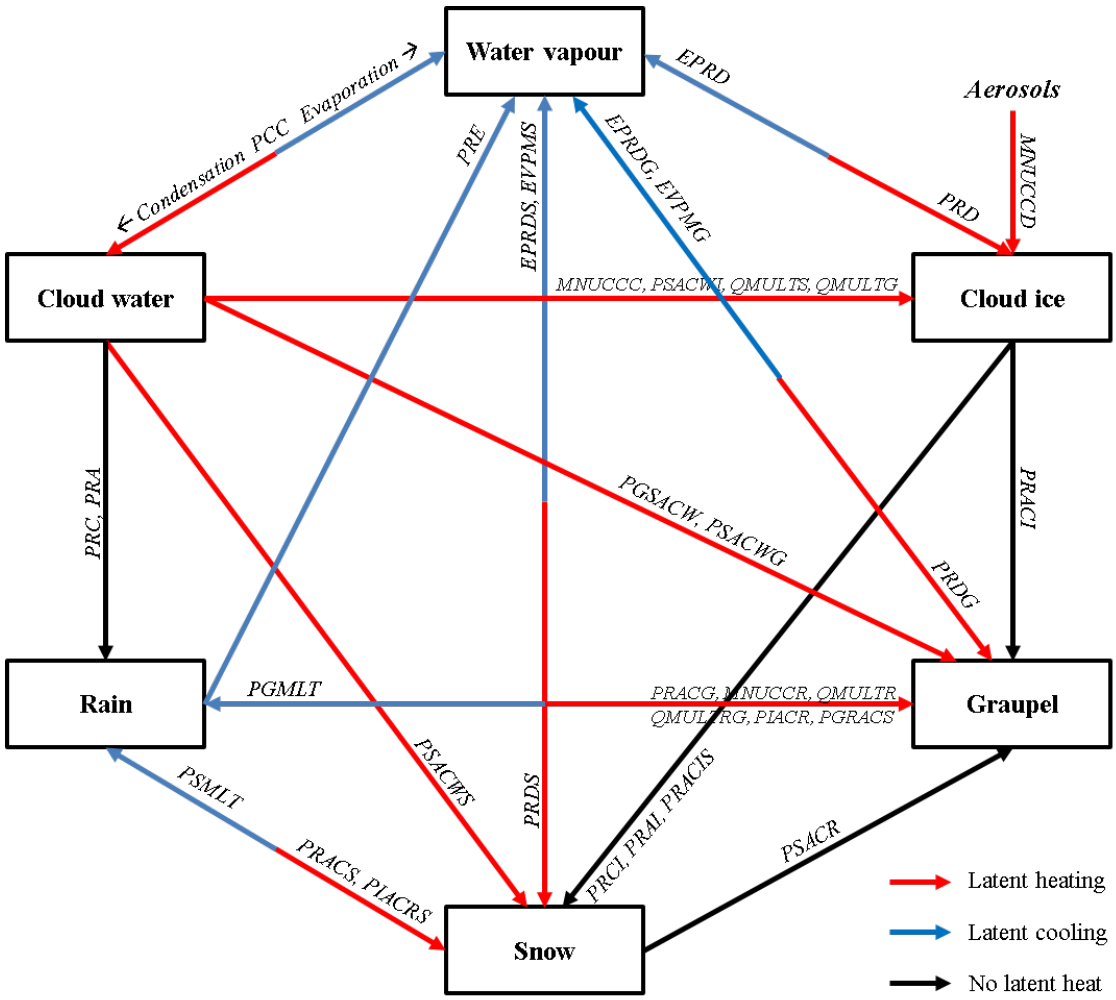

Figure 3.2: Box diagram of Morrison double-moment microphysics scheme.

The cloud microphysical process rates involving droplet activation, warm phase and ice phase processes are described below.

a. **Droplet activation**

The droplet activity spectrum follows Twomey (1959), that is, the power-law relationship. The potential number of droplets activated is given in Equation 3.13 following the formulation from Rogers and Yau (1989).

$$N' = min(0.88C_T^{2/(k+2)}(0.07{w_{ef}}^{3/2})^{k/(k+2)}, N_a), \tag{3.13}$$

where w_{ef} is the effective vertical velocity, N_a is the total aerosol number concentration, and C_T and k relate to the aerosol size and composition as given in Equations 3.14 and 3.15.

$$C_T = \frac{10^{2k}}{k} 2N_a r_{min}^{\mu-1} R(\frac{27b_a}{4B^3})^R \tag{3.14}$$

$$k = \frac{\mu - 1}{1 + \beta} \tag{3.15}$$

where b_a and β depend on the composition of the aerosol (as discussed in Khvorostyanov and Curry (1999)), B is the Kelvin parameter, and R is as given in Equation 3.16 where μ is the slope of the dry aerosol size distribution following Junge (1952) size distribution.

$$R = \frac{\mu - 1}{2(1 + \beta)} \tag{3.16}$$

C_T is a rearrangement of the Köhler parameterisation (Equation 3.17), where the supersaturation required for droplet activation S is modulated by the

curvature effect (second term) and the solute effect (third term). In this study, the values for C_T and k are not derived from these parameterisations but are instead retrieved from Villanueva-Birriel *et al.* (2014) as listed in 3.4. However, it is noteworthy to note that, if these parameterisations are used in future studies that assumes a greater relative humidity with increased warming, then it is expected that the curvature effect would dominate over the solute effect. This is because the greater relative humidity would increase the aerosol size and this would dilute the solute in the aerosol particle, thus diminishing the solute effect.

$$S = 1 + \frac{a}{r} - \frac{b}{r} \tag{3.17}$$

Table 3.4: Parameters for droplet activity spectrum

Location	C_T	k
MIN	900	1.2
DAY	1800	0.7
AND	800	0.7
JAS	700	0.7
OWE	700	0.7
CHA	1400	0.9
BIR	1200	0.9
MAD	1000	0.7

Upon droplet activation, a series of microphysical processes follows, presenting the source and sink terms in Equations 3.8-3.12 as illustrated in Figure 3.2 *(refer Table 3.3 for microphysical process terms)*. In the model, hydrometeors typically grow via autoconversion, collision-coalescence (due to accretion and collection of hydrometeors) and vapour diffusion to the liquid, mixed and ice phases. For mixed and ice phases, additional microphysical processes take place depending on the temperature, shapes and habits of the ice crystals. These microphysical processes will be discussed briefly in the following paragraphs.

b. **Warm (liquid) phase**

i. **Autoconversion of cloud water to rain**

First, autoconversion represents the transfer of N and q from the droplet class to rain for the liquid phase, and cloud ice to snow for the ice phase, owing to the growth by vapour diffusion and coalescence. The autoconversion of cloud droplets to rain is given by formulation from Kogan (2013) and is defined in Equation 3.18. The droplet radius threshold at which cloud droplets are converted to raindrops is equal to 40 μm and occurs when q_c is greater than 0.001 g kg^{-1}.

$$S_{PRC} = 7.98 \times 10^{10} q_c^{4.22} \frac{N_c}{\rho \times 10^6}^{-3.01} \tag{3.18}$$

ii. **Production of rain hydrometeors**

Rain hydrometeors are produced at the expense of cloud water and from the melting of large solid particles like graupel/hail and snow. The former includes the autoconversion of cloud water into rain as mentioned in the previous paragraph, and the accretion of cloud water by rain drops. The accretion of cloud water by rain occurs when large rain drops collect small cloud water particles and occurs when both q_c and q_r exceed 0.00001 g kg^{-1}. This process is also known as the collision-coalescence process and is parameterised following formulation from Kogan (2013) as defined in Equation 3.19.

$$S_{PRA} = 8.53 q_c^{1.05} q_r^{0.98} \tag{3.19}$$

The melting of graupel (S_{PGMLT}) below the freezing level, along with shedding due to collection of graupel by rain contributes to rain and are defined in Equation 3.20 and 3.22, respectively. In these equations, L_f, K_a, and μ represent the latent heat of freezing, thermal conductivity of air, and viscosity of air respectively. The Schmidt number S_c represents the ratio of kinematic viscosity (μ/ρ) to diffusivity of water vapour in

air. c_w is the specific heat of water equal to 4187 J kg^{-1} K^{-1}.

$$S_{PGMLT} = 2\pi K_a N_{0g} \frac{(273.15 - T)}{L_f} \{ \frac{0.86}{\lambda_g^2} + 0.28 (\frac{\eta a_g \rho}{\mu})^{\frac{1}{2}} \frac{S_c^{\frac{1}{3}} \Gamma(\frac{b_g}{2} + \frac{5}{2})}{\lambda_g^{b_g/2+5/2}} \} + \chi \tag{3.20}$$

$$\chi = \frac{c_w}{L_f} (273.15 - T) S_{PRACG} \tag{3.21}$$

$$S_{PSMLT} = 2\pi K_a N_{0s} \frac{(273.15 - T)}{L_f} \{ \frac{0.86}{\lambda_s^2} + 0.28 (\frac{\eta a_s \rho}{\mu})^{\frac{1}{2}} \frac{S_c^{\frac{1}{3}} \Gamma(\frac{b_s}{2} + \frac{5}{2})}{\lambda_s^{b_s/2+5/2}} \} + \chi \tag{3.22}$$

$$\chi = \frac{c_w}{L_f} (273.15 - T) S_{PRACS} \tag{3.23}$$

c. **Ice phase**

i. **Heterogeneous and homogeneous ice nucleation**

At temperatures below freezing and warmer than approximately −35 °C, rain and droplets can remain in liquid form (supercooled droplets or rain) and are also assumed to freeze instantaneously upon collision. This is known as heterogeneous freezing and is assumed to occur through immersion and contact freezing (e.g. Lohmann *et al.*, 2001). The freezing of cloud droplets is a function of temperature and droplet size based on observations of mixed-phase stratus described by Rangno and Hobbs (2001). The droplet effective radius must be ≥ 12 μm to initiate contact and immersion freezing of cloud droplets at $-10 < T < -4$ °C. At $T \leq -10$ °C, contact freezing is allowed for all droplet sizes while droplet effective radius must be ≥ 10 μm for the initiation of immersion freezing.

Immersion freezing dominates at $T \lesssim -25$ to -15 °C, while contact freezing is more important at warmer temperatures depending on drop size (freezing rates are a function of volume and drop radius for immersion and contact freezing, respectively).

The formulation for contact freezing is based on a flux of contact nuclei (IN) to the droplets due to Brownian motion as given in 3.24, where the effective diffusion coefficient, DAP given by Young (1974) is presented in Equation 3.25, and the number of contact nuclei is given by Meyers curve Meyers *et al.* (1992) as in 3.27.

$$S_{MNUCCC} = \frac{\pi^2}{3\rho} \times DAP \times NACNT \times \exp\left(\log(\frac{N_c}{\Gamma(\mu_c+1)}))+ \log(\Gamma(\mu_c+5)) - 4\times\log(\lambda_c)\right), \tag{3.24}$$

$$DAP = 4\pi(\frac{1.38e^{-23}}{6\pi RIN})T\frac{(1+\frac{\frac{7.37T}{(288\times10\times P)/100}}{RIN})}{\mu}, \tag{3.25}$$

where RIN is the radius of contact nuclei, that is 0.1e^{-6}, μ is the dynamic viscosity of air given in 3.26.

$$\mu = \frac{1.496e^{-6}T^{1.5}}{T+120} \tag{3.26}$$

$$NACNT = exp(-2.80 + 0.262(273.15 - T)) * 1000 \tag{3.27}$$

On the other hand, the formulation for immersion freezing follows from Bigg (1953) and are given in 3.28 and 3.29 for the freezing of cloud droplets and rain water, respectively. For the freezing of rain water in Equation 3.29, A' and B' are equal to 0.66 K^{-1} and 100 m^{-3} s^{-1}, respectively.

$$S_{MNUCCC} = S_{MNUCCC} + \frac{\pi^2}{36} 100 \rho_w \times \exp\left(\log(\frac{N_c}{\Gamma(\mu_c + 1}) + \log(\Gamma(7 + \mu_c)) - 6 \times \log(\lambda_c)\right) \times \exp\left(0.66(273.15 - T) - 1\right) \tag{3.28}$$

$$S_{MNUCCR} = 20\pi^2 \frac{\rho_w}{\rho} B' N_{0r} exp(A'^{(273.15-T)}) \lambda_r^{-7} \tag{3.29}$$

At cold temperatures below −40 °C, homogeneous freezing of aerosol and cloud water/ain occur instantly to form ice and graupel/hail, respectively, using the formula from Rutledge and Hobbs (1984) and Rasmussen *et al.* (2002), respectively.

ii. **Autoconversion of cloud ice to snow**

Similar to cloud droplet that undergoes autoconversion to rain, cloud ice undergoes autoconversion into large ice particles, labelled as snow. The autoconversion of cloud ice to snow is parameterised in terms of the vapour diffusion growth rate similar to Harrington et al. (1995) due to small crystals growing primarily by water vapour diffusion in many conditions (Pruppacher and Klett, 1997). Here, the autoconversion of cloud ice to snow is assumed to occur only when the ice is growing, i.e. cloud ice mass mixing ratio greater than 0.00001 g kg^{-1}, size threshold above 125 μm, and in conditions of ice supersaturation greater than 1%.

iii. **Aggregation of snow particles**

When snow mass mixing ratio exceeds 0.00001 g kg^{-1}, snow particles aggregate to form larger snow particles. The aggregation of snow follows from Passarelli (1978) and is given in 3.30, with collection efficiency, E_{is} of 0.1.

$$S_{NSAGG} = \frac{\frac{1108(E_{is})\pi^{(\frac{1-b_s}{3})}\rho_s^{(\frac{-2-b_s}{3})}}{4(720)}\eta a_s \rho_s^{(\frac{2+b_s}{3})} q_s^{(\frac{2+b_s}{3})} N_s^{(\frac{4-b_s}{3})}}{\rho} \tag{3.30}$$

iv. **Collection of cloud water by cloud ice**

Cloud ice start to collect cloud water when the cloud ice mass mixing ratios ice exceeds 0.00001 g kg^{-1} and when the ice diameter is greater than 100 μm. This process assumes that rime from cloud water collected on cloud ice does not lead to splintering. The formulation is given in 3.31, where the collection efficiency for cloud ice-droplet collisions, E_{ci} is 0.7.

$$S_{PSACWI} = \frac{(\frac{\Gamma(b_i+3)\pi}{4E_{ci}})\eta a_s q_s \rho N_{o_i}}{\lambda_i^{b_i+3}} \tag{3.31}$$

v. **Collection of snow by rain**

When both snow and rain mass mixing ratios exceed 0.1 g kg^{-1}, snow collection by rain is converted into graupel/hail and the process is as in 3.32.

$$\begin{aligned} S_{PSACR} = (1-\alpha_{rs})\pi^2 E_{rs}\sqrt{(\alpha V_{q_r} - \beta V_{q_s})^2 + \gamma V_{q_r} V_{q_s}} \\ [\frac{\rho_s}{\rho} N_{0r} N_{0s} (\frac{5}{\lambda_r^6 \lambda_s} + \frac{2}{\lambda_r^5 \lambda_s^2} + \frac{0.5}{.} \lambda_r^4 \lambda_s^3)] \end{aligned} \tag{3.32}$$

vi. **Accretion of cloud water onto snow**

The accretion of cloud water onto snow occurs when snow mass mixing ratio exceeds 0.00001 g kg^{-1}. The formulation uses continuous collection equation with simple gravitational kernel (e.g. Rogers and Yau, 1989; Pruppacher and Klett, 1997) as given in Equation 3.33. In the equation, E_{cs} equals 0.7 and represents the collection efficiency for ice-droplet collisions.

$$S_{PSACWS} = \Gamma(b_s + 3)\frac{\pi}{4}E_{cs}\eta a_s q_c \rho \frac{N_{0s}}{\lambda_s^{b_s+3}} \tag{3.33}$$

vii. **Accretion of rain water by snow**

When both rain and snow mass mixing ratios exceed 0.00001 g kg^{-1}, rain water is accreted by snow following the formula from Ikawa and Saito (1991) as given in Equation 3.34, where the collection efficiency for rain-snow collisions, E_{rs} is 1.

$$\begin{aligned} S_{PRACS} = (\pi^2 E_{rs}\rho_w)\times \\ \Bigg([(1.2(\frac{\Gamma(4+b_r)/6}{\lambda_r^{b_r}}) - 0.95(\frac{\Gamma(4+b_s)/6}{\lambda_s^{b_s}}))^2 + \\ 0.08(\eta a_s \frac{\Gamma(4+b_r)/6}{\lambda_s^{b_s}}\frac{\Gamma(4+b_r)/6}{\lambda_r^{b_r}})]^{0.5}\times \\ \rho N_{0r}\frac{N_{0s}}{\lambda_r^3}\times\frac{5}{\lambda_r^3\lambda_s} + \frac{2}{\lambda_r^2\lambda_s^2} + \frac{0.5}{\lambda_r\lambda_s^3}\Bigg) \end{aligned} \tag{3.34}$$

viii. **Collection of cloud water by hail**

The collection of cloud water by hail occurs when hail mass mixing ratio exceed 0.00001 g kg^{-1}, and the formula is given in Equation 3.35.

$$S_{PSACWG} = \Gamma(b_g + 3)\frac{\pi}{4}E_{cs}\eta a_g q_c \rho \frac{N_{0g}}{\lambda_g^{b_g+3}} \tag{3.35}$$

ix. **Collection of rain water by hail**

Similar to accretion of rain water by snow, the collection of rain water by hail follows the formula from Ikawa and Saito (1991) as given in Equation 3.36, and occurs when both rain and hail mass mixing ratio exceed 0.00001 g kg^{-1}.

$$\begin{aligned} S_{PRACG} = (\pi^2 E_{rs}\rho_w)\times \\ \Bigg([(1.2(\frac{\Gamma(4+b_r)/6}{\lambda_r^{b_r}}) - 0.95(\frac{\Gamma(4+b_g)/6}{\lambda_g^{b_g}}))^2 + \\ 0.08(\eta a_s \frac{\Gamma(4+b_g)/6}{\lambda_g^{b_s}} \frac{\Gamma(4+b_r)/6}{\lambda_r^{b_r}})]^{0.5}\times \\ \rho N_{0r}\frac{N_{0g}}{\lambda_r^3}\times\frac{5}{\lambda_r^3\lambda_s} + \frac{2}{\lambda_r^2\lambda_g^2} + \frac{0.5}{\lambda_r\lambda_g^3}\Bigg) \end{aligned} \tag{3.36}$$

x. **Hallet-Mossop rime-splintering: Ice multiplication**

The above four microphyiscal processes, i.e. S_{PSACWS}, S_{PRACS}, S_{PSACWG}, S_{PRACG} contribute to ice multiplication via the Hallet-Mossop rime-splintering process. The formulations for these processes are given in Equations 3.37-3.40, where $FMULT$ is a temperature-dependent parameter for the rime-splintering process as listed in Table 3.5

$$S_{QMULTS} = 35e^4(S_{PSACWS})FMULT(1000)\frac{4}{3}\pi\rho_i(0.000005)^3 \tag{3.37}$$

$$S_{QMULTR} = 35e^4(S_{PRACS})FMULT(1000)\frac{4}{3}\pi\rho_i(0.000005)^3 \tag{3.38}$$

$$S_{QMULTG} = 35e^4(S_{PSACWG})FMULT(1000)\frac{4}{3}\pi\rho_i(0.000005)^3 \tag{3.39}$$

$$S_{QMULTRG} = 35e^4(S_{PRACG})FMULT(1000)\frac{4}{3}\pi\rho_i(0.000005)^3 \tag{3.40}$$

Table 3.5: Temperature-dependent parameter $FMULT$ for rime-splintering

Temperature (°C)	**FMULT**
$T > -3$	0
$-5 < T < -3$	$(-3 - T)/2$
$-8 < T < -3$	$[T - (-8)]/3$
$T < -8$	0

xi. **Conversion of rimed cloud water and rain onto snow to graupel/ hail**

After rime-splintering, a portion of rimed cloud water and rain onto snow from S_{PSACWS} and S_{PRACS} are converted into graupel/hail via S_{PGSACW} (Equation 3.41) and S_{PGRACS} (Equation 3.42), respectively. This conversion occurs when snow, cloud water and rain mass mixing ratios exceed 0.1 g kg^{-1}, 0.5 g kg^{-1} and 0.1 g kg^{-1}, respectively. In Equation 3.41, E_{cs} equals 0.7 and represents the collection efficiency of ice-droplet collisions, while Δt is the time step in the model.

$$S_{PGSACW} = \eta^2 \Delta t \frac{3\rho_0 \pi N_{0s} q_c^2 E_{cs}^2 a_s^2 \Gamma(2b_s + 2)}{8(\rho_g - \rho_s)\lambda_s^{2b_s+2}} \tag{3.41}$$

$$S_{PGRACS} = \left(1 - \frac{\rho_s^2 (\frac{4}{\lambda_s})^3 (\frac{4}{\lambda_s})^3}{\rho_s^2 (\frac{4}{\lambda_s})^3 (\frac{4}{\lambda_s})^3 + \rho_w^2 (\frac{4}{\lambda_r})^3 (\frac{4}{\lambda_r})^3}\right) \times (S_{PRACS}) \tag{3.42}$$

xii. **Ice-rain collisions**

Ice-rain collisions that produce graupel/hail occur when q_r exceeds 0.1 g kg^{-1} and q_i is greater than 0.00001 g kg^{-1}, and occur in two ways: collection of ice by rain (S_{PRACI}, Equation 3.43) and rain freezing due to collisions with ice (S_{PIACR}, Equation 3.44) where the collection efficiency between rain and cloud ice (E_{ir}) is equal to 1.

$$S_{PRACI} = \frac{\eta \pi a_r q_i E_{ir} N_{0r}}{4} \frac{\Gamma(b_r + 3)}{\lambda_r^{b_r+3}} \tag{3.43}$$

$$S_{PIACR} = \frac{\eta \pi^2 \rho_w a_r E_{ir} N_i N_{0r}}{24} \frac{\Gamma(b_r + 6)}{\lambda_r^{b_r+6}} \tag{3.44}$$

3.4 Radiative transfer model

The Fu-Liou radiative transfer model (Fu and Liou, 1992; Fu and Liou, 1993) is used to quantitatively assess the cloud radiative properties through the vertical structure of clouds.

3.4.1 Basic equation sets

The radiative transfer equation is solved using a discrete-ordinate δ four-stream solution approach. The δ four-stream solution is a 1D solution, which is applied to the columns with clouds of interest. This scheme uses six and twelve spectral bands for solar and thermal infrared regions, respectively. The spectral division for solar region are $0.2 - 0.7$ μm, 0.7–1.3 μm, 1.3–1.9 μm, 1.9–2.5 μm, 2.5–3.5 μm, 3.5–4.0 μm, while the spectral division for thermal infrared region are 2200 – 1900 cm^{-1}, 1900 – 1700 cm^{-1}, 1700 – 1400 cm^{-1}, 1400 – 1250 cm^{-1}, 1250 – 1100 cm^{-1}, 1100 – 980 cm^{-1}, 980 – 800 cm^{-1}, 800 – 670 cm^{-1}, 670 – 540 cm^{-1}, 540 – 400 cm^{-1}, 400 – 280 cm^{-1}, 280 – 0 cm^{-1}. The solar albedo at the surface is 0.2 and the infrared emissivity is 1.0.

The model takes initialisation input of cloud water and ice mixing ratios, as well as vertical thermodynamic profiles comprising pressure, temperature and water vapour mixing ratio. The correlated k-distribution method, an approximation technique to perform accelerated calculation of radiative fluxes with an extreme reduction of the number of operations, is used to treat the gaseous absorption by 0_3, CO_2, CH_4, N_2O and H_2O. The CO_2, CH_4 and N_2O are assumed to have uniform mixing ratios throughout the atmosphere, with concentrations of 330, 1.6 and 0.28 ppmv, respectively. The radiative transfer scheme computes the radiation through the 1D column accounting for scattering and absorption of the cloud particles as well as the gases in the air (Rayleigh scattering).

3.5 A brief description on the main assessments performed in the thesis

A total of three main assessments are performed in this thesis and they are presented in **Chapters 4, 5 and 6** respectively. In this section, a description on the overall methodology and analysis method are described for **Chapter 4**. The description for **Chapters 5 and 6** are given in detail in the respective chapters.

Chapter 4 of this thesis aims to assess the responses of clouds to a warming climate. This is achieved by comparing the cloud responses between the past and future environments. Here, the past environment is labelled as 'cold' to indicate that it is colder than the projected warmer temperature in the future environment. The vertical atmospheric thermodynamic profiles for the periods 1970-1999 and 2070-2099 mentioned in **Section 3.2.1** were used as an initialisation to simulate idealised deep convective clouds for the past and future environment, respectively. The simulations are performed by using the WRF model described in **Section 3.3**. A comparison of the cloud responses between the past and the future environments are then made.

The comparison begins by assessing how the past and future thermodynamic environments differ. The parameters involved in this assessment are the initial conditions of temperature, specific humidity and relative humidity. From these parameters, the convective available potential energy (CAPE) and convective inhibition (CIN) are evaluated. These parameters are indicators for determining the potential and intensity of convection. Next, the cloudy regions from the idealised simulations are selected for analysis. The cloudy grid cells are defined with the following thresholds at each level: total cloud condensates that exceed 0.001 g m^{-3} with convective updraught speed of 1 m s^{-1}, following the thresholds adopted in other studies (e.g. Fan *et al.*, 2013; Villanueva-Birriel, 2014). Furthermore, the cloud condensate threshold of 0.001 g m^{-3} is the minimum amount of condensate visible in the simulation. A threshold value lower than this yields similar results, hence 0.001 g m^{-3} is deemed valid. From these cloudy grid cells, the cloud properties are analysed by computing the vertical or horizontal average values of each prop-

erty, i.e. hydrometeor mixing ratio, microphysical tendency rates at five minutes interval. The findings from this assessment are presented in **Chapter 4**.

Chapter 5 delves into understanding which factors of the changed environment are causing which effect on the cloud development found from the results of **Chapter 4**. A change in the thermodynamic environment involves a change in the temperature structure and relative humidity structure, as well as in the increase in temperature. In **Chapter 6**, the cloud radiative properties from the modelled clouds in the past and future environments performed in **Chapter 4** are assessed. It compares and assesses the cloud radiative properties between the past and future environments.

3.6 Summary

This chapter describes the eight locations in the United States chosen as the study cases (**Section 3.2.1**) in this thesis. The atmospheric thermodynamic profiles for these locations were obtained from the NCAR CCSM 3 global climate model, as described in **Section 3.2.2**. These profiles are used to initialise the WRF model that is used as a cloud-resolving model (**Section 3.3**) to create idealised simulations of deep convective clouds for the past and future environments, as well as for further three different thermodynamic conditions performed in **Chapter 5**. These simulations are performed in order to understand how different thermodynamic conditions affect cloud development as well as the cloud radiative properties. Finally, the findings from these assessment are presented in **Chapter 4**, **5** and **6**.

Chapter 4

Comparison between the responses of deep convective clouds in the past and future environments

4.1 Introduction

This chapter presents the results from the simulated deep convective clouds conducted in this study. The study is centred on the comparison between the responses of deep convective clouds in the past and future environments. **Section 4.2** describes the characteristics of the thermodynamic environment of the past and future climates and their resulting effects on the cloud structure, dynamics and microphysical evolution. **Section 4.3** discusses the implication of different thermodynamic structures on the cloud development, and **Section 4.4** contains discussion and provides a summary of the Chapter's findings.

4.2 Results

4.2.1 Vertical profiles of atmospheric temperature and moisture content

Figure 4.1 shows the vertical profiles of temperature for both past and future environments in all locations studied. All locations in the future environment exhibit warming throughout the depth of the atmosphere as compared to the past environment. The vertical profiles of specific humidity in Figure 4.2 shows that the future environment was moister than that in the past environment. Even though the future environment was moister than the past environment throughout the atmosphere, the saturation of air between the two environments was different. Figure 4.3 depicts the vertical profiles of relative humidity for both past and future environments for all locations.

The major differences in the relative humidity between the two environments were seen at the lower levels. From the surface up to 500 m, the air in the future environment was more saturated than that in the past environment. Above 500 m, however, the relative humidity in the future environment decreased substantially and remained lower than that of the past until at approximately 4 - 5 km when the air of both environments were at similar saturation. Given the important role moisture plays in convection, it is imperative to assess how the different trends in saturation of air influence the convective potential.

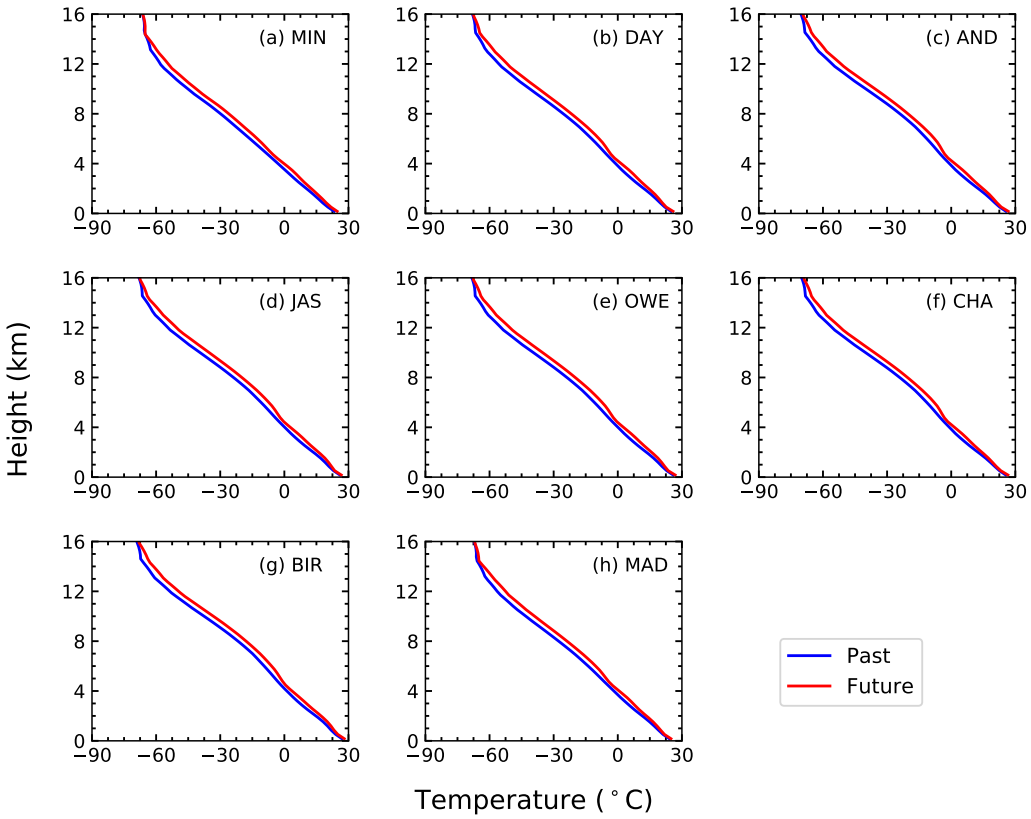

Figure 4.1: Vertical profiles of atmospheric temperature at initial condition

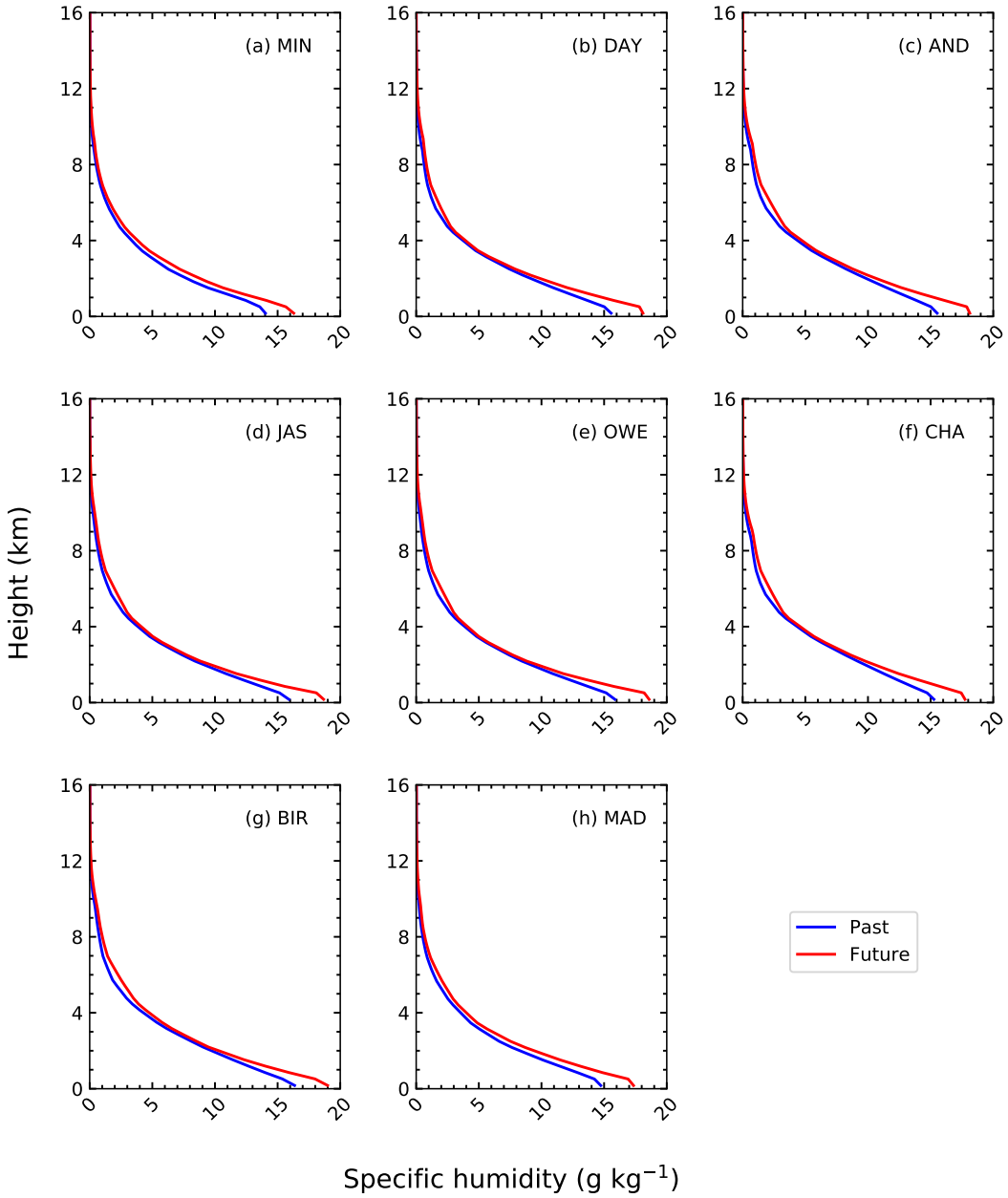

Figure 4.2: Vertical profiles of specific humidity at initial condition

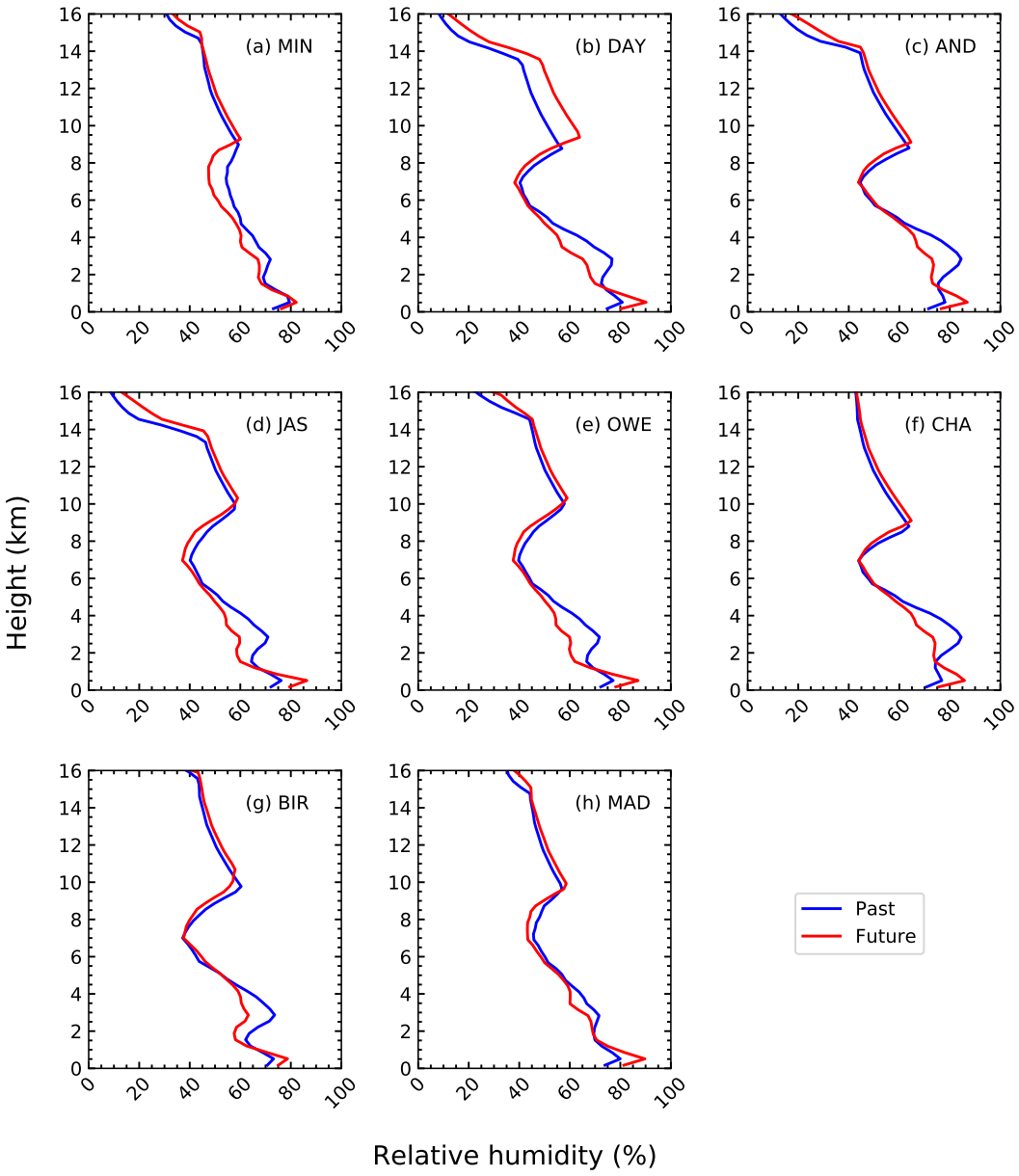

Figure 4.3: Vertical profiles of relative humidity at initial condition

4.2.2 Vertical profiles of convective available potential energy

Convective potential is commonly measured by the convective available potential energy (CAPE). CAPE is widely known as an indicator for the potential and intensity of convection. It is a measure of how much potential energy is available for the air parcel once the air parcel breaks through the energy barrier (known as convective inhibition, CIN) during convective initiation. Table 4.1 presents the column-integrated values of CAPE at the initial thermodynamic environment from the surface to the equilibrium level. The column-integrated values of CAPE were higher in the future than that in the past environment, which is consistent with previous studies that projected greater CAPE in a future warmer environment (e.g. Trapp *et al.*, 2009; Diffenbaugh *et al.*, 2013; Seeley and Romps, 2015; Rasmussen *et al.*, 2017). However, even though the values were higher in the future, the vertical structure of the profiles differed significantly as illustrated in Figure 4.4. In Figure 4.4, CIN corresponds to the negative values, while CAPE corresponds to the positive values. Overall, the CAPE in the future was greater than in the past, with clearly greater values at three levels. These levels are approximately below 500 m, between 4.0 - 5.5 km, and above 7 km.

Beginning from the lowest level, the zoomed-in profiles of CIN/CAPE in Figure 4.5 shows that the future profiles exhibited positive values, that is CAPE, all the way up from the surface. In contrast, the past profiles exhibited negative values, that is CIN, and stretched from the surface up to approximately 500 m. At 500 m, another significant difference was noted between the two profiles. The difference between the two environments lies in the vertical gradient of CAPE, in particular the change in CAPE values between the model layers, denoted here as dCAPE. In the past, the dCAPE was greater than in the future. In other words, we see a sharp increase in CAPE in the past environment compared to the gradual increase in the future environment. This trend continued until approximately 4 km, when the trend switched between the two environments; the future environment exhibited greater CAPE than in the past, up until 5.5 km. From there, the CAPE values between the two environments remained similar until approximately 7 km, beyond which the CAPE was greater again in the future environment.

The CAPE calculation employed in this study account for the effect of latent processes on the buoyancy of the air parcel by using the virtual temperature parameter instead of the temperature parameter (Markowski and Richardson, 2011). Because the humidity of planetary boundary layer sets the potential for deep convection (Donner and Phillips, 2003; Stevens *et al.*, 2017, CAPE is calculated from the surface up to the equilibrium level. That said, the vertical structures of atmospheric moisture content, both specific and relative humidity, correlates to CAPE, and largely dictate the cloud vertical structure as presented in **Section 4.2.3**. In addition, Weisman and Klemp (1982) demonstrated the importance of bulk cape on storm structure and intensity. Under idealised conditions, if a fixed fraction of CAPE is transformed into kinetic energy, the square root of CAPE gives an estimate of the maximum possible vertical velocity achieved in the updraught of an ascending air parcel (Bluestein, 1993). The relationship between CAPE and maximum vertical velocity is presented in **Section 4.2.4**.

Table 4.1: Column-integrated CAPE at the initial condition

Location	**CIN/CAPE (J kg^{-1})**	
	Past	**Future**
MIN	3392.9	4042.0
DAY	3731.2	4540.0
AND	3676.1	4488.6
JAS	3736.5	4519.4
OWE	3729.8	4554.6
CHA	3455.0	4236.0
BIR	3830.3	4561.3
MAD	3413.8	4232.5

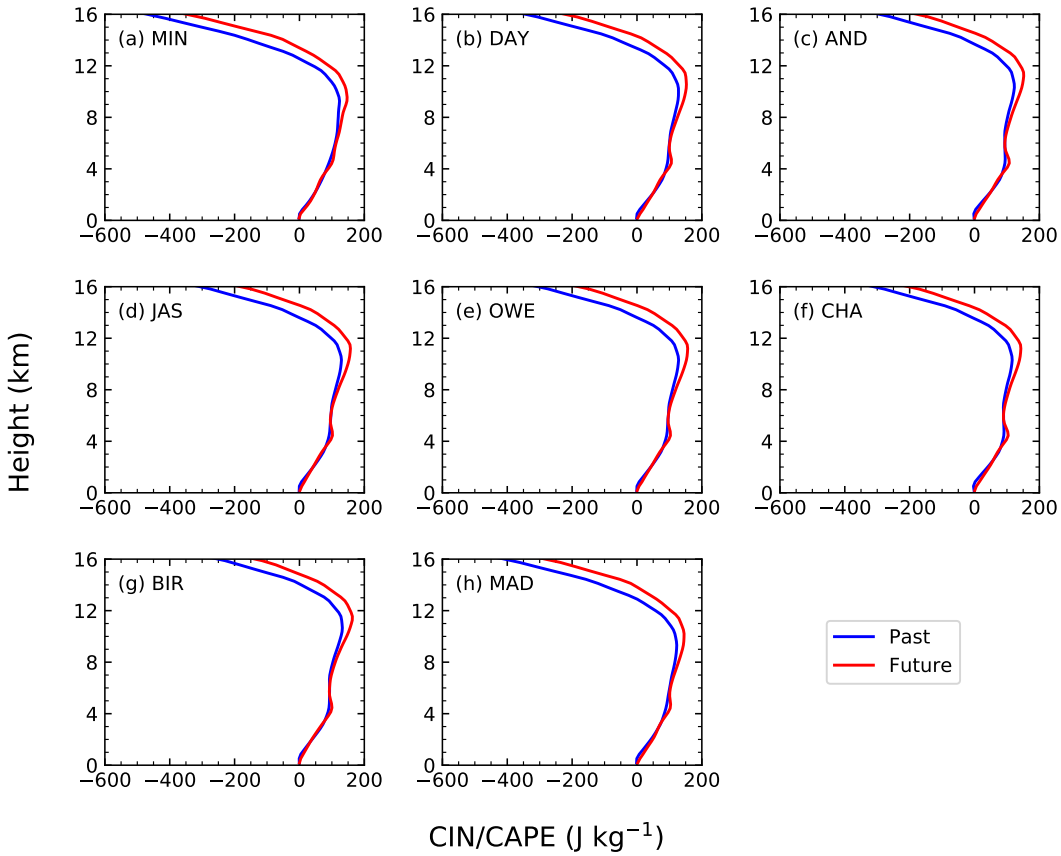

Figure 4.4: Vertical profiles of CIN and CAPE at initial condition

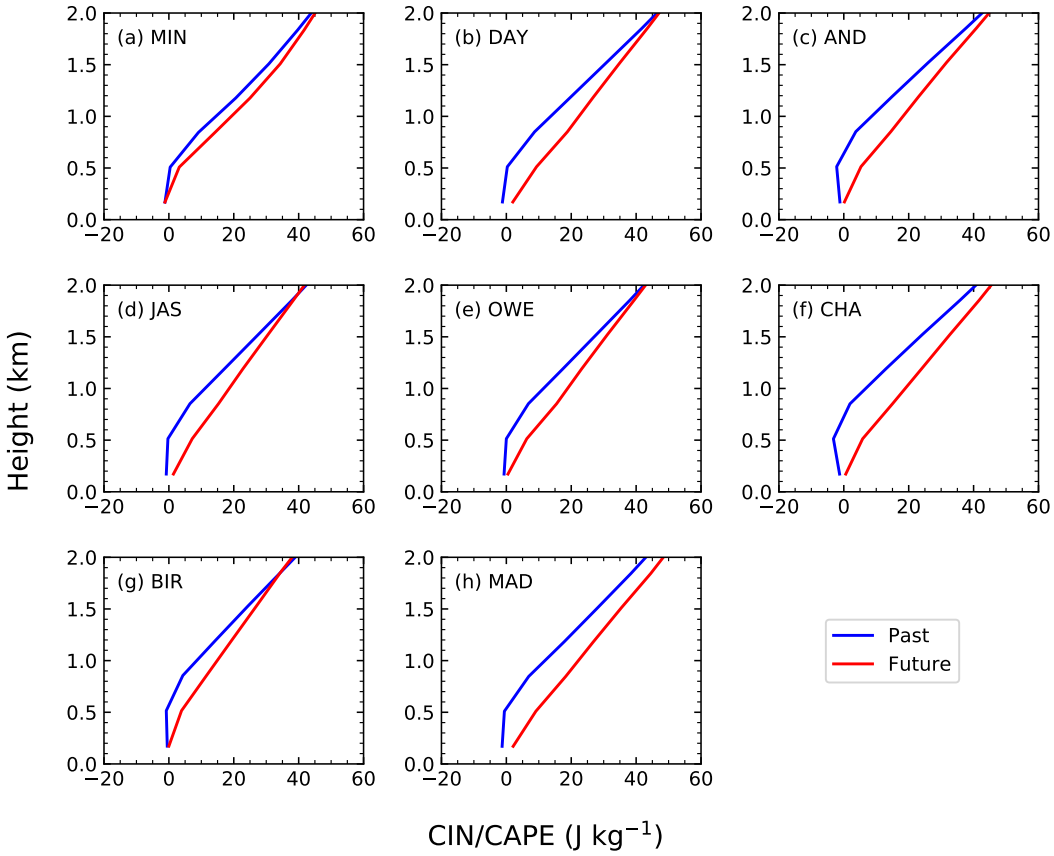

Figure 4.5: Vertical profiles of CIN and CAPE at initial condition from the surface up to 2 km in altitude

4.2.3 The effects of vertical structure of initial thermodynamic environment on cloud structure

At the lowest level (below 500 m), the past environment's low relative humidity gives rise to the convective inhibition (CIN). In contrast, the high relative humidity in the future environment generates CAPE right from the surface in the future environment. As a result, the presence of CIN from the dry boundary layer in the past environment dictates the height at which the cloud forms. This is because convection can only occur when CIN is overcome. On the other hand, the absence of CIN in the future environment permits the vertical motion of air parcel, and being already in near-saturated boundary layer, the air parcel need not rise further up to achieve saturation for clouds to form. In other words, the planetary boundary layer is deep and less saturated in the past, and shallow and more saturated in the future environment. Consequently, this results in higher cloud bases in the past, and lower cloud bases in the future environment as seen in Table 4.2. The average cloud base in the future environment was 32% lower than in the past environment. the boundary layer is lower in the future than in the past environment.

A caveat in the characteristics of the boundary layers in the past and future environments is that it could be caused by a model bias in the boundary layer parameterisation scheme used in the CCSM3 climate model. The previous versions of this global climate model has a shallow bias in the boundary layer depth. However, in the version used in this thesis, the bias is substantially reduced Collins *et al.* (2006). Nonetheless, a dry bias is still present in the profiles used in this thesis, but has been corrected by Villanueva-Birriel (2014) using the reanalysis data as mentioned in **Section 3.2.2**. Other plausible reasons for the shallow boundary layer could be due to the interactions between the enhanced land-sea near-surface temperature contrast and the advection of maritime air over land (Rowell, 2009). Increased temperature enhances the rate of evaporation, and the air water-holding capacity increases with increasing temperature. As the land warms faster than the sea, the air over land has higher water-holding capacity and therefore can contain more water vapour, thus increasing both the specific and relative humidity over land. In contrast, the slower warming of the sea lowers the rate of evaporation, resulting in air that is lower in moisture content relative to that over land. When

the maritime air advects over land, this air experiences a fall in relative humidity due to the higher water-holding capacity of air over land.

From 500 m to 4 km, the relative humidity in the past environment increases, and the vertical gradient of CAPE increases sharply. Conversely, the relative humidity in the future environment decreases, and the vertical gradient of CAPE increases gradually. From 4 - 5.5 km, the relative humidity of both environments are similar. However, due to the greater specific humidity throughout the atmosphere in the future environment, the additional moisture contributes to the higher CAPE in the future environment than it is in the past environment, and it remains so until the upper troposphere. Stevens *et al.* (2017) reported that the effect of relative humidity on the intensity of convection is especially pronounced at the layer between the cloud base and the freezing level. This layer is referred to as the warm-phase cloud layer in this study. The depth of this layer provides a measure of the intensity and evolution of warm rain process.

Table 4.2 shows that the freezing level is lower in the past than in the future environment, owing to the colder (warmer) environment in the past (future). The difference between the heights of the cloud base and the freezing level gives the depth of the warm-phase cloud layer. The average depth of the warm-phase cloud layer was 15% greater in the future than that in the past environment. In other words, the lower cloud bases and higher freezing levels in the future resulted in greater cloud depth than that in the past. An example of a 2D cross section of the simulated cloud structure for MIN is given in Figures C.1 and C.2 in **Appendix C** for the past and future environments, respectively.The effects of the depth of the warm-phase cloud layer on the development of clouds are presented in **Section 4.2.5**.

Table 4.2: Heights of cloud base (m), freezing level (km), and warm-phase cloud depths (km)

Locations	Cloud base heights (m)		Freezing levels (km)		Warm-phase cloud depths (km)	
	Past	Future	Past	Future	Past	Future
MIN	691	583	3.5	4.1	2.8	3.5
DAY	661	487	3.8	4.1	3.1	3.6
AND	747	586	3.8	4.1	3.0	3.5
JAS	732	507	4.1	4.4	3.4	3.9
OWE	730	543	4.1	4.4	3.4	3.9
CHA	766	611	3.8	4.1	3.0	3.5
BIR	774	626	4.1	4.5	3.4	3.8
MAD	676	456	3.8	4.1	3.1	3.6

4.2.4 The effects of vertical structure of initial thermodynamic environment on cloud dynamics

The thermodynamic environment profoundly dictates the characteristics and evolution of convective development. Figure 4.6 shows the time-series profiles of maximum vertical velocity for the clouds in the past and future environments. The time-evolution of maximum vertical velocity reflects the evolutionary stages of the cloud development. The first peak at 10 min indicates the onset of nucleation where latent heat of condensation is released from the condensation of water vapour into cloud water. The latent heat further drives the vertical velocity, reaching a peak at 25 min and subsequently decreases in strength until around 60 - 80 min, where the vertical velocity increases again due to secondary convection. As the focus of this study is on the influence of thermodynamic environment on cloud development, the study is limited to the primary convection.

Apart from the similar vertical velocity between the past and future clouds during the first 10 mins, the vertical velocity in the past clouds remain consistently higher than in the future clouds. This shows a stronger convection in the past than in the future clouds. The strength of the vertical velocity has a prominent influence on the vertical transport of water vapour and condensates within the clouds. This is especially seen in the vertical distribution of cloud water at the early stage as

shown in Figure 4.7. Here, the cloud water is distributed over a greater depth in the past clouds, and over a smaller depth in the future clouds. Subsequently, this has an implication on the overall cloud microphysical evolution as presented in **Section 4.2.5**.

In **Section 4.2.2**, it is mentioned that the square root of CAPE corresponds to the maximum possible vertical velocity achieved in the updraught of an ascending air parcel. This relationship is seen manifested in the past, but not in the future environment. This is because the theoretical argument ignores several effects that could influence the cloud buoyancy such as vertical wind shear and entrainment. The findings discussed in **Sections 4.2.2** and **4.2.3** suggest that the vertical gradient of the increase in CAPE and the conditions of the warm-phase cloud layer play a role in influencing the cloud buoyancy. This has ramifications on the intensity and evolution of cloud development as presented in **Section 4.2.5**.

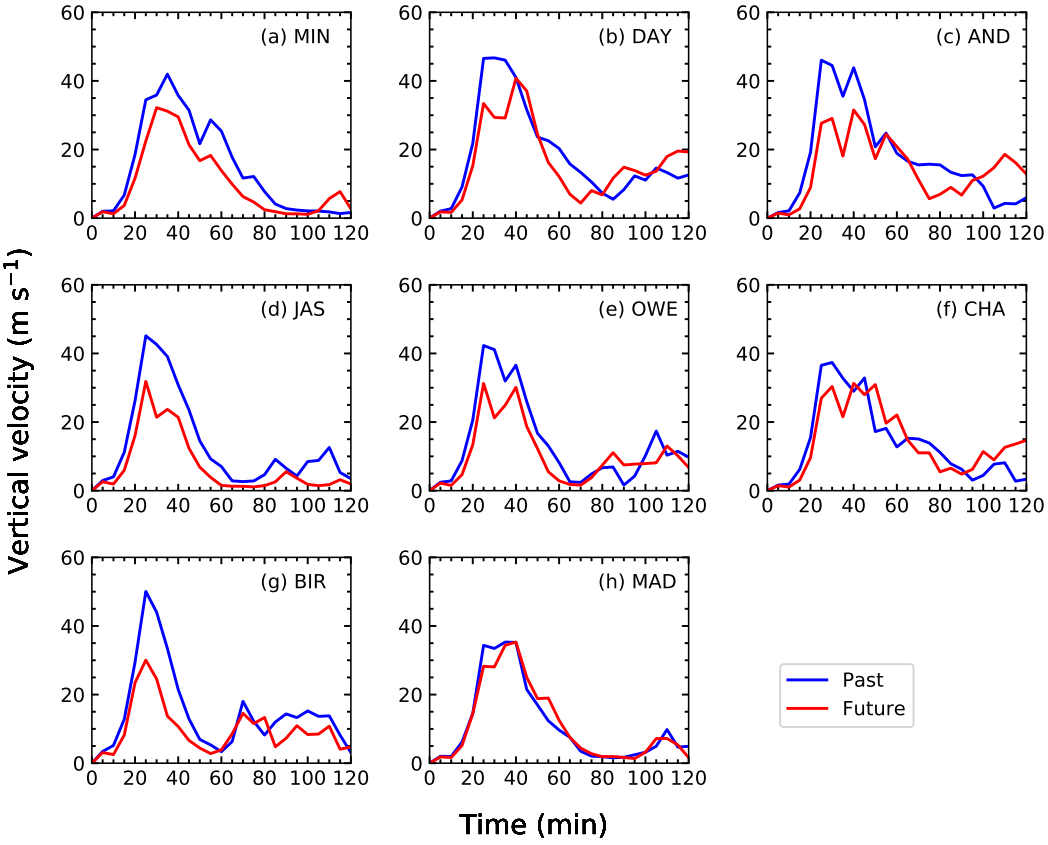

Figure 4.6: Time-series profiles of maximum vertical velocity

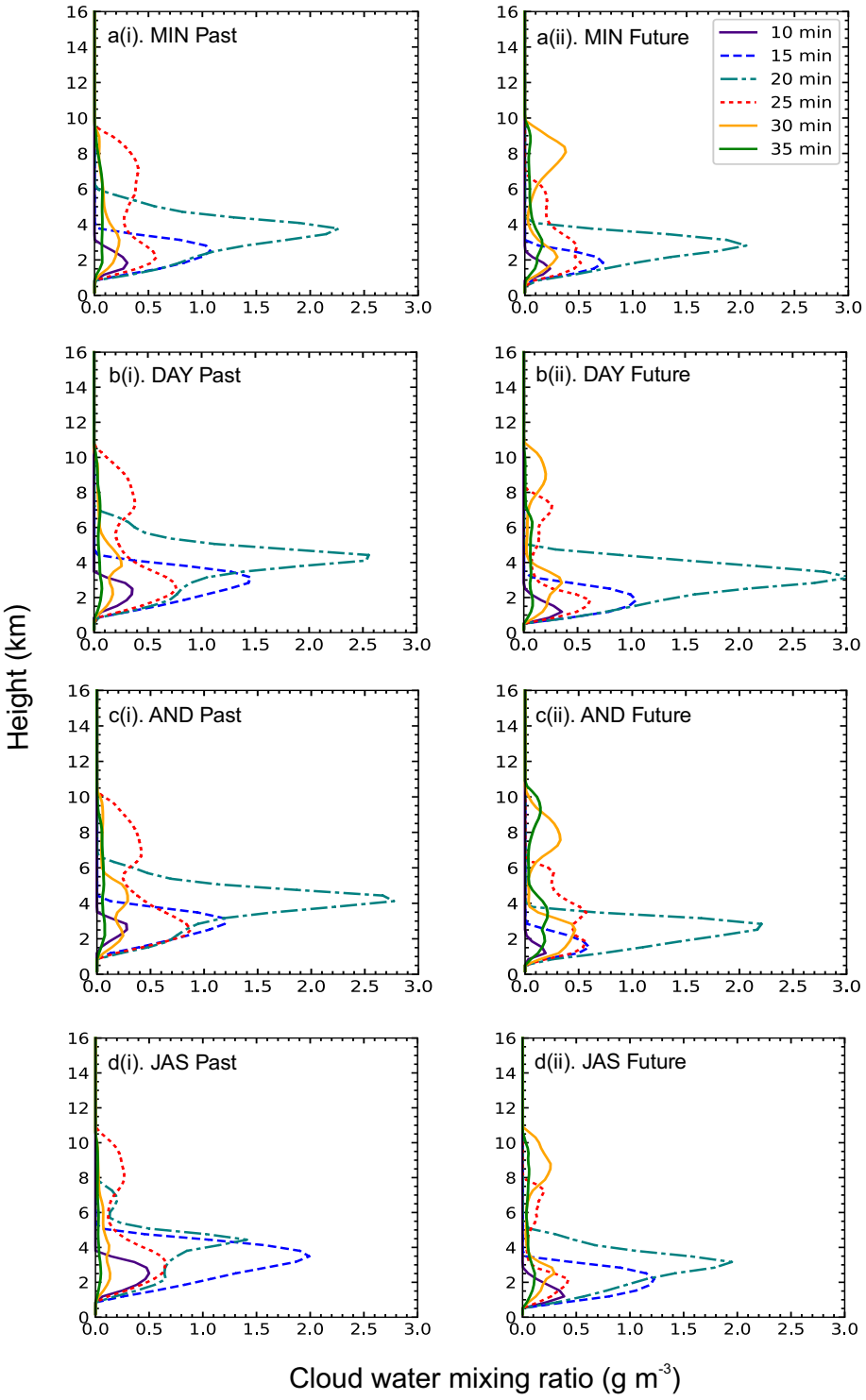

Figure 4.7: Vertical distribution of cloud water mixing ratio

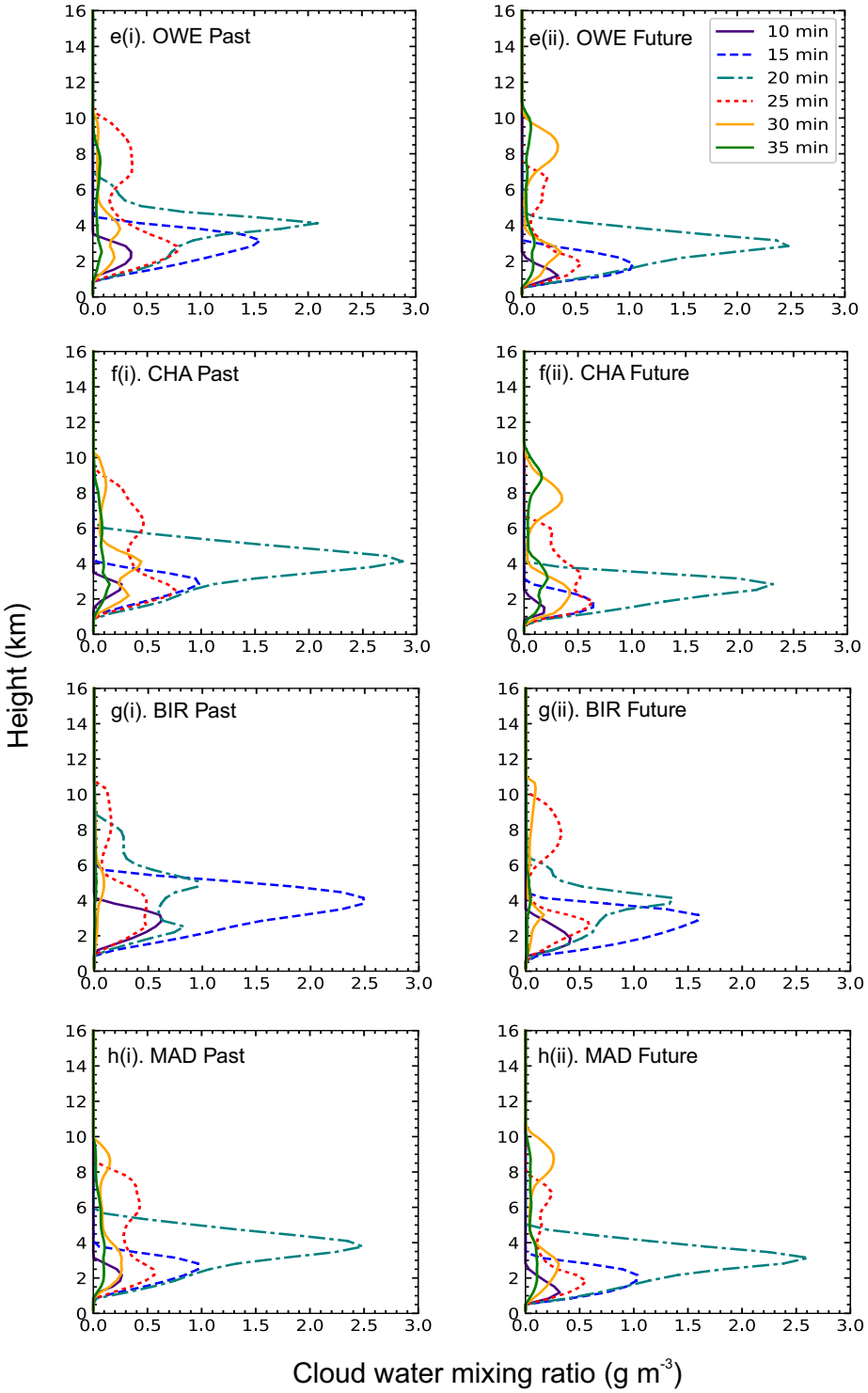

Figure 4.7: Vertical distribution of cloud water mixing ratio

4.2.5 Cloud microphysical evolution at a glance

Figures 4.8, 4.9, 4.10, 4.11 and 4.12 depict the time-series profiles of mass mixing ratio for cloud water, rain, cloud ice, snow and hail, respectively. In all cases, the average cloud water mass mixing ratio between the clouds in the past and future environments were similar, although some locations recorded a higher peak in the past than in the future environment. The profile shows an increasing trend of cloud water mass mixing ratio until 20 min, when it started to decrease, indicating the transport and use of water in other microphysical processes. Thereafter, the trends of cloud water mass mixing ratio between the two environments remained consistently similar. Rain formation started at 20 min for all clouds in the past and future environments, in conjunction with the decrease in cloud water mass mixing ratio.

Key differences between the clouds in the past and future environments emerge from the rain formation. This is seen in the higher production of rain in the future than in the past clouds. Figure 4.9 shows that the average rain mass mixing ratio during the peak production was 42% higher in the future than in the past environment. This further led to other key differences in the ice phase microphysics between the past and future clouds. The ice processes in the past environment initiated earlier and the production of ice hydrometeors were greater than in the future environment. Depending on the locations, ice processes started around 20 - 30 min into the simulations. The greater production of ice hydrometeors indicate greater release of the latent heat of freezing. As a result, this enhances the updraught and more condensate is transported higher as seen in the higher cloud top height in the past compared to that in the future. Table 4.3 also shows the cold-phase cloud depth for both past and future clouds at the mature stage, i.e. 25 – 30 min. The table shows an average decrease in the cloud-top height and cold-phase cloud depths by 9% and 18% in the future relative to the past environment. Just as the greater warm-phase cloud depth enhances warm rain process in the future clouds, so does greater cold-phase cloud depth enhances the cold rain process in the past clouds. Following that, rainfall in both past and future environments began.

Figure 4.13 shows the time-series profiles of maximum rain rate (left y-axis) and accumulated surface precipitation (right y-axis) for clouds in past and future environments in all locations. From the figure, it is seen that the rainfall in both past and future clouds started at the same time, i.e. 30 or 35 min depending on the locations, during which time both clouds have developed into ice phase. This is a typical characteristic of continental deep convective clouds where the surface precipitation is sourced primarily from the cold rain process. In cold rain process, the melting of hail accounts for 60 - 70% of the surface precipitation (Xu and Zipser, 2012). It is noted however, that, earlier studies (e.g. Ghosh and Jonas, 1998) found that the onset times of precipitation are mediated by parameterisation of autoconversion of cloud water to rain. They found that higher initial cloud water content leads to earlier onset times of precipitation. In this thesis, because of the structural changes predicted in the future environment, the onset time of precipitation is the same for both past and future environments despite the latter having higher initial cloud water content.

The differences between the characteristics of the precipitation between the clouds in the past and future environments are noted in the initial rain rate and the overall accumulated surface precipitation. The clouds in the future recorded higher initial maximum rain rate than the clouds in the past. However, the clouds in the future accumulated less surface rainfall than in the past clouds. In addition, the past clouds are noted to have two peaks in the rain rate and they last longer than those in the future. The results suggest that these differences arise due to the key differences in the warm and ice phase microphysics between the cloud in the past and future environments. As the precipitation in both clouds originates from the ice phase, it is informative to explore the hail microphysical budgets between the past and future clouds, and this is presented in **Section 4.2.6**.

Table 4.3: Cloud-top heights and cold-phase cloud depths for all locations

Locations	**Cloud-top heights (m)**		**Cold-phase cloud depths (km)**	
	Past	**Future**	**Past**	**Future**
MIN	13.5	12.0	10.0	7.9
DAY	14.8	12.8	11.0	8.7
AND	15.0	14.3	11.2	10.2
JAS	14.3	12.8	10.2	8.4
OWE	14.3	12.0	10.2	7.6
CHA	13.3	13.3	9.5	9.2
BIR	15.8	14.3	11.7	9.8
MAD	12.8	12.8	9.0	8.7

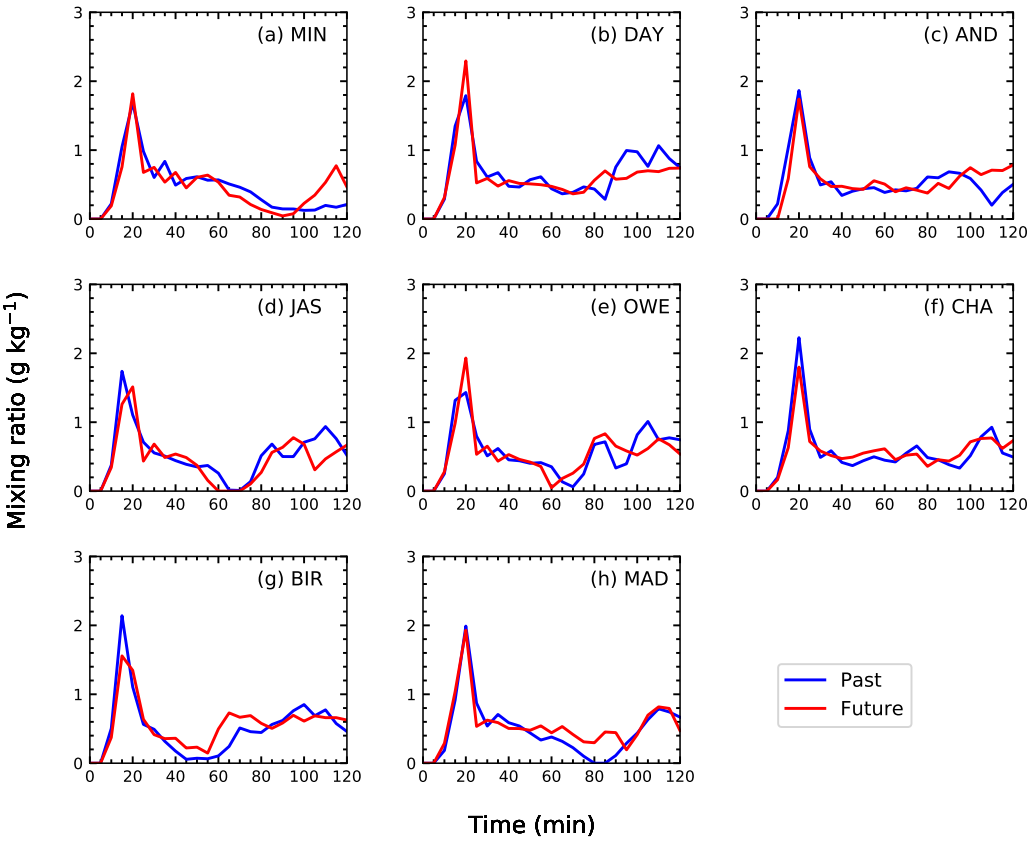

Figure 4.8: Time series profile of cloud water mass mixing ratio

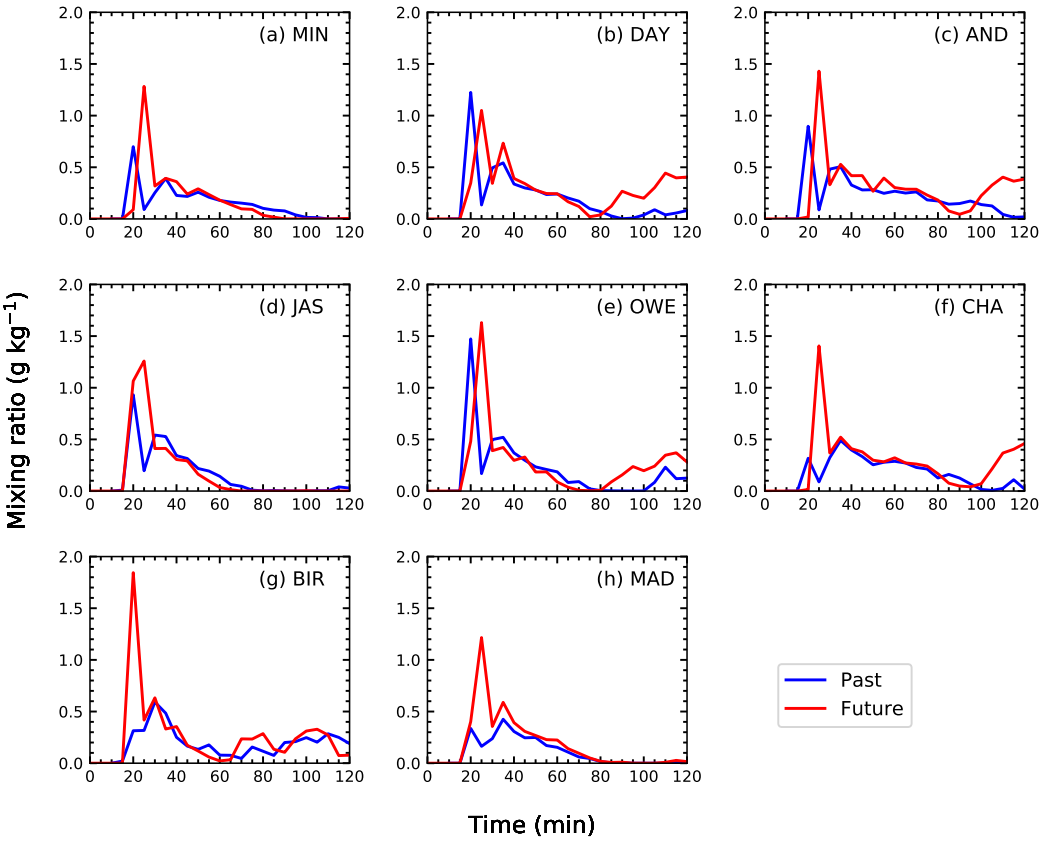

Figure 4.9: Time series profile of rain mass mixing ratio

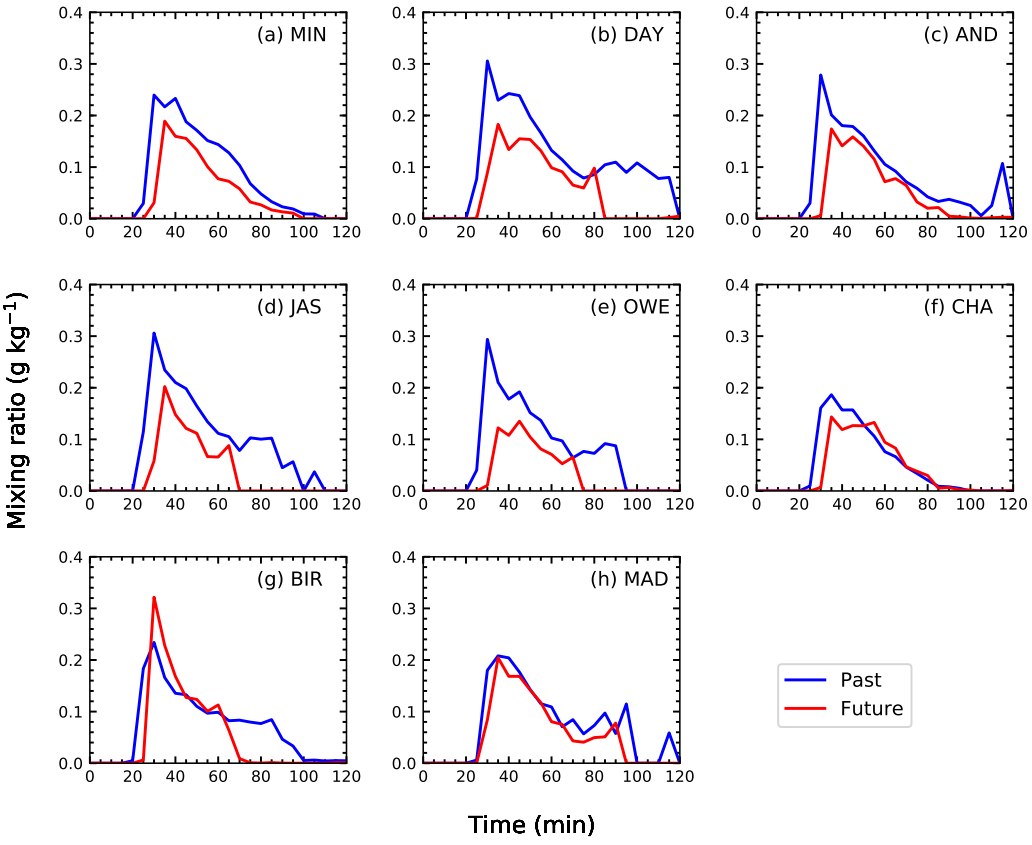

Figure 4.10: Time series profile of cloud ice mass mixing ratio

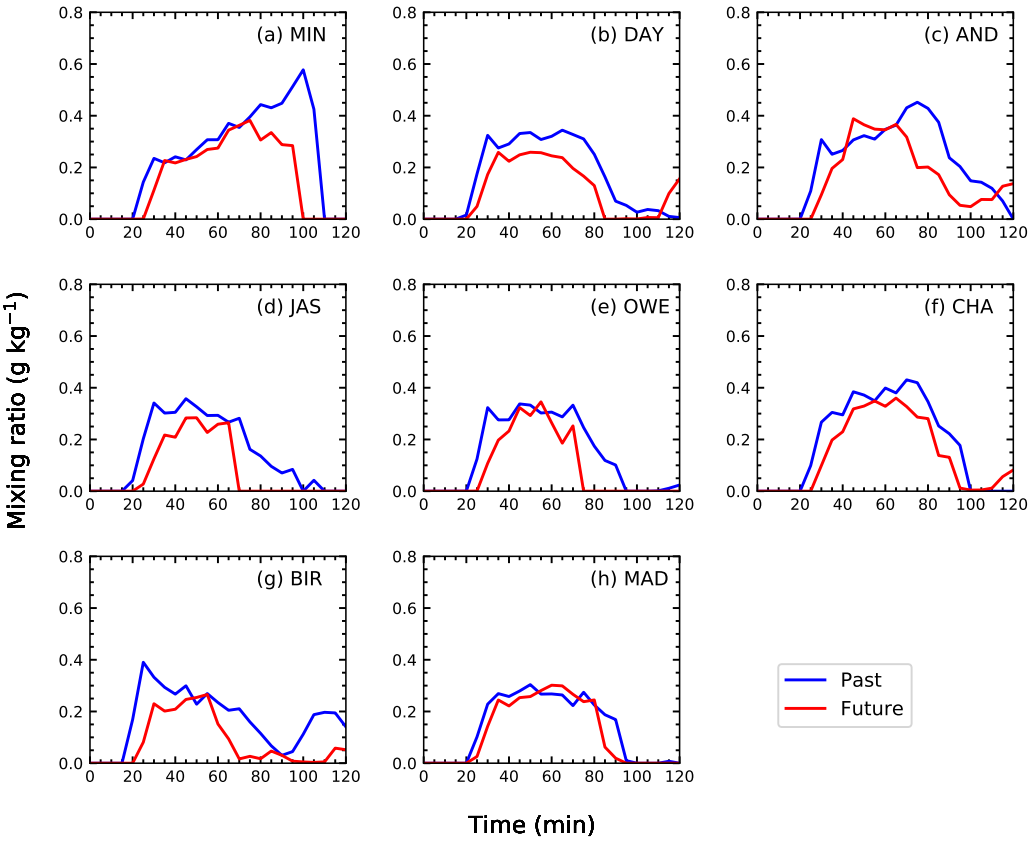

Figure 4.11: Time series profile of snow mass mixing ratio

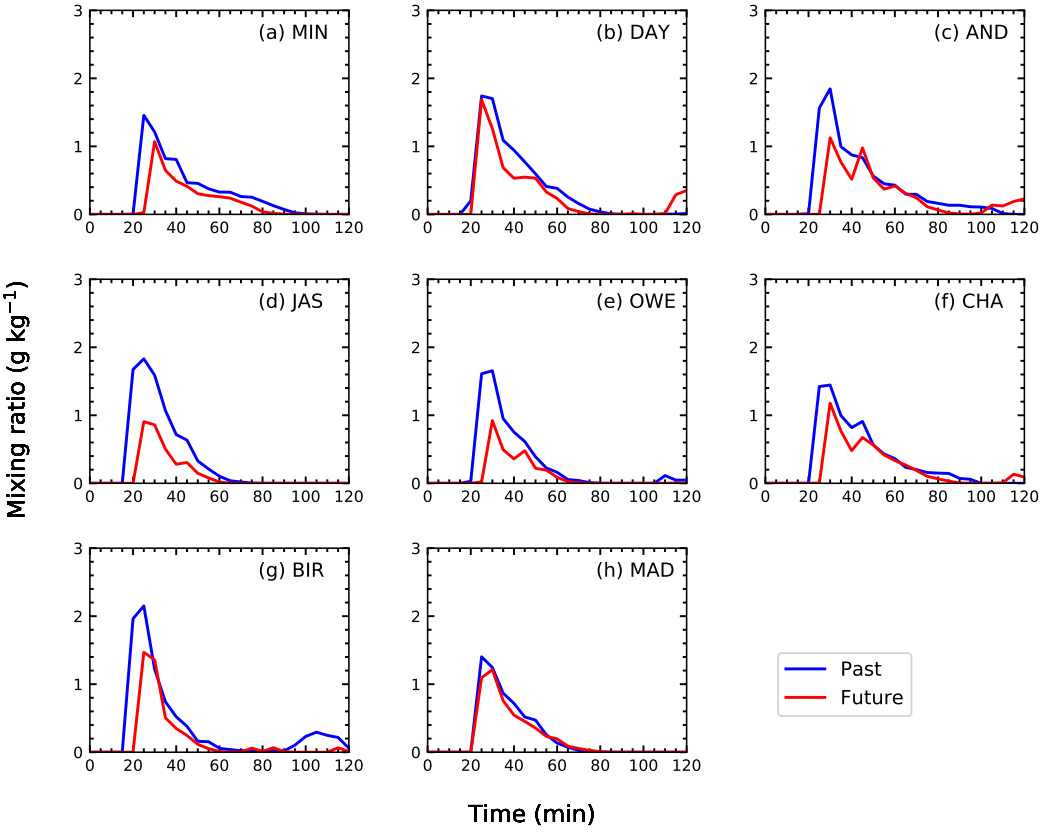

Figure 4.12: Time series profile of hail mass mixing ratio

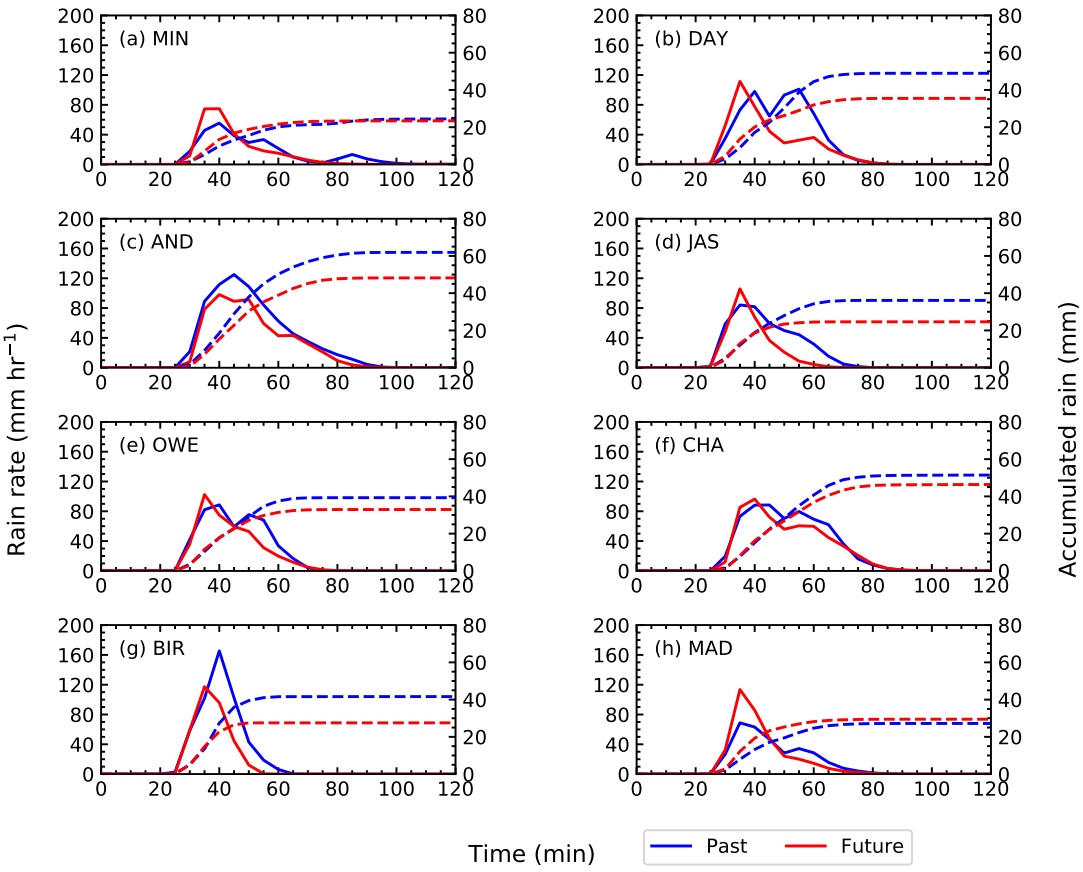

Figure 4.13: Maximum initial rain rate and accumulated surface precipitation

4.2.6 Differences in the hail microphysical budgets between the past and future clouds

Figures 4.14 and 4.15 depict the hail microphysical budgets for the past and future clouds in Jasper. In general, the formation of hail in both clouds involves the same microphysical processes, i.e. ice-rain collision (PIACR), rain collection by hail (PRACG), droplet collection by hail (PSACWG), hail conversion due to snow collection by rain (PSACR), hail conversion due to rain collection by snow (PGRACS), and deposition of hail (PRDG). However, due to the differences in the warm rain microphysics between the past and future clouds, there are three hail-forming microphysical processes that are less prominent in the future cloud than in the past cloud. These processes are PSACWG, PGRACS and PRACG.

The first process, PSACWG, is less prominent in the future cloud due to the lack of droplet availability in terms of amount of droplet and the smaller vertical distribution compared to that in the past cloud. The second process, PGRACS, is due to the lack of snow as a result of weaker ice processes in the future cloud. The third process, PRACG, is due to rain falling out as a result of strong collision-coalescence process that produces larger raindrops and cannot be sustained by the updraught longer. As such, there is insufficient rain for this process. In short, the lack of cloud water, snow and hail in the future impacted the associated microphysical process involved in the formation of hail.

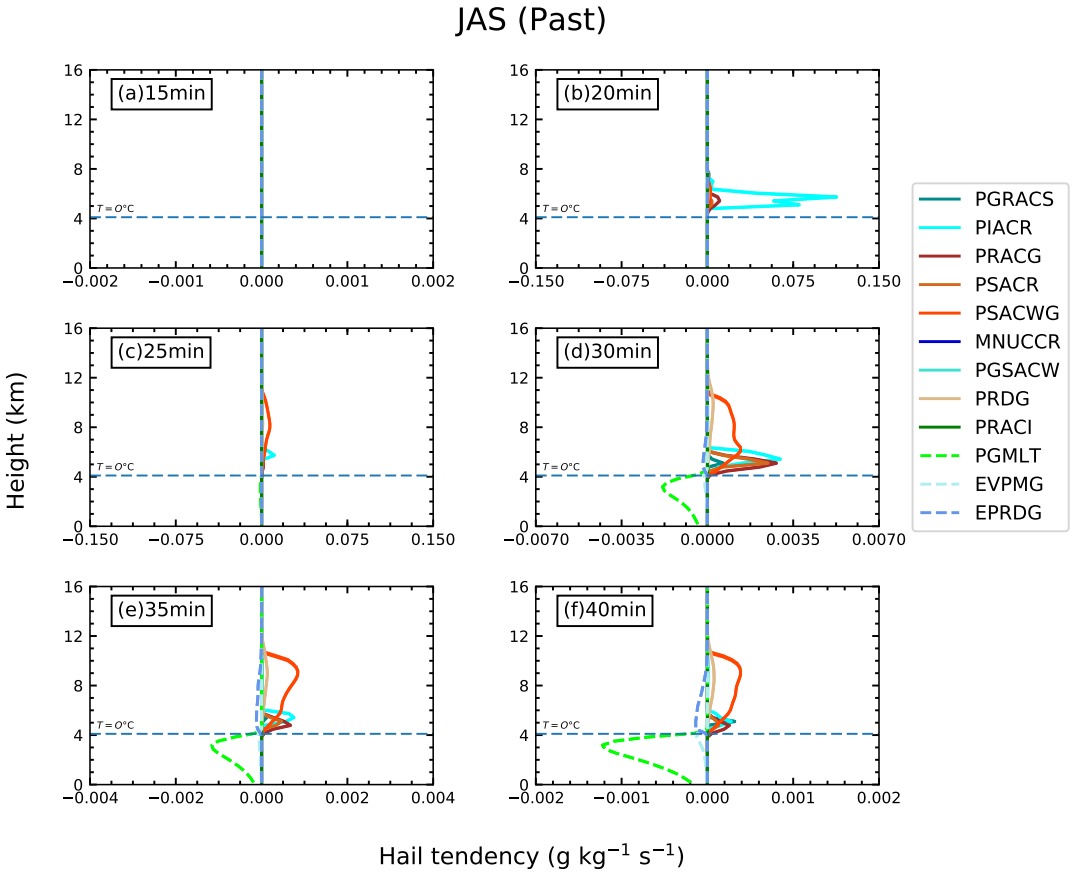

Figure 4.14: Hail microphysical budget for Jasper in the past environment

Note: Refer to Table 3.3 for the microphysical process terms.

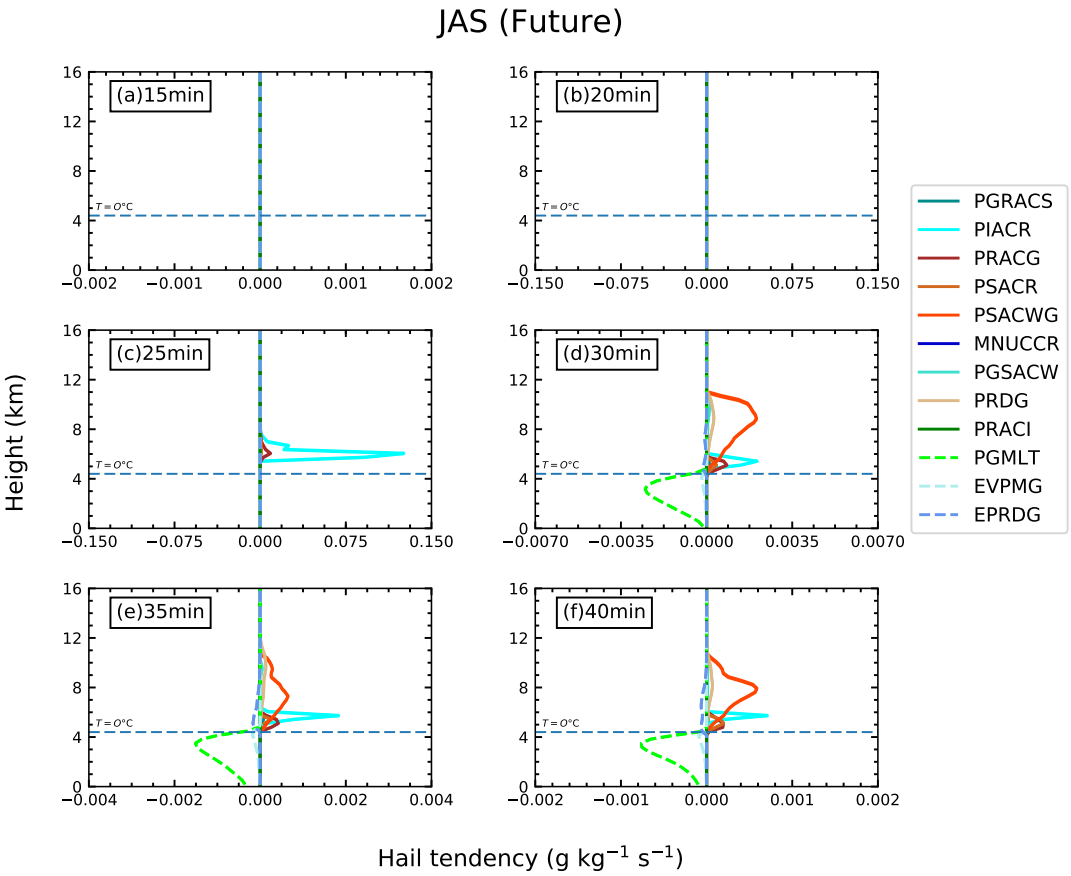

Figure 4.15: Hail microphysical budget for Jasper in the future environment

Note: Refer to Table 3.3 for the microphysical process terms.

4.3 Discussion

In this study, both clouds in the past and future environments formed at the same time, that is at 10 min into the simulations as indicated from the formation of cloud water in Figure 4.8. Thereafter, however, the evolution of the cloud microphysical processes differ between the past and future environments. These differences are described in this Section by drawing together all the results presented in **Section 4.2**.

From the results presented in **Section 4.2.1**, the boundary layer in the past environment is less saturated than the future environment. Convective inhibition (CIN) is present in the boundary layer in the past environment and absent in the future environment. Due to the overall warmer troposphere in the future environment, the freezing level (T = 0 °C) is higher than in the past environment. These differences result in subsequent differences on the cloud structure between the two environments as presented in **Section 4.2.2**.

In the past environment, the air parcel rising from the surface has to overcome the CIN to initiate convection. In addition, being in a less saturated environment, the air parcel has to rise further to reach saturation for condensation to occur. In contrast, the absence of CIN in the future environment allows for air parcel to rise and being in near-saturated environment, the air parcel need not rise further for condensation to occur. As a consequence, clouds form at a higher altitude in the past relative to that of the future. Further, the height of the freezing level dictates the spatial boundary of the warm rain process. The difference between the heights of cloud base and freezing level gives the depth of the warm-phase cloud layer. The high cloud base and low freezing level in the past environment results in a shallow warm-phase cloud depth. On the contrary, the low cloud base and high freezing level in the future environment results in a deep warm-phase cloud depth.

The differences in the warm-phase cloud depth between the past and future environments result in major differences in the cloud microphysical evolution, particularly made obvious by the differences in the rain mixing ratio. This will be further discussed in the following paragraphs.

For clouds in the past environment, the high cloud base resulted in cloud water forming at high altitude and the more saturated warm-phase cloud layer enhances nucleation (Castillo *et al.*, 2015; Costa *et al.*, 2017), thus distributing the cloud water over a greater depth. The enhanced nucleation also resulted in the production of numerous small cloud droplets. This leads to less efficient collision-coalescence process, hence less rain formation (Tao and Li, 2016) as seen in the decreasing rain mass mixing ratio at 20 min in Figure 4.9. In addition, the release of latent heat of condensation from the enhanced nucleation drives the vertical transport of cloud droplets to higher heights. Given the low freezing level, the cloud droplets are carried above the freezing level. Above the freezing level, cloud droplets become supercooled and this creates a favourable condition for the initiation of ice nucleation (Westbrook and Illingworth, 2011), thus initiating ice nucleation as early as 15 min. In addition, the earlier transport of cloud droplets into the ice phase allows for the clouds to consume the CAPE thus enhancing convection and can be seen in the high cloud top height. The early initiation of ice processes further limits the rain formation due to the lack of cloud water in the warm-phase layer. The early and strong development of ice phase produces a great amount of ice and snow as well as the presence of more cloud water aloft that they dominate the microphysical processes involved in the formation of hail. This leads to more release of latent heat of freezing that sustain the condensates from falling out quickly, thus the low initial rain rate recorded in the past clouds. The longer residence of condensates in the clouds allow for further cloud development that lengthens the cloud's lifetime, resulting in more rainfall throughout the cloud's lifetime.

On the other hand, for clouds in the future environment, the near-saturated boundary layer resulted in cloud water forming at low altitude and the less saturated warm-phase cloud layer above the cloud base slows down the nucleation rate. This results in reduced formation of cloud droplets and less latent heat of condensation released. Consequently, the updraught speed is weaker due to less latent heat released. Albeit the weak updraught speed, the greater depth of the warm-phase cloud layer increases the time in which cloud water and rain reside within the clouds. This allows more time for raindrops to grow into larger sizes. The prolonged and efficient collision-coalescence process delays and limits the transport of liquid condensates above the freezing level. As a result, not only the onset of ice

phase is delayed, but the strength of the ice phase development is also weaker. Consequently, ice and snow particles are produced in small amount and are therefore not prominent in the formation of hail. Instead, the formation of hail is mainly initiated by microphysical processes associated with rain. When rain is finally transported into the ice phase at 25 min, it immediately forms hail as seen in Figure 4.15(c). Even though the formation of hail releases latent heat of freezing, the latent heat is not sufficient to supply the updaught speed to sustain the large hail particles formed from the large rain particles. As a result, hail falls out as soon as it is produced, thus the high initial rain rate recorded. After the rainfall, ice phase still persists. However, the intense initial rainfall has depleted most of the water and therefore remain limited for ice processes. This leads to the subsequent rainfall to remain lower than that in the past clouds for the rest of the cloud's lifetime.

4.4 Summary

The different thermodynamic structures of the past and future environments resulted in the different cloud development as presented in this chapter. To summarise, the thermodynamic structure of the past environment are more favourable for stronger convection compared to that of the future environment. This is seen in the greater accumulated surface precipitation in the past clouds than in the future clouds. The clouds in the past environments are characterised by a weaker warm rain process due to the shallow warm-phase cloud layer, and a stronger cold rain process as manifested in the greater depth of cold-phase layer with high cloud top height. On the other hand, the clouds in the future environments are characterised by a stronger warm rain process due to the deep warm-phase cloud layer in which most of the cloud water is consumed for growth of raindrops into larger particles. This reduces the amount of water available for ice processes, hence the weaker cold rain process as manifested in the shallow cold-phase cloud layer with low cloud top height. However, it is noteworthy to note that this analysis does not extend to cover the occurrence of extreme weather events which was suggested to occur more frequently in a future warmer environment (e.g. Kendon *et al.*, 2014).

Chapter 5

The responses of deep convective clouds to thermodynamic perturbations

5.1 Introduction

Deep convective clouds were studied in the previous chapter for past (current) and future climate scenarios. Differences in the development of the clouds for past and future environments were explored. The result showed that differences due to the thermodynamic structure resulted in weaker convection in the future than in the past environment and the differences in the way the clouds developed was investigated. In this chapter, we delve into understanding which factors of the changed climate are causing which effect on the cloud development. Four experiments were conducted and are described in **Section 5.2** and the results and discussion are presented in **Section 5.3**. Finally, **Section 5.4** provides a summary of the Chapter's findings.

5.2 Experimental designs

Climate warming brings about many changes to the thermodynamic and dynamic components of the earth's climate system (Bony *et al.*, 2004; Palmer, 2013). While the thermodynamic and dynamic effects are recognised to influence cloud properties, questions still remain as to which effect or effects play the most important

role (e.g. Emori and Brown, 2005; Palmer, 2013). For example, as the atmosphere warms, the specific humidity of the air increases. This increases the amount of water vapour available for latent heat processes. The release of latent heat when water vapour condenses and the cooling of air through evaporation or sublimation of condensates influences the dynamic processes that shape the global circulation of the atmosphere. Many observational and modelling studies (e.g. Bengtsson *et al.*, 2009; Sharmila and Walsh, 2018) have reported a poleward shift in storm tracks due to warming. This affects the distribution of water vapour not only throughout the atmosphere but also across the globe.

From **Chapter 4**, it was found that the future climate is characterised by a different thermodynamic structure as well as changes in the moisture content that has come about from increased warming. In this chapter, we are interested to understand the role of each factor on cloud development. To do this, we will isolate different effects. For example, we will eliminate the temperature increase that arises from warming and test how temperature structure and moisture content affect the cloud development, and how they differ from the cloud development in the past environment. We then test the effects of temperature structure and moisture content on cloud development between non-warmed and warmed environments in terms of the water-holding capacity. This is achieved by performing idealised simulations of deep convective cloud in three different thermodynamic environments and by making comparisons of the cloud development between the altered thermodynamic environments and that of the original past or future thermodynamic environments. A total of four experiments or comparisons are performed as outlined in Table 5.1. The first three experiments involve the elimination of the temperature increase that arise from climate warming, while the fourth experiment considers the temperature increase from climate warming. Table 5.1 is an introduction to the experiments. More detailed explanations are provided afterwards with diagrams.

Next, the details on the preparation of the environmental profiles used in the experiments described in Table 5.1 are described in the Table 5.2.

Table 5.1: Description of the experiments

Experiment	Details
1	The first experiment assesses the effects of both temperature structure and relative humidity on the cloud development if the temperature increase from climate warming is eliminated. This is to see the structural and relative humidity effects of a future climate without the increase in mean temperature. How would the clouds developed in this condition and how would it differ from the clouds in the past environment?
2	Also with the elimination of temperature increase from warming, the second experiment isolates the temperature structure effect from the moisture content effect. It aims to test the influence of the temperature structure on the cloud development. This is to see what would happen to the cloud development if everything is like the past environment except that the temperature structure is that of the future environment.
3	The third experiment isolates the moisture content effect from the temperature structure effect. It aims to test what cloud development effects occur from a changed relative humidity profile have on cloud development. Similar to the second experiment, this experiment is looking to see what would happen to the cloud development if everything is like the past environment except that the relative humidity profile is that of the future environment.
4	The fourth experiment tests the effects of warming on cloud development in terms of the water-holding capacity. This is to see if the temperature structure and relative humidity profiles are the same for non-warmed and warmed environments, but temperature is different between the two environments, how is the cloud development different between the two environments?

Table 5.2: Details on the preparation of the altered environmental profiles

Experiment 1

Which original environment is altered:
Future environment

What is altered:
The average potential temperature and temperature of the original future environment is reduced to that of the past environment.

What is it compared to:
Original past environment

Schematic diagram:

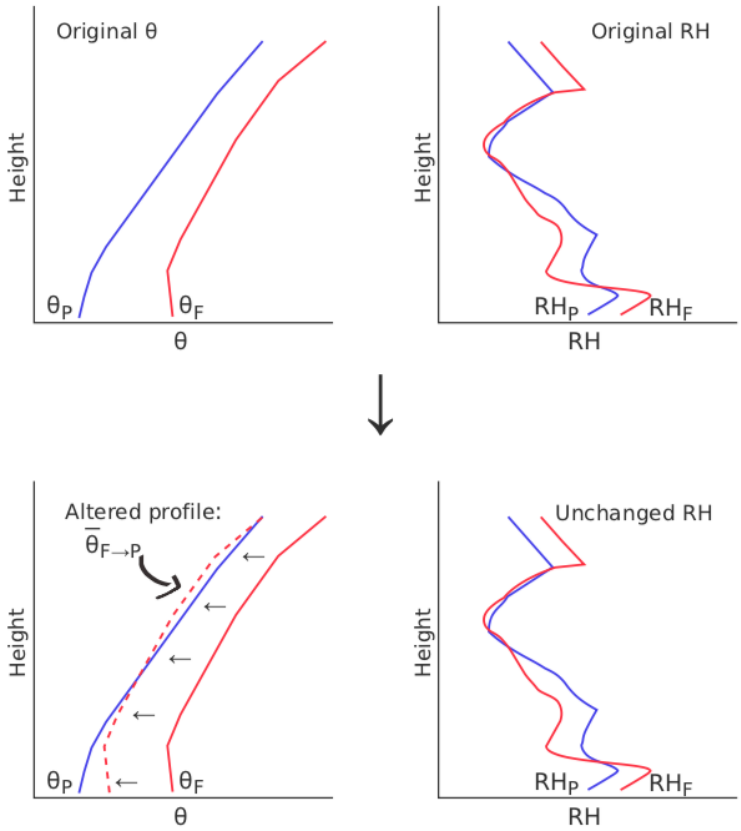

Symbol for altered environment:
$\overline{\theta}_{F \rightarrow P} RH_F$

Table 5.2 (continued)

Experiment 2

Which original environment is altered:
Future environment

What is altered:
- Average potential temperature and temperature of the original future environment is reduced to that of the past environment.
- Relative humidity profile of the original future environment is replaced to that of the past environment.

What is it compared to:
Original past environment

Schematic diagram:

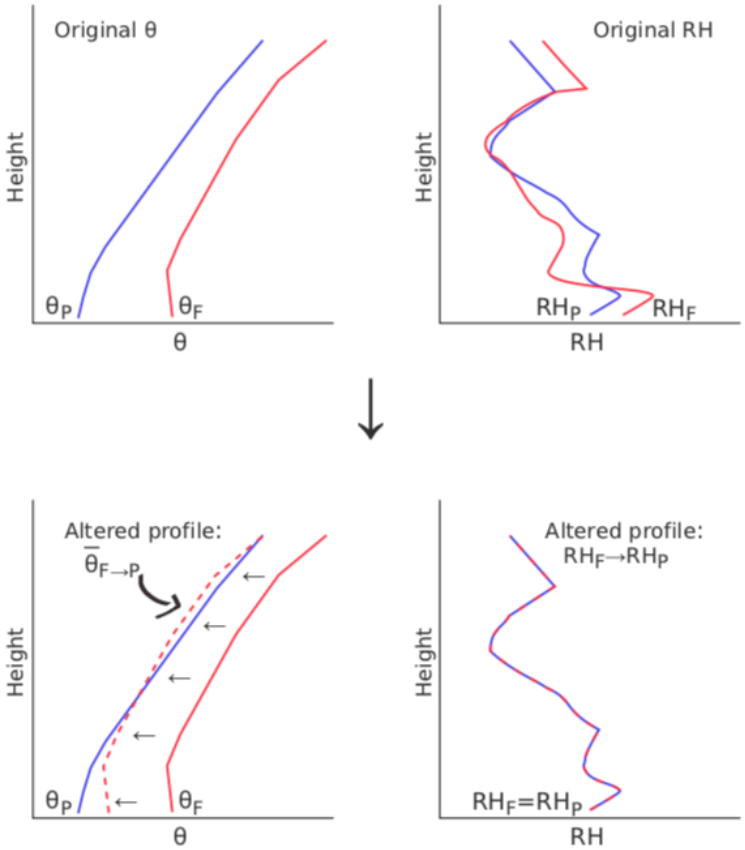

Symbol for altered environment:
$\overline{\theta}_{F\rightarrow P}RH_{F\rightarrow P}$

Table 5.2 (continued)

Experiment 3

Which original environment is altered:
Past environment

What is altered:
Relative humidity profile of the original past environment is replaced to that of the future environment.

What is it compared to:
Original past environment

Schematic diagram:

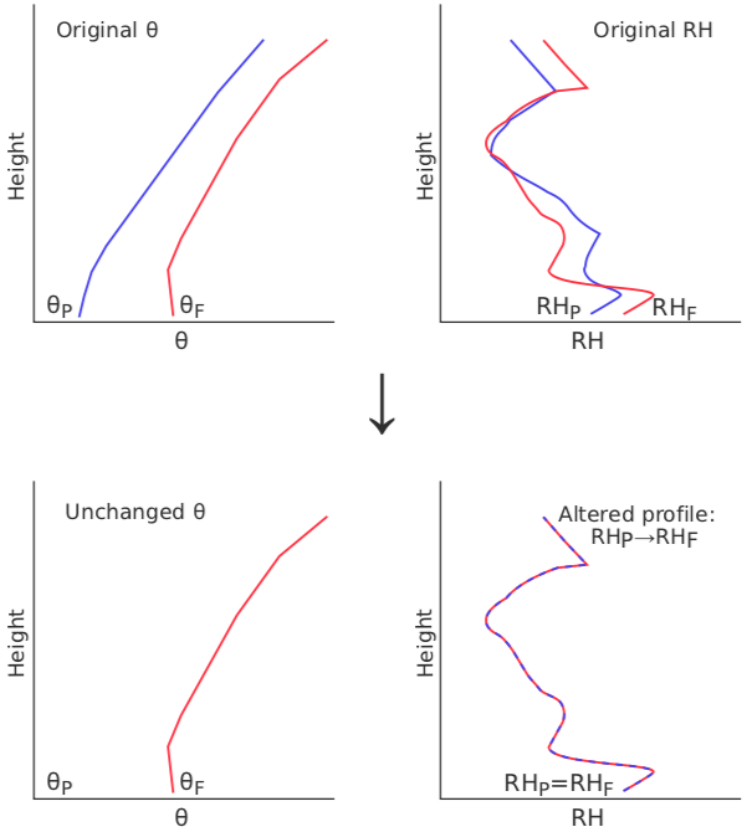

Symbol for altered environment:
$\theta_P RH_{P\rightarrow F}$

Table 5.2 (continued)

Experiment 4

Which original environment is altered:
Future environment

What is altered:
The average potential temperature and temperature of the original future environment is reduced to that of the past environment.

What is it compared to:
Original future environment

Schematic diagram:

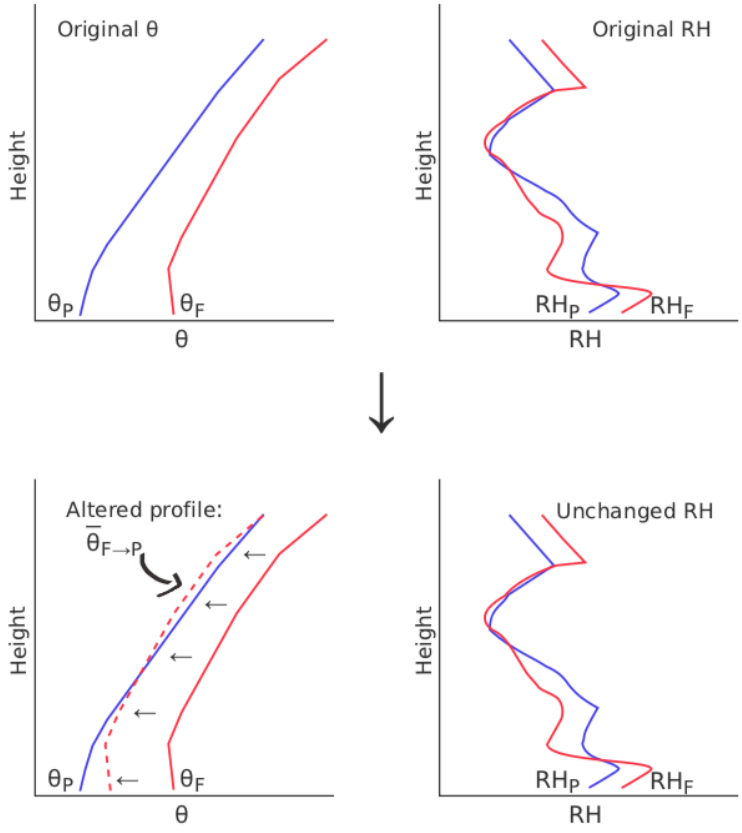

Symbol for altered environment:
$\overline{\theta}_{F \rightarrow P} RH_F$

The details of the alterations are explained as follows.

1. Reducing the mean potential temperature and temperature of the original future environment to that of the original past environment (for Experiments 1, 2 and 3): The average potential temperature from the lowest level up to the level slightly above 0 °C for both the past and future environments are used in the calculation. The range of heights from the lowest level to the level just above 0 °C was chosen because they are key to cloud development. Then, the difference between the two averages is evaluated and this difference is then subtracted from the potential temperature of the original future environment.

2. Relative humidity (for Experiments 2 and 3): The vertical structure of relative humidity of the original future environment is replaced by that of the original past environment, and vice versa.

Next, a summary of the experiments is provided in Table 5.3.

Table 5.3: Summary of the experiments

Exp.	**Symbols of altered profiles**	**Compare with**	**Tests**
1	$\overline{\theta}_{F\rightarrow P}RH_F$	Original past environment $\theta_P RH_P$	To test the effects of both temperature structure and relative humidity changes on the cloud development if the mean temperature increase from warming is eliminated.
2	$\overline{\theta}_{F\rightarrow P}RH_{F\rightarrow P}$		To test the effects of temperature structure on the cloud development.
3	$\theta_P RH_{P\rightarrow F}$		To test the effects of future changes in relative humidity on the cloud development.
4	$\overline{\theta}_{F\rightarrow P}RH_F$	Original future environment $\theta_F RH_F$	To test the effects of future warming on cloud development in terms of the water-holding capacity.

5.3 Results and Discussion

This section presents the results and discussion from the four experiments mentioned in **Section 5.2**. Each experiment is discussed in separate sections as follows: **Section 5.3.1** for Experiment 1, **Section 5.3.2** for Experiment 2, **Section 5.3.3** for Experiment 3, and **Section 5.3.4** for Experiment 4.

5.3.1 Experiment 1: The effects of both temperature structure and relative humidity changes on the cloud development if temperature increase from warming is eliminated

Exp. 1 Introduction

Experiment 1 removes the mean temperature shift in the future environment and assess the effects on the cloud development. This is achieved by keeping everything the same in the past and future runs except eliminating the mean warming effects that arise from climate warming in the future. The modification to the thermodynamic conditions of the future environment is as described in Table 5.2 (Exp. 1), and is labelled as $\overline{\theta}_{\mathrm{F}\rightarrow\mathrm{P}}\mathrm{RH}_{\mathrm{F}}$. For the remainder of this chapter, all the altered environments will be referred to as the altered environment for brevity.

Prior to presenting the comparison between the altered environment and the past environment, a description of the environmental conditions of the altered environment, i.e. how it differs from the original future environment, is described as follows. The altered environment exhibits a temperature profile that is lower than the original future environment due to its mean potential temperature being reduced to that of the past environment. As such, the water-holding capacity of the altered environment is indirectly lowered and therefore contains less moisture content than the original future environment.

Exp. 1 Results

In this experiment, the results highlight the effects of the removal of the mean temperature shift on the cloud macro- and microphysical features. We first explore how the vertical thermodynamic profiles between the two environments differ. Figures 5.1, 5.2 and 5.3 show the vertical profiles of relative humidity, specific humidity and convective available potential energy (CAPE), respectively, for the altered and past environments. The relative humidity of the two environments are the same as that described for the past and future environments in **Chapter 4**. The boundary layer in the altered environment is characterised as having higher relative humidity than in the past, while the mid-layer in the altered environment has lower relative humidity than in the past. On the other hand, the specific humidity in the altered environment throughout the atmosphere is greater than in the past environment, and is significantly greater at the boundary layer. This contributes to CAPE in the altered environment. If we consider the change in the CAPE between the model layers and call it differential CAPE (dCAPE), we see in Figure 5.3 that the dCAPE in the altered environment is also greater in the boundary layer than in the past environment. However, at the mid- and upper levels, the dCAPE in the past environment is greater than the altered environment. From **Chapter 4**, it was noted that the high specific humidity and large dCAPE at the boundary layer lead to clouds forming at low altitudes. In this experiment, it is also seen that the clouds in the altered environment formed at lower altitudes than that in the past environment. The clouds in the past environment formed at higher altitudes due to the presence of convective inhibition (CIN) in the boundary layer.

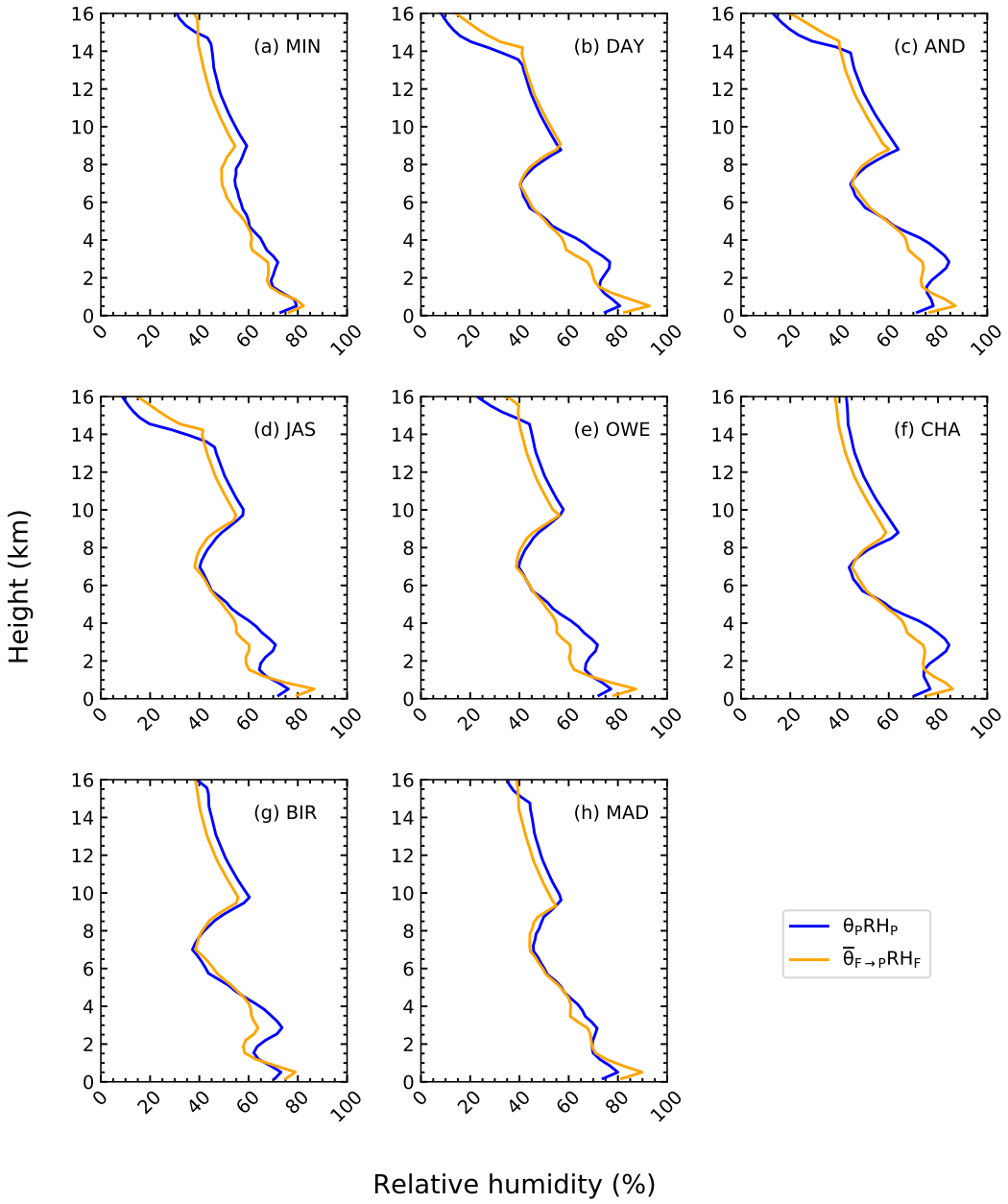

Figure 5.1: Vertical profiles of relative humidity at the initial time for all locations between the altered environment ($\overline{\theta}_{F\rightarrow P}RH_F$) and the past environment

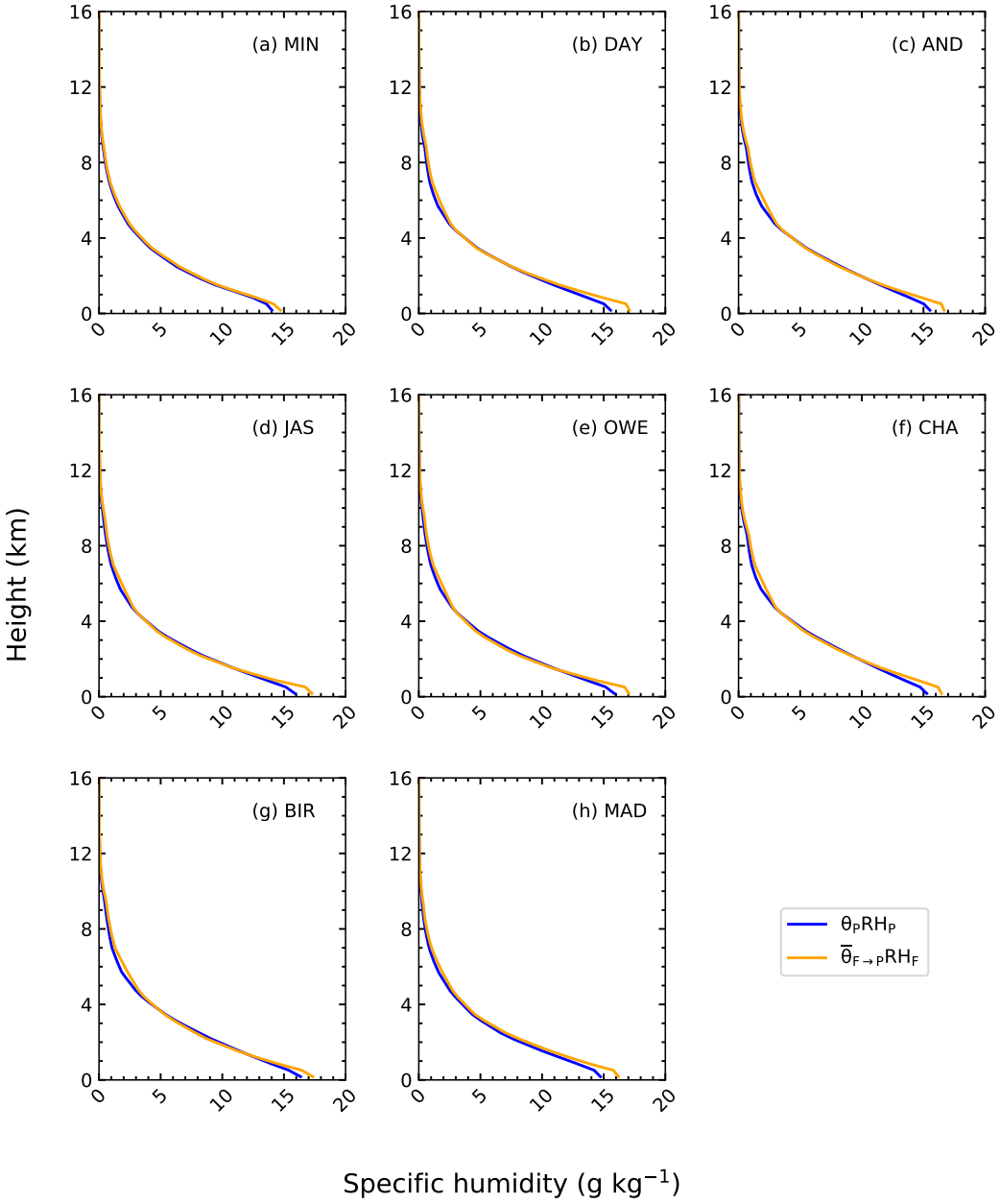

Figure 5.2: Vertical profiles of specific humidity at the initial time for all locations in the altered environment ($\overline{\theta}_{F\rightarrow P}RH_F$) and the past environment.

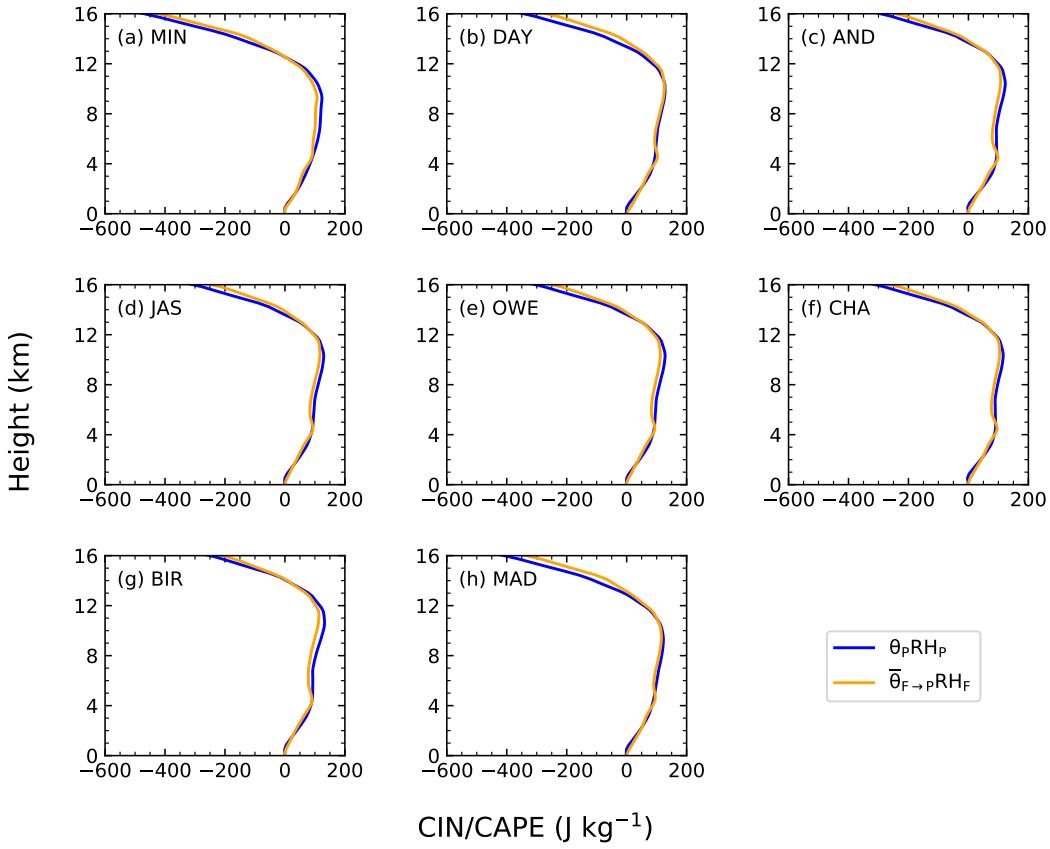

Figure 5.3: Vertical profiles of convective inhibition (CIN) and convective available potential energy (CAPE) at the initial time for all locations in altered environment ($\overline{\theta}_{F\rightarrow P} RH_F$) and past environment.

Exp. 1 Cloud macrophysical properties

Table 5.4 shows the cloud base heights, freezing levels and the warm-phase cloud depths, while Table 5.5 shows the cloud-top heights and cold-phase cloud depths for the two environments. The mean differences for each cloud properties between the two environments are given in Table 5.6. On average, the cloud base in the altered environment is 190 m or 37% lower than in the past environment. We also see that the average freezing level in the altered environment is 240 m or 6% higher than in the past environment, a feature that comes from the temperature structure of the future environment. A combination of low cloud base and high freezing level in the altered environment yields a warm-phase cloud depth that is deeper than in the past environment. On average, the warm-phase cloud depth in the altered environment is 430 m or 10% deeper than in the past environment. For the cloud-top heights and cold-phase cloud depths, the altered environment exhibit an average cloud-top height that is 2 km or 15% lower than in the past environment. This yields average cold-phase cloud depth that is 2.2 km or 27% shallower than in the past environment. An example of a 2D cross section of the simulated cloud structure in the altered environment is given in Figure C.3 in **Appendix C** In **Chapter 4**, it was established that cloud microphysical processes dictate much of the cloud macrophysical properties once convection is initiated. Therefore, drawing from these cloud macrophysical properties, we can infer the cloud microphysical processes that occurred within the clouds. There are no changes in the freezing levels, cloud-top heights, and depths of warm- and cold-phase cloud layers in JAS and OWE, nonetheless, we still see some microphysical differences that are similar to the other locations.

Table 5.4: Heights of cloud base (m), freezing level (km), and warm-phase cloud depths (km) for all locations in the altered environment ($\overline{\theta}_{F\rightarrow P}RH_F$) and the past environment.

Locations	**Cloud base heights (m)**		**Freezing levels (km)**		**Warm-phase cloud depths (km)**	
	$\theta_P RH_P$	$\overline{\theta}_{F\rightarrow P}RH_F$	$\theta_P RH_P$	$\overline{\theta}_{F\rightarrow P}RH_F$	$\theta_P RH_P$	$\overline{\theta}_{F\rightarrow P}RH_F$
MIN	691	572	3.5	3.8	2.8	3.2
DAY	661	424	3.8	4.1	3.1	3.7
AND	747	577	3.8	4.1	3.0	3.5
JAS	732	499	4.1	4.1	3.4	3.6
OWE	730	534	4.1	4.1	3.4	3.6
CHA	766	602	3.8	4.1	3.0	3.5
BIR	774	615	4.1	4.5	3.4	3.8
MAD	676	450	3.8	4.1	3.1	3.6

Table 5.5: Cloud-top heights (km) and cold-phase cloud depths (km) for all locations in the altered environment ($\overline{\theta}_{F\rightarrow P}RH_F$) and the past environment.

Locations	**Cloud-top heights (m)**		**Cold-phase cloud depths (km)**	
	$\theta_P RH_P$	$\overline{\theta}_{F\rightarrow P}RH_F$	$\theta_P RH_P$	$\overline{\theta}_{F\rightarrow P}RH_F$
MIN	13.5	11.3	10.0	7.5
DAY	14.8	14.3	11.0	10.2
AND	15.0	12.0	11.2	7.9
JAS	14.3	12.0	10.2	7.9
OWE	14.3	12.0	10.2	7.9
CHA	13.3	12.0	9.5	7.9
BIR	15.8	12.8	11.7	8.3
MAD	12.8	12.0	9.0	7.9

Table 5.6: Mean differences for the properties of cloud structures for all locations between the altered environment ($\overline{\theta}_{F\rightarrow P}RH_F$) and the past environments.

Cloud structures	**Mean differences (Altered - Past)**
Cloud base height	-188 m
Freezing level	240 m
Warm-phase cloud depth	400 m
Cloud-top height	-2 km
Cold-phase cloud depth	-2.2 km

Exp. 1 Synthesis

Drawing from the results reported in **Chapter 4**, the deep warm-phase cloud depth in the altered environment indicates an active collision-coalescence process, in contrast to the shallow warm-phase cloud depth with less efficient collision-coalescence process in the past environment. Another factor that contribute to the collision-coalescence process is the relative humidity in the warm-phase layer, particularly above the boundary layer which is referred to as the mid-layer here. In this layer, the altered environment is less saturated than in the past environment, causing a decrease in cloud nucleation rate thus limiting latent heat release as seen in the weaker updraught speed (Figure 5.4) relative to that in the past environment. The lower nucleation rate produces less droplets and the longer residence time of the droplets due to the weaker sedimentation and weak updraught speed increases the time for droplets to grow into larger sizes via collision-coalesce process. As a result, more rain is produced in the altered environment than in the past environment as seen in Figure 5.5.

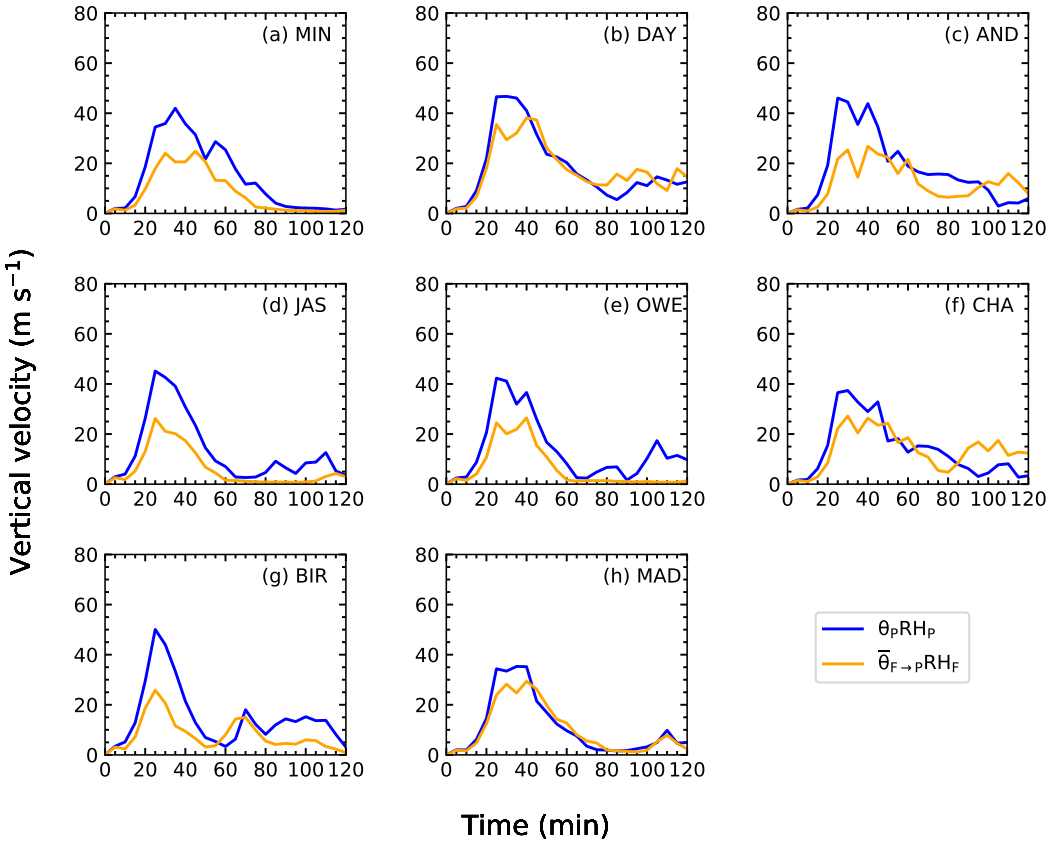

Figure 5.4: Time-series profiles of maximum vertical velocity for all locations in the altered environment ($\overline{\theta}_{F\rightarrow P}RH_F$) and the past environment.

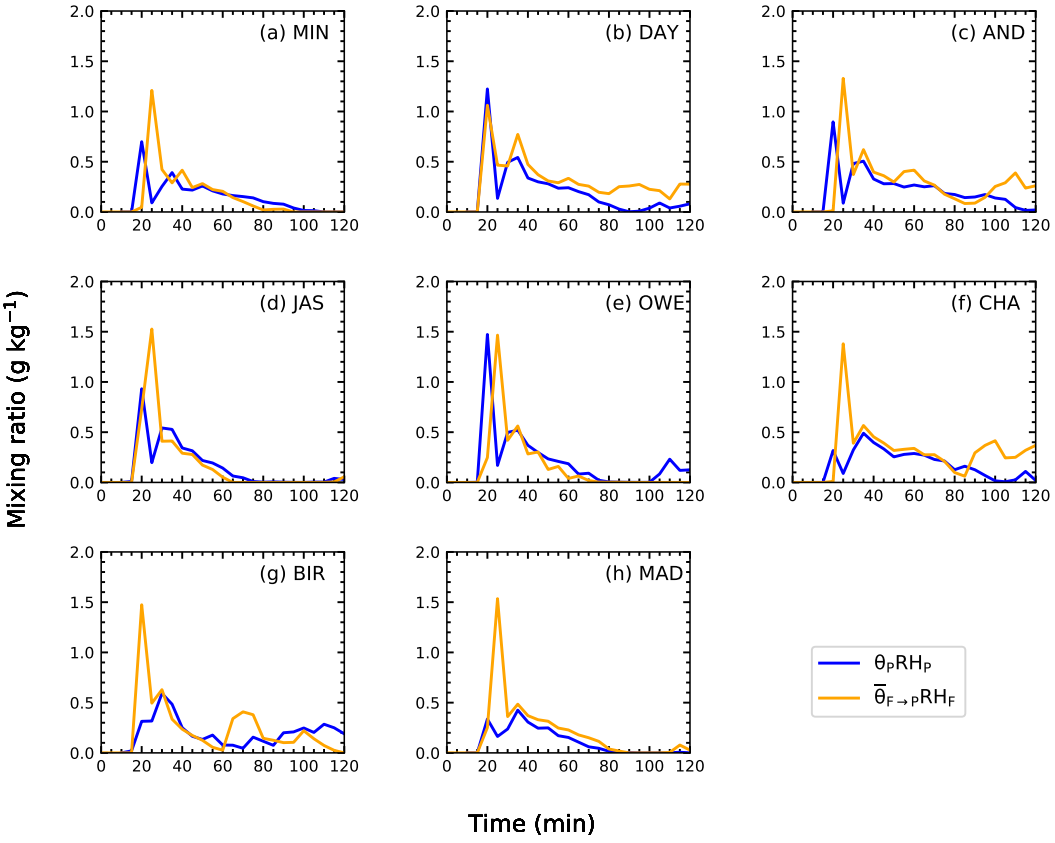

Figure 5.5: Time-series profiles of average rain mass mixing ratio for all locations in the altered environment ($\overline{\theta}_{F \rightarrow P}RH_F$) and the past environment.

As in **Chapter 4**, one of the main features of the differences between the altered and past environments was in the production of rain as depicted in Figure 5.5. In the altered environment, it takes a while before rain production reaches its peak and decreases afterwards, whereas in the past environment, as soon as rain forms, it reaches its peak production and then immediately decreased afterwards. In the altered environment, the decrease in the rain production after reaching its peak occurs at the same time as rainfall begins, that is at 25 min. On the other hand, the decrease in the rain production after the peak production is reached in the past environment does not occur at the same time as rainfall begins. Instead, what happens in the past environment is that ice processes begin earlier and that reduces the availability of water for rain production as discussed in **Chapter 4**. The active collision-coalescence process in the altered environment results in intense initial rainfall (Figure 5.6) that removes water from the clouds thereby reducing the availability of water of ice processes. This explains the lower cloud-top height and shallower cold-phase cloud depth in the altered environment than in the past environment.

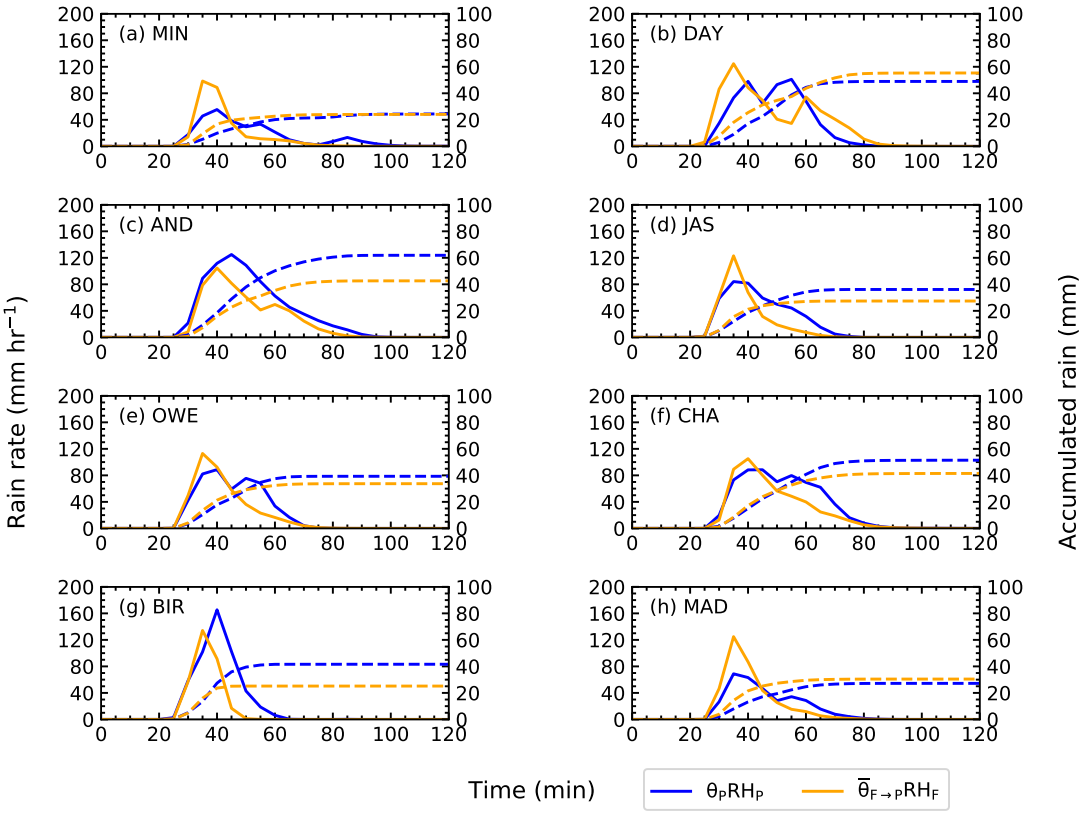

Figure 5.6: Time-series profiles of maximum rain rate (left y-axis) and maximum accumulated surface rain (right y-axis) for all locations in the altered environment ($\overline{\theta}_{F\rightarrow P}RH_F$) and the past environment.

Exp. 1 Conclusion

The results from Experiment 1 shows that reducing the mean temperature but keeping the structures of temperature and relative humidity of the future environment leads to an average warm-phase cloud depth that is approximately 400 m deeper than in the past environment. The greater warm-phase enhances the collision-coalescence process that increases the rain mixing ratio by a factor of 10 than in the past environment, especially during the peak rain production. This leads to an intense initial rainfall that removes large mass of rain water in the altered environment, thus reducing the availability of water for ice processes in the altered environment. As a result, the ice processes in the altered environment is weakened as seen in the average decrease of cloud-top height and cold-phase cloud depth by 2 km and 2.2 km, respectively, compared to that in the past environment. The results from this experiment is similar to that performed for the past and future environment in **Chapter 4**. In comparison to the results in **Chapter 4**, the reduced mean temperature in the altered environment in Experiment 1 results in minimal changes in the average cloud base height but a lowering of the freezing level by an average of 45%. This reduces the average warm-phase cloud depth by 25%, and a further reduction in the average cloud-top height and cold-phase cloud depth by 40% and 30%, respectively. Therefore, this shows that the temperature structure and relative humidity of the future environment substantially influences the cloud development, with or without the mean increase in warming that climate change brings.

5.3.2 Experiment 2: Isolating and assessing the effects of temperature structure on the cloud development

Exp. 2 Introduction

Experiment 2 aims to isolate the temperature structure effects whilst removing the differences of relative humidity and mean warming so as to assess the sole effects of temperature structure on the cloud development. To isolate the effect of temperature structure from relative humidity, the relative humidity profile of the future environment is replaced to that of the past environment, whereas to remove

the mean warming in the future environment, the mean potential temperature and temperature of the future environment are reduced to that of the past environment. This will produce an altered environment that retains the temperature structure of the future environment. The modifications performed are as described in Table 5.2 (Exp. 2), and the altered environment is labelled as $\overline{\theta}_{F\rightarrow P}RH_{F\rightarrow P}$.

As in the previous section, the environmental conditions of the altered environment will be described prior to presenting the results on the comparison between the altered environment and the past environment. In this experiment, the altered environment exhibits a temperature profile that is lower than that of the original future environment due to its mean potential temperature being reduced to that of the past environment. This lowers the water-holding capacity of the altered environment thus indirectly reduces the moisture content in the altered environment. The moisture content in the altered environment is also reduced from the future environment due to the relative humidity profile being replaced with that of the past.

When compared with the past environment, the moisture content in the altered environment is lower in the boundary layer but greater in the mid- and upper layer than in the past environment as shown in Figure 5.7. The lower moisture content in the boundary layer of the altered environment results in convective inhibition (CIN) that is greater than the past environment as seen in Figure 5.8. In addition, the CAPE in the altered environment is also lower in the altered environment throughout the atmosphere. In the following, we will begin to explore the results and discuss the comparison of the cloud development between the altered environment and the past environment.

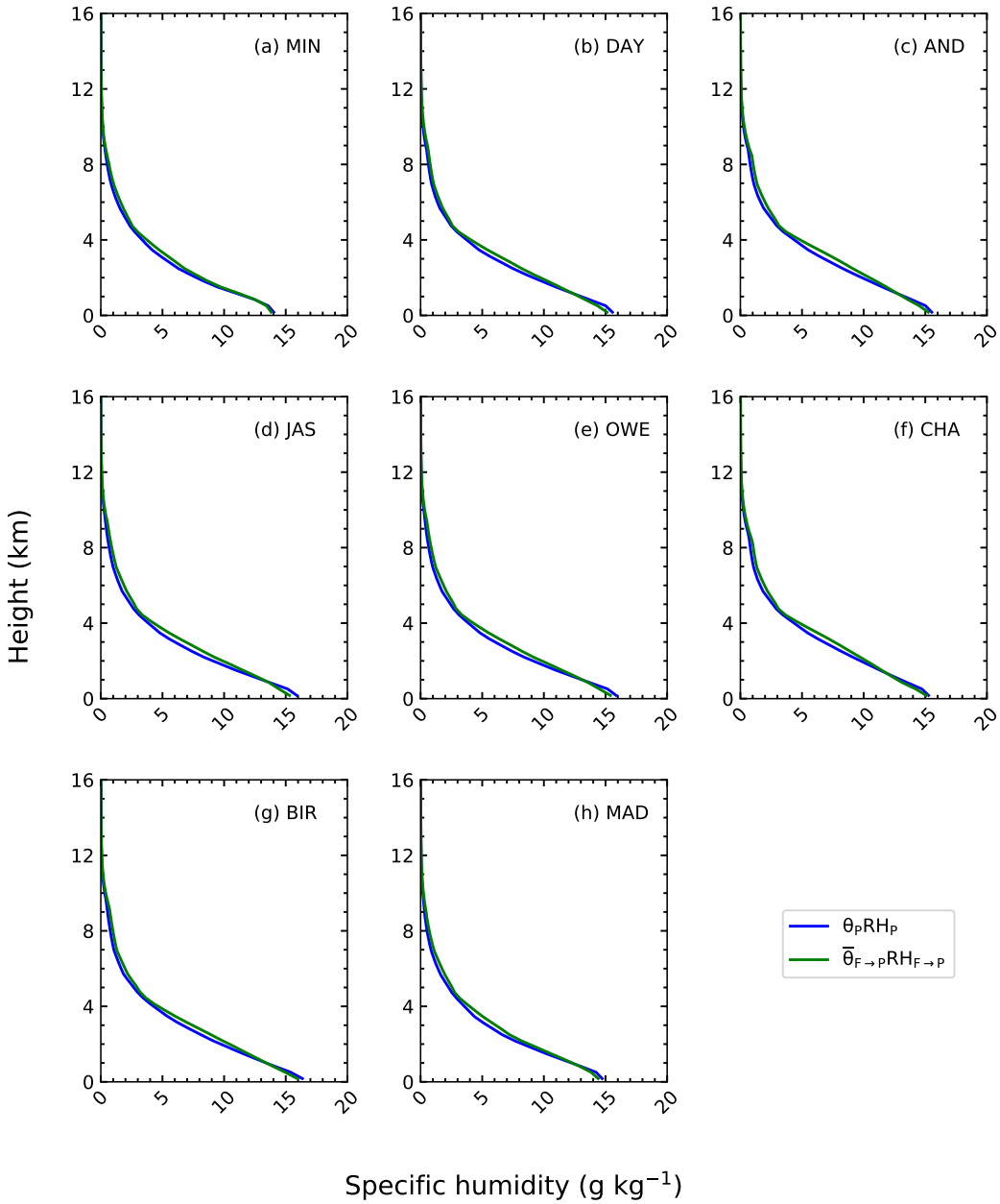

Figure 5.7: Vertical profiles of relative humidity at the initial time for all locations between the altered environment ($\overline{\theta}_{F\to P}RH_{F\to P}$) and the past environment

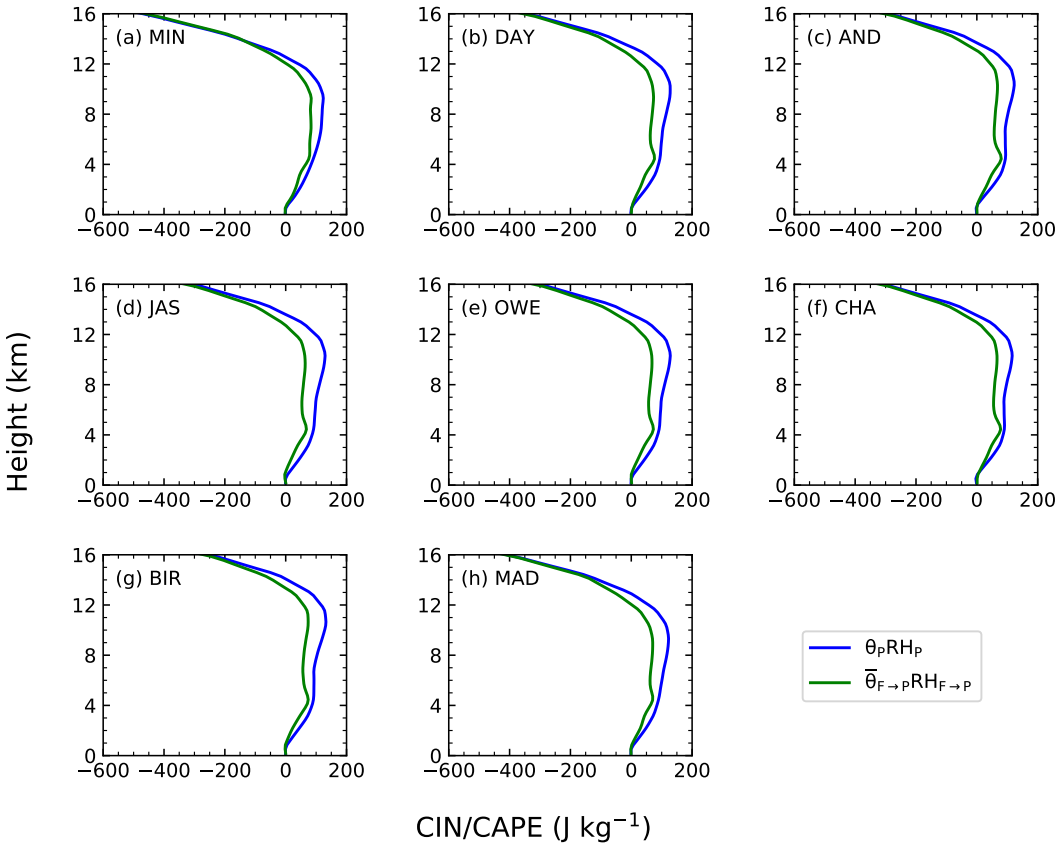

Figure 5.8: Vertical profiles of convective inhibition (CIN) and convective available potential energy (CAPE) at the initial time for all locations in altered environment ($\overline{\theta}_{F\to P} RH_{F\to P}$) and past environment.

Exp. 2 Results

For this experiment, the highlight of the results is on the strength of convection. The strength of convection can be inferred from the maximum vertical velocity in Figure 5.9 and the total water content in Figure 5.10. The maximum vertical velocity in the altered environment is on average 75% weaker than in the past environment. Similarly, the total water content in the altered environment is on average 80% lower than in the past environment. This tells us that the altered environment is far less conducive for convection. We see this in the macrophysical properties of the clouds.

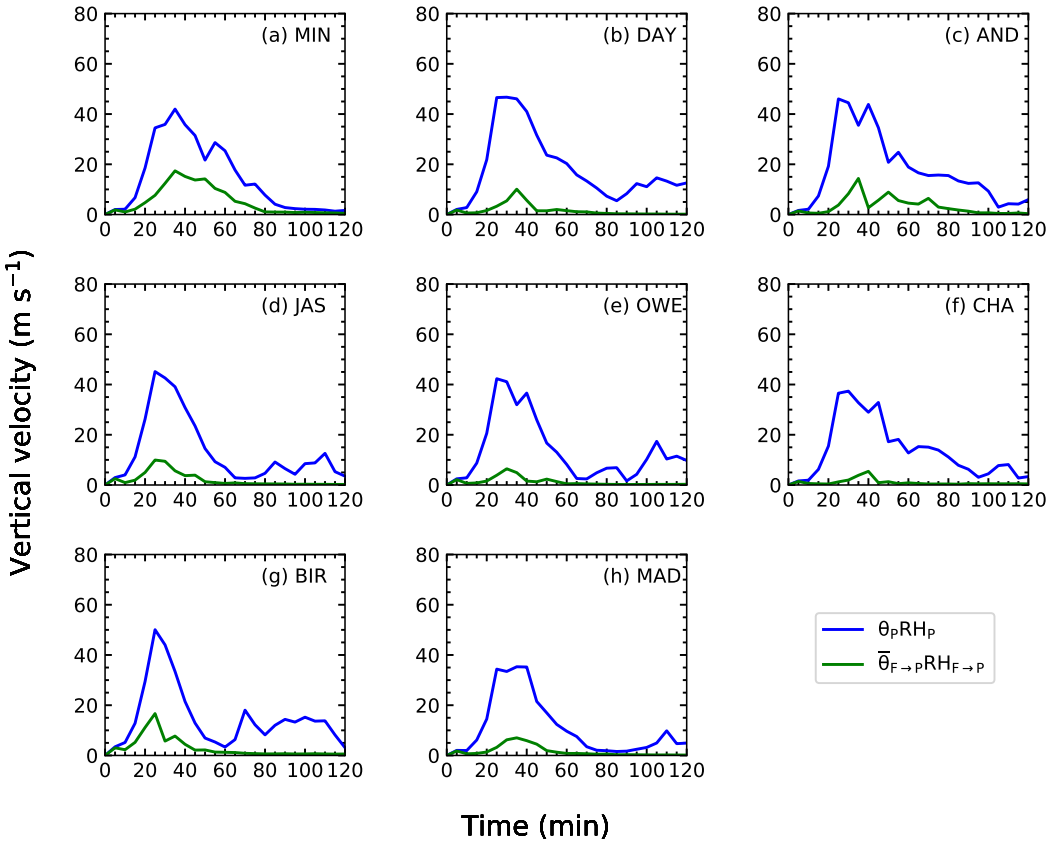

Figure 5.9: Time-series profiles of maximum vertical velocity for all locations in the altered environment ($\overline{\theta}_{F\rightarrow P} RH_{F\rightarrow P}$) and the past environment.

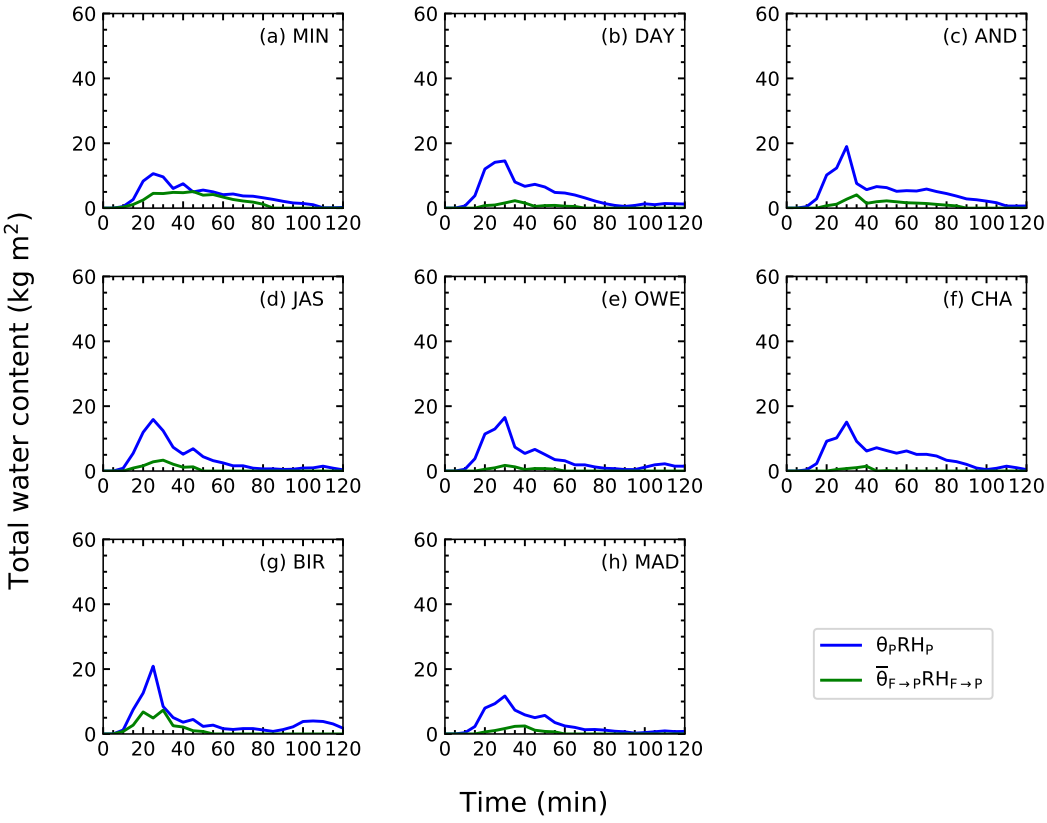

Figure 5.10: Time-series profiles of average total water content for all locations in the altered environment ($\overline{\theta}_{F\rightarrow P}RH_{F\rightarrow P}$) and the past environment.

Exp. 2 Cloud macrophysical properties

Table 5.7 provides the heights and depths associated with the warm-phase cloud layers, while Table 5.8 gives the cloud-top heights and cold-phase cloud depths for the two environments. The mean differences for each cloud properties between the two environments are given in Table 5.9. Figure C.4 in **Appendix C** shows an example of 2D cross section of the simulated cloud structure for the altered environment. Beginning from the cloud formation, the altitudes at which clouds in both altered and past environment form remain similar due to the same relative humidity profiles exhibited by both environments. The freezing levels, on the other hand, are on average 240 m higher in the altered environment than in the past environment due to the temperature structure of the future environment. Subsequently, the warm-phase cloud depths are also on average 240 m deeper in the altered environment than in the past environment. Next, we explore the heights and depths associated with the cold-phase cloud layers in both environments. It is seen that the average cloud-top height in the altered environment is 8 km lower than in the past environment. Despite the greater freezing levels in the altered environment, the cold-phase cloud depths are still on average 8 km shallower than in the past environment. This is a very profound feature of the altered environment and indicates that the ice phase in the altered environment is weak or barely existent at all as evident in solid hydrometeor mixing ratio (ice, snow and hail) in Figure 5.11. Figure 5.11 shows that solid hydrometeors are almost non-existent or minimal in all locations.

Table 5.7: Heights of cloud base (m), freezing level (km), and warm-phase cloud depths (km) for all locations in the altered environment ($\overline{\theta}_{F\rightarrow P}RH_{F\rightarrow P}$) and the past environment.

Loc.	**Cloud base heights (m)**		**Freezing levels (km)**		**Warm-phase cloud depths (km)**	
	$\theta_P RH_P$	$\overline{\theta}_{F\rightarrow P}RH_{F\rightarrow P}$	$\theta_P RH_P$	$\overline{\theta}_{F\rightarrow P}RH_{F\rightarrow P}$	$\theta_P RH_P$	$\overline{\theta}_{F\rightarrow P}RH_{F\rightarrow P}$
MIN	691	688	3.5	3.8	2.8	3.1
DAY	661	661	3.8	4.1	3.1	3.4
AND	747	743	3.8	4.1	3.0	3.4
JAS	732	727	4.1	4.1	3.4	3.4
OWE	730	725	4.1	4.1	3.4	3.4
CHA	766	763	3.8	4.1	3.0	3.4
BIR	774	770	4.1	4.5	3.4	3.7
MAD	676	673	3.8	4.1	3.1	3.4

Table 5.8: Cloud-top heights (km) and cold-phase cloud depths (km) for all locations in the altered environment ($\overline{\theta}_{F\rightarrow P}RH_{F\rightarrow P}$) and the past environment.

Locations	**Cloud-top heights (m)**		**Cold-phase cloud depths (km)**	
	$\theta_P RH_P$	$\overline{\theta}_{F\rightarrow P}RH_{F\rightarrow P}$	$\theta_P RH_P$	$\overline{\theta}_{F\rightarrow P}RH_{F\rightarrow P}$
MIN	13.5	9.0	10.0	5.2
DAY	14.8	4.5	11.0	0.4
AND	15.0	6.0	11.2	1.9
JAS	14.3	6.0	10.2	1.9
OWE	14.3	5.3	10.2	1.2
CHA	13.3	5.3	9.5	1.2
BIR	15.8	7.5	11.7	3.0
MAD	12.8	5.3	9.0	1.2

Table 5.9: Mean differences for the properties of cloud structures for all locations between the altered environment ($\overline{\theta}_{F\rightarrow P}RH_{F\rightarrow P}$) and the past environments.

Cloud structures	Mean differences (Altered - Past)
Cloud base height	-3.4 m
Freezing level	240 m
Warm-phase cloud depth	250 m
Cloud-top height	-8 km
Cold-phase cloud depth	-8.4 km

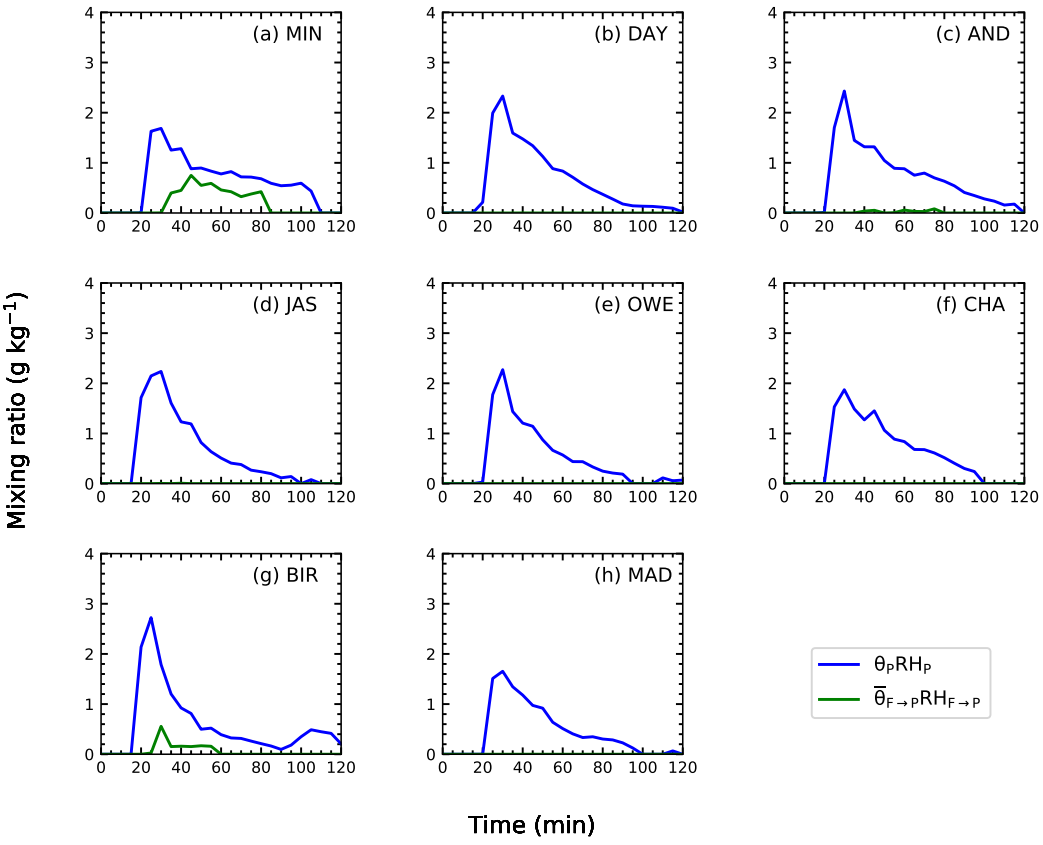

Figure 5.11: Time-series profiles of average solid hydrometeor mixing ratio (ice, snow and hail) for all locations in the altered environment ($\overline{\theta}_{F\rightarrow P}RH_{F\rightarrow P}$) and the past environment.

Exp. 2 Synthesis

Even though the altered environment and past environment exhibit the same relative humidity, the specific humidity differ as seen in Figure 5.7. Due to the temperature structure of the altered environment, the specific humidity in the boundary is lower than in the past environment. The lower water vapour mixing ratio in the boundary layer in the altered environment not only limits the amount of water vapour for cloud nucleation, but also leads to greater convective inhibition (CIN, Figure 5.8) that affects the buoyancy of the air parcel, thus resulting in a weakened updraught speed. In addition, the updraught strength in the altered environment is also weakened due to the less amount of latent heat released from the lower nucleation rate. Consequently, the weak updraught in the altered environment could not sustain or transport more water vapour and condensates to higher heights for further nucleation and growth of condensates, thus the overall weaker convection relative to the past environment.

Exp. 2 Conclusion

In conclusion, we see from the results that the temperature structure has important effects on the moisture at lower levels that gives to the significant cloud differences, especially in the dramatic reduction in cloud-top height and cold-phase cloud depth by an average of 8 km, thus signalling a weak cold rain process. This illustrates that the vertical extent of clouds is hugely affected by the temperature structure.

5.3.3 Experiment 3: Isolating and assessing the relative humidity structure on the cloud development

Exp. 3 Introduction

In this section, we investigate the impact of relative humidity structure whilst keeping the other effects. By isolating the effects of relative humidity structure from the temperature structure, it enables us to test what effects the implied transport of water vapour associated with future warming climate have on the cloud development in the past environment. In this experiment, the past environment is used as the altered environment. To isolate the effect of relative humidity structure from temperature structure, the temperature structure, potential temperature and temperature are all kept the same and only the relative humidity structure of the past environment is replaced to that of the future environment. This modification is as described in Table 5.2 (Exp. 3), and the altered environment is labelled as $\theta_{\mathrm{P}}\mathrm{RH}_{\mathrm{P}\rightarrow\mathrm{F}}$. This altered environment is then compared to the past environment.

Prior to presenting the results and discussion for this experiment, the environmental conditions of the altered environment is described here. In this experiment, the altered environment exhibits a temperature profile that is the same as the original past environment but the moisture content is markedly greater than the original past environment, especially in the boundary layer as depicted in Figure 5.12. The increase in the moisture content of the altered environment was due to the greater relative humidity of the future environment in the boundary layer. This makes the altered environment saturated relative to the past environment as depicted in Figure 5.13. This added moisture and increased saturation also lead to greater CAPE in the altered environment than in the past environment as seen in Figure 5.14. In the upcoming paragraphs, we will explore how the cloud development in the altered environment is different from the past environment.

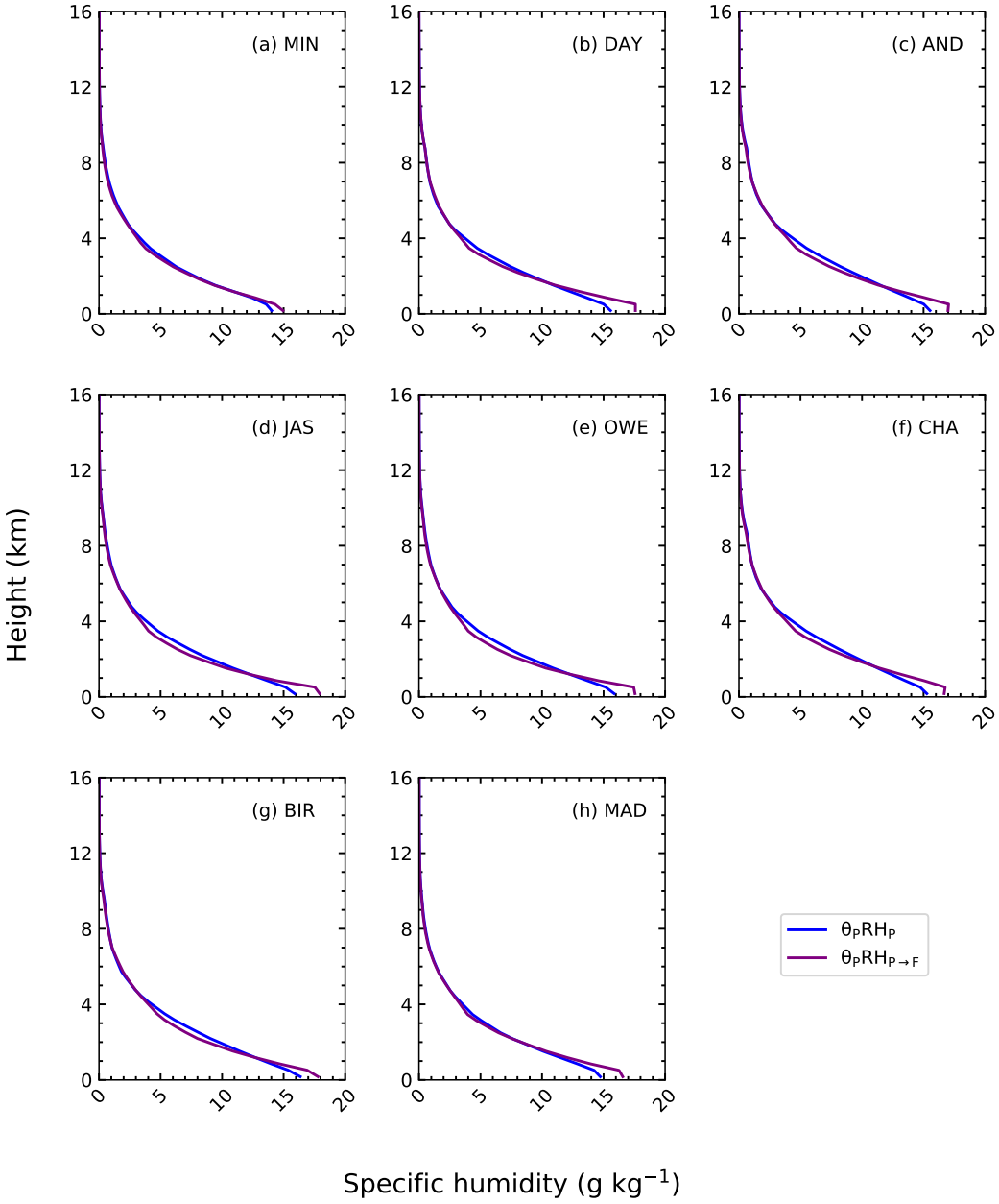

Figure 5.12: Vertical profiles of specific humidity at the initial time for all locations in the altered environment ($\theta_P RH_{P\rightarrow F}$) and the past environment.

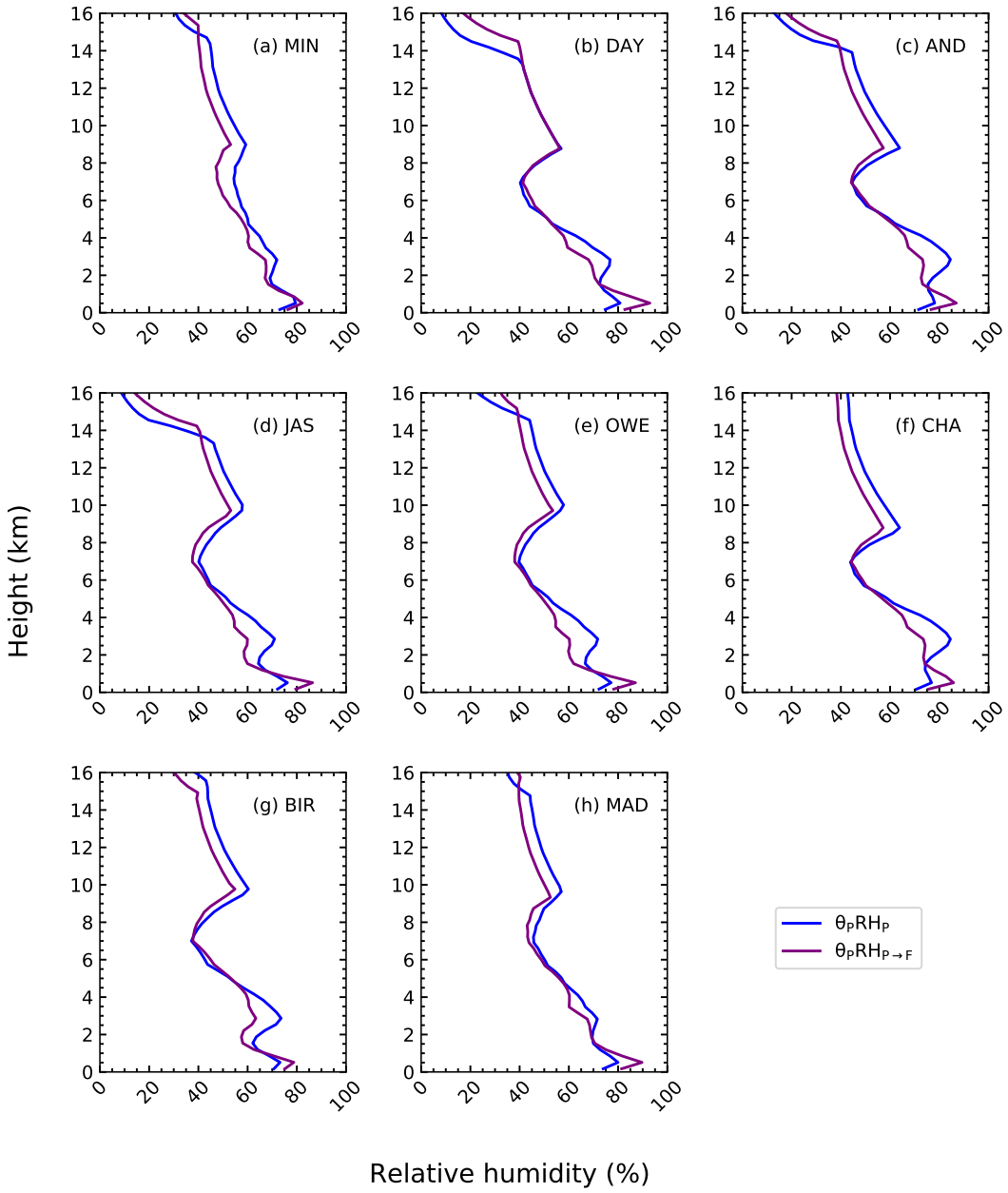

Figure 5.13: Vertical profiles of relative humidity at the initial time for all locations between the altered environment ($\theta_P RH_{P\rightarrow F}$) and the past environment

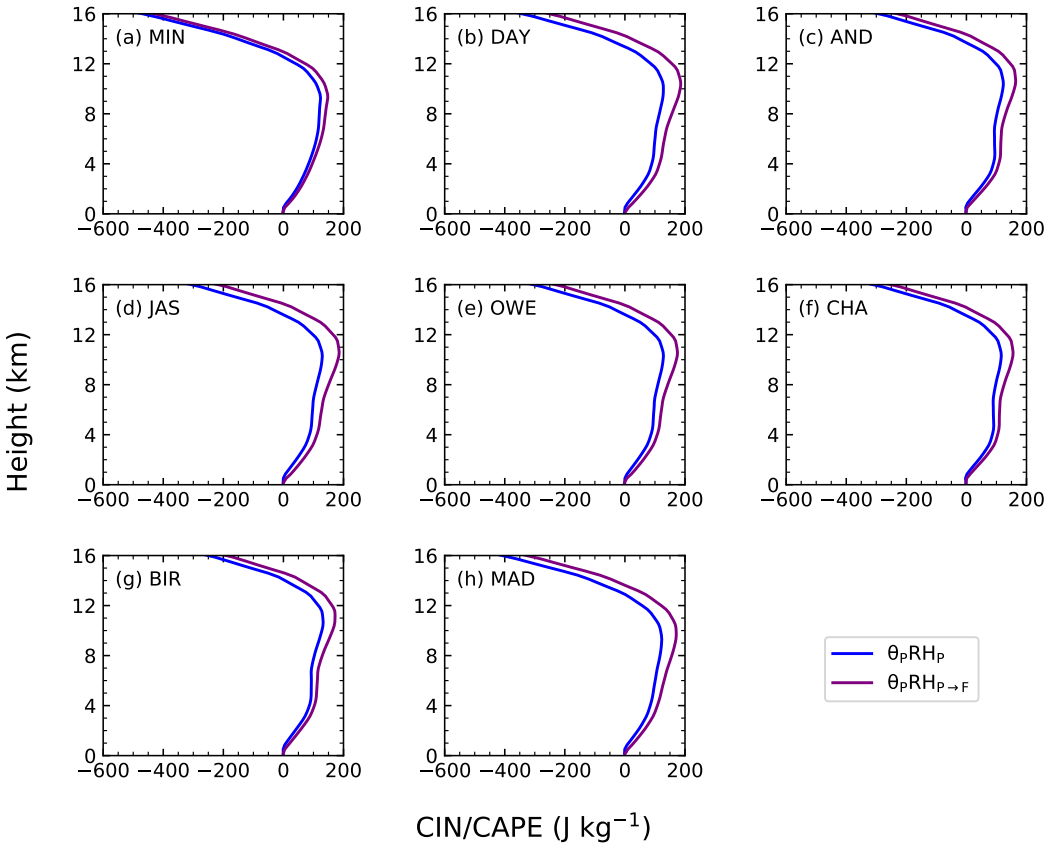

Figure 5.14: Vertical profiles of convective inhibition (CIN) and convective available potential energy (CAPE) at the initial time for all locations in altered environment ($\theta_P RH_{P\rightarrow F}$) and past environment.

Exp. 3 Results

As in Experiment 2, the highlight of the results from this experiment is on the strength of convection as seen in the modelling results from the maximum vertical velocity and total water content in the clouds, as depicted in Figures 5.15 and 5.16 respectively. The average maximum vertical velocity in the altered environment is 35% stronger than in the past environment, while the average total water content throughout the simulation time is 70% greater in the altered environment than in the past environment. This suggests that the altered environment is very conducive and favourable for convection to occur. We will now delve deeper into the cloud macrophysical and microphysical properties.

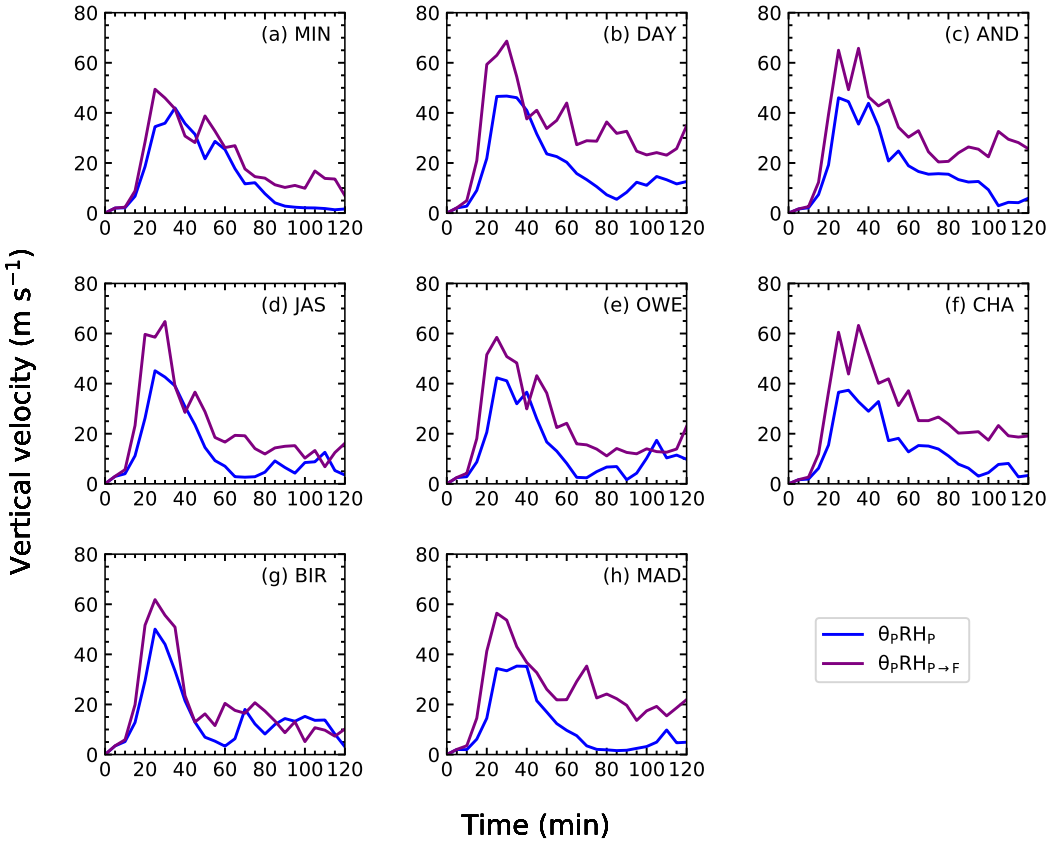

Figure 5.15: Time-series profiles of maximum vertical velocity for all locations in the altered environment ($\theta_P RH_{P\rightarrow F}$) and the past environment.

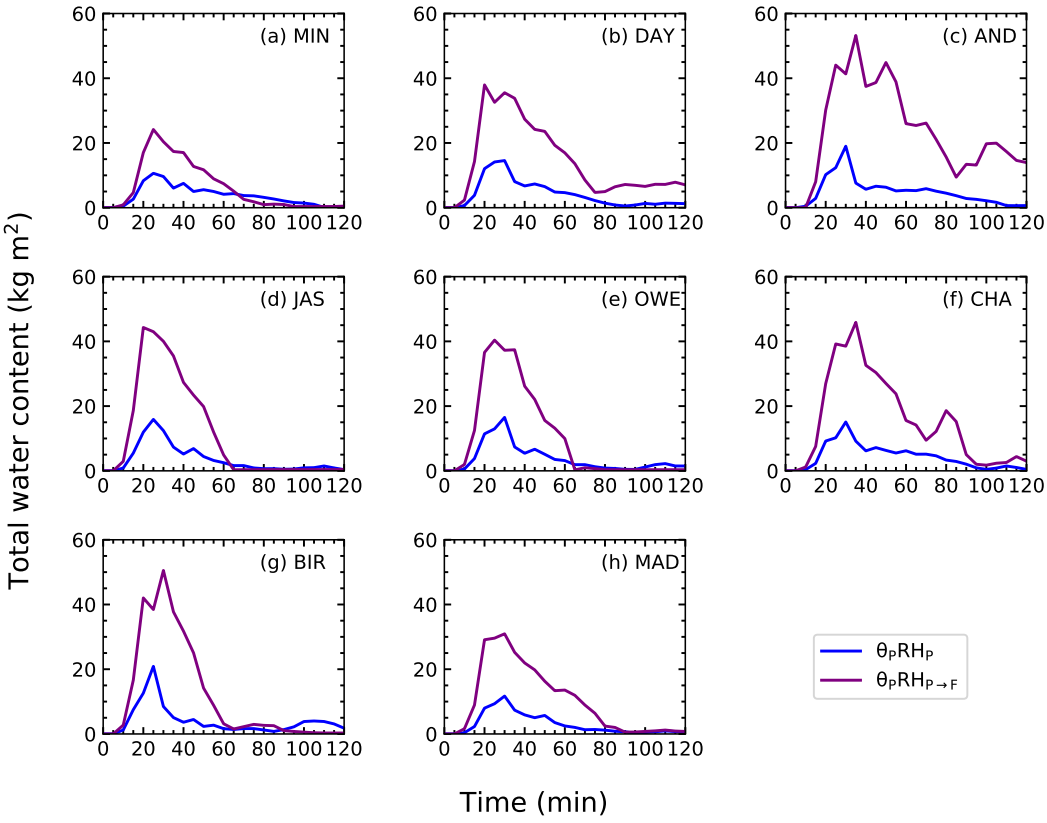

Figure 5.16: Time-series profiles of average total water content for all locations in the altered environment ($\theta_P RH_{P\rightarrow F}$) and the past environment.

Exp. 3 Cloud macrophysical properties

Table 5.10 lists the heights and depths associated with the warm-phase cloud layers, while Table 5.11 gives the cloud-top heights and cold-phase cloud depths for the two environments. The mean differences for each cloud properties between the two environments are given in Table 5.12. Figure C.5 in **Appendix C** shows an example of 2D cross section of the simulated cloud structure for the altered environment. To begin with, the clouds in the altered environment form at altitude that is on average 185 m lower than in the past environment. On the other hand, the freezing levels in both environments remain at the same heights. This yields an average warm-phase cloud depth that is 185 m deeper in the altered environment than in the past environment. Next, we explore the cloud-top heights and cold-phase cloud depths in both environments. The average cloud-top height in the altered environment is 1.8 km higher than in the past environment and the average cold-phase cloud depth is 1.8 km deeper in the altered environment than in the past environment. The greater cloud depths of both the warm and cold phases in the altered environment are features of cloud structure that are different from the previous two experiments. These deeper depths imply stronger convection in the altered environment relative to the past environment, as is also evident in the stronger updraught strength (Figure 5.15) in the altered environment.

Table 5.10: Heights of cloud base (m), freezing level (km), and warm-phase cloud depths (km) for all locations in the altered environment ($\theta_P RH_{P\rightarrow F}$) and the past environment.

Locations	**Cloud base heights (m)**		**Freezing levels (km)**		**Warm-phase cloud depths (km)**	
	$\theta_P RH_P$	$\theta_P RH_{P\rightarrow F}$	$\theta_P RH_P$	$\theta_P RH_{P\rightarrow F}$	$\theta_P RH_P$	$\theta_P RH_{P\rightarrow F}$
MIN	691	575	3.5	3.5	2.8	3.0
DAY	661	422	3.8	3.8	3.1	3.4
AND	747	580	3.8	3.8	3.0	3.2
JAS	732	503	4.1	4.1	3.4	3.6
OWE	730	538	4.1	4.1	3.4	3.6
CHA	766	605	3.8	3.8	3.0	3.2
BIR	774	619	4.1	4.1	3.4	3.5
MAD	676	452	3.8	3.8	3.1	3.3

Table 5.11: Cloud-top heights (km) and cold-phase cloud depths (km) for all locations in the altered environment ($\theta_P RH_{P\rightarrow F}$) and the past environment.

Locations	**Cloud-top heights (m)**		**Cold-phase cloud depths (km)**	
	$\theta_P RH_P$	$\theta_P RH_{P\rightarrow F}$	$\theta_P RH_P$	$\theta_P RH_{P\rightarrow F}$
MIN	13.5	13.5	10.0	10.0
DAY	14.8	16.5	11.0	12.7
AND	15.0	16.5	11.2	12.7
JAS	14.3	16.5	10.2	12.4
OWE	14.3	16.5	10.2	12.4
CHA	13.3	16.5	9.5	12.7
BIR	15.8	17.3	11.7	13.2
MAD	12.8	15.0	9.0	11.2

Table 5.12: Mean differences for the properties of cloud structures for all locations between the altered environment ($\theta_P RH_{P\rightarrow F}$) and the past environments.

Cloud structures	**Mean differences (Altered - Past)**
Cloud base height	-185 m
Freezing level	No difference
Warm-phase cloud depth	350 m
Cloud-top height	1.8 km
Cold-phase cloud depth	1.8 km

Exp. 3 Synthesis

The stronger convection in the altered environment is attributed to the increased moisture content and saturation in the boundary layer. Referring to the relative humidity profiles in Figure 5.13, the changes made to produce the altered environment results in abundant low-level moisture as seen in the greater specific humidity and relative humidity in Figure 5.12. In the mid-layer, however, the moisture content is lower than in the past environment and beyond that the moisture content between the two environments remain similar. Despite the less saturated condition and lower moisture content in the mid-layer of the altered environment relative to the past environment, the total water content (Figure 5.16) throughout the simulation time is still substantially higher in the altered environment than in the past environment. Thus, it is again suggested that the boundary layer moisture and saturation play a prominent role in dictating the cloud development in the altered environment.

The high relative humidity (Figure 5.13) in the boundary layer in the altered environment signifies an environment that is close to saturation, making it easier to achieve saturation, thus enhances cloud nucleation. This strengthened updraught then carries cloud droplets aloft, and due to the small size of the droplets, they are easily lofted past the freezing level, thus initiating an earlier ice processes than in the past environment as seen in Figure 5.17. In fact, the ice processes and formation of rain (Figure 5.18) occur at the same time, i.e. 15 min in the altered environment; whereas in the past environment, ice processes succeeds after the

formation of rain drops, i.e. at 20 min. In addition to the earlier ice processes in the altered environment, the mass mixing ratio of solid hydrometeors (ice, snow and hail) formed (Figure 5.17) are also greater than in the past environment. The more active ice processes subsequently release more latent heat of freezing which further boosts the updraught speed (Figure 5.15), thus allowing for further vertical movement within the clouds. Due to the greater CAPE (Figure 5.14) throughout the troposphere in the altered environment, the clouds are able to consume more CAPE at any given level the clouds develop. This further contributes to positive buoyancy which drives the kinetics and microphysical processes within the clouds, as seen in the greater production of solid hydrometeors (Figure 5.17) in the altered environment. Ultimately, the more developed ice phase in the altered environment results in higher rain rate and more accumulation of surface rain fall than in the past environment, as seen in Figure 5.19.

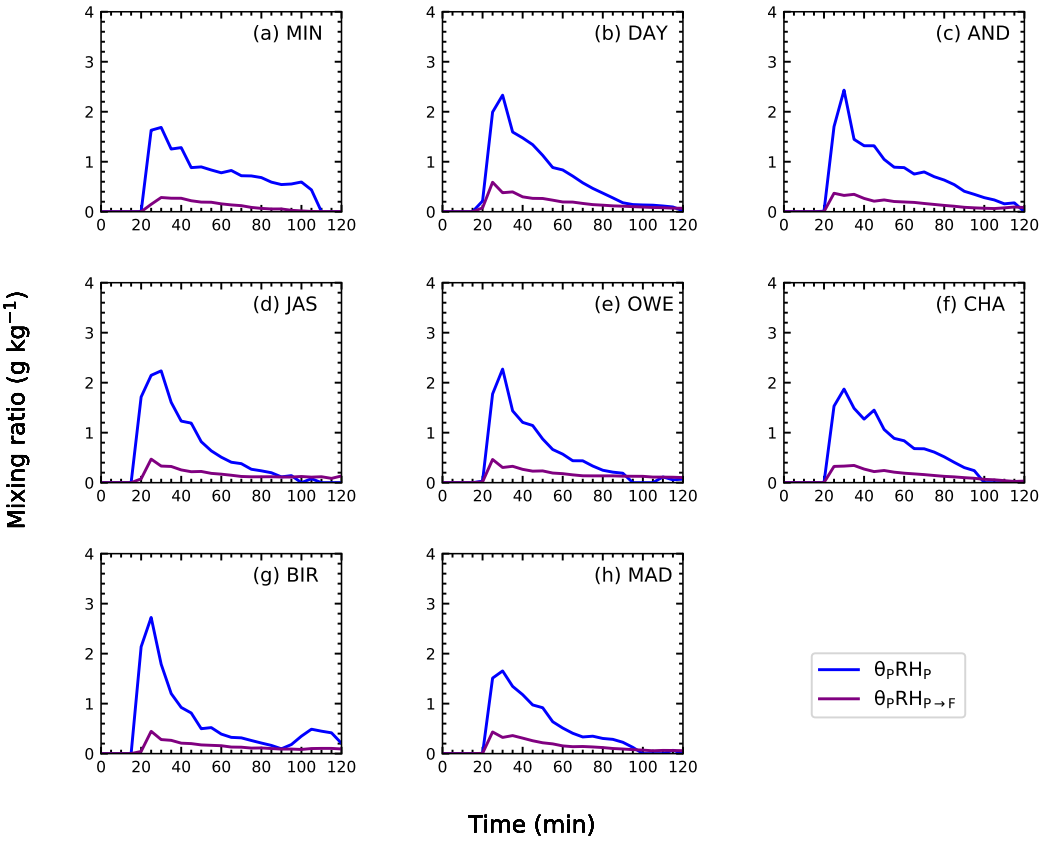

Figure 5.17: Time-series profiles of average solid hydrometeor (ice, snow and hail) mixing ratio for all locations in the altered environment ($\theta_P RH_{P\rightarrow F}$) and the past environment.

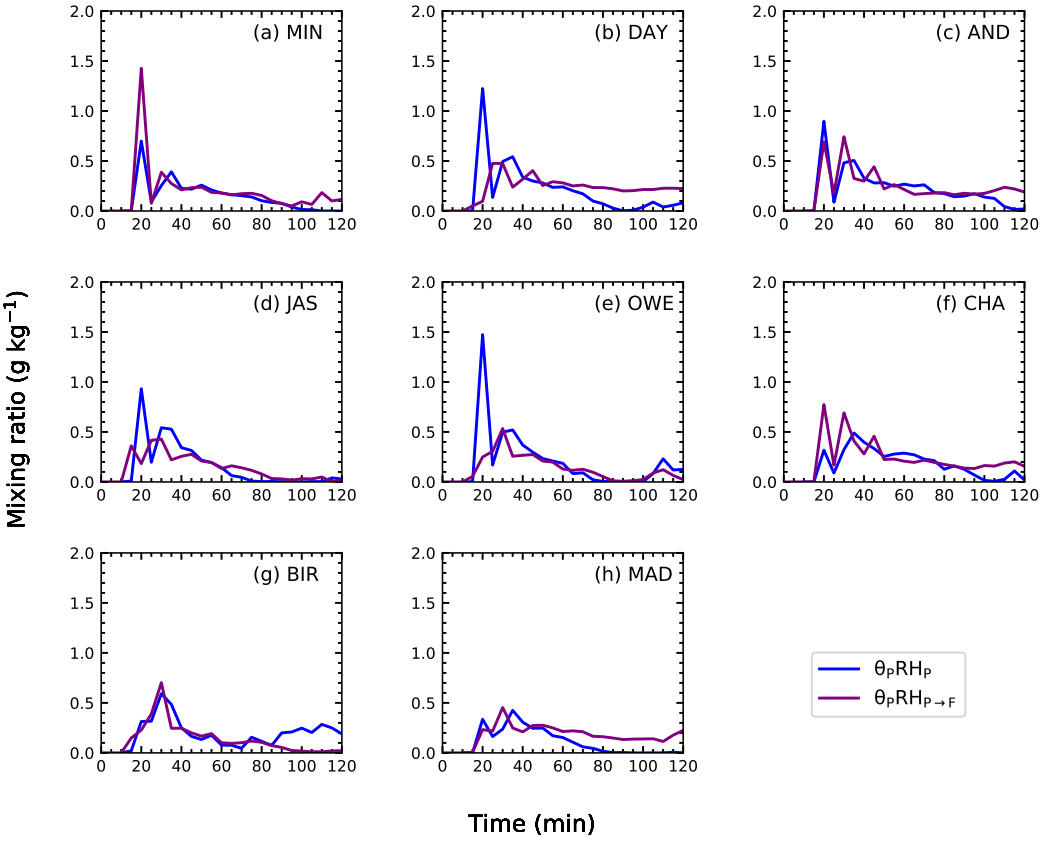

Figure 5.18: Time-series profiles of average rain mass mixing ratio for all locations in the altered environment ($\theta_P RH_{P\rightarrow F}$) and the past environment.

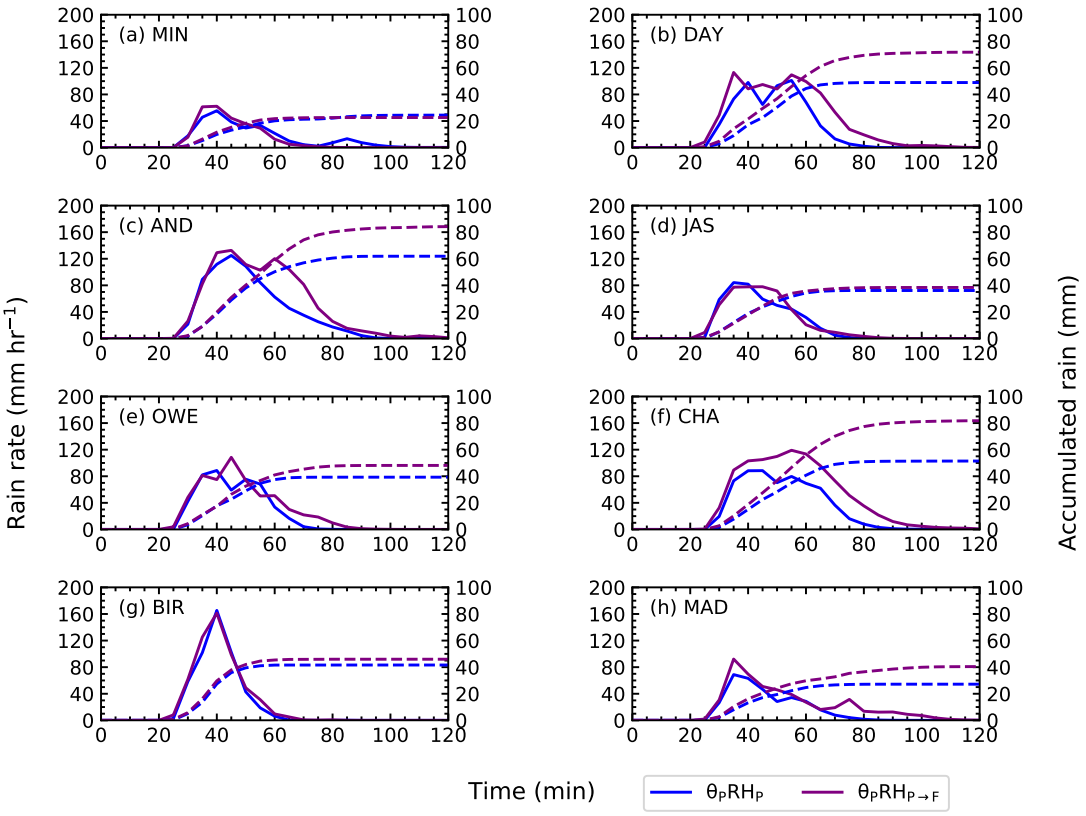

Figure 5.19: Time-series profiles of maximum rain rate (left y-axis) and maximum accumulated surface rain (right y-axis) for all locations in the altered environment ($\theta_P RH_{P\rightarrow F}$) and the past environment.

Exp. 3 Conclusion

This experiment shows that the increased moisture and saturation from the relative humidity in the boundary layer of the altered environment results in stronger convection as seen in the more developed ice phase in terms of mixing ratio that is an order of magnitude higher than the past environment, as well as the average cloud vertical extent that is about 1.8 km higher than the past environment results.

5.3.4 Experiment 4: Assessing the effects of warming on cloud development in terms of the water-holding capacity

Exp. 4 Introduction

Warmer worlds will hold more moisture and this would be the case without any vertical structural changes as well. Experiment 4 in this section sets out to understand the effect of the increased moisture content that comes with a higher mean temperature. In this test, the temperature and relative humidity structure are kept unchanged so it isolates just the effects of increased temperature and hence moisture content. For this experiment, the altered environment from Experiment 1, that is $\overline{\theta}_{\mathrm{F}\rightarrow\mathrm{P}}\mathrm{RH}_{\mathrm{F}}$, is used as the altered environment here. This altered environment is then compared to the unaltered future environment. In the following, a comparison between the thermodynamic conditions in the altered environment and the future environment is further described. By comparing the altered environment to the future environment, it enables us to test the effects of different concentration or reservoir of water vapour, in environments that have the same temperature structure and relative humidity structure, on the cloud development.

The mean temperature in the altered environment is reduced to the past environment and this decreases the water-holding capacity of the altered environment as portrayed in the vertical profiles of specific humidity in Figure 5.20. Figure 5.20 shows that the specific humidity in the altered environment is lower than in the future environment throughout the atmosphere. As it was established in previous studies and in **Chapter 4** that water vapour contributes to the convective available potential energy (CAPE) in an environment, it is seen that the lower specific humidity in the altered environment results in lower CAPE than in the future environment (Figure 5.21). This then results in weaker convection than in the future environment. This results are also seen in this experiment as portrayed in the maximum vertical velocity profiles in Figure 5.22.

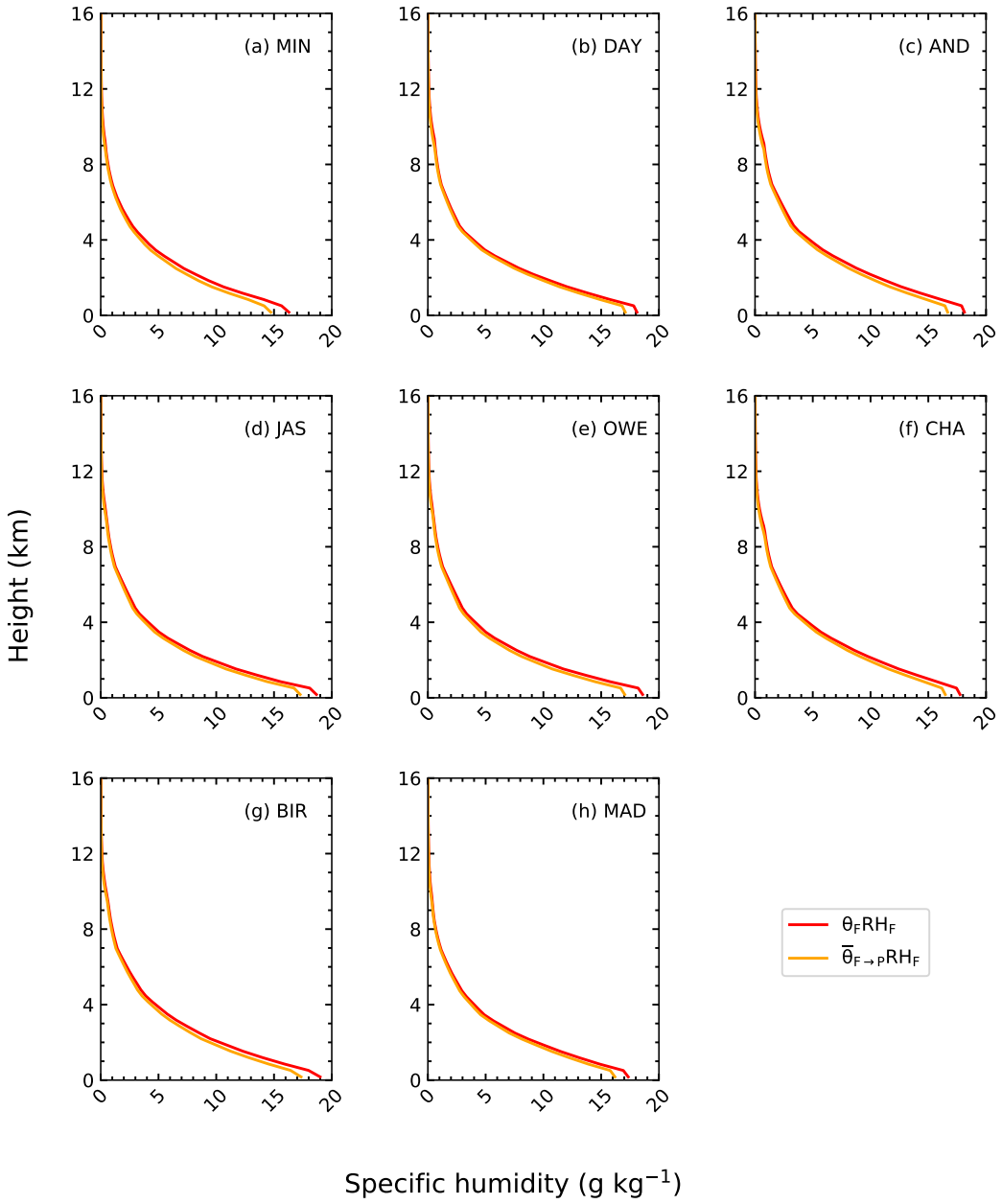

Figure 5.20: Vertical profiles of specific humidity at the initial time for all locations in the altered environment ($\overline{\theta}_{F\rightarrow P} RH_F$) and the past environment.

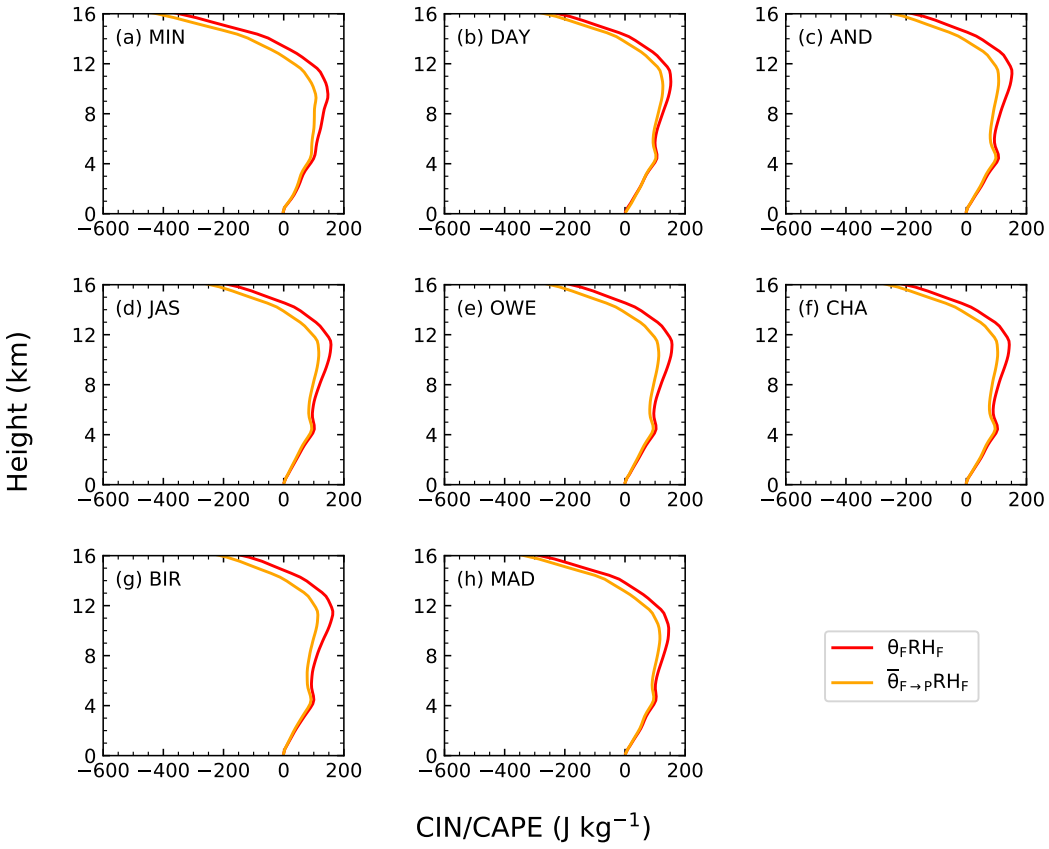

Figure 5.21: Vertical profiles of convective inhibition (CIN) and convective available potential energy (CAPE) at the initial time for all locations in altered environment ($\overline{\theta}_{F\rightarrow P} RH_F$) and past environment.

Exp. 4 Results

The strength of convection can be inferred from the maximum vertical velocity profiles. Figure 5.22 shows that the maximum vertical velocities in the two environments are mostly similar, but on average, the maximum vertical velocity in the altered environment is lower than in the future environment. From **Chapter 4**, it was found that the lower vertical velocity enhances collision-coalescence process in the production of rain drops which results in intense initial rainfall due to the large raindrop sizes that could not be supported by the cloud updraught. In this experiment therefore, since the vertical velocity in the altered environment is lower than the future environment, does that enhances the collision-coalescence process even more? To find out, we will look into the time-series profiles of rain mass mixing ratio, and the subsequent rain rate and accumulated surface rainfall of both environments as depicted in Figures 5.23 and 5.24. Figure 5.23 shows minimal differences in the rain mixing ratio in all the locations between the altered and unaltered environments. This suggests that the collision-coalescence process in the rain formation between the two environments remain similar. A major difference is actually seen in the initial rain rate (left y-axis in Figure 5.24). The initial rain rate for all the locations in the altered environment is on average 10% greater than in the unaltered future environment. However, the total accumulated surface rainfall remains similar between the altered and unaltered future environments for most locations except in DAY, AND, and CHA. DAY (AND and CHA) accumulated more (less) surface rainfall in the altered environment than in the unaltered future environment. Therefore, it is suggested that the weaker velocity in the altered environment influences the rain rate in terms of the concentration or transport of water in the vertical as will be discussed in the next paragraph.

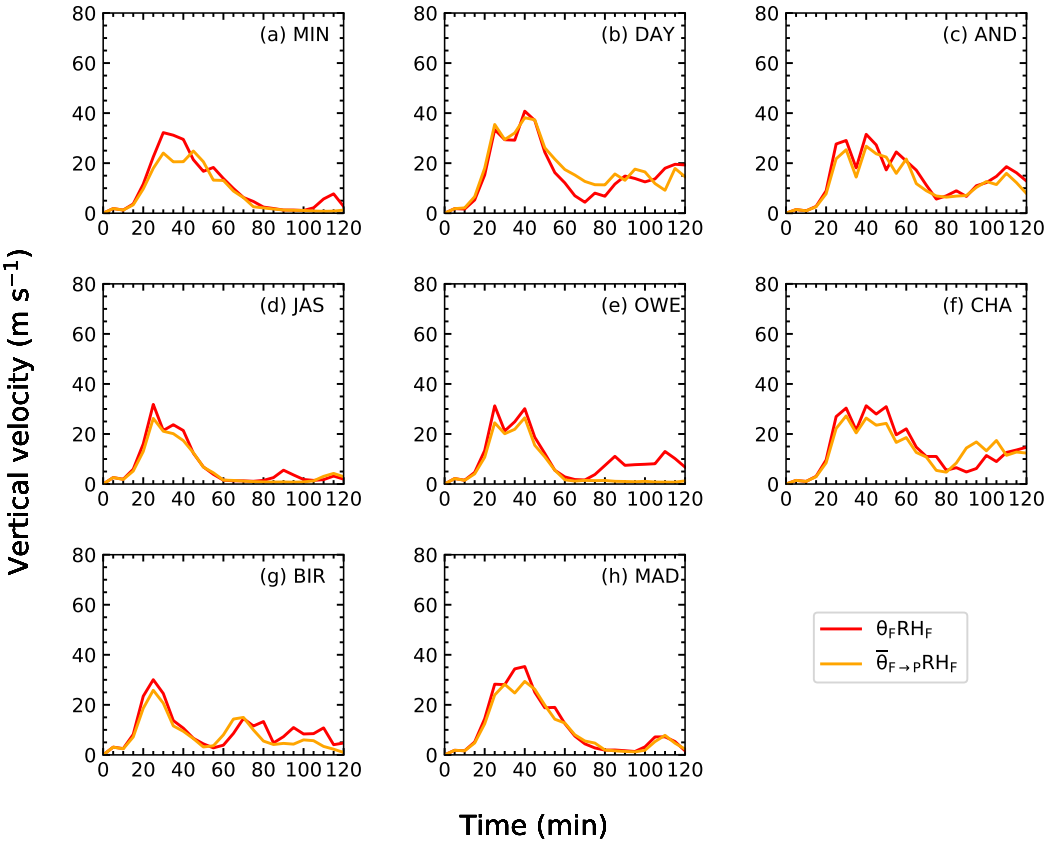

Figure 5.22: Time-series profiles of maximum vertical velocity for all locations in the altered environment ($\overline{\theta}_{F\rightarrow P}RH_F$) and the past environment.

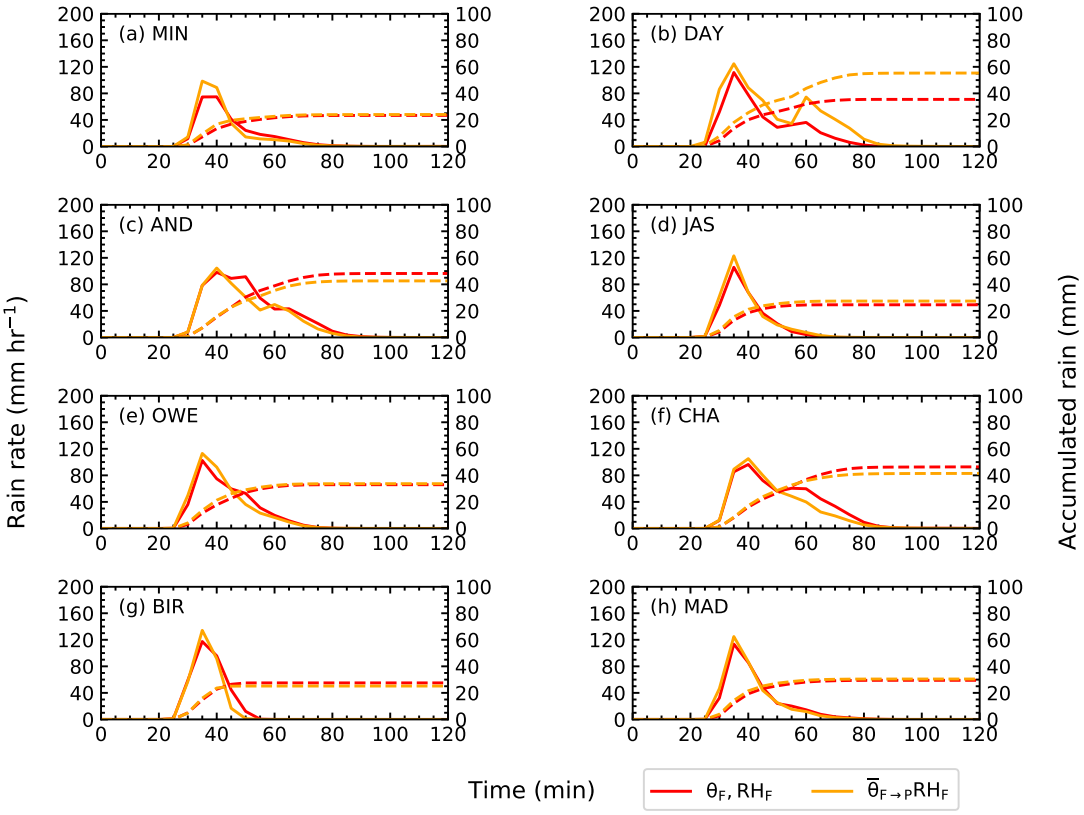

Figure 5.23: Time-series profiles of maximum rain rate (left y-axis) and maximum accumulated surface rain (right y-axis) for all locations in the altered environment ($\overline{\theta}_{F\rightarrow P}RH_F$) and the past environment.

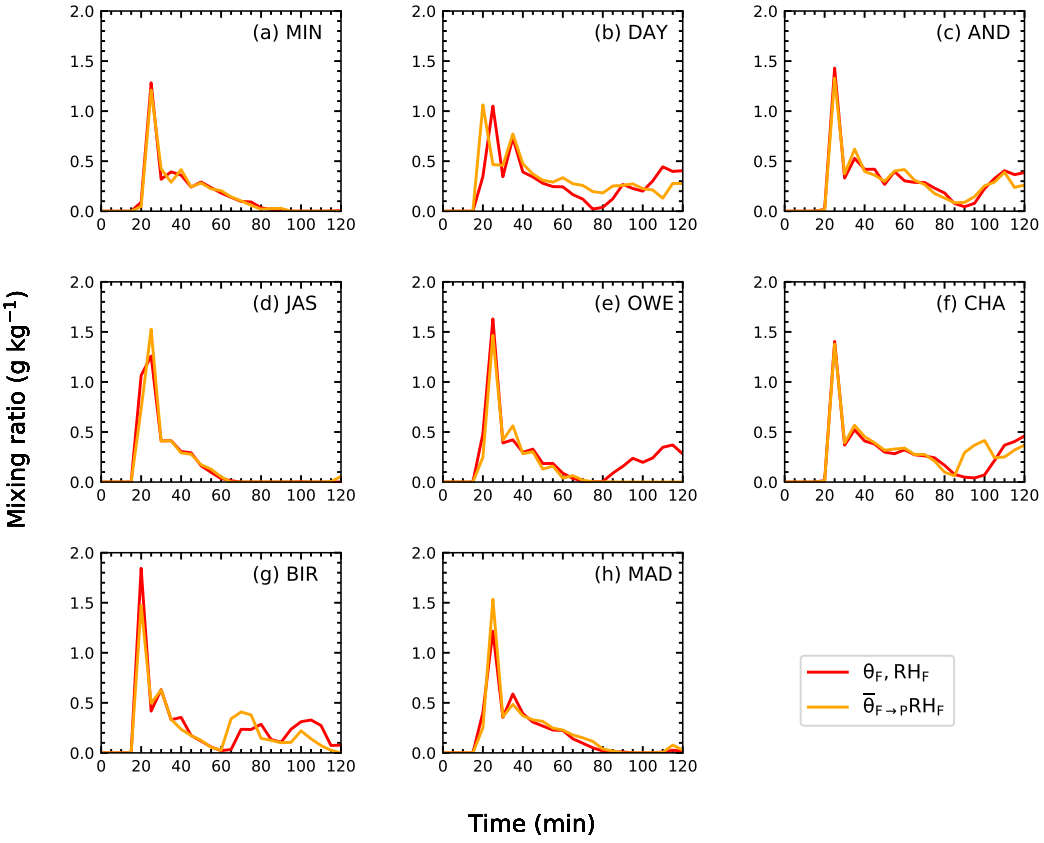

Figure 5.24: Time-series profiles of average rain mass mixing ratio for all locations in the altered environment ($\overline{\theta}_{F \rightarrow P} RH_F$) and the past environment.

Exp. 4 Synthesis

One possible explanation for the differences seen between the cloud development in the altered and unaltered future environments can be inferred from the vertical velocities within the clouds since the differences in the warm-phase cloud structure (i.e. cloud bases, freezing levels and warm-phase cloud depth in Table 5.13) and warm rain process between the two environments are very minimal and therefore negligible. Instead, the difference in the vertical velocity influences the initial rain rate seen in the 10% greater initial rain rate in the altered environment than in the unaltered environment. This is suggested to be due to the lower water-holding capacity of the altered environment that results in lower amount of moisture, subsequently resulting in the lower CAPE (Figure 5.21) and weaker vertical velocity (Figure 5.22) than in the unaltered future environment. The weaker vertical velocity in the altered environment limits the vertical extent to which condensates are lofted. Therefore, when rain starts to fall out in the altered environment, the rain particles fall out in shorter vertical distance than in the unaltered future environment. Consequently, this results in the greater initial rain rate in the altered environment than the unaltered future environment. The earlier and greater removal of rain from the altered environment thus reduces the availability of water for ice processes relative to the future environment. This is seen in the average decrease of cloud-top height and cold-phase cloud depth by 740 m and 625 m, respectively, in the altered environment than in the unaltered future environment, as shown in Tables 5.14 and 5.15. Again, an exception is seen in DAY where the cloud-top height and cold-phase cloud depth in the altered environment are greater than in the unaltered future environment. Therefore, it is acknowledged that some other factors not considered in this study could be causing the exception and therefore warrants further investigation in future studies.

Table 5.13: Heights of cloud base (m), freezing level (km), and warm-phase cloud depths (km) in the altered environment ($\overline{\theta}_{F\rightarrow P}RH_F$) and the past environment.

Locations	**Cloud base heights (m)**		**Freezing levels (km)**		**Warm-phase cloud depths (km)**	
	$\theta_F RH_F$	$\overline{\theta}_{F\rightarrow P}RH_F$	$\theta_F RH_F$	$\overline{\theta}_{F\rightarrow P}RH_F$	$\theta_F RH_F$	$\overline{\theta}_{F\rightarrow P}RH_F$
MIN	583	572	4.1	3.8	3.5	3.2
DAY	487	424	4.1	4.1	3.6	3.7
AND	586	577	4.1	4.1	3.5	3.5
JAS	507	499	4.1	4.1	3.9	3.6
OWE	543	534	4.1	4.1	3.9	3.6
CHA	611	602	4.1	4.1	3.5	3.5
BIR	626	615	4.5	4.5	3.8	3.8
MAD	456	450	4.1	4.1	3.6	3.6

Table 5.14: Cloud-top heights (km) and cold-phase (km) cloud depths for all locations in the altered environment ($\overline{\theta}_{F\rightarrow P}RH_F$) and the past environment.

Locations	**Cloud-top heights (m)**		**Cold-phase cloud depths (km)**	
	$\theta_F RH_F$	$\overline{\theta}_{F\rightarrow P}RH_F$	$\theta_F RH_F$	$\overline{\theta}_{F\rightarrow P}RH_F$
MIN	12.0	11.3	7.9	7.5
DAY	12.8	14.3	8.7	10.2
AND	14.3	12.0	10.2	7.9
JAS	12.8	12.0	8.4	7.9
OWE	12.0	12.0	7.6	7.9
CHA	13.3	12.0	9.2	7.9
BIR	14.3	12.8	9.8	8.3
MAD	12.8	12.0	8.7	7.9

Table 5.15: Mean differences for the properties of cloud structures for all locations between the altered environment ($\overline{\theta}_{F\rightarrow P}RH_F$) and the past environments.

Cloud structures	**Mean differences (Altered - Past)**
Cloud base height	-16 m
Freezing level	-37.5 m
Warm-phase cloud depth	-10 m
Cloud-top height	-740 km
Cold-phase cloud depth	-625 km

Exp. 4 Conclusion

The result from this experiment shows that the water-holding capacity of environmental temperature affect mainly the initial rain rate and the cold-phase cloud structure in the altered environment. On average, the initial rain rate in the altered future environment is 10% higher than the unaltered future environment, even though the average rain mixing ratio remain fairly similar. This suggests that the collision-coalescence process between the two environments is fairly similar and that the differences seen in the initial rain rate arise from the updraught speed's role in the vertical distribution of condensates. The weaker updraught speed in the altered environment limits the vertical extent to which condensates are lofted. As a result, when rain starts to fall, the rain particles in the altered environment falls over a smaller vertical distance than in the unaltered environment. This leads to faster removal of rain water mass thus limiting the availability of water for ice processes. As a result, the average cloud-top height and cold-phase cloud depth are 740 m and 625 m lower than the unaltered future environment.

5.4 Summary

With changing climate, various factors change including the mean temperature, the amount of water vapour in the air, and the structural changes of the relative humidity and temperature. This chapter has investigated each of these factors and the following results are found.

1. The results from Experiment 1 shows that reducing the mean temperature but keeping the structures of temperature and relative humidity of the future environment leads to average warm-phase cloud depth that is approximately 400 m deeper than in the past environment. The greater warm-phase enhances the collision-coalescence process that increases the rain mixing ratio by a factor of 10 than in the past environment, especially during the peak rain production. This leads to an intense initial rainfall that removes large mass of rain water in the altered environment, thus reducing the availability of water for ice processes in the altered environment. As a result, the ice processes in the altered environment is weakened as seen in the average decrease of cloud-top height and cold-phase cloud depth by 2 km and 2.2 km, respectively, compared to that in the past environment. The results from this experiment is similar to that performed for the past and future environment in **Chapter 4**. In comparison to the results in **Chapter 4**, the reduced mean temperature in the altered environment in Experiment 1 results in minimal changes in the average cloud base height but a lowering of the freezing level by an average of 45%. This reduces the average warm-phase cloud depth by 25%, and a further reduction in the average cloud-top height and cold-phase cloud depth by 40% and 30%, respectively. Therefore, this shows that the temperature structure and relative humidity of the future environment substantially influences the cloud development, with or without the mean increase in warming that climate change brings.

2. Experiment 2 isolates the temperature structure from relative humidity. The results from Experiment 2 shows that the temperature structure has a huge effect on the cold-phase cloud properties. From the results, the altered environment exhibit lower moisture in the boundary layer. This results in convect-

ive inhibition (CIN) energy and lower convective available energy (CAPE), thus weakening the convective development as seen in vertical velocity that is 75% weaker and total water content that is 80% lower in the altered environment than in the past environment. Ultimately, this leads to less-developed clouds in the altered environments as seen in the huge average reduction of cloud-top height and cold-phase cloud depth by 1.8 km from the past environments. Hence, this illustrates that the vertical extent of clouds is greatly affected by the temperature structure.

3. Experiment 3 isolates the relative humidity structure from the temperature structure. The results from this experiment give the most dramatic effect on the cold-phase cloud properties. The results show that the relative humidity of the future environment leads to an increased moisture and saturation in the boundary layer of the altered environment. The increased moisture and high saturation lead to greater CAPE that enhances the average maximum vertical velocity by 30% from the past environment. Consequently, this enhances the convection as seen in the average increase in total water content by 70% in the altered environment than in the past environment. The greater updraught strength in the altered environment also facilitates the vertical transport of condensates into higher heights, thus invigorating or strengthening the ice processes as seen in mixing ratio of solid hydrometeors that is an order of magnitude higher than the past environment. Subsequently, the cloud-top height and cold-phase cloud depth are also seen to increase by an average of 1.8 km from the past environment. Overall, this experiment shows that the increased moisture and saturation from the relative humidity in the boundary layer results in stronger convection as seen in the more developed ice phase.

4. Experiment 4 compares the non-warmed and warmed future environment and tests the effect of the increased moisture content that comes with a higher mean temperature from warming. The reduced mean temperature of non-warmed altered environment exhibit lower water-holding capacity than the unaltered future environment, and the results from this experiment show that the main effect from this is on the initial rain rate, which subsequently affects the cold-phase cloud properties of the altered environment. On average, the

initial rain rate in the altered future environment is 10% higher than the unaltered future environment, even though the average rain mixing ratio remain fairly similar. This suggests that the collision-coalescence process between the two environments is fairly similar and that the differences seen in the initial rain rate arise from the updraught speed's role in the vertical distribution of condensates. The weaker updraught speed in the altered environment limits the vertical extent to which condensates are lofted. As a result, when rain starts to fall, the rain particles in the altered environment falls over a smaller vertical distance than in the unaltered environment. This leads to faster removal of rain water mass thus limiting the availability of water for ice processes. As a result, the average cloud-top height and cold-phase cloud depth are 740 m and 625 m lower than the unaltered future environment.

In summary, given the assumed thermodynamic structure changes predicted from the CCSM3 global climate model, the study in this thesis found that the thermodynamic structural changes have a greater influence on the cloud development than changes in the mean temperature. The thermodynamic structures assessed in this study are the potential temperature (or temperature) and relative humidity structures. The study isolated and assessed each structure and found that each produces large differences in the cloud development when compared to the cloud development in the past environment. The temperature structure effect seen from Experiment 2 results significantly reduces the average cloud vertical extent by 8km, along with an average reduction of 80% and 75% in the the total water content and maximum vertical velocity, respectively. On the other hand, the relative humidity structure effect seen from Experiment 3 results significantly increases the average maximum vertical velocity by 30% and the total water content by 70%. In particular, the production of solid hydrometeors increased by an order of magnitude which subsequently increases the cloud-top height by 1.8 km. When the temperature structure and relative humidity structure effects are added together (as they are in the future thermodynamic environment), the effects cancel out slightly but they still result in weaker cloud development than in the past environment.

Chapter 6

The comparison between the radiative properties of deep convective clouds in the past and future climates

6.1 Introduction

In **Chapters 4** and **5**, we have seen that the DCCs exhibit a complex variability of cloud macro- and microphysical structure such as the occurrence of layers where phase transitions between liquid water and ice particles take place, and the initiation time for ice phase, under different thermodynamic perturbations. Thus, it is speculated that the changes in cloud properties and formation processes would induce changes in the cloud radiative properties. The last IPCC report AR5 (Boucher *et al.*, 2013) also highlighted the importance in advancing the understanding on the cloud properties particularly in the convective regions. This chapter presents the results of the radiative properties of the simulated DCCs in **Chapter 4** and discusses the comparison between the radiative properties of the DCCs in the past and future thermodynamic environments.

The remaining sections in this chapter include the definition of terms and cloud thresholds in **Section 6.2**, followed by results in **Section 6.3** and discussion in **Section 6.4**.

6.2 Definition of terms and cloud thresholds

This section describes the methodology employed in the evaluation of cloud radiative properties for the simulated deep convective clouds in the past and future environments. Previous studies (e.g. Hartmann *et al.*, 2001; Thampi and Roca, 2014) have established that the shortwave and longwave radiative effects of deep convective clouds balance each other out at the top of the atmosphere. This balance, however, may be disturbed if the cloud's macro- and microphysical properties are modified (Behrangi *et al.*, 2012). In **Chapter 4**, it was found that the cloud-top heights in the future were lower than that in the past. This is due to the weakly-developed ice processes that resulted from the loss of water in the intense initial rainfall in the future environment. Subsequently, there are now less condensates and latent heat from the weak ice processes thus reducing the strength and amount of detrainment into anvils. The shrinkage in the size of anvils can have a large radiative impacts, especially in terms of the cloud greenhouse effect due to the cold temperature of the anvil clouds. Therefore, in this study, we evaluate the radiative properties of deep convective clouds in two parts, namely, the whole cloud and the anvil cloud. The whole cloud refers to the entire deep convective cloud comprising the deep convective tower and the attached anvil canopy, while the anvil cloud refers to the anvil canopy that is detached from the deep convective tower.

Here, the details of evaluation of the cloud radiative properties are described. The Fu-Liou radiative transfer model (Fu and Liou, 1992; Fu and Liou, 1993), described in **Section 3.3**, **Chapter 3** was used to quantitatively estimate the cloud radiative properties in the past and future environments. The vertical environmental profiles and cloud properties acquired from the idealised deep convective cloud simulations performed in **Chapter 4** were used to initialise the Fu-Liou radiative transfer model. The vertical environmental profiles comprise pressure, temperature and water vapour mixing ratio, while the vertical cloud properties comprise effective radii and mixing ratios of cloud water, combined ice and snow, and hail. These profiles were selected from the cloudy regions in the deep convective cloud simulations. We define cloudy air as having total cloud condensate above 0.001 g m^{-3} (as used by others such as Fan *et al.*, 2013; Villanueva-Birriel, 2014) so as to

exclude quiescent cloudy air. The entire cloudy air was selected for the evaluation of radiative properties of the whole cloud. For the evaluation of radiative properties of the anvil cloud, an additional threshold was applied to the cloudy air to extract regions that consist wholly of ice particles to represent the detached anvil cloud. The detached anvil cloud region is defined as having ice water path that is greater than 0.001 g m^{-2}, and liquid water path that is less than 0.000001 g m^{-2}.

A total of six radiative fluxes computed in the Fu-Liou radiative transfer model are assessed in this study. They are the upward shortwave (SW) and longwave (LW) radiation at the top of the atmosphere (TOA), upward SW and LW radiation at the surface, and downward SW and LW radiation at the surface. In the model, these radiative fluxes are computed for each grid cell at each time interval (i.e. five minutes). An average of each of the radiative flux is then computed at each time interval for the assessment of cloud radiative forcing.

The results from this assessments are presented in **Section 6.3**, which includes all the six radiative fluxes mentioned above, and the cloud radiative forcing at the TOA is highlighted.

6.3 Results

This section presents the results for the evaluation of cloud radiative effects between the past and future environments. We begin the analysis by evaluating the extent of the clouds and how this changes from the past to future environment. The results are presented in **Section 6.3.1**. We then evaluate the cloud radiative forcing at the TOA and the surface for the whole clouds and anvil clouds in **Section 6.3.2**.

6.3.1 Differences in cloud cover between the past and future environments

Figure 6.1 shows the cloud fraction of the main clouds between the past and future environments from the time clouds are formed, i.e. 10 min until the end of the simulation time, i.e. 120 min. On the other hand, Figure 6.2 shows the cloud fraction of the anvil clouds between the past and future environments from the time when anvils are formed until the end of the simulation time. The time of formation of anvils in some locations are different between the past and future environments. This follows from the results presented in **Chapter 4**, where the initiation of ice phase occurred earlier in the past than in the future. Consequently, anvils formed earlier in the past than in the future. Anvils started to form between 20 and 25 minutes in the past, and 25 – 30 min in the future. In most cases (MIN, AND, OWE, BIR, and CHA), the anvils in the future formed five minutes later than in the past, and in one case (JAS), the anvils in the future formed ten minutes later than in the past, while the other two cases (DAY and MAD) have anvils forming at the same time in the past and future. Five or ten minutes may not sound like a long time but for a parcel of air in a deep convective cloud ascending in a moderate updraught of 10 m s^{-1} can travel over 3 km vertically and undergo very different microphysical changes during this period. Looking at both the figures again, both figures are showing significant differences in that we find in many locations and times that the cloud fraction in the future is lower than that in the past. This again, follows from **Chapter 4** where the clouds in the past have well-developed ice phase than the clouds in the future.

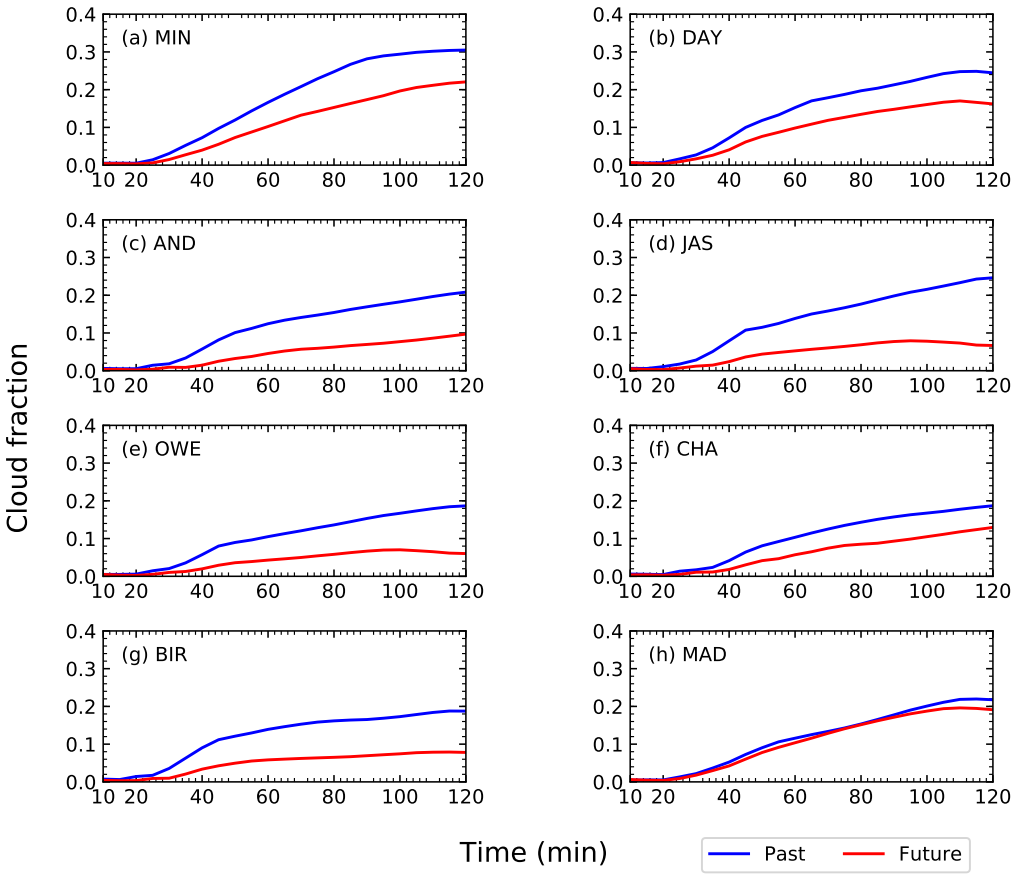

Figure 6.1: Cloud fraction for the main clouds. Blue line represents the past climate, red liner represents the future climate.

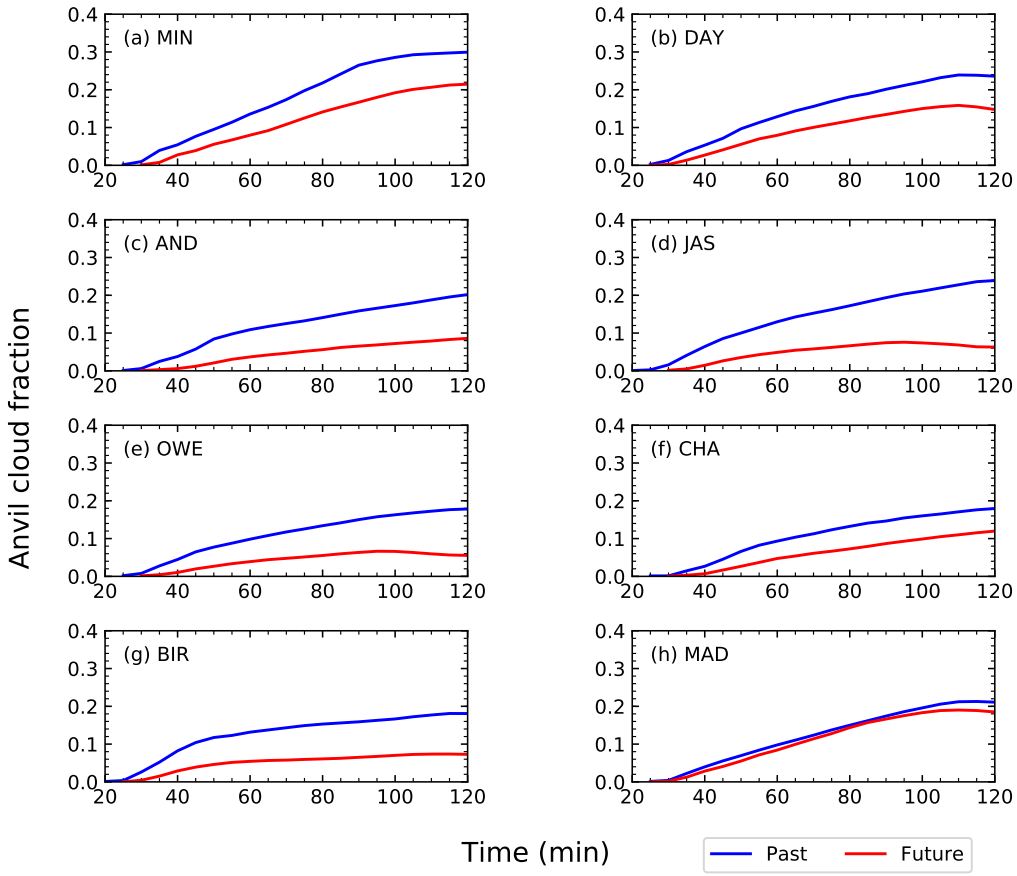

Figure 6.2: Cloud fraction for the anvil clouds. Blue line represents the past climate, red liner represents the future climate.

6.3.2 Cloud radiative forcing at the top of the atmosphere (TOA)

6.3.2.1 Outgoing shortwave and longwave radiation at the TOA for the main clouds

Figures 6.3 and 6.4 present the outgoing shortwave (SW) and longwave (LW) radiation at the TOA of the simulated deep convective clouds in the past and future environments from **Chapter 4**. Overall, the outgoing SW radiation at the TOA is greater in the past than that in the future clouds. In terms of the time-series trends between the past and future clouds, most of them showed similar trends and can be inferred from the cloud lifecycle. Although clouds in both the past and future environments formed at the same time, i.e. 10 min, they developed at different rates as discussed in **Chapter 4**. The implications that resulted from the different cloud development can be seen in the different radiative fluxes described in this section. The outgoing SW radiation was approximately between 350 – 490 W m^{-2} in the past, and 310 – 430 W m^{-2} in the future clouds. The outgoing SW radiation continued to increase as the cloud developed until up to 20 min, then it started to decrease due to clouds starting to dissipate towards the end of the simulation with some small fluctuations between approximately 25 – 35 min.

On the other hand, the outgoing LW radiation at the TOA was greater in the future than that in the past. The largest difference occurred between 20 and 35 min into the simulation, where the outgoing LW radiation decreased greatly in the past, signifying the strong ice phase that exhibit high cloud-top height, hence colder temperature that traps the LW radiation and emitting them at lower temperatures. This trend is otherwise subtle or absent in the future where the clouds have less developed ice phase. After the decrease, however, the outgoing LW radiation started increasing again and reaching asymptotes, indicating the dissipation of clouds towards the end of the simulations. It is noted that the outgoing LW radiation remained greater in the future than in the past due to the greater surface temperature in the future, hence the higher LW emission.

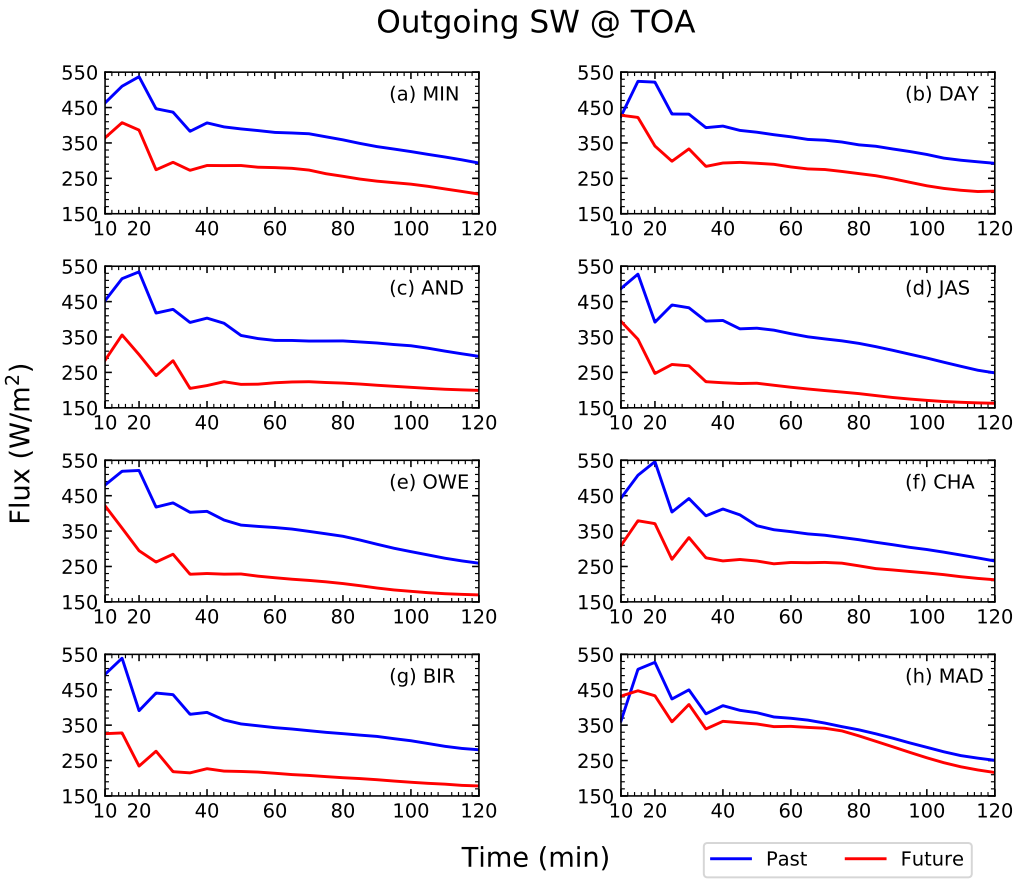

Figure 6.3: Outgoing shortwave radiation at the top of the atmosphere for the main clouds between the past and future environments.

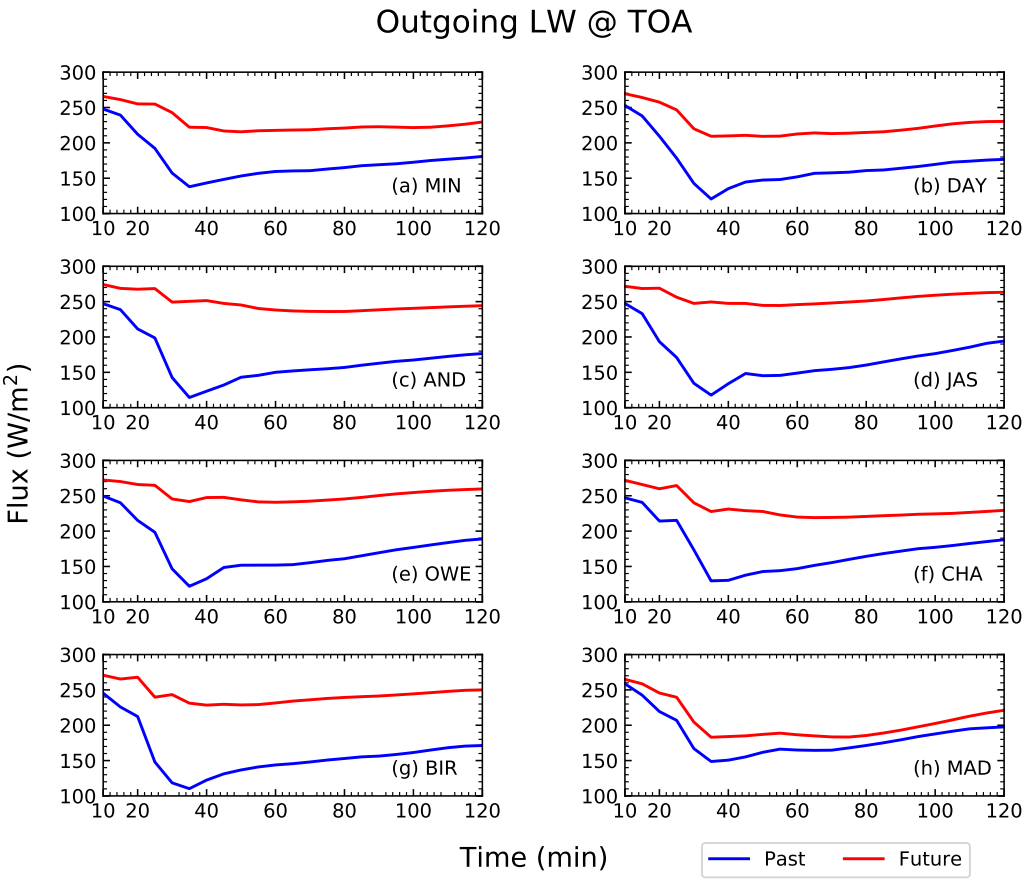

Figure 6.4: Outgoing longwave radiation at the top of the atmosphere for the main clouds between the past and future environments.

The difference between the outgoing SW and LW radiation can be seen in terms of the percentage difference shown in Figure 6.5. In all cases, the outgoing SW (LW) radiation in the future was lower (higher) than in the past. The decrease in the SW radiation in the future signifies a reduction in the cloud cover in that there is less cloud to reflect SW radiation, thus allowing more SW radiation to reach the surface and warm the earth. However, it could also be due to the significantly higher temperature throughout the future atmosphere thus emitting LW radiation at greater temperature than in the past. By evaluating the sum of the average SW and LW fluxes at the TOA, we calculate the radiative forcing (RF) between the past and future environments. RF is defined as the difference between the downward and upward fluxes at the top of the atmosphere as given in Equation 6.1. By adding SW and LW fluxes in each of the term, where $F_{\mathrm{F}\downarrow\mathrm{P}}$ refers to downward SW and LW fluxes, while $F_{\mathrm{F}\uparrow\mathrm{P}}$ refers to upward SW and LW fluxes, we can rewrite Equation 6.1 to Equation 6.2. By incorporating Equations 6.1 and 6.2 together, we get Equation 6.3 that is further elaborated in Equation 6.4 and finalised in Equation 6.5 which gives the RF between the two environments as listed in Table 6.1. If RF $>$ 0, it indicates warming in the future; in contrast, if RF $<$ 0, then it indicates cooling in the future. Table 6.1 shows that RF $>$ 0 in all the locations, with an average warming of 43.7 W m^{-2} in the future environment. It is thus concluded that this warming is a result of reduction of cloud cover that allow for greater solar insolation that warms the atmosphere in the future.

$$RF = F_{\downarrow} - F_{\uparrow} \tag{6.1}$$

$$RF = F_{\downarrow SW+LW} - F_{\uparrow SW+LW} \tag{6.2}$$

$$RF = F_{\downarrow SW+LW_{FUTURE}} - F_{\uparrow SW+LW_{PAST}} \tag{6.3}$$

$$RF = \left(F_{\downarrow SW+LW_{FUTURE}} - F_{\uparrow SW+LW_{FUTURE}}\right) - \left(F_{\downarrow SW+LW_{PAST}} - F_{\uparrow SW+LW_{PAST}}\right) \tag{6.4}$$

$$RF = F_{\uparrow SW+LW_{PAST}} - F_{\uparrow SW+LW_{FUTURE}} \tag{6.5}$$

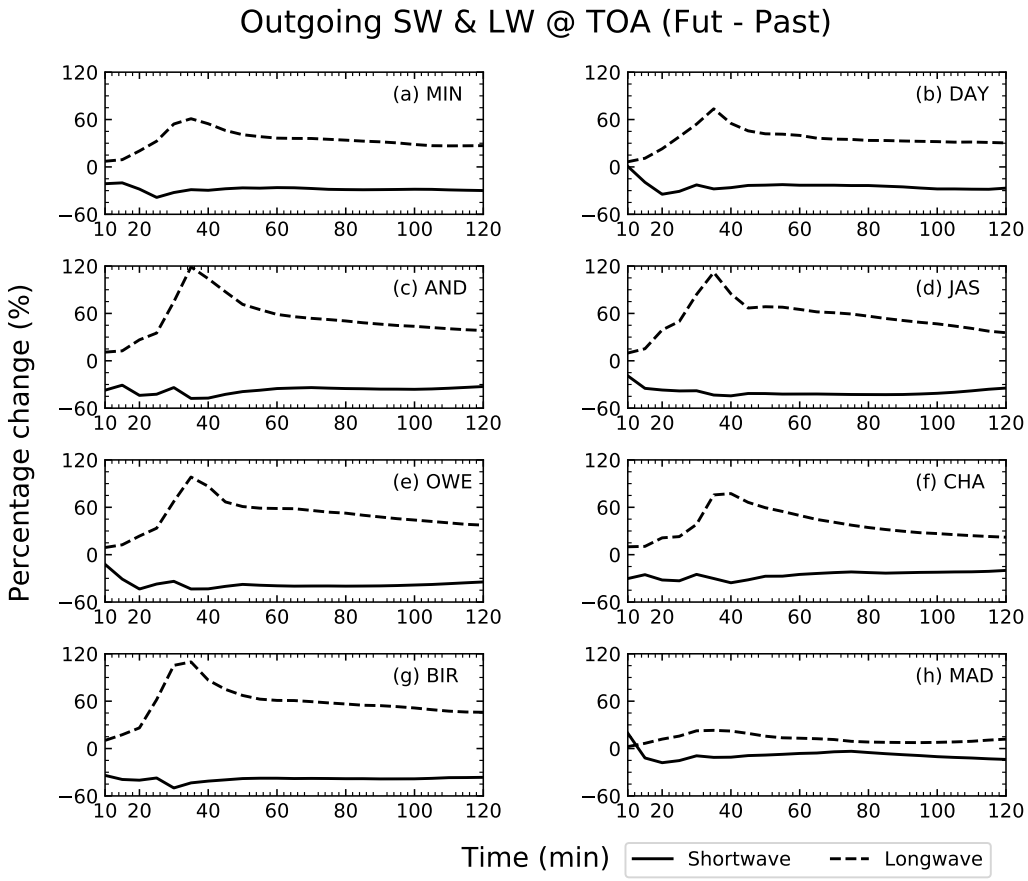

Figure 6.5: Percentage change between the shortwave and longwave radiation at the top of the atmosphere (Future - Past) for the main clouds.

Table 6.1: The radiative forcing at the top of the atmosphere (W m^{-2}) in the past and future environments for all locations.

Locations	**Radiative forcing (W m^{-2})**
MIN	51.9
DAY	33.6
AND	57.1
JAS	53.2
OWE	54.9
CHA	35.5
BIR	54.7
MAD	8.8
Average	43.7

6.3.2.2 Outgoing shortwave and longwave radiation at the TOA for anvil clouds

Figures 6.6 and 6.7 shows the time-series profiles of outgoing SW and LW radiation at the TOA for anvil clouds, respectively. Similar to Figures 6.4 and 6.5, the amount of outgoing SW radiation is greater in the past than in the future, while the amount of outgoing LW radiation is greater in the future than that in the past. The trends of outgoing SW radiation for both anvils in the past and future climates in Figure 6.6 were similar. The trends began with an increasing trend up until 30 – 35 min (40 – 55 min) in the past (future), indicating the growing stage of clouds, and then began to decrease towards asymptotes until the end of the simulations. On the other hand, the trends of outgoing LW radiation for both anvils in the past and future environments were similar, except that the trends in the future were smoother than that in the past. Both profiles show a decreasing trend from the beginning until approximately 30 – 40 min (40 – 60 min) in the past (future). Note that the time difference between the clouds in the past and future environments is due to the earlier initiation of ice phase in the past and delayed initiation of ice in the future, as discussed in **Chapter 4**. Thereafter, both trends increased and reached asymptotes until the end of the simulations. The asymptotes indicate that the clouds have either stopped growing or have dissipated, hence maintaining a constant radiative flux. It is interesting to note that the past profiles have defined troughs compared to the future profiles. This shows that the well-developed clouds in the past exhibit large spatial extent that greatly influence the SW and LW fluxes.

Finally, Figure 6.8 shows the percentage change for both outgoing SW and LW at the TOA relative to the future climates. The figure shows a reduction of up to 50% in the outgoing SW radiation, and an increase of up to 120% in the outgoing LW radiation in the future, as compared to that in the past. Table 6.2 presents the radiative forcing (RF) between the past and future environments. As in Table 6.1 in **Section 6.3.2.1**, the RF is greater than zero in all locations, with an average warming of 54.7 W m^{-2} in the future, which is due to the reduction in the anvil cloud cover as was found for the whole cloud.

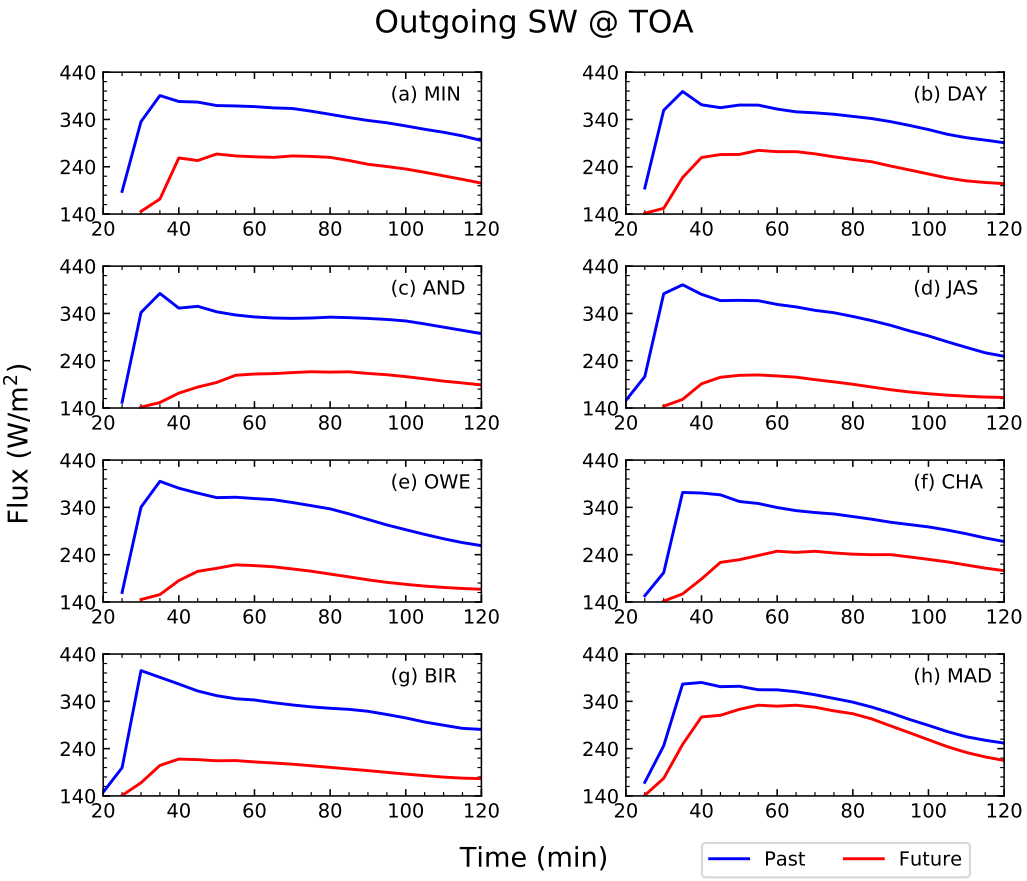

Figure 6.6: Outgoing shortwave radiation at the top of the atmosphere for the anvil clouds between the past and future environments.

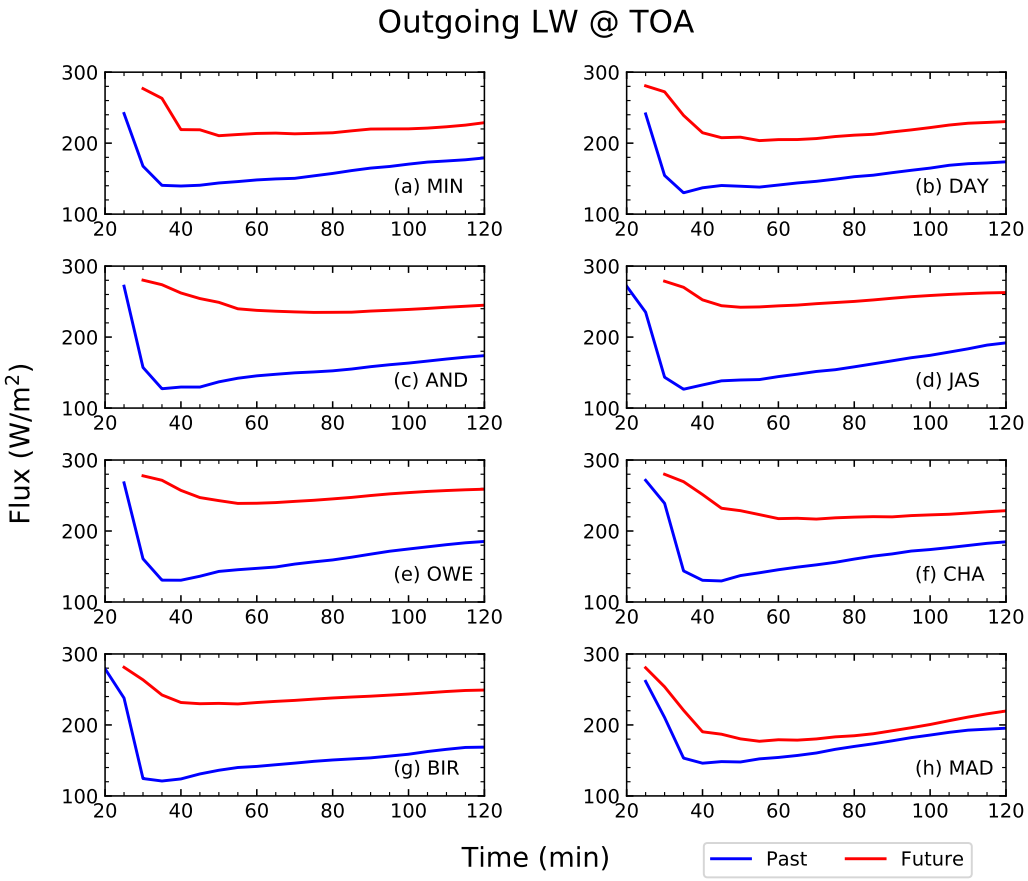

Figure 6.7: Outgoing longwave radiation at the top of the atmosphere for the anvil clouds between the past and future environments.

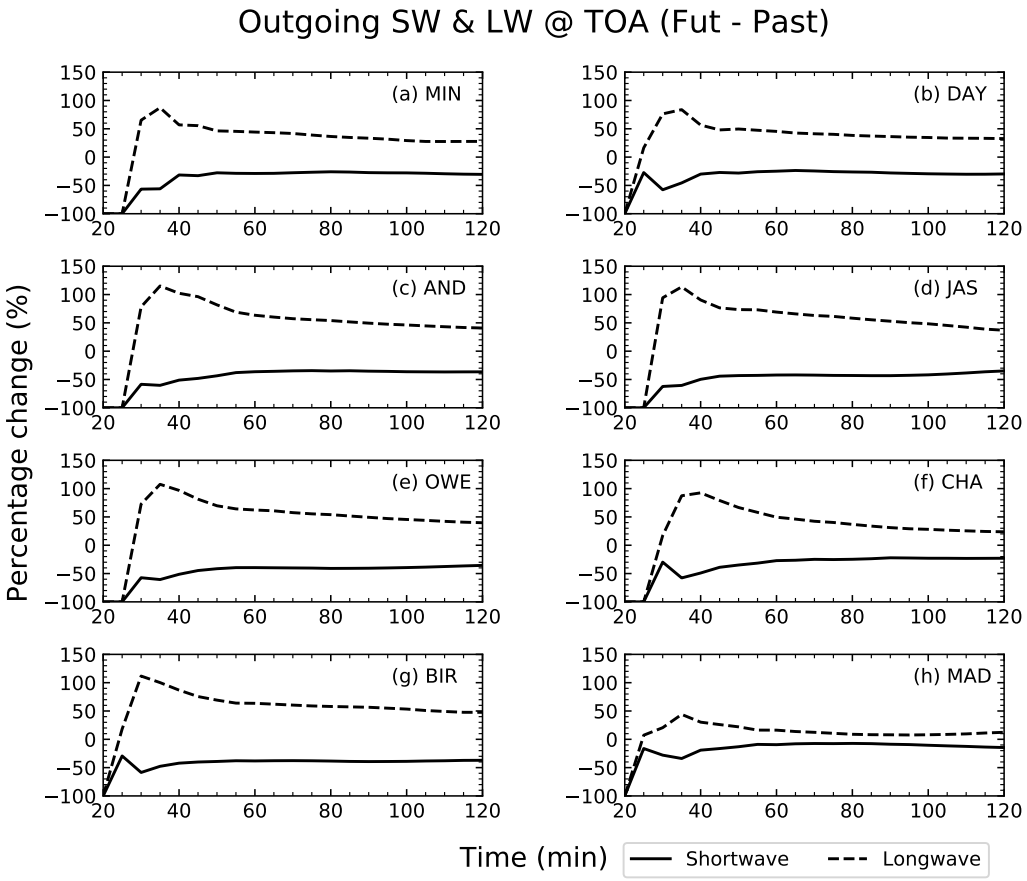

Figure 6.8: Percentage change between the shortwave and longwave radiation at the top of the atmosphere (Future - Past) for the anvil clouds.

Table 6.2: The radiative forcing at the top of the atmosphere (W m^{-2}) in the past and future environments for all locations.

Locations	**Radiative forcing (W m^{-2})**
MIN	63.9
DAY	36.1
AND	60.5
JAS	87.5
OWE	67.7
CHA	47.1
BIR	58.7
MAD	16.0
Average	54.7

6.3.3 Cloud radiative effects at the surface

This section presents the results for downward and upward SW and LW radiation at the surface, for the main clouds (**Sections 6.3.3.1** and **6.3.3.2**) and the anvil clouds (**Sections 6.3.3.3** and **6.3.3.4**). The downward SW radiation at the surface refers to how much SW radiation gets through the clouds and reaches the surface. Subsequently, the amount of SW radiation that gets reflected from the surface is termed as the upward SW radiation, which is set at 20% or 0.2 surface albedo. On the other hand, the downward LW radiation refers to the emission of LW radiation from the clouds to the surface, while the upward LW radiation refers to the emission of LW radiation from the surface.

6.3.3.1 Downward and upward shortwave radiation at the surface for the main clouds

Figures 6.9 and 6.10 show the time-series profiles of the downward and upward SW radiation at the surface, respectively. In general, all figures show that the amount of SW radiation was greater in the future than that in the past. From Figure 6.9, most profiles show a decreasing trend in the first 20 minutes of the simulation. The trend then increased for about 5 – 10 min before it decreased again at 30 min, and thereafter slowly increased towards asymptotes. These trends correspond to the growth of clouds at the early stage thus effectively reflects SW radiation from coming through, followed by rainfall that allows SW radiation to come through the clouds, and finally the clouds' mature stage in which the clouds begin to dissipate thus allowing for more SW radiation to be transmitted to the surface. As the SW radiation gets transmitted to the surface, 20% of it is reflected back due to the surface albedo of 0.2. Therefore, the trend in Figure 6.10 is similar to that in Figure 6.9, only that the amount is reduced by 20%.

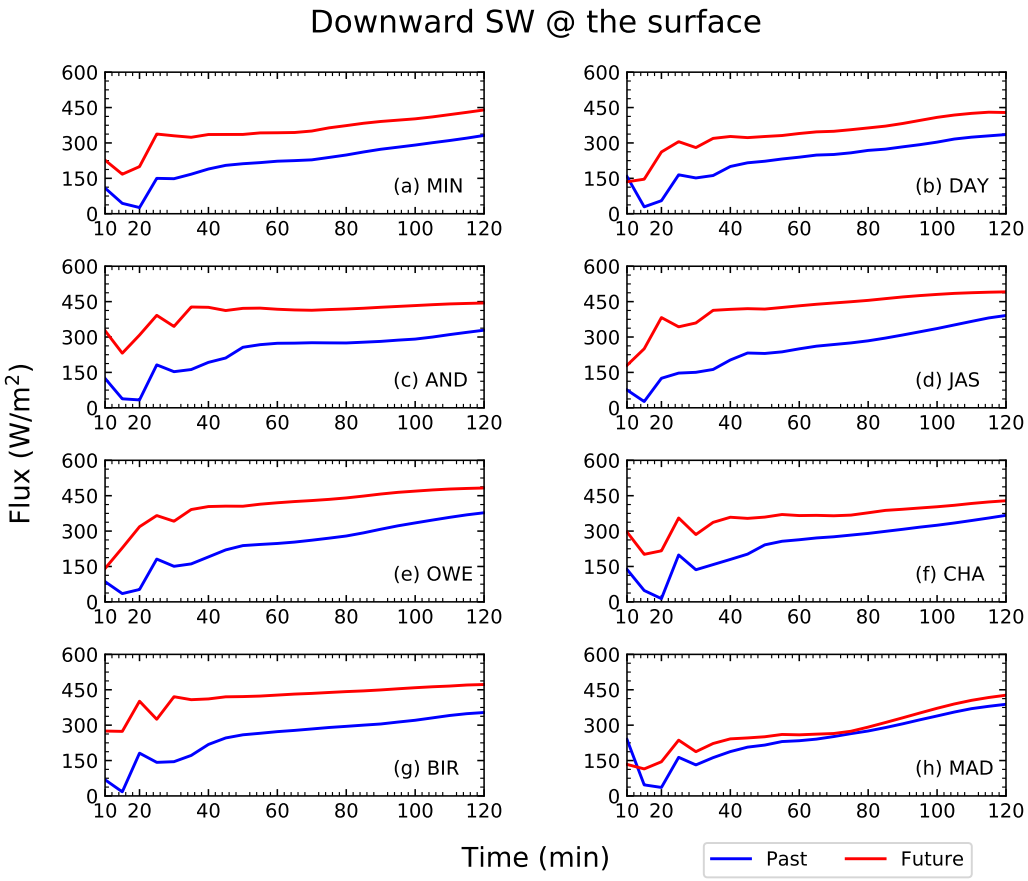

Figure 6.9: The downward shortwave radiation at the surface for the main clouds between the past and future environments.

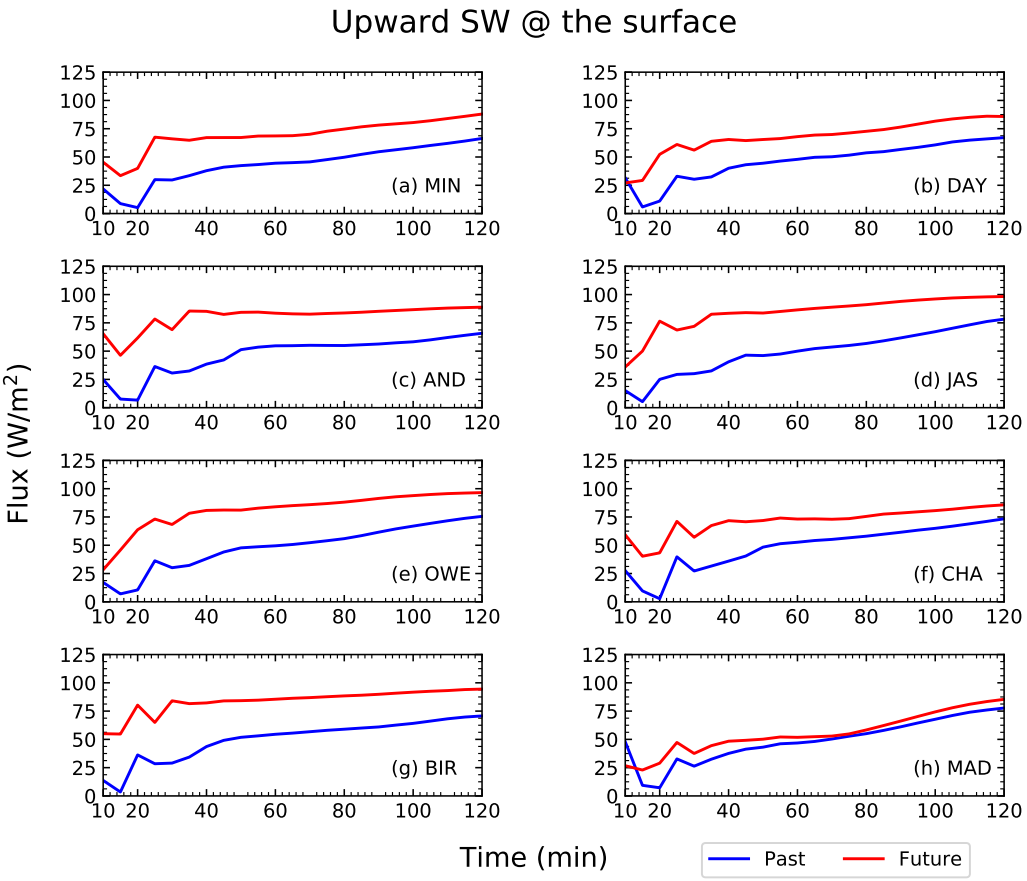

Figure 6.10: The upward shortwave radiation at the surface for the main clouds between the past and future environments.

6.3.3.2 Downward and upward longwave radiation at the surface for the main clouds

Figures 6.11 and 6.12 show the downward and upward LW radiation at the surface, respectively. Both figures show that the downward and upward LW radiation at the surface are greater in the future than in the past due to the warmer temperature in the future than in the past. In Figure 6.11, some fluctuations were seen in the first 40 min. The fluctuations consist of two dips around 20 - 25 min and at 35 min. These dips were likely to be due to changes in the cloud cover where an increase in cloud cover due to initiation of ice phase increases the number of grid cells, and a decrease in the cloud cover due to rainfall reduces the number of grid cells, both of which contributed to the reduced downward LW radiation at the surface. Thereafter, the clouds start to dissipate thus the trends remained at the end of the simulation. On the other hand, in Figure 6.12, the upward LW radiation at the surface in both past and future environments remain constant throughout the simulation because it is dependent on the surface temperature which is kept fairly constant in the model.

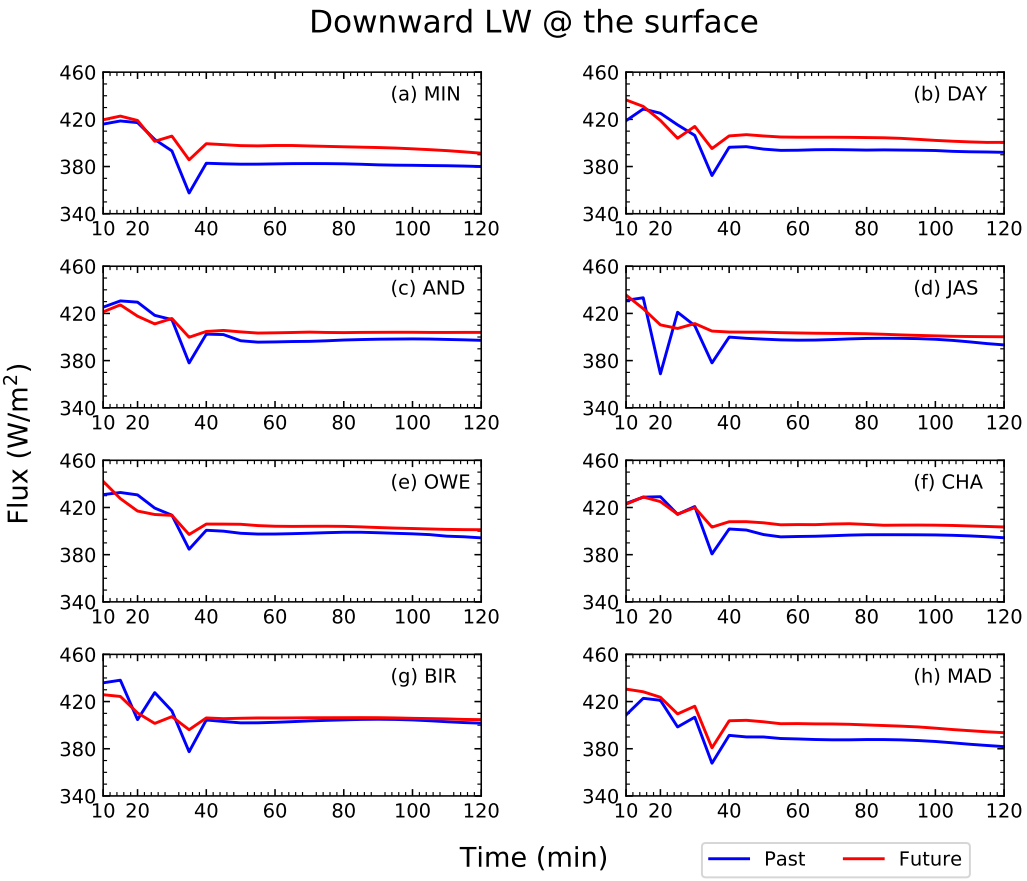

Figure 6.11: The downward longwave radiation at the surface for the main clouds between the past and future environments.

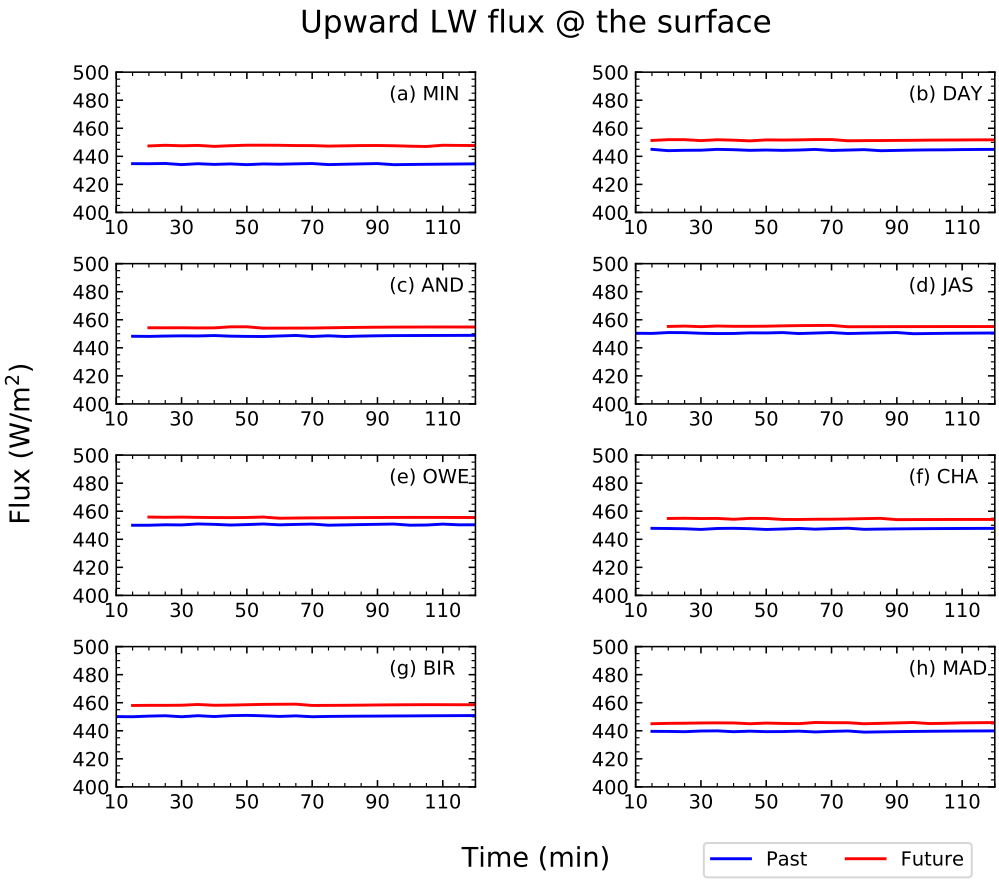

Figure 6.12: The upward longwave radiation at the surface for the main clouds between the past and future environments.

6.3.3.3 Downward and upward shortwave radiation at the surface for anvil clouds

The time-series profiles of downward and upward SW radiation at the surface are depicted in Figures 6.13 and 6.14, respectively. In all of the profiles, the amount of downward SW radiation between the past and future was similar to begin with, that is about 470 – 520 W m^{-2}. However, decreasing trends followed in both past and future profiles and are seen in the first 30 – 35 min (35 - 40 min) in the past (future). This decrease indicates that both clouds are developing vertically, and as they develop, the incoming SW radiation is reflected at the cloud-top thus reducing the SW radiation reaching the surface. It is noted that the amount of SW radiation reaching the surface is greater in the future than in the past environment. This is because of the weaker cloud development (e.g. weak updraught that limits the cloud vertical motion hence resulting in lower cloud-top heights) in the future than in the past environment. It is also noted that the decrease in the amount of SW radiation reaching the surface was greater in the past than that in the future, especially seen in the obvious dip at around 30 – 35 min in the past compared to the subtler dip in the future around 40 – 45 min. The amount of SW radiation reaching the surface reduced approximately 260 – 320 W m^{-2} in the past, and about 70 – 120 W m^{-2} in the future. This again shows that the cloud properties and development in the past environment pose significant influence on the radiative fluxes. The defined dip seen in the past environment indicates a strong reflection of SW radiation due to the strong ice phase (i.e. optically thick and spatially wide), thus resulting in less SW radiation reaching the surface. In the future environment, the dip is subtler due to the less significant growth of clouds, in terms of both the cloud vertical and spatial extent. After this time, the trends slowly increased toward asymptotes until the end of the simulation time, indicating that the clouds have dissipated, hence more SW radiation reaches the surface and reflected by the surface.

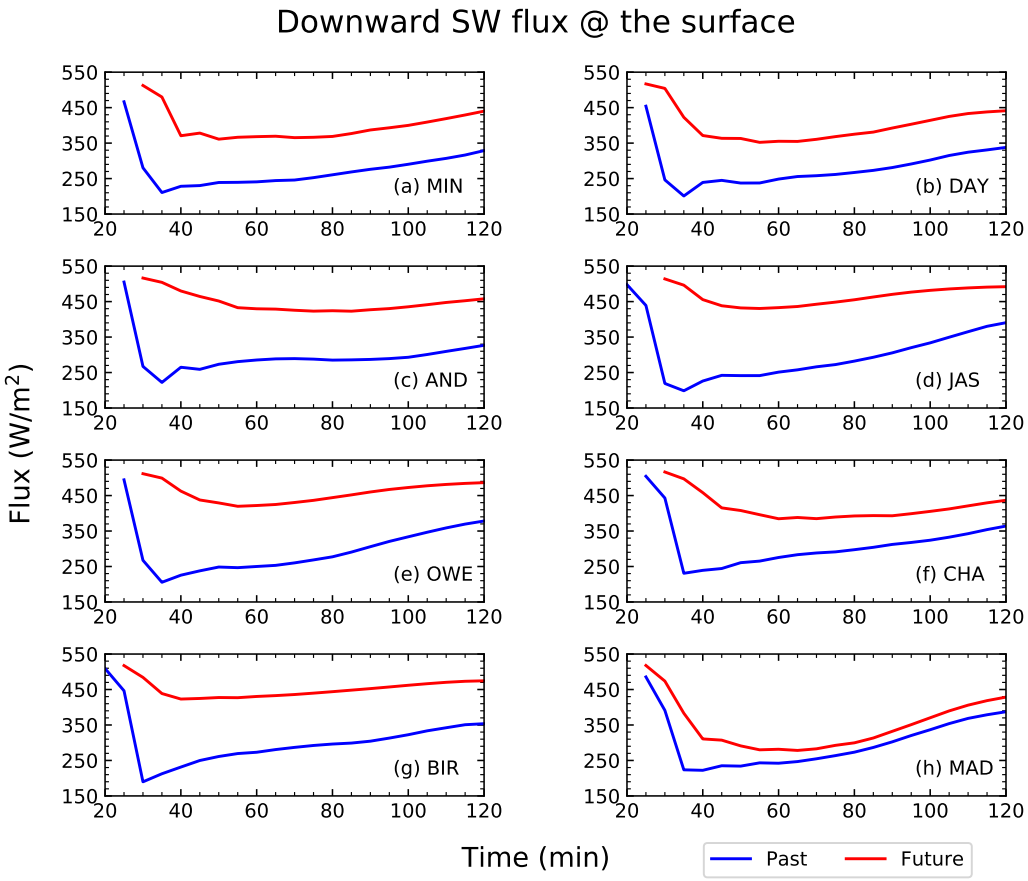

Figure 6.13: The downward shortwave radiation at the surface for the anvil clouds between the past and future environments.

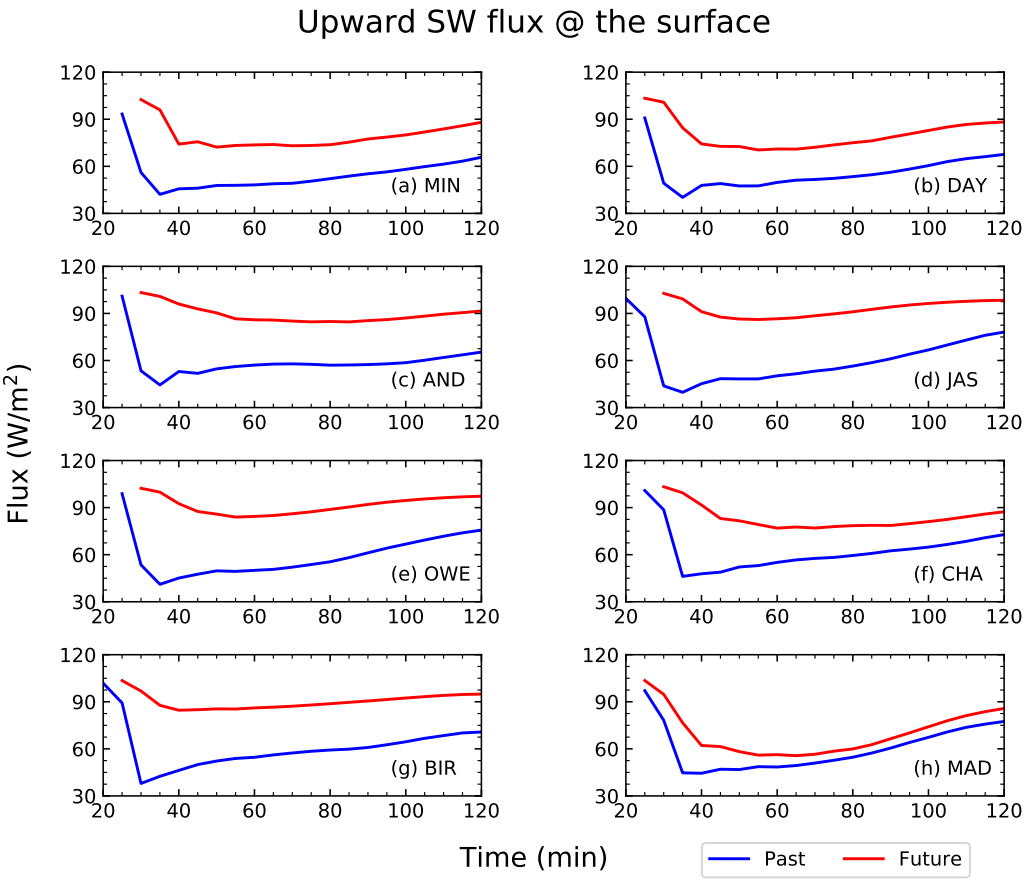

Figure 6.14: The upward shortwave radiation at the surface for the anvil clouds between the past and future environments.

6.3.3.4 Downward and upward longwave radiation at the surface for anvil clouds

Figures 6.15 and 6.16 depict the downward and upward LW radiation at the surface, respectively. Overall, as in other LW radiative flux profiles, the future recorded greater amount of downward and upward LW radiation than the past due to the greater temperature in the future. The amount of downward LW radiation in the future remained fairly constant between 395 – 405 W m^{-2} throughout the simulation time. In contrast, there are some initial fluctuations in the amount of downward LW radiation in the past. At the time of anvil formation, the amount of downward LW radiation began with 370 – 390 W m^{-2} and continued increasing for 5 – 10 min, reaching a peak of 370 – 408 W m^{-2} at 30 – 35 min. After that, when the anvils develop more and reach higher heights, the amount of downward LW radiation decreased to about 375 – 405 W m^{-2} at 40 min. This decrease is due to the cold temperature of the anvil clouds that reduces the emission of downward LW radiation. Thereafter, the amount of downward LW radiation remain fairly constant towards the end of the simulations.

As for the upward LW radiation at the surface in Figure 6.16, most of the profiles in the future show constant upward LW radiation of approximately 456 W m^{-2}, except for the profiles in MIN and MAD. These profiles have a decreasing trend starting from 454 W m^{-2} in the beginning to 448 W m^{-2} at 40 min, and thereafter remained fairly constant. In the past, the upward LW radiation in all profiles were also fairly constant at 435 – 460 W m^{-2} throughout the simulations, with a slight dip of about 2 – 4 W m^{-2} around 35 – 40 min.

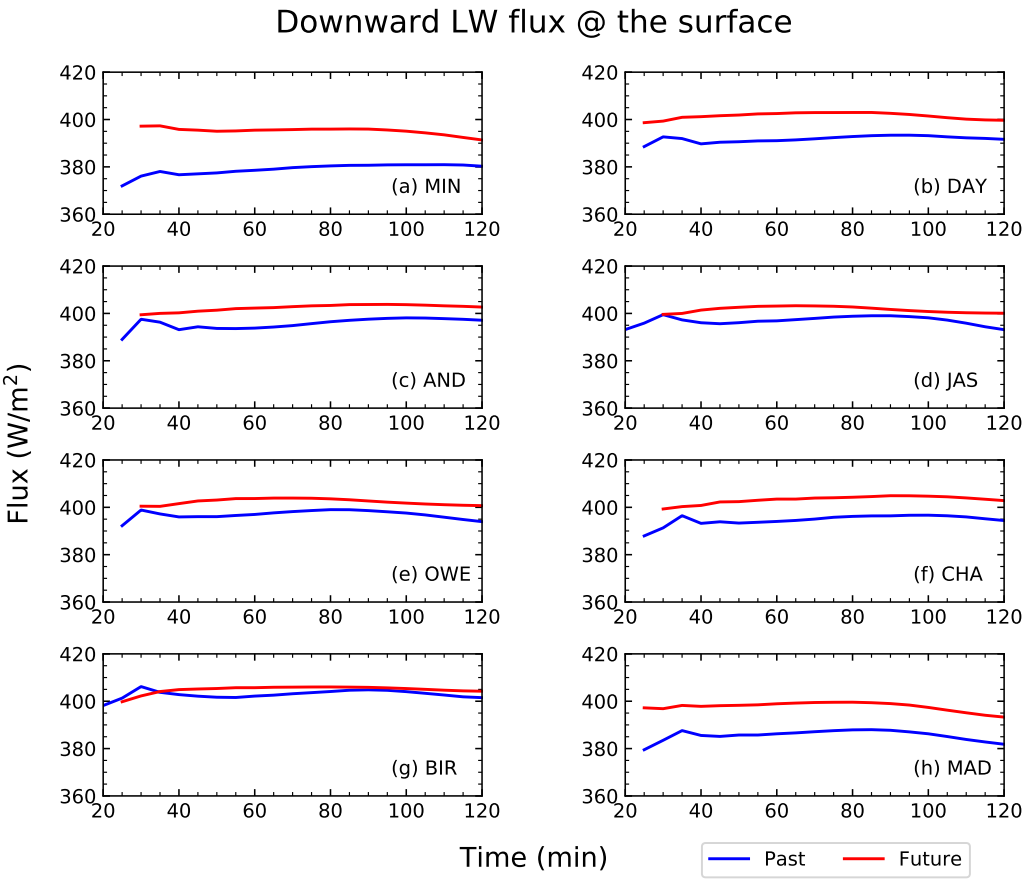

Figure 6.15: The downward longwave radiation at the surface for the anvil clouds between the past and future environments.

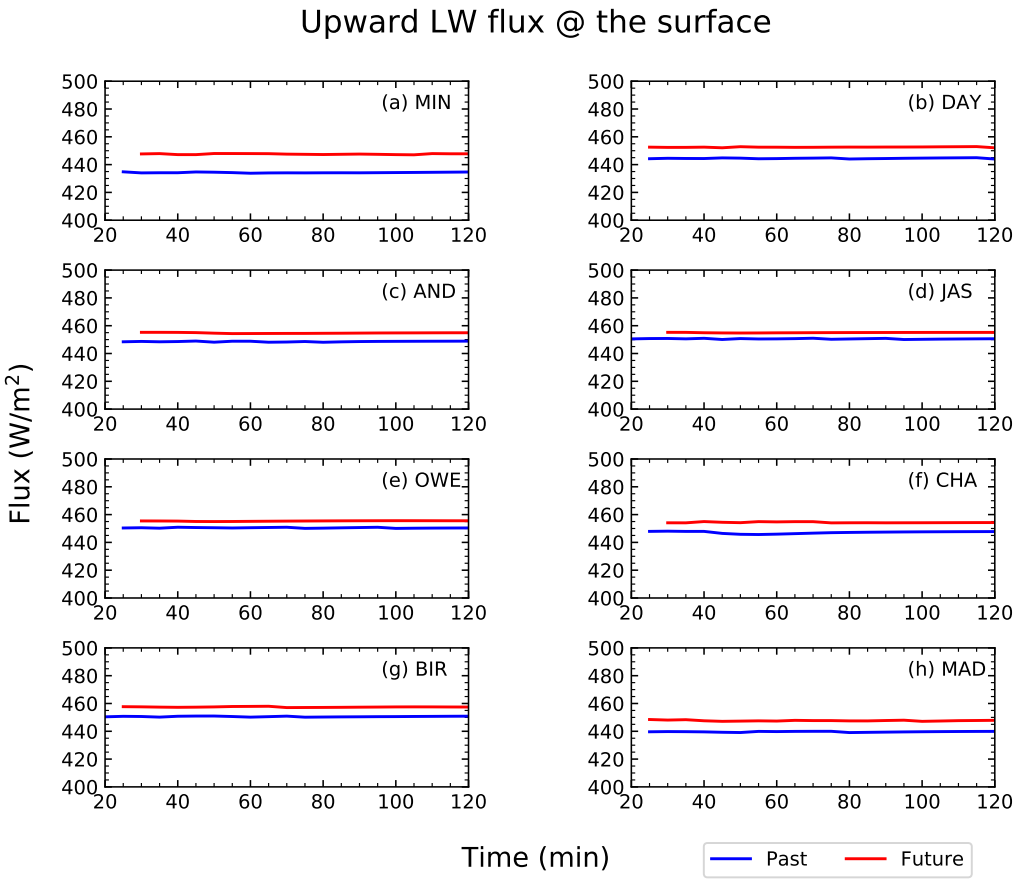

Figure 6.16: The upward longwave radiation at the surface for the anvil clouds between the past and future environments.

6.4 Discussion and summary

The results presented in **Section 6.3** follows from the results presented in **Chapter 4**. The greater outgoing SW radiation in the past relative to the future (Figure 6.3) is primarily due to the more developed convection and greater anvils in the past than that in the future. The greater nucleation rate at the beginning of cloud formation in the past produces numerous, small droplets than that in the future. The high nucleation rate is associated with great release of latent heat that boost the cloud updraught that transports these cloud droplets past the freezing levels. This results in the earlier initiation of ice phase that produces even more ice particles as well as detrainment of condensates that cover a wider spatial extent as seen in the greater cloud fraction in the past. The high amount of condensates and the high vertical extent of the clouds in the past contribute to the optical thickness of the clouds which effectively reflected the SW radiation in addition to the high cloud fraction. Due to more SW radiation being reflected at the top of the atmosphere, a reduced radiation is thus reaching the surface, thus explaining the lower amount of downward SW radiation at the surface (Figures 6.9 and 6.13) in the past. Subsequently, the upward SW radiation from the surface (Figures 6.10 and 6.14) is also lower than that in the future, given the same surface albedo of 0.2 in the past and future environments.

Clouds always reduce the outgoing LW radiation to space. They trap LW radiation emitted at higher temperatures from lower in the atmosphere and reemit the radiation with reduced magnitude due to these lower cloud-top temperatures, thus reducing the LW radiative flux out to space. Therefore, in terms of the interaction between clouds and LW radiation, the presence of clouds always warms the earth. Figures 6.4 and 6.7 show that the outgoing LW radiation at the TOA is greater in the future than in the past. This is, first and foremost, due to the warmer temperature in the future than in the past. Secondly, it is due to the weaker cloud development in the future that results in lower cloud-top height. The lower cloud-top height is associated with warmer cloud-top temperature. Since the amount of radiative emission is proportional to T^4 according to the Stefan-Boltzmann law, clouds with warmer temperature emit more radiation than those with lower temperature. Thus, the LW radiation emitted by the clouds both at the top of the

atmosphere and at the surface is greater in the future than in the past.

To sum up, the study found that the reduction in the cloud fraction of both the whole cloud and the anvil cloud in the future environment resulted in radiative forcing that is greater than zero (refer Tables 6.1 and 6.2), and this indicates warming in the future. Tables 6.1 and 6.2 show an increased warming in the future of about 43.7 and 54.7 W m^{-2} in the whole cloud and anvil cloud, respectively. If we perform a very simplistic approximation of the cloud radiative forcing over midlatitude land areas with a 3% coverage of deep convective clouds, we would obtain an estimate of +1.31 W m^{-2} warming in the future, given the the structural changes predicted by the CCSM3 model is observed in the real future climate. If we further extend this estimation to the global coverage of deep convective cloud of say less than 1% percent, we would then get an estimate of +0.44 W m^{-2} warming in the future. This is opposite to the radiative forcing from the cloud-aerosol interaction estimated at -0.55 W m^{-2} for the period 1980-2011 (Myhre *et al.*, 2013), which suggests a cooling of the climate due to the indirect effects of aerosol on cloud properties. Therefore, if structural changes of the thermodynamic environment are expected in the future, then it is important that climate modelling groups pay particular attention to the way their models forecast future climate thermodynamic structure both in temperature and moisture. The finding in this study, particularly on the spatial extent of anvils is similar with recent modelling studies that found a strong decrease in the high cloud fraction with increasing surface temperatures (e.g. Mauritsen and Stevens, 2015; Bony *et al.*, 2016). These studies put forth different conjectures to the mechanisms (e.g. adaptive iris effect and fixed-anvil temperature hypothesis) that contribute to the shrinkage in high cloud cover. This thesis, on the other hand, provides an explanation to the reduced cloud amount and the subsequent reduction in the net cooling cloud radiative effect in a future, warmer climate from the perspective of cloud microphysical processes that results from the thermodynamic differences between the past and future environments.

Chapter 7

Discussion and Conclusions

7.1 Introduction

This chapter provides a summary for the overall discussion and conclusions of the thesis in **Section 7.2**, as well as the study limitations and recommendations for future work in **Section 7.3**.

7.2 Overall discussion and conclusions

This thesis sets out to understand the differences that changed thermodynamic structure has on deep convective clouds. The work focused on mainland United States (US) at several locations in the Midwest and Southeast region of the US, and explore how structural changes brought about climate change will impact the development of deep convective clouds. Much work has been done on factors such as aerosol effects but much less has been done on assessing the effects of thermodynamic environments on the cloud development. It is commonly known that temperatures will be warmer in the future climate and this will allow more moisture to be contained in the vapour phase in the atmosphere. However, we can also expect changes to the thermodynamic structure of the atmosphere in the future. The changes in the thermodynamic structure as well as in the amount of moisture need to be understood and the impacts on the development of deep convective clouds need to be explored. The development of deep convective clouds is chosen and emphasised in this thesis due to their substantial role in regulating the earth's

water and energy budget as presented in **Chapter 2**.

One of the main questions of the work in this thesis was to determine how deep convective clouds behave in a warmer climate. This question is explored by investigating the way in which the future climate will change the thermodynamic structure of the atmosphere, and understand how the changes brought about by a changed thermodynamic environment affect the macroscopic features (i.e. warm-phase cloud depths, cold-phase cloud depths, cloud cover, anvil extent, etc.) of deep convective clouds relative to our current climate. The investigation also includes the aim to understand the microphysical changes in the clouds that give rise to the macroscopic changes. This include temperature and moisture changes that give rise to changes in cloud buoyancy, updraught speeds, rates of nucleation, warm rain process and cold rain process. Finally, the work in this thesis aims to assess the consequential impact on the radiative properties that result from the changes in the cloud development to warming. The above mentioned aims are achieved by performing idealised simulations of deep convective clouds using atmospheric profiles derived from a global climate model. First of all, simulations of deep convective clouds were performed for the past (current) and future climate to assess the differences in the cloud development between the past and future climates. The results from this simulations are presented and discussed in **Chapter 4**. In **Chapter 5**, four sets of experiments were performed to investigate the factors associated with changes in the thermodynamic conditions that were causing the changes in the cloud development. Lastly, **Chapter 6** assesses the implications on the cloud radiative properties that results from the changes in cloud development. In the following paragraphs, the results from the study of this thesis is are summarised.

In **Chapter 4**, it was found that the deep convective clouds developed differently between the past and future environments. On average, the future environment exhibited an average cloud base height that was 32% lower and freezing level that was 8.5% higher in the future than in the past environment. This gave rise to an average of 14.5% increase in the warm-phase cloud depth of the future environment than the past environment. On the other hand, the average cloud-top height in the future environment was 9% lower than the past environment, thus resulting in

average cold-phase cloud depth that is 18% shallower than the past environment. The most significant changes in the results were the warm-phase and cold-phase clouds depths. These depths provide insights into the precipitation-forming processes, i.e. warm rain process and cold rain process, in deep convective clouds. Traditionally, cold rain process is known to play the more dominant role in deep convective clouds. In this study, we found that warm rain process can play the more dominant role especially in the future climate. From the results in this study, the past environment was found to be favourable for stronger convection than the future environment. The clouds in the past environment are characterised as having shallow warm-phase cloud depths and deep cold-phase cloud depths in contrast to the clouds in the future environment with deep warm-phase cloud depths and shallow cold-phase cloud depths. This translates into the clouds in the past as having a less active warm rain process but a strong cold rain process, while the modelled future clouds have a more active warm rain process and weak cold rain process. Consequently, this results in less intense but prolonged rainfall in the past environment, and more intense but shortened period of rainfall in the future environment. To explore these results, this thesis focused in on the differences in the cloud microphysical properties resulted from the thermodynamic differences between the past and future environment so as to achieve the third aim of this thesis. The future thermodynamic environment predicted by the CCSM3 global climate model shows significant changes from the thermodynamic environment in the past. The changes include an overall warmer troposphere which results in the higher freezing level in the future than in the past environment. In addition, the boundary layer is lower in the future than in the past environment. It is noted that the previous versions of this global climate model has a shallow bias in the boundary layer depth, however, in the version used in this thesis, the bias is substantially reduced (Collins *et al.*, 2006). Nonetheless, a dry bias is still present in the profiles used in this thesis, but has been corrected by Villanueva-Birriel (2014) using the reanalysis data as mentioned in **Section 3.2.2**. Other plausible reasons for the shallow boundary layer could be due to the interactions between the enhanced land-sea near-surface temperature contrast and the advection of maritime air over land (Rowell, 2009) as mentioned in **Section 4.2.3**. Assuming this mechanism takes place in the future thermodynamic environment predicted by CCSM3, we see that the specific humidity throughout the atmosphere is higher in the future

than in the past, subsequently contributes to greater convective available potential energy (CAPE) throughout the atmosphere in the future than in the past. In terms of relative humidity, the boundary layer is more saturated in the future than in the past, however, the mid-layer is less saturated in the future than in the past. It was found that this is one of the first key points that led to the differences in the cloud macro- and microphysical properties between the clouds in the past and future environment. The higher saturation and the greater CAPE at the boundary layer in the future results in clouds forming at lower altitudes than in the past. However, as the clouds in the future develop vertically, they were in less saturated conditions in the mid-layer in the future environment. This reduces the cloud nucleation rate in the future which limits the number concentration of cloud droplets, thus producing droplets that were larger in size. In contrast, as the clouds in the past develop vertically, they were in highly saturated condition due to the high saturation at the mid-layer in the past environment. This enhances cloud nucleation which produces numerous and small cloud droplets. In addition, the higher nucleation rate releases more latent heat that enhances the cloud updraught speed than in the future. The consequences from the number and size of cloud droplets on the subsequent microphysical properties are further amplified by the warm-phase cloud depths and updraught strength associated with the cloud nucleation rate as discussed next.

The updraught speed and warm-phase cloud depths provide distinct production of rain between the past and future environments. It was found that the average rain mass mixing ratio during the peak production was 42% higher in the future than in the past environment. In the following, we will see how the updraught speed and warm-phase cloud depths result in this distinct differences in the rain mixing ratio between the two environments. The weak updraught and deep warm-phase cloud depth in the future results increases the time residence for cloud droplets to grow to even larger sizes. The presence of large cloud droplets promotes an efficient collision-coalescence process in the formation of rain, consequently producing large rain drops that fall out before they are lofted to the freezing level because they could not be sustained by the weak cloud updraught. This results in heavy rainfall that removes a large amount of water hence impacting the availability of water that could have been used for ice processes. As a result, the rainfall period is shortened.

On the contrary, in addition to the numerous small cloud droplets formed from the enhanced nucleation, the strong updraught and shallow warm-phase cloud depth in the past environment shorten the time residence for growth of cloud droplets and rain via collision-coalescence process. Instead, the cloud droplets are lofted above the freezing level due to the small droplet size, strong updraught and low freezing level. This leads to an early initiation of ice processes that further boosts the cloud updraught from the release of latent heat of freezing, thus further moderates both the time residence and fall out of condensates within the cloud, leading to a less intense but prolonged rainfall.

Since the future environment brings about various changes such as structural changes of the potential temperature and relative humidity profiles, mean temperature changes and moisture content changes, the next aim was to unravel the relative importance of each of these factors. The result from this investigation was presented in **Chapter 5** and is summarised as follows. In **Chapter 5**, a set of three idealised deep convective cloud simulations were performed for three different thermodynamic conditions. In these three thermodynamic conditions, the mean temperature increase from the future warming climate was eliminated so as to test the two factors that are believed to cause the differences in the cloud development. These two factors are the temperature structure and relative humidity structure.

To begin with, the first test (Experiment 1) assessed if the temperature structure and relative humidity structure of the future environment would still produce the same cloud development as that in **Chapter 4** in the absence of the mean climate warming. This is to identify if the mean decrease in temperature still produces the changes in cloud development that were due to the temperature structure and relative humidity structure of the future environment. The results from Experiment 1 shows that reducing the mean temperature but keeping the structures of temperature and relative humidity resulted in an average warm-phase cloud depth that is 400 m deeper than in the past environment. This led to an increase in the rain mixing ratio by a factor of 10 than in the past environment, leading to an intense initial rainfall that removes a large mass of rain water that is otherwise available for ice processes. As a result, the average cloud-top height and cold-phase

cloud depth in the altered environment were a couple of kilometre lower than in the past environment. In addition, the findings from Experiment 1 also produced similar cloud development as that in **Chapter 4**, albeit in a smaller magnitude. In comparison to **Chapter 4**, the average changes in the warm-phase cloud depth, cloud-top height and cold-phase cloud depth were 35%, 40% and 30% lower in Experiment 1 than those found in **Chapter 4**. In short, the temperature structure and relative humidity substantially influences the cloud development, with or without the mean increase in warming that climate change brings.

Thereafter, we begin to isolate these two factors in order to investigate what effects each factor have on the cloud development. The isolation of temperature structure from relative humidity refers to Experiment 2, while the isolation of relative humidity structure from the temperature structure refers to Experiment 3 as specified in Tables 5.1 and 5.2, **Chapter 5**. The findings from Experiment 2 suggests that the temperature structure of the future environment has a huge effect on the cloud development, particularly on the cold-phase cloud properties. The results from Experiment 2 showed increased convective inhibition energy (CIN) and decreased convective available potential energy (CAPE) in the altered environment, thus weakening the cloud development. This is seen in the average vertical velocity that was 75% weaker and average total water content that was 80% lower in the altered environment than in the past environment. Ultimately, this led to less-developed clouds in the altered environment especially seen in the huge reduction in the average cloud-top height and cold-phase cloud depth by 8 km from the past environments. Therefore, this illustrates that e temperature structure substantially influence the vertical extent of clouds.

On the other hand, Experiment 3, which isolates the relative humidity structure from the temperature structure, in order to see the effects of relative humidity on the cloud development, yields the most dramatic result on the cold-phase cloud properties. The modelling results show that the relative humidity structure of the future environment provides for a conducive and favourable environment for cloud development, mainly due to the high saturation in the boundary layer that promotes for increased cloud nucleation which invigorates the ice processes in the clouds hence making the convection stronger. This is seen in the maximum ver-

tical velocity that was on average 30% greater than the past environment, and an average increase of 70% in the total water content than the past environment. The ice processes were seen to be stronger in the altered environment in that the solid hydrometeor mixing ratio was an order of magnitude higher than in the past environment, resulting in the average increase of 1.8 km in the cloud-top height and cold-phase cloud depths of the altered environment.

In the next experiment, i.e. Experiment 4, a comparison was made between non-warmed and warmed future environments. This is to test what effects the water-holding capacity of the environmental temperature have on the two environments. It was found that the effects on the cloud development between the two environments were minimal, except in the maximum vertical velocity and intensity of precipitation, i.e. the initial rain rate. The maximum vertical velocity in the altered future environment were only slightly lower than the unaltered future environment, while the average initial rain rate in the altered future environment was found to be 10% higher than the unaltered future environment. However, the average rain mixing ratio between the two environments remained similar. Therefore, it is suggested that the rate of rain formation was similar between the two environments and so the differences in the initial rain rate was mainly due to the smaller vertical distribution of the rain particles due to the lower updraught speed in the altered future environment. As a result, when rain starts to fall, the rain particles in the altered environment falls over a smaller vertical distance than in the unaltered environment, thus adding to the 10% increase in the rain rate, and a faster removal of rain water. Consequently, this limits the availability of water for ice processes, thus resulting in the average decrease of cloud-top height and cold-phase cloud depth by 740 m and 625 m, respectively, from the unaltered future environment. Therefore, the non-warmed altered environment is found to substantially affect the cold-phase cloud properties. However, a caveat in this experiment is that it was tested for the future environments and not for the past environments. It would be ideal to have it tested for the past environments and is therefore recommended for future studies.

In summary, this study found that the thermodynamic structure changes has a greater influence on the cloud development than changes in the mean temperature.

The thermodynamic structures assessed in this study are the potential temperature (or temperature) and relative humidity structures. The study isolated and assessed each structure and found that each produces large differences in the cloud development when compared to the cloud development in the past environment. The temperature structure effect seen from Experiment 2 results significantly reduces the average cloud vertical extent by 8km, along with an average reduction of 80% and 75% in the the total water content and maximum vertical velocity, respectively. On the other hand, the relative humidity structure effect seen from Experiment 3 results significantly increases the average maximum vertical velocity by 30% and the total water content by 70%. In particular, the production of solid hydrometeors increased by an order of magnitude which subsequently increases the cloud-top height by an average of 1.8 km. When the temperature structure and relative humidity structure effects are added together (as they are in the future thermodynamic environment), the effects cancel out slightly but they still result in weaker cloud development than in the past environment.

In the remaining paragraphs, the differences in the cloud radiative properties between the deep convective clouds in the past and future environments are summarised. The enhanced warm rain process in the future environment results in intense heavy rainfall that removes a large amount of water that is otherwise available for the cold rain process. On the other hand, the enhanced cold rain process in the past environment results in less intense but prolonged rainfall. The dominance of either of the precipitation-forming process in the environments results in cloud macro-physical structure that influences the cloud radiative properties as explored and presented in **Chapter 6**. The intense heavy rainfall attributed to the strong warm rain process in the future environment reduces the amount of detrainment into the upper level of the atmosphere, hence generating small coverage of anvil extent, as well as the entire cloud fraction. In contrast, the enhanced cold rain process in the past environment increases the cloud fraction as well as the amount of detrainment into anvil canopy, thus generating large coverage of anvil cloud fraction. The finding in this study, particularly on the spatial extent of anvils is similar with recent modelling studies that found a strong decrease in the high cloud fraction with increasing surface temperatures (e.g. Mauritsen and Stevens, 2015; Bony *et al.*, 2016). These studies put forth different conjectures to the mechanisms

(e.g. adaptive iris effect and fixed-anvil temperature hypothesis) that contribute to the shrinkage in high cloud cover. This thesis, on the other hand, provides an explanation to the reduced cloud amount in a warmer climate from the perspective of cloud microphysical processes that results from the thermodynamic differences between the past and future environments. The differences in the spatial extent of both the whole cloud and anvil cloud lead to significant differences in the cloud radiative properties as presented in **Chapter 6**. Here, we highlight the cloud radiative forcing at the top of the atmosphere (TOA) for the whole cloud and the anvil clouds between the past and future environments.

The study from this thesis found that for both the whole cloud and the anvil cloud, the average cloud radiative forcing at the TOA are greater than zero, which indicates an increased warming in the future environment. The average radiative forcing for the whole cloud and anvil cloud are 43.7 and 54.7 W m^{-2}, respectively. The increased warming in the future is due to the reduction in cloud cover that allows for greater solar insolation that warms the atmosphere. If we perform a very simplistic approximation of the cloud radiative forcing over midlatitude land areas with a 3% coverage of deep convective clouds, we would obtain an estimate of +1.31 W m^{-2} warming in the future. If we further extend this estimation to the global coverage of deep convective cloud of say less than 1% percent, we would then get an estimate of +0.44 W m^{-2} warming in the future. This is opposite to the radiative forcing from the cloud-aerosol interaction estimated at -0.55 W m^{-2} for the period 1980-2011 (Myhre *et al.*, 2013), which suggests a cooling of the climate due to the indirect effects of aerosol on cloud properties. Given the structural changes in the future climate predicted by the CCSM3 global climate model, the results of this thesis observe a preponderance of warm rain microphysics over cold rain microphysics which leads to a weakened development of deep convective clouds and subsequently an increased warming of the atmosphere. It is therefore important that climate modelling groups pay particular attention to the way their models forecast future climate thermodynamic structure both in temperature and moisture.

7.3 Study limitations and recommendations for future work

The idealised simulations of deep convective clouds performed in this study is limited to using only vertical atmospheric profiles derived from NCAR CCSM 3 (National Center for Atmospheric Research Community Climate System Model 3) global climate model as used by Trapp *et al.* (2009). The use of dataset from one model as opposed to that obtained from model ensembles might introduce biases that may affect the resulting simulations. It is thus recommended to use profiles from model ensembles in a future study. Another limitation in this study is with regards to the use of cloud microphysical schemes. In this study, the Morrison two-moment bulk scheme was used for the simulations. It is recognised that different microphysical schemes have different representations on the cloud microphysical processes, thus it would be ideal to compare the cloud responses between multiple cloud microphysics schemes.

In addition, it is also recommended that the work undertaken in this thesis be extended to tropical regions. Possible future work could look to see if deep convection in tropical region is inhibited in the future as this would have an impact on the Hadley circulation. Recent studies as reviewed comprehensively by Ma *et al.* (2018) suggest that changes in atmospheric moisture and stratification slows down the tropical circulation, which leads to a weakening of the Hadley cell that expands the Hadley cell poleward, as well as a shift in the inter-tropical convergence zone. Given that the result obtained from this thesis, that is, increased atmospheric moisture and stability that arise from increased warming leads to a weaker convection, this would then give way for other processes to create changes to the Hadley cell. The Hadley cell is likely weaker and shallower in the vertical extent if the warming is spread out more laterally. Therefore, it is also suggested that future studies look at the convective population to see if convection is more localised or spread out in response to warming. This work is currently undertaken in the midlatitudes by Rasmussen *et al.* (2017), and thus can also be extended to the tropics.

References

Allan, R. P. 2011. Combining satellite data and models to estimate cloud radiative effect at the surface and in the atmosphere. *Meteorological applications*, **18** (3), 324–333.

Allan, R. P. and Soden, B. J. 2008. Atmospheric warming and the amplification of precipitation extremes. *Science*, **321** (5895), 1481–1484.

Allen, M. R. and Ingram, W. J. 2002. Constraints on future changes in climate and the hydrologic cycle. *Nature*, **419** (6903), 224.

Andreae, M. and Rosenfeld, D. 2008. Aerosol–cloud–precipitation interactions. Part 1. The nature and sources of cloud-active aerosols. *Earth-Science Reviews*, **89** (1-2), 13–41.

Arking, A. 1991. The radiative effects of clouds and their impact on climate. *Bulletin of the American Meteorological Society*, **72** (6), 795–814.

Baker, M. 1993. Variability in concentrations of cloud condensation nuclei in the marine cloud—topped boundary layer. *Tellus B: Chemical and Physical Meteorology*, **45** (5), 458–472.

Ban, N., Schmidli, J. and Schär, C. 2015. Heavy precipitation in a changing climate: Does short-term summer precipitation increase faster? *Geophysical Research Letters*, **42** (4), 1165–1172.

Beheng, K. 1994. A parameterization of warm cloud microphysical conversion processes. *Atmospheric Research*, **33** (1-4), 193–206.

Behrangi, A., Kubar, T. and Lambrigtsen, B. 2012. Phenomenological description of tropical clouds using CloudSat cloud classification. *Monthly Weather Review*, **140** (10), 3235–3249.

Bengtsson, L., Hodges, K. I. and Keenlyside, N. 2009. Will extratropical storms intensify in a warmer climate? *Journal of Climate*, **22** (9), 2276–2301.

Bennett, L. J., Browning, K. A., Blyth, A. M., Parker, D. J. and Clark, P. A. 2006. A review of the initiation of precipitating convection in the United Kingdom. *Quarterly Journal of the Royal Meteorological Society: A journal of the atmospheric sciences, applied meteorology and physical oceanography*, **132** (617), 1001–1020.

Berg, P., Moseley, C. and Haerter, J. O. 2013. Strong increase in convective precipitation in response to higher temperatures. *Nature Geoscience*, **6** (3), 181.

Bergeron, T. 1935. On the physics of clouds and precipitation. *Proc. 5th Assembly UGGI, Lisbon, Portugal, 1935*, 156–180.

Berry, E. X. 1968. 'Modification of the warm rain process'. In: *Proc. First Conf. on Weather Modification, AMS, 1968*, 81–85.

Berry, E. X. and Reinhardt, R. L. 1974. An analysis of cloud drop growth by collection: Part II. Single initial distributions. *J. Atmos. Sei*, **31**, 1825–1831.

Bigg, E. 1953. The formation of atmospheric ice crystals by the freezing of droplets. *Quarterly Journal of the Royal Meteorological Society*, **79** (342), 510–519.

Bluestein, H. B. 1993. Synoptic-dynamic meteorology in midlatitudes. Volume II. Observations and theory of weather systems.

Bony, S. and Dufresne, J.-L. 2005. Marine boundary layer clouds at the heart of tropical cloud feedback uncertainties in climate models. *Geophysical Research Letters*, **32** (20).

Bony, S., Dufresne, J.-L., Le Treut, H., Morcrette, J.-J. and Senior, C. 2004. On dynamic and thermodynamic components of cloud changes. *Climate Dynamics*, **22** (2-3), 71–86.

Bony, S., Stevens, B., Coppin, D., Becker, T., Reed, K. A., Voigt, A. and Medeiros, B. 2016. Thermodynamic control of anvil cloud amount. *Proceedings of the National Academy of Sciences*, **113** (32), 8927–8932.

Boucher, O., Randall, D., Artaxo, P., Bretherton, C., Feingold, G., Forster, P., Kerminen, V.-M., Kondo, Y., Liao, H., Lohmann, U., Rasch, P., Satheesh, S., Sherwood, S., Stevens, B. and Zhang, X. 2013. Clouds and Aerosols. In: *Climate Change 2013: The Physical Science Basis. Contribution of Working Group I to the Fifth Assessment Report of the Intergovernmental Panel on Climate Change*. Ed. by T. Stocker, D. Qin, G.-K. Plattner, M. Tignor, S. Allen, J. Boschung, A. Nauels, Y. Xia, V. Bex and P. Midgley. Cambridge, United Kingdom and New York, NY, USA: Cambridge University Press. Chap. 7, 571–658.

Bouniol, D., Roca, R., Fiolleau, T. and Poan, D. E. 2016. Macrophysical, microphysical, and radiative properties of tropical mesoscale convective systems over their life cycle. *Journal of Climate*, **29** (9), 3353–3371.

Bourgeois, Q., Ekman, A. M., Igel, M. R. and Krejci, R. 2016. Ubiquity and impact of thin mid-level clouds in the tropics. *Nature communications*, **7**, 12432.

Browning, K. A., Blyth, A. M., Clark, P. A., Corsmeier, U., Morcrette, C. J., Agnew, J. L., Ballard, S. P., Bamber, D., Barthlott, C., Bennett, L. J. *et al.* 2007. The convective storm initiation project. *Bulletin of the American Meteorological Society*, **88** (12), 1939–1956.

Bryan, G. H. and Morrison, H. 2012. Sensitivity of a simulated squall line to horizontal resolution and parameterization of microphysics. *Monthly Weather Review*, **140** (1), 202–225.

Caracena, F., Maddox, R. A., Hoxit, L. R. and Chappell, C. F. 1979. Mesoanalysis of the Big Thompson storm. *Monthly Weather Review*, **107** (1), 1–17.

Castillo, J. E., Weibel, J. A. and Garimella, S. V. 2015. The effect of relative humidity on dropwise condensation dynamics. *International Journal of Heat and Mass Transfer*, **80**, 759–766.

Cess, R. D. and Udelhofen, P. M. 2003. Climate change during 1985–1999: Cloud interactions determined from satellite measurements. *Geophysical research letters*, **30** (1).

Chen, Q., Koren, I., Altaratz, O., Heiblum, R. H., Dagan, G. and Pinto, L. 2017. How do changes in warm-phase microphysics affect deep convective clouds? *Atmospheric Chemistry and Physics*, **17** (15), 9585–9598.

Chen, T., Rossow, W. B. and Zhang, Y. 2000. Radiative effects of cloud-type variations. *Journal of climate*, **13** (1), 264–286.

Cheng, C.-T., Wang, W.-C. and Chen, J.-P. 2007. A modelling study of aerosol impacts on cloud microphysics and radiative properties. *Quarterly Journal of the Royal Meteorological Society*, **133** (623), 283–297.

Coley, P. F. and Jonas, P. R. 1999. Back to basics: Clouds and the earth's radiation budget. *Weather*, **54** (3), 66–70.

Collins, W. D., Bitz, C. M., Blackmon, M. L., Bonan, G. B., Bretherton, C. S., Carton, J. A., Chang, P., Doney, S. C., Hack, J. J., Henderson, T. B. *et al.* 2006. The community climate system model version 3 (CCSM3). *Journal of Climate*, **19** (11), 2122–2143.

Corfidi, S. F., Corfidi, S. J. and Schultz, D. M. 2008. Elevated convection and castellanus: Ambiguities, significance, and questions. *Weather and Forecasting*, **23** (6), 1280–1303.

Costa, A., Meyer, J., Afchine, A., Luebke, A., Günther, G., Dorsey, J. R., Gallagher, M. W., Ehrlich, A., Wendisch, M., Baumgardner, D. *et al.* 2017. Classification of Arctic, midlatitude and tropical clouds in the mixed-phase temperature regime. *Atmospheric Chemistry and Physics*, **17**, 12219–12238.

Cotton, R., Osborne, S, Ulanowski, Z, Hirst, E, Kaye, P. H. and Greenaway, R. 2010. The ability of the Small Ice Detector (SID-2) to characterize cloud particle and aerosol morphologies obtained during flights of the FAAM BAe-146 research aircraft. *Journal of Atmospheric and Oceanic Technology*, **27** (2), 290–303.

Cotton, W. R., Tripoli, G. J., Rauber, R. M. and Mulvihill, E. A. 1986. Numerical simulation of the effects of varying ice crystal nucleation rates and aggregation processes on orographic snowfall. *Journal of climate and applied meteorology*, **25** (11), 1658–1680.

Del Genio, A. D. and Kovari, W. 2002. Climatic properties of tropical precipitating convection under varying environmental conditions. *Journal of climate*, **15** (18), 2597–2615.

Diffenbaugh, N. S., Scherer, M. and Trapp, R. J. 2013. Robust increases in severe thunderstorm environments in response to greenhouse forcing. *Proceedings of the National Academy of Sciences*, 201307758.

Donner, L. J. and Phillips, V. T. 2003. Boundary layer control on convective available potential energy: Implications for cumulus parameterization. *Journal of Geophysical Research: Atmospheres*, **108** (D22).

Dufresne, J.-L. and Bony, S. 2008. An assessment of the primary sources of spread of global warming estimates from coupled atmosphere–ocean models. *Journal of Climate*, **21** (19), 5135–5144.

Emanuel, K. 1994. *Atmospheric Convection*. Oxford University Press.

Emori, S. and Brown, S. 2005. Dynamic and thermodynamic changes in mean and extreme precipitation under changed climate. *Geophysical Research Letters*, **32** (17).

Fan, J., Leung, L. R., Rosenfeld, D., Chen, Q., Li, Z., Zhang, J. and Yan, H. 2013. Microphysical effects determine macrophysical response for aerosol impacts on deep convective clouds. *Proceedings of the National Academy of Sciences*, **110** (48), E4581–E4590.

Farmer, D. K., Cappa, C. D. and Kreidenweis, S. M. 2015. Atmospheric processes and their controlling influence on cloud condensation nuclei activity. *Chemical reviews*, **115** (10), 4199–4217.

Feng, Z., Dong, X., Xi, B., Schumacher, C., Minnis, P. and Khaiyer, M. 2011. Top-of-atmosphere radiation budget of convective core/stratiform rain and anvil clouds from deep convective systems. *Journal of Geophysical Research: Atmospheres*, **116** (D23).

Feng, Z., Dong, X., Xi, B., McFarlane, S. A., Kennedy, A., Lin, B. and Minnis, P. 2012. Life cycle of midlatitude deep convective systems in a Lagrangian framework. *Journal of Geophysical Research: Atmospheres*, **117** (D23).

Field, P. R., Lawson, R. P., Brown, P. R., Lloyd, G., Westbrook, C., Moisseev, D., Miltenberger, A., Nenes, A., Blyth, A., Choularton, T. *et al.* 2017. Secondary ice production: Current state of the science and recommendations for the future. *Meteorological Monographs*, **58**, 7–1.

Findeisen, W. 1938. Kolloid-meteorologische Vorgänge bei Neiderschlags-bildung. *Meteor. Z*, **55**, 121–133.

French, A. J. and Parker, M. D. 2008. The initiation and evolution of multiple modes of convection within a meso-alpha-scale region. *Weather and Forecasting*, **23** (6), 1221–1252.

Fu, Q. and Liou, K. N. 1993. Parameterization of the radiative properties of cirrus clouds. *Journal of the Atmospheric Sciences*, **50** (13), 2008–2025.

Fu, Q. and Liou, K. 1992. On the correlated k-distribution method for radiative transfer in nonhomogeneous atmospheres. *Journal of the Atmospheric Sciences*, **49** (22), 2139–2156.

Gettelman, A, Kay, J. and Shell, K. 2012. The evolution of climate sensitivity and climate feedbacks in the Community Atmosphere Model. *Journal of Climate*, **25** (5), 1453–1469.

Ghosh, S and Jonas, P. 1998. 'On the application of the classic Kessler and Berry schemes in Large Eddy Simulation models with a particular emphasis on cloud autoconversion, the onset time of precipitation and droplet evaporation'. In: *Annales Geophysicae*. Vol. 16. 5. Springer, 628–637.

– 2001. Some analytical calculations on the effect of turbulence on the settling and growth of cloud droplets. *Geophysical research letters*, **28** (20), 3883–3886.

Ghosh, S., Gumber, S. and Varotsos, C. 2017. A sensitivity study of diffusional mass transfer of gases in tropical storm hydrometeors. *Theoretical and Applied Climatology*, 1–18.

Guichard, F. and Couvreux, F. 2017. A short review of numerical cloud-resolving models. *Tellus A: Dynamic Meteorology and Oceanography*, **69** (1), 1373578.

Hack, J. J., Caron, J. M., Yeager, S. G., Oleson, K. W., Holland, M. M., Truesdale, J. E. and Rasch, P. J. 2006. Simulation of the global hydrological cycle in the CCSM Community Atmosphere Model version 3 (CAM3): Mean features. *Journal of climate*, **19** (11), 2199–2221.

Haerter, J. O. and Berg, P. 2009. Unexpected rise in extreme precipitation caused by a shift in rain type? *Nature Geoscience*, **2** (6), 372.

Hallett, J and Mossop, S. 1974. Production of secondary ice particles during the riming process. *Nature*, **249** (5452), 26.

Hamada, A., Takayabu, Y. N., Liu, C. and Zipser, E. J. 2015. Weak linkage between the heaviest rainfall and tallest storms. *Nature communications*, **6**, 6213.

Harrison, E., Minnis, P, Barkstrom, B., Ramanathan, V, Cess, R. and Gibson, G. 1990. Seasonal variation of cloud radiative forcing derived from the Earth Radiation Budget Experiment. *Journal of Geophysical Research: Atmospheres*, **95** (D11), 18687–18703.

Hartmann, D. L. and Berry, S. E. 2017. The balanced radiative effect of tropical anvil clouds. *Journal of Geophysical Research: Atmospheres*, **122** (9), 5003–5020.

Hartmann, D. L. and Larson, K. 2002. An important constraint on tropical cloud-climate feedback. *Geophysical Research Letters*, **29** (20), 12–1.

Hartmann, D. L., Ockert-Bell, M. E. and Michelsen, M. L. 1992. The effect of cloud type on Earth's energy balance: Global analysis. *Journal of Climate*, **5** (11), 1281–1304.

Hartmann, D. L., Moy, L. A. and Fu, Q. 2001. Tropical convection and the energy balance at the top of the atmosphere. *Journal of Climate*, **14** (24), 4495–4511.

Held, I. M. and Soden, B. J. 2006. Robust responses of the hydrological cycle to global warming. *Journal of climate*, **19** (21), 5686–5699.

Heymsfield, A. J. and Sabin, R. M. 1989. Cirrus crystal nucleation by homogeneous freezing of solution droplets. *Journal of the Atmospheric Sciences*, **46** (14), 2252–2264.

Heymsfield, A. J., Miloshevich, L. M., Schmitt, C., Bansemer, A., Twohy, C., Poellot, M. R., Fridlind, A. and Gerber, H. 2005. Homogeneous ice nucleation in subtropical and tropical convection and its influence on cirrus anvil microphysics. *Journal of the atmospheric sciences*, **62** (1), 41–64.

Hibino, K., Takayabu, I., Wakazuki, Y. and Ogata, T. 2018. Physical responses of convective heavy rainfall to future warming condition: case study of the Hiroshima event. *Frontiers in Earth Science*, **6**, 35.

Houze, R. 1993. *Cloud Dynamics*. Cloud Dynamics. Academic Press.

Huang, Y., Blyth, A. M., Brown, P. R., Choularton, T. W. and Cui, Z. 2017. Factors controlling secondary ice production in cumulus clouds. *Quarterly Journal of the Royal Meteorological Society*, **143** (703), 1021–1031.

Igel, M. R., Drager, A. J. and Van Den Heever, S. C. 2014. A CloudSat cloud object partitioning technique and assessment and integration of deep convective anvil sensitivities to sea surface temperature. *Journal of Geophysical Research: Atmospheres*, **119** (17), 10515–10535.

Ikawa, M and Saito, K. Dec. 1991. *Description of a Non-hydrostatic Model Developed at the Forecast Research Department of the MRI.* Vol. 28, 238pp.

Johnson, J., Cui, Z, Lee, L., Gosling, J., Blyth, A. and Carslaw, K. 2015. Evaluating uncertainty in convective cloud microphysics using statistical emulation. *Journal of Advances in Modeling Earth Systems*, **7** (1), 162–187.

Junge, C. 1952. *Die konstitution des atmosphärischen aerosols.* Selbstverl. d. Meteorolog. Amtes f. Nordwestdtschl.

Kalnay, E., Kanamitsu, M., Kistler, R., Collins, W., Deaven, D., Gandin, L., Iredell, M., Saha, S., White, G., Woollen, J. *et al.* 1996. The NCEP/NCAR 40-year reanalysis project. *Bulletin of the American meteorological Society*, **77** (3), 437–472.

Kato, S., Rose, F. G., Sun-Mack, S., Miller, W. F., Chen, Y., Rutan, D. A., Stephens, G. L., Loeb, N. G., Minnis, P., Wielicki, B. A. *et al.* 2011. Improvements of top-of-atmosphere and surface irradiance computations with CALIPSO-, CloudSat-, and MODIS-derived cloud and aerosol properties. *Journal of Geophysical Research: Atmospheres*, **116** (D19).

Kendon, E. J., Roberts, N. M., Senior, C. A. and Roberts, M. J. 2012. Realism of rainfall in a very high-resolution regional climate model. *Journal of Climate*, **25** (17), 5791–5806.

Kendon, E. J., Roberts, N. M., Fowler, H. J., Roberts, M. J., Chan, S. C. and Senior, C. A. 2014. Heavier summer downpours with climate change revealed by weather forecast resolution model. *Nature Climate Change*, **4** (7), 570.

Kessler, E. 1969. On the distribution and continuity of water substance in atmospheric circulations. In: *On the distribution and continuity of water substance in atmospheric circulations.* Springer, 1–84.

Khain, A., Beheng, K., Heymsfield, A, Korolev, A, Krichak, S., Levin, Z, Pinsky, M, Phillips, V., Prabhakaran, T, Teller, A *et al.* 2015. Representation of microphysical processes in cloud-resolving models: Spectral (bin) microphysics versus bulk parameterization. *Reviews of Geophysics*, **53** (2), 247–322.

Khairoutdinov, M. and Kogan, Y. 2000. A new cloud physics parameterization in a large-eddy simulation model of marine stratocumulus. *Monthly weather review*, **128** (1), 229–243.

Kharin, V. V., Zwiers, F., Zhang, X. and Wehner, M. 2013. Changes in temperature and precipitation extremes in the CMIP5 ensemble. *Climatic change*, **119** (2), 345–357.

Khvorostyanov, V. I. and Curry, J. A. 1999. Toward the theory of stochastic condensation in clouds. Part I: A general kinetic equation. *Journal of the atmospheric sciences*, **56** (23), 3985–3996.

Kiehl, J. and Ramanathan, V. 1990. Comparison of cloud forcing derived from the Earth Radiation Budget Experiment with that simulated by the NCAR Community Climate Model. *Journal of Geophysical Research: Atmospheres*, **95** (D8), 11679–11698.

King, N., Bower, K., Crosier, J and Crawford, I. 2013. Evaluating MODIS cloud retrievals with in situ observations from VOCALS-REx. *Atmospheric Chemistry and Physics*, **13** (1), 191–209.

Kogan, Y. 2013. A cumulus cloud microphysics parameterization for cloud-resolving models. *Journal of the Atmospheric Sciences*, **70** (5), 1423–1436.

Köhler, H. 1936. The nucleus in and the growth of hygroscopic droplets. *Transactions of the Faraday Society*, **32**, 1152–1161.

Koop, T., Luo, B., Tsias, A. and Peter, T. 2000. Water activity as the determinant for homogeneous ice nucleation in aqueous solutions. *Nature*, **406** (6796), 611.

Kraemer, M., Rolf, C., Luebke, A., Afchine, A., Spelten, N., Costa, A., Meyer, J., Zoeger, M., Smith, J., Herman, R. L. *et al.* 2016. A microphysics guide to cirrus clouds-Part 1: Cirrus types. *Atmospheric Chemistry and Physics*, **16**, 3463–3483.

Krisna, T. C., Wendisch, M., Ehrlich, A., Jäkel, E., Werner, F., Weigel, R., Borrmann, S., Mahnke, C., Pöschl, U., Andreae, M. O. *et al.* 2018. Comparing airborne and satellite retrievals of cloud optical thickness and particle effective

radius using a spectral radiance ratio technique: two case studies for cirrus and deep convective clouds. *Atmospheric Chemistry & Physics*, **18** (7).

Lau, K.-M. and Wu, H.-T. 2007. Detecting trends in tropical rainfall characteristics, 1979–2003. *International Journal of Climatology*, **27** (8), 979–988.

– 2011. Climatology and changes in tropical oceanic rainfall characteristics inferred from Tropical Rainfall Measuring Mission (TRMM) data (1998–2009). *Journal of Geophysical Research: Atmospheres*, **116** (D17).

Launder, B. 2017. Hurricanes: An Engineering View of their Structure and Strategies for their Extinction. *Flow, Turbulence and Combustion*, **98** (4), 969–985.

Lawson, R. P., Woods, S. and Morrison, H. 2015. The microphysics of ice and precipitation development in tropical cumulus clouds. *Journal of the Atmospheric Sciences*, **72** (6), 2429–2445.

Lee, H. and Baik, J.-J. 2017. A physically based autoconversion parameterization. *Journal of the Atmospheric Sciences*, **74** (5), 1599–1616.

Lee, L. A., Reddington, C. L. and Carslaw, K. S. 2016. On the relationship between aerosol model uncertainty and radiative forcing uncertainty. *Proceedings of the National Academy of Sciences*, **113** (21), 5820–5827.

Lenderink, G, Mok, H., Lee, T. and Van Oldenborgh, G. 2011. Scaling and trends of hourly precipitation extremes in two different climate zones–Hong Kong and the Netherlands. *Hydrology and Earth System Sciences*, **15** (9), 3033–3041.

Lenderink, G. and Van Meijgaard, E. 2008. Increase in hourly precipitation extremes beyond expectations from temperature changes. *Nature Geoscience*, **1** (8), 511.

Lenschow, D. and Stephens, P. 1980. The role of thermals in the convective boundary layer. *Boundary-Layer Meteorology*, **19** (4), 509–532.

Lepore, C., Veneziano, D. and Molini, A. 2015. Temperature and CAPE dependence of rainfall extremes in the eastern United States. *Geophysical Research Letters*, **42** (1), 74–83.

Li, R. C. and Zhou, W. 2012. Changes in western Pacific tropical cyclones associated with the El Niño–Southern Oscillation cycle. *Journal of Climate*, **25** (17), 5864–5878.

Lim, K.-S. S. and Hong, S.-Y. 2010. Development of an effective double-moment cloud microphysics scheme with prognostic cloud condensation nuclei (CCN) for weather and climate models. *Monthly weather review*, **138** (5), 1587–1612.

Lin, B., Wielicki, B. A., Chambers, L. H., Hu, Y. and Xu, K.-M. 2002. The iris hypothesis: A negative or positive cloud feedback? *Journal of Climate*, **15** (1), 3–7.

Lin, Y.-L., Farley, R. D. and Orville, H. D. 1983. Bulk parameterization of the snow field in a cloud model. *Journal of Climate and Applied Meteorology*, **22** (6), 1065–1092.

Lindzen, R. S., Chou, M.-D. and Hou, A. Y. 2001. Does the earth have an adaptive infrared iris? *Bulletin of the American Meteorological Society*, **82** (3), 417–432.

Liou, K.-N. 1986. Influence of cirrus clouds on weather and climate processes: A global perspective. *Monthly Weather Review*, **114** (6), 1167–1199.

Liu, Y. and Daum, P. H. 2004. Parameterization of the autoconversion process. Part I: Analytical formulation of the Kessler-type parameterizations. *Journal of the atmospheric sciences*, **61** (13), 1539–1548.

Lohmann, U, Humble, J, Leaitch, W., Isaac, G. and Gultepe, I. 2001. Simulations of ice clouds during FIRE ACE using the CCCMA single-column model. *Journal of Geophysical Research: Atmospheres*, **106** (D14), 15123–15138.

Lohmann, U., Lüönd, F. and Mahrt, F. 2016. *An Introduction to Clouds: From the Microscale to Climate*. Cambridge University Press.

Longman, R. J., Giambelluca, T. W., Alliss, R. J. and Barnes, M. L. 2014. Temporal solar radiation change at high elevations in Hawai ʻi. *Journal of Geophysical Research: Atmospheres*, **119** (10), 6022–6033.

Ma, J., Chadwick, R., Seo, K.-H., Dong, C., Huang, G., Foltz, G. R. and Jiang, J. H. 2018. Responses of the tropical atmospheric circulation to climate change and connection to the hydrological cycle. *Annual Review of Earth and Planetary Sciences*, (0).

Machado, L. and Rossow, W. 1993. Structural characteristics and radiative properties of tropical cloud clusters. *Monthly Weather Review*, **121** (12), 3234–3260.

Markowski, P. and Richardson, Y. 2011. *Mesoscale Meteorology in Midlatitudes*. Advancing Weather and Climate Science. Wiley.

Masunaga, H. and Luo, Z. J. 2016. Convective and large-scale mass flux profiles over tropical oceans determined from synergistic analysis of a suite of satellite observations. *Journal of Geophysical Research: Atmospheres*, **121** (13), 7958–7974.

Mauritsen, T. and Stevens, B. 2015. Missing iris effect as a possible cause of muted hydrological change and high climate sensitivity in models. *Nature Geoscience*, **8** (5), 346.

Mayor, Y. G. and Mesquita, M. D. 2015. Numerical simulations of the 1 May 2012 deep convection event over Cuba: sensitivity to cumulus and microphysical schemes in a high-resolution model. *Advances in Meteorology*, **2015**.

McFiggans, G, Artaxo, P, Baltensperger, U., Coe, H, Facchini, M., Feingold, G, Fuzzi, S, Gysel, M, Laaksonen, A, Lohmann, U *et al.* 2006. The effect of physical and chemical aerosol properties on warm cloud droplet activation. *Atmospheric Chemistry and Physics*, **6** (9), 2593–2649.

Mesinger, F., DiMego, G., Kalnay, E., Mitchell, K., Shafran, P. C., Ebisuzaki, W., Jović, D., Woollen, J., Rogers, E., Berbery, E. H. *et al.* 2006. North American regional reanalysis. *Bulletin of the American Meteorological Society*, **87** (3), 343–360.

Meyers, M. P., DeMott, P. J. and Cotton, W. R. 1992. New primary ice-nucleation parameterizations in an explicit cloud model. *Journal of Applied Meteorology*, **31** (7), 708–721.

Meyers, M. P., Walko, R. L., Harrington, J. Y. and Cotton, W. R. 1997. New RAMS cloud microphysics parameterization. Part II: The two-moment scheme. *Atmospheric Research*, **45** (1), 3–39.

Milbrandt, J. and Yau, M. 2005. A multimoment bulk microphysics parameterization. Part I: Analysis of the role of the spectral shape parameter. *Journal of the atmospheric sciences*, **62** (9), 3051–3064.

Miller, R. C., Anderson, R. J., Kassner Jr, J. and Hagen, D. E. 1983. Homogeneous nucleation rate measurements for water over a wide range of temperature and nucleation rate. *The Journal of Chemical Physics*, **78** (6), 3204–3211.

Mizuta, R., Murata, A., Ishii, M., Shiogama, H., Hibino, K., Mori, N., Arakawa, O., Imada, Y., Yoshida, K., Aoyagi, T. *et al.* 2017. Over 5,000 years of ensemble future climate simulations by 60-km global and 20-km regional atmospheric models. *Bulletin of the American Meteorological Society*, **98** (7), 1383–1398.

Morice, C. P., Kennedy, J. J., Rayner, N. A. and Jones, P. D. 2012. Quantifying uncertainties in global and regional temperature change using an ensemble of observational estimates: The HadCRUT4 data set. *Journal of Geophysical Research: Atmospheres*, **117** (D8).

Morrison, H., Curry, J. and Khvorostyanov, V. 2005. A new double-moment microphysics parameterization for application in cloud and climate models. Part I: Description. *Journal of the Atmospheric Sciences*, **62** (6), 1665–1677.

Morrison, H., Thompson, G. and Tatarskii, V. 2009. Impact of cloud microphysics on the development of trailing stratiform precipitation in a simulated squall line: Comparison of one-and two-moment schemes. *Monthly Weather Review*, **137** (3), 991–1007.

Murakami, M. 1990. Numerical modeling of dynamical and microphysical evolution of an isolated convective cloud. *Journal of the Meteorological Society of Japan. Ser. II*, **68** (2), 107–128.

Murray, B., O'sullivan, D, Atkinson, J. and Webb, M. 2012. Ice nucleation by particles immersed in supercooled cloud droplets. *Chemical Society Reviews*, **41** (19), 6519–6554.

Myhre, G., Shindell, D., Breon, F.-M., Collins, W., Fuglestvedt, J., Huang, J., Koch, D., Lamarque, J.-F., Lee, D., Mendoza, B., Nakajima, T., Robock, A., Stephens, G., Takemura, T. and Zhang, H. 2013. Anthropogenic and Natural Radiative Forcing. In: *Climate Change 2013: The Physical Science Basis. Contribution of Working Group I to the Fifth Assessment Report of the Intergovernmental Panel on Climate Change*. Ed. by T. Stocker, D. Qin, G.-K. Plattner, M. Tignor, S. Allen, J. Boschung, A. Nauels, Y. Xia, V. Bex and P. Midgley. Cambridge, United Kingdom and New York, NY, USA: Cambridge University Press. Chap. 8, 659–740.

Norris, J. R. and Slingo, A. 2009. Trends in Observed Cloudiness and Earth's Radiation Budget What Do We Not Know and What Do We Need to Know? In: *Clouds in the perturbed climate system: Their relationship to energy balance, atmospheric dynamics, and precipitation*. Ed. by J. Heintzenberg and R. Charlson. Cambridge, Massachusetts: MIT Press.

Ohmura, A. 2009. Observed decadal variations in surface solar radiation and their causes. *Journal of Geophysical Research: Atmospheres*, **114** (D10).

Pall, P., Allen, M. and Stone, D. A. 2007. Testing the Clausius–Clapeyron constraint on changes in extreme precipitation under CO 2 warming. *Climate Dynamics*, **28** (4), 351–363.

Pall, P., Patricola, C. M., Wehner, M. F., Stone, D. A., Paciorek, C. J. and Collins, W. D. 2017. Diagnosing conditional anthropogenic contributions to heavy Colorado rainfall in September 2013. *Weather and Climate Extremes*, **17**, 1–6.

Palmer, T. 2013. Climate extremes and the role of dynamics. *Proceedings of the National Academy of Sciences*, **110** (14), 5281–5282.

Passarelli Jr., R. E. 1978. An approximate analytical model of the vapor deposition and aggregation growth of snowflakes. *Journal of the Atmospheric Sciences*, **35** (1), 118–124.

Peter, T., Marcolli, C., Spichtinger, P., Corti, T., Baker, M. B. and Koop, T. 2006. When dry air is too humid. *Science*, **314** (5804), 1399–1402.

Phillips, V. T. and Donner, L. J. 2006. Cloud microphysics, radiation and vertical velocities in two-and three-dimensional simulations of deep convection. *Quarterly Journal of the Royal Meteorological Society*, **132** (621C), 3011–3033.

Prein, A., Gobiet, A., Truhetz, H., Keuler, K., Goergen, K., Teichmann, C., Maule, C. F., Van Meijgaard, E, Déqué, M, Nikulin, G. *et al.* 2016. Precipitation in the EURO-CORDEX 0.11° and 0.44° simulations: high resolution, high benefits? *Climate dynamics*, **46** (1-2), 383–412.

Prein, A. F., Langhans, W., Fosser, G., Ferrone, A., Ban, N., Goergen, K., Keller, M., Tölle, M., Gutjahr, O., Feser, F. *et al.* 2015. A review on regional convection-permitting climate modeling: Demonstrations, prospects, and challenges. *Reviews of geophysics*, **53** (2), 323–361.

Prein, A. F., Rasmussen, R. M., Ikeda, K., Liu, C., Clark, M. P. and Holland, G. J. 2017. The future intensification of hourly precipitation extremes. *Nature Climate Change*, **7** (1), 48.

Pretor-Pinney, G. 2007. *The Cloudspotter's Guide: The Science, History, and Culture of Clouds*. Perigee Book. Berkley Publishing Group.

Protopapadaki, S. E., Stubenrauch, C. J. and Feofilov, A. G. 2017. Upper tropospheric cloud systems derived from IR sounders: properties of cirrus anvils in the tropics. *Atmospheric Chemistry and Physics*, **17** (6), 3845–3859.

Pruppacher, H and Klett, J. 1997. *Microphysics of Clouds and Precipitation. Atmospheric and Oceanographic Sciences Library, Vol. 18*.

Ramanathan, V. and Collins, W. 1991. Thermodynamic regulation of ocean warming by cirrus clouds deduced from observations of the 1987 El Nino. *Nature*, **351** (6321), 27.

Ramanathan, V., Cess, R., Harrison, E., Minnis, P, Barkstrom, B., Ahmad, E and Hartmann, D. 1989. Cloud-radiative forcing and climate: Results from the Earth Radiation Budget Experiment. *Science*, **243** (4887), 57–63.

Randall, D. A., Wood, R. A., Bony, S., Colman, R., Fichefet, T., Fyfe, J., Kattsov, V., Pitman, A., Shukla, J., Srinivasan, J. *et al.* 2007. Climate models and their evaluation. In: *Climate change 2007: The physical science basis. Contribution of Working Group I to the Fourth Assessment Report of the IPCC (FAR)*. Cambridge University Press, 589–662.

Rangno, A. L. and Hobbs, P. V. 2001. Ice particles in stratiform clouds in the Arctic and possible mechanisms for the production of high ice concentrations. *Journal of Geophysical Research: Atmospheres*, **106** (D14), 15065–15075.

– 2005. Microstructures and precipitation development in cumulus and small cumulonimbus clouds over the warm pool of the tropical Pacific Ocean. *Quarterly Journal of the Royal Meteorological Society: A journal of the atmospheric sciences, applied meteorology and physical oceanography*, **131** (606), 639–673.

Rasmussen, K., Prein, A., Rasmussen, R., Ikeda, K and Liu, C. 2017. Changes in the convective population and thermodynamic environments in convection-permitting regional climate simulations over the United States. *Climate Dynamics*, 1–26.

Rasmussen, R. M., Geresdi, I., Thompson, G., Manning, K. and Karplus, E. 2002. Freezing drizzle formation in stably stratified layer clouds: The role of radiative cooling of cloud droplets, cloud condensation nuclei, and ice initiation. *Journal of the atmospheric sciences*, **59** (4), 837–860.

Read, P., Barstow, J, Charnay, B., Chelvaniththilan, S, Irwin, P., Knight, S., Lebonnois, S., Lewis, S., Mendonça, J and Montabone, L. 2016. Global energy budgets and 'Trenberth diagrams' for the climates of terrestrial and gas giant

planets. *Quarterly Journal of the Royal Meteorological Society*, **142** (695), 703–720.

Reisner, J, RaSmuSSen, R. M. and Bruintjes, R. 1998. Explicit forecasting of supercooled liquid water in winter storms using the MM5 mesoscale model. *Quarterly Journal of the Royal Meteorological Society*, **124** (548), 1071–1107.

Rogers, R. and Yau, M. 1989. *A Short Course in Cloud Physics*. Elsevier Science.

Rosenfeld, D. and Woodley, W. L. 2000. Deep convective clouds with sustained supercooled liquid water down to-37.5 C. *Nature*, **405** (6785), 440.

Rowell, D. P. 2009. Projected midlatitude continental summer drying: North America versus Europe. *Journal of Climate*, **22** (11), 2813–2833.

Rutledge, S. A. and Hobbs, P. V. 1984. The mesoscale and microscale structure and organization of clouds and precipitation in midlatitude cyclones. XII: A diagnostic modeling study of precipitation development in narrow cold-frontal rainbands. *Journal of the Atmospheric Sciences*, **41** (20), 2949–2972.

Sassen, K. and Dodd, G. C. 1988. Homogeneous nucleation rate for highly supercooled cirrus cloud droplets. *Journal of the Atmospheric Sciences*, **45** (8), 1357–1369.

Satoh, M., Iga, S.-i., Tomita, H., Tsushima, Y. and Noda, A. T. 2012. Response of upper clouds in global warming experiments obtained using a global nonhydrostatic model with explicit cloud processes. *Journal of Climate*, **25** (6), 2178–2191.

Schneider, T., Teixeira, J., Bretherton, C. S., Brient, F., Pressel, K. G., Schär, C. and Siebesma, A. P. 2017. Climate goals and computing the future of clouds. *Nature Climate Change*, **7** (1), 3.

Schumacher, R. S. and Johnson, R. H. 2008. Mesoscale processes contributing to extreme rainfall in a midlatitude warm-season flash flood. *Monthly Weather Review*, **136** (10), 3964–3986.

Seeley, J. T. and Romps, D. M. 2015. Why does tropical convective available potential energy (CAPE) increase with warming? *Geophysical Research Letters*, **42** (23), 10–429.

Seifert, A. and Beheng, K. D. 2001. A double-moment parameterization for simulating autoconversion, accretion and selfcollection. *Atmospheric research*, **59**, 265–281.

Seinfeld, J. H., Bretherton, C., Carslaw, K. S., Coe, H., DeMott, P. J., Dunlea, E. J., Feingold, G., Ghan, S., Guenther, A. B., Kahn, R. *et al.* 2016. Improving our fundamental understanding of the role of aerosol- cloud interactions in the climate system. *Proceedings of the National Academy of Sciences*, **113** (21), 5781–5790.

Sharmila, S and Walsh, K. 2018. Recent poleward shift of tropical cyclone formation linked to Hadley cell expansion. *Nature Climate Change*, **8** (8), 730.

Sherwood, S., Roca, R., Weckwerth, T. and Andronova, N. 2010. Tropospheric water vapor, convection, and climate. *Reviews of Geophysics*, **48** (2).

Shiogama, H., Watanabe, M., Imada, Y., Mori, M., Kamae, Y., Ishii, M. and Kimoto, M. 2014. Attribution of the June-July 2013 heat wave in the southwestern United States. *Sola*, **10**, 122–126.

Shrestha, R. K., Connolly, P. J. and Gallagher, M. W. 2017. Sensitivity of WRF cloud microphysics to simulations of a convective storm over the Nepal Himalayas. *The Open Atmospheric Science Journal*, **11** (1).

Skamarock, W., Klemp, J., Dudhia, J, Gill, D., Barker, D., Duda, M., Huang, X., Wang, W and Powers, J. 2008. A description of the advanced research WRF Version 3, NCAR technical note, Mesoscale and Microscale Meteorology Division. *National Center for Atmospheric Research, Boulder, Colorado, USA*.

Sohn, B., Ryu, G.-H., Song, H.-J. and Ou, M.-L. 2013. Characteristic features of warm-type rain producing heavy rainfall over the Korean Peninsula inferred from TRMM measurements. *Monthly Weather Review*, **141** (11), 3873–3888.

Song, H.-J., Sohn, B.-J., Hong, S.-Y. and Hashino, T. 2017. Idealized numerical experiments on the microphysical evolution of warm-type heavy rainfall. *Journal of Geophysical Research: Atmospheres*, **122** (3), 1685–1699.

Spracklen, D. V., Carslaw, K., Merikanto, J, Mann, G., Reddington, C., Pickering, S, Ogren, J., Andrews, E, Baltensperger, U., Weingartner, E *et al.* 2010. Explaining global surface aerosol number concentrations in terms of primary emissions and particle formation. *Atmospheric Chemistry and Physics*, **10** (10), 4775–4793.

Stephens, G. L. 2005. Cloud feedbacks in the climate system: A critical review. *Journal of climate*, **18** (2), 237–273.

Stephens, G. L. and Webster, P. J. 1981. Clouds and climate: Sensitivity of simple systems. *Journal of the Atmospheric Sciences*, **38** (2), 235–247.

Stevens, B., Brogniez, H., Kiemle, C., Lacour, J.-L., Crevoisier, C. and Kiliani, J. 2017. Structure and dynamical influence of water vapor in the lower tropical troposphere. *Surveys in Geophysics*, **38** (6), 1371–1397.

Straka, J. 2009. *Cloud and Precipitation Microphysics: Principles and Parameterizations*. Cambridge University Press, 152–153.

Takahashi, T., Nagao, Y. and Kushiyama, Y. 1995. Possible high ice particle production during graupel–graupel collisions. *Journal of the atmospheric sciences*, **52** (24), 4523–4527.

Takayabu, I., Hibino, K., Sasaki, H., Shiogama, H., Mori, N., Shibutani, Y. and Takemi, T. 2015. Climate change effects on the worst-case storm surge: a case study of Typhoon Haiyan. *Environmental Research Letters*, **10** (6), 064011.

Tao, W.-K. and Li, X. 2016. The relationship between latent heating, vertical velocity, and precipitation processes: The impact of aerosols on precipitation in organized deep convective systems. *Journal of Geophysical Research: Atmospheres*, **121** (11), 6299–6320.

Tao, W.-K., Chen, J.-P., Li, Z., Wang, C. and Zhang, C. 2012. Impact of aerosols on convective clouds and precipitation. *Reviews of Geophysics*, **50** (2).

Thampi, B. and Roca, R. 2014. Investigation of negative cloud radiative forcing over the Indian subcontinent and adjacent oceans during the summer monsoon season. *Atmospheric Chemistry and Physics*, **14** (13), 6739–6758.

Tian, B. and Ramanathan, V. 2002. Role of tropical clouds in surface and atmospheric energy budget. *Journal of climate*, **15** (3), 296–305.

Tian, B., Soden, B. J. and Wu, X. 2004. Diurnal cycle of convection, clouds, and water vapor in the tropical upper troposphere: Satellites versus a general circulation model. *Journal of Geophysical Research: Atmospheres*, **109** (D10).

Trapp, R. J., Diffenbaugh, N. S., Brooks, H. E., Baldwin, M. E., Robinson, E. D. and Pal, J. S. 2007. Changes in severe thunderstorm environment frequency during the 21st century caused by anthropogenically enhanced global radiative forcing. *Proceedings of the National Academy of Sciences*, **104** (50), 19719–19723.

Trapp, R. J., Diffenbaugh, N. S. and Gluhovsky, A. 2009. Transient response of severe thunderstorm forcing to elevated greenhouse gas concentrations. *Geophysical Research Letters*, **36** (1).

Trenberth, K. E., Dai, A., Rasmussen, R. M. and Parsons, D. B. 2003. The changing character of precipitation. *Bulletin of the American Meteorological Society*, **84** (9), 1205–1218.

Twomey, S. 1959. The nuclei of natural cloud formation part II: The supersaturation in natural clouds and the variation of cloud droplet concentration. *Geofisica pura e applicata*, **43** (1), 243–249.

UNFCCC, V. 2015. Adoption of the Paris agreement. *United Nations Office at Geneva, Geneva Google Scholar*.

Utsumi, N., Kim, H., Kanae, S. and Oki, T. 2016. Which weather systems are projected to cause future changes in mean and extreme precipitation in CMIP5 simulations? *Journal of Geophysical Research: Atmospheres*, **121** (18).

Viisanen, Y, Strey, R and Reiss, H. 1993. Homogeneous nucleation rates for water. *The Journal of chemical physics*, **99** (6), 4680–4692.

Villanueva-Birriel, C. 2014. Impacts of regional climate change upon the warm rain process and surface precipitation from deep convective storms: A numerical modeling study. PhD thesis. Purdue University.

Villanueva-Birriel, C. M., Lasher-Trapp, S., Trapp, R. J. and Diffenbaugh, N. 2014. Sensitivity of the Warm Rain Process in Convective Clouds to Regional Climate Change in the Contiguous US. *Journal of Clouds, Aerosols and Radiation*, **1**, 1–17.

Voigt, C., Schumann, U., Minikin, A., Abdelmonem, A., Afchine, A., Borrmann, S., Boettcher, M., Buchholz, B., Bugliaro, L., Costa, A. *et al.* 2017. ML-CIRRUS: The airborne experiment on natural cirrus and contrail cirrus with the high-altitude long-range research aircraft HALO. *Bulletin of the American Meteorological Society*, **98** (2), 271–288.

Volosciuk, C., Maraun, D., Semenov, V. A. and Park, W. 2015. Extreme precipitation in an atmosphere general circulation model: Impact of horizontal and vertical model resolutions. *Journal of Climate*, **28** (3), 1184–1205.

Wallace, J. M. 1975. Diurnal variations in precipitation and thunderstorm frequency over the conterminous United States. *Monthly Weather Review*, **103** (5), 406–419.

Webb, M. J., Senior, C., Sexton, D., Ingram, W., Williams, K., Ringer, M., McAvaney, B., Colman, R, Soden, B., Gudgel, R *et al.* 2006. On the contribution of local feedback mechanisms to the range of climate sensitivity in two GCM ensembles. *Climate Dynamics*, **27** (1), 17–38.

Wegener, A. 1911. *Thermodynamik der atmosphäre*. JA Barth.

Weisman, M. L. and Klemp, J. B. 1982. The dependence of numerically simulated convective storms on vertical wind shear and buoyancy. *Monthly Weather Review*, **110** (6), 504–520.

Westbrook, C. D. and Illingworth, A. J. 2011. Evidence that ice forms primarily in supercooled liquid clouds at temperatures¿- 27° C. *Geophysical Research Letters*, **38** (14).

White, B. A. 2012. Modelling of elavated mesoscale convective systems. PhD thesis. University of Leeds.

Wielicki, B. A., Barkstrom, B. R., Harrison, E. F., Lee III, R. B., Smith, G. L. and Cooper, J. E. 1996. Clouds and the Earth's Radiant Energy System (CERES): An earth observing system experiment. *Bulletin of the American Meteorological Society*, **77** (5), 853–868.

Witte, M. K., Ayala, O., Wang, L.-P., Bott, A. and Chuang, P. Y. 2017. Estimating collision–coalescence rates from in situ observations of marine stratocumulus. *Quarterly Journal of the Royal Meteorological Society*, **143** (708), 2755–2763.

Xu, W. 2013. Precipitation and convective characteristics of summer deep convection over East Asia observed by TRMM. *Monthly Weather Review*, **141** (5), 1577–1592.

Xu, W. and Zipser, E. J. 2012. Properties of deep convection in tropical continental, monsoon, and oceanic rainfall regimes. *Geophysical Research Letters*, **39** (7).

Yang, G.-Y. and Slingo, J. 2001. The diurnal cycle in the tropics. *Monthly Weather Review*, **129** (4), 784–801.

Young, K. C. 1974. The role of contact nucleation in ice phase initiation in clouds. *Journal of the Atmospheric Sciences*, **31** (3), 768–776.

Zelinka, M. D. and Hartmann, D. L. 2010. Why is longwave cloud feedback positive? *Journal of Geophysical Research: Atmospheres*, **115** (D16).

Zelinka, M. D., Klein, S. A., Taylor, K. E., Andrews, T., Webb, M. J., Gregory, J. M. and Forster, P. M. 2013. Contributions of different cloud types to feedbacks and rapid adjustments in CMIP5. *Journal of Climate*, **26** (14), 5007–5027.

Zhang, G. J. and McFarlane, N. A. 1995. Sensitivity of climate simulations to the parameterization of cumulus convection in the Canadian Climate Centre general circulation model. *Atmosphere-ocean*, **33** (3), 407–446.

Zhou, C., Zelinka, M. D. and Klein, S. A. 2017. Analyzing the dependence of global cloud feedback on the spatial pattern of sea surface temperature change with a Green's function approach. *Journal of Advances in Modeling Earth Systems*, **9** (5), 2174–2189.

Appendix A

Parameters used in the WRF model setup

Table A.1: List of parameters used in the WRF model setup

Parameters	**Value**
Domains	
time_step	3
time_step_fract_num	0
time_step_fract_den	1
max_dom	1
s_we	1
e_we	200
s_sn	1
e_sn	120
s_vert	1
e_vert	70
dx	500
dy	500
ztop	24000
grid_id	1
parent_id	0
i_parent_start	0
j_parent_start	0
parent_grid_ratio	1
parent_time_step_ratio	1
feedback	1
smooth_option	0
Physics	
mp_physics	101
hail_opt	1
ra_lw_physics	0
ra_sw_physics	0
radt	1
sf_sfclay_physics	0
sf_surface_physics	0

Continued on next page

Table A.1 – continued from previous page

Parameters	**Value**
bl_pbl_physics	0
bldt	0
cu_physics	0
cudt	5
num_soil_layers	5
do_radar_ref	0
Dynamics	
rk_ord	3
diff_opt	2
km_opt	2
damp_opt	2
zdamp	5000.
dampcoef	0.003
khdif	500
kvdif	500
smdiv	0.1
emdiv	0.01
epssm	0.1
time_step_sound	6
h_mom_adv_order	5
v_mom_adv_order	3
h_sca_adv_order	5
v_sca_adv_order	3
moist_adv_order	1
scalar_adv_order	1
chem_adv_order	1
tke_adv_order	1
non_hydrostatic	.true.
mix_full_fields	.true.

Continued on next page

Table A.1 – continued from previous page

Parameters	**Value**
Boundary control	
periodic_x	.false.
symmetric_xs	.false.
symmetric_xe	.false.
open_xs	.true.
open_xe	.true.
periodic_y	.false.
symmetric_ys	.false.
symmetric_ye	.false.
open_ys	.true.
open_ye	.true.
nested	.false.

Appendix B

Switches used in Morrison two-moment bulk microphysics scheme

Table B.1: List of microphysical switches employed in the Morrison two-moment bulk microphysics scheme

Switches	Value	Description
INUM	0	Predict droplet concentration
IACT	1	Use power-law CCN spectra, $NCCN = CS^K$
IBASE	1	Neglect droplet activation at lateral cloud edges due to unresolved entrainment and mixing, activate at cloud base or in region with little cloud water using non-equilibrium supersaturation assuming no initial cloud water; in cloud interior, activate using equilibrium supersaturation
ISUB	1	Exclude sub-grid vertical velocity W, only use grid-scale W
ILIQ	0	Include ice
INUC	0	Use formula from Rasmussen et al. 2002 (midlatitdue)
IGRAUP	0	Include graupel
IHAIL	1	Dense precipitating ice is hail
IRAIN	0	Warm rain (autoconversion, accretion, self-collection) from Khairoutdinov and Kogan (2001) which in this thesis is replaced by that of Kogan (2013)

Appendix C

2D vertical cross section of averaged total water content of the simulated deep convective clouds

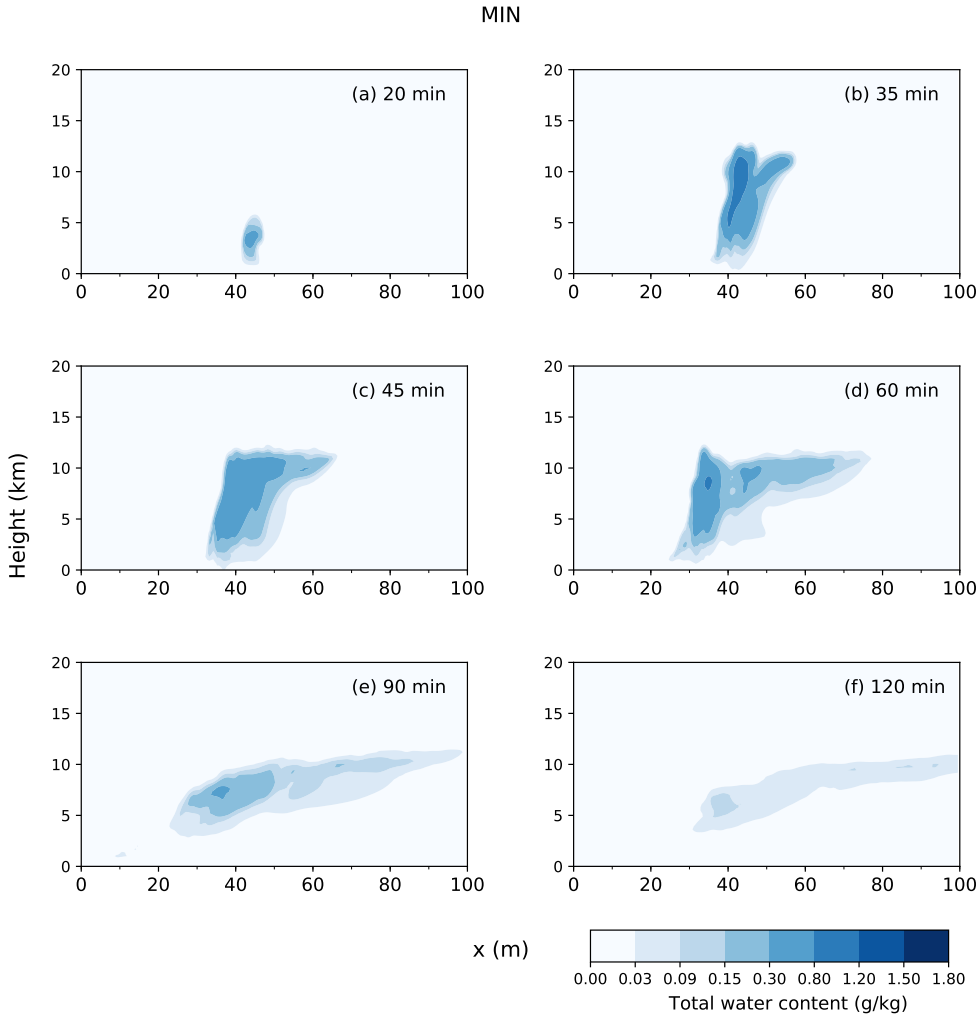

Figure C.1: 2D vertical cross section of averaged total water content in simulated deep convective clouds in $\theta_P RH_P$ (past environment) for Minneapolis, MIN at (a) 20 min, (b) 35 min, (c) 45 min, (d) 60 min, (e) 90 min, and (f)120 min.

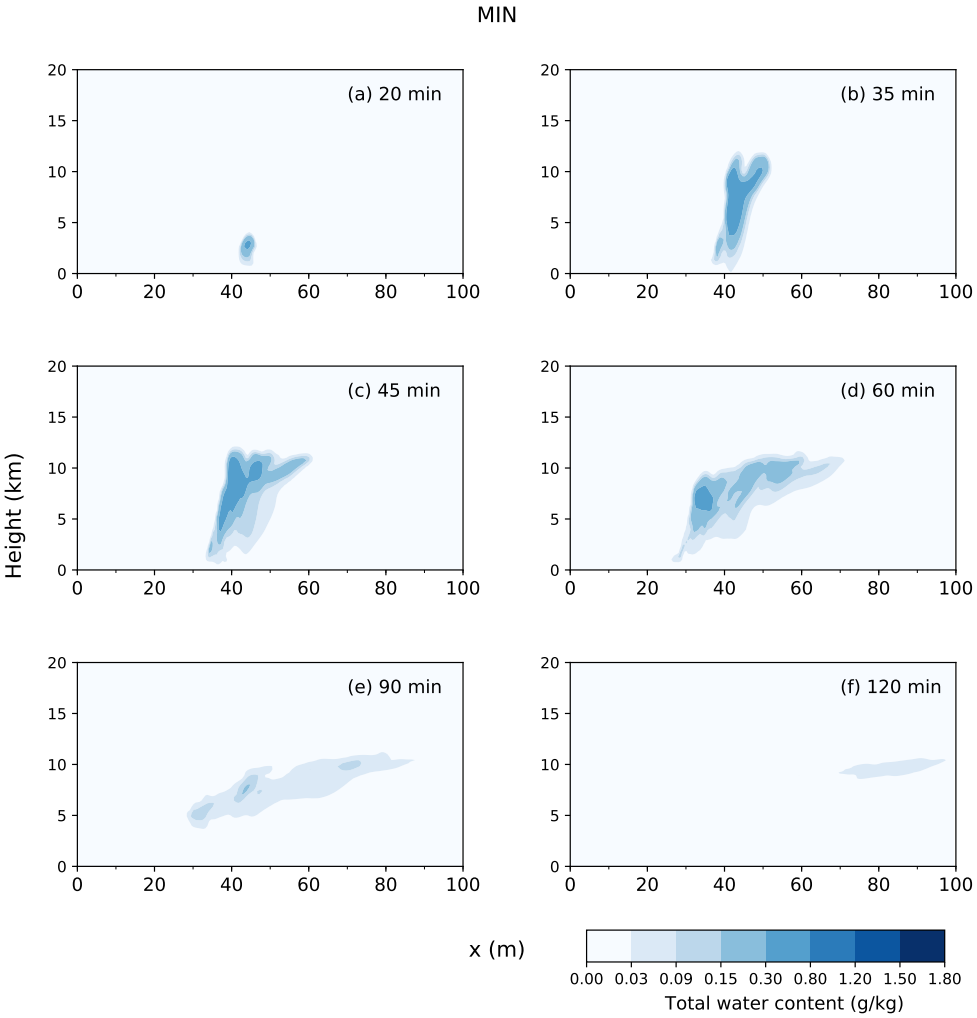

Figure C.2: 2D vertical cross section of averaged total water content in simulated deep convective clouds in $\theta_F RH_F$ (future environment) for Minneapolis, MIN at (a) 20 min, (b) 35 min, (c) 45 min, (d) 60 min, (e) 90 min, and (f)120 min.

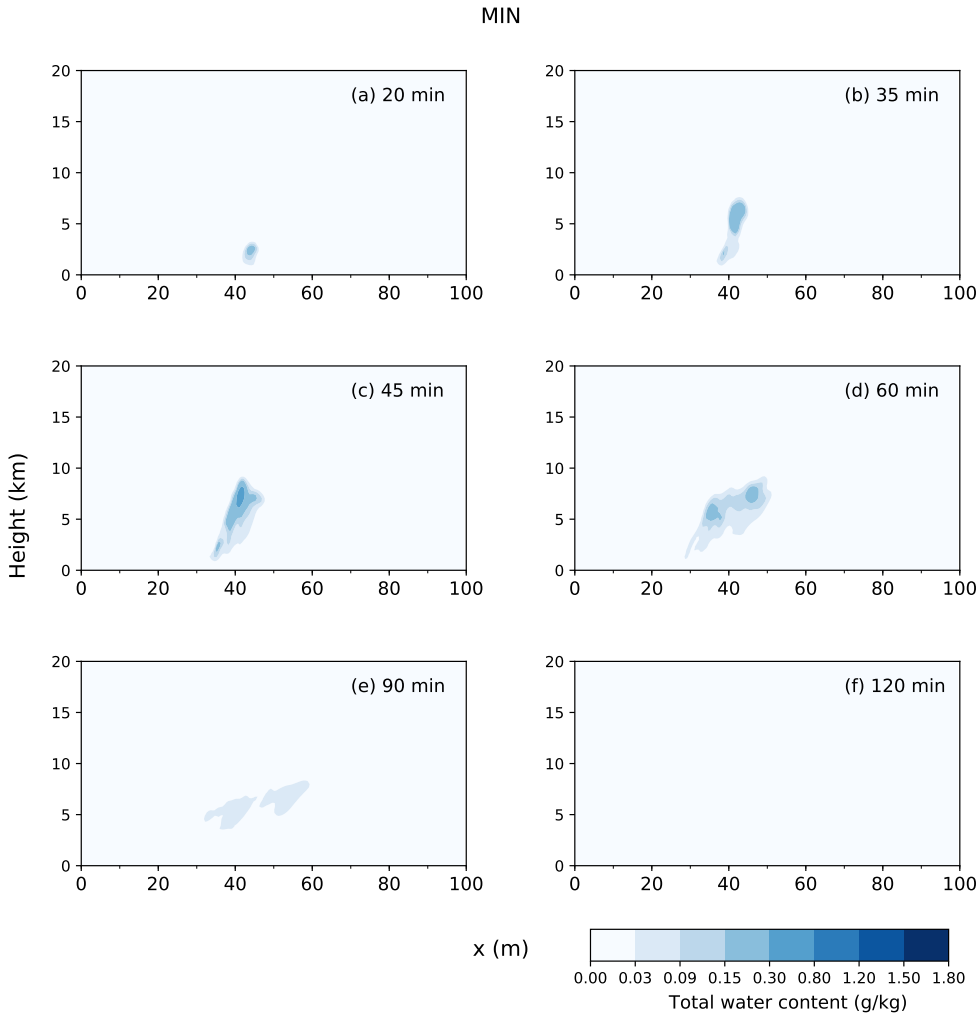

Figure C.3: 2D vertical cross section of averaged total water content in simulated deep convective clouds in $\overline{\theta}_{F \rightarrow P} RH_F$ for Minneapolis, MIN at (a) 20 min, (b) 35 min, (c) 45 min, (d) 60 min, (e) 90 min, and (f)120 min.

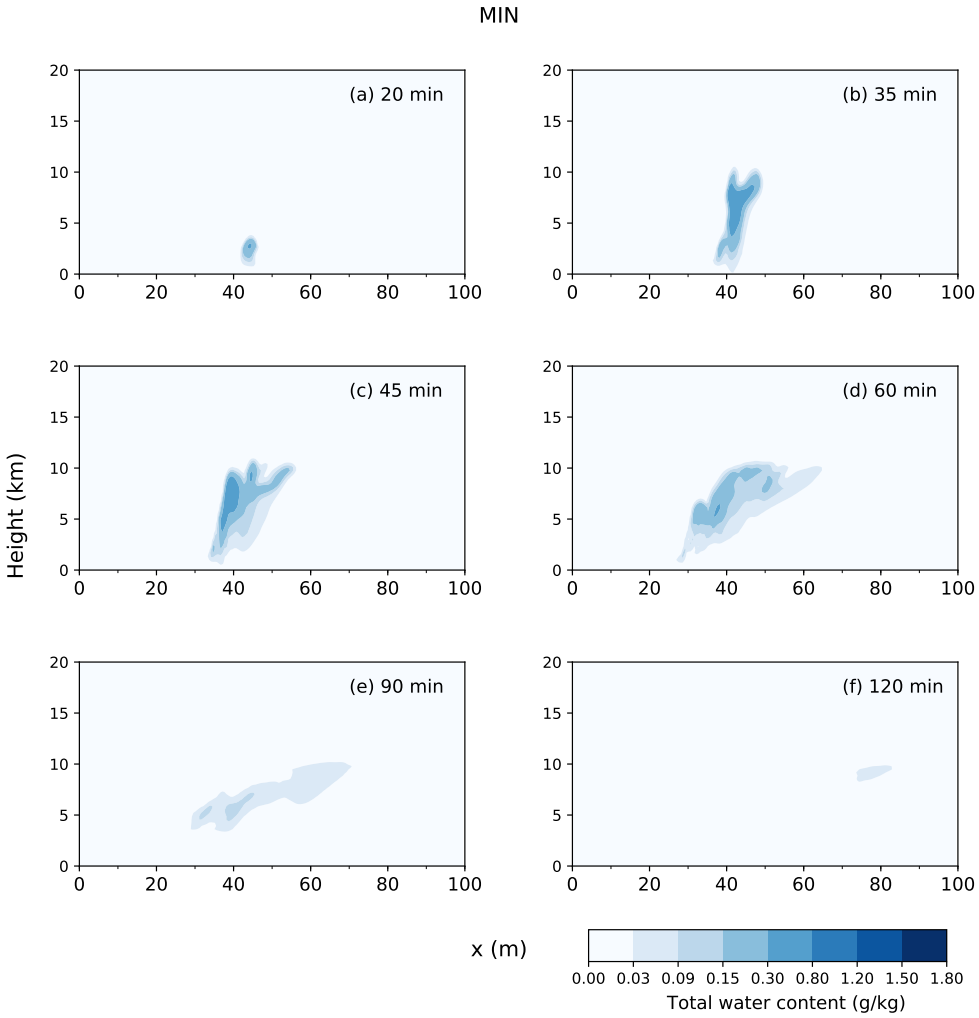

Figure C.4: 2D vertical cross section of averaged total water content in simulated deep convective clouds in $\overline{\theta}_{F\rightarrow P}RH_{F\rightarrow P}$ for Minneapolis, MIN at (a) 20 min, (b) 35 min, (c) 45 min, (d) 60 min, (e) 90 min, and (f)120 min.

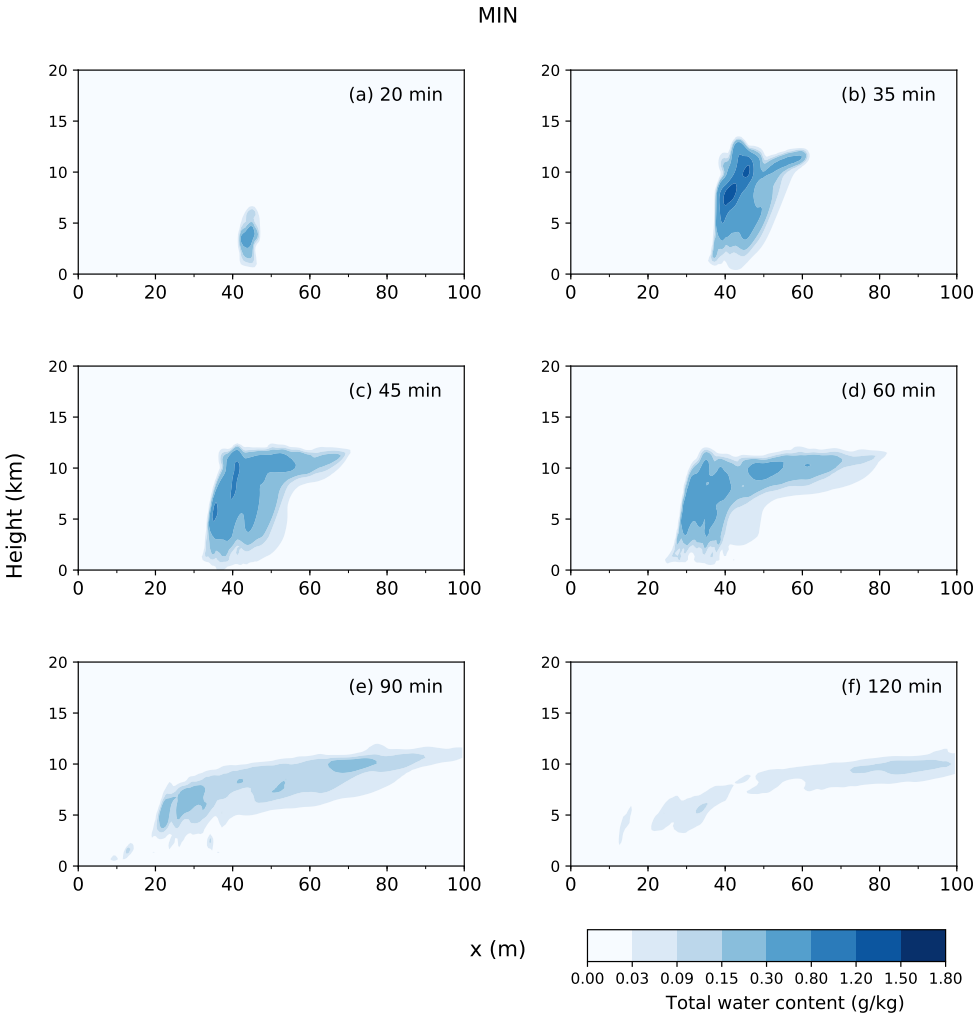

Figure C.5: 2D vertical cross section of averaged total water content in simulated deep convective clouds in $\theta_P RH_{P\rightarrow F}$ for Minneapolis, MIN at (a) 20 min, (b) 35 min, (c) 45 min, (d) 60 min, (e) 90 min, and (f)120 min.